

**Measurement of Electron Anti-Neutrino Oscillation Parameters
with a Large Volume Liquid Scintillator Detector, KamLAND**

PhD thesis

Osamu Tajima

**Department of Physics, Tohoku University
Sendai 980-8578, Japan**

March, 2003

Acknowledgment

I must first thank Professor Atsuto Suzuki. He introduced me to experimental physics and encouraged me to study. Also, I must thank Asst. Prof. Junpei Shirai, Fumihiko Suekane and Kunio Inoue for giving me many advices. I could no have made this study without them.

I would like to thank the entire KamLAND collaboration for the successful construction and operation of the experiment. I could not study without their efforts. Also, I would like to thank for all of people who support my life in Kamioka.

I would like to thank for all of people in Research Center for Neutrino Science (RCNS) at Tohoku university. Prof. Akira Yamaguchi taught me basic concepts of the high energy physics. Prof. Hitoshi Yamamoto taught me the statistics for data analysis. Prof. Toshio Kitagaki, all of the students in RCNS admire his attitude to the study. Prof. Koya Abe taught me his precious experience. Many thanks to Asst. Prof. Tomoki Hayashino, Dr. Tadashi Nagamine, Dr. Takuya Hasegawa and Dr. Masayuki Koga. Special thanks to Dr. M. Koga again for his strict but kind teaching. Thanks to Tomoaki Takayama, Hiromitsu Hanada, Takashi Nakajima and Minoru Nakajima, for their technical support. Thanks to Kyoko Tamae for her various support. Thanks to all members of the secretarial, postdoctoral and other staffs for their kindly support. Special thanks to Dr. Jesse Goldman for his advice about English.

Thanks to Toshiyuki Iwamoto, Hiroshi Ogawa and Sanshiro Enomoto for their kind support, advices and many discussions with me. Special thanks to Hideki Watanabe. I could not have made of this thesis without his support and encouragement. I also thank them for their friendship. Thanks to all the graduates and seniors of RCNS for their friendship.

And finally, I thank my parents, Noboru and Hideko Tajima, grandmother Kayo Tajima, and brothers Minoru and Akihiro Tajima for their unfailing support in my life.

Abstract

The solar neutrino anomaly, deficit of solar neutrinos, had not been solved more than 30 years. Recently, neutrino oscillation of ν_μ and flavor transition of solar neutrinos are evident. Yet, oscillation parameters of ν_e to explain the solar neutrino anomaly had not been determined strictly. The “large mixing angle” (LMA) region is the most convincing parameter region from the global analysis using all solar neutrino experiments. But there was no experiment to determine it by itself. The determination of oscillation parameters is the last subject for the solar neutrino anomaly.

KamLAND (a $\bar{\nu}_e$ detector with a 1,000 ton large volume liquid scintillator) measured reactor $\bar{\nu}_e$ flux from distant nuclear reactors from March 4 to October 6, 2002 (145.09 days livetime). Due to the ambiguity associated with Geo $\bar{\nu}_e$, analysis threshold is given for $\bar{\nu}_e$ energy 3.4 MeV usually. It is observed fewer $\bar{\nu}_e$ events (54 events) than expectation (86.78 ± 5.59 events) from standard assumptions about $\bar{\nu}_e$ propagation at the 99.95% C.L.

The ratio of the observed inverse β -decay events to the expected number without $\bar{\nu}_e$ disappearance is $0.611 \pm 0.085(\text{stat}) \pm 0.041(\text{syst})$. In the context of two-flavor neutrino oscillation with CPT invariance, all solutions to the solar neutrino problem except for the LMA region and lower part of LMA are excluded by the hypothesis test between detected event rate and expected event rate for each oscillation parameter set. It is no exaggeration to say that the last subject of the solar neutrino anomaly is solved. Considering with the energy spectrum shape distortion as well as the rate gives more precise oscillation parameters. The Δm^2 is limited $6 \sim 8 \times 10^{-5} \text{ eV}^2$ at 90% C.L. with no limitation for the mixing angle. The higher mixing angle is favored but its allowed range is not narrow: $\theta = 27^\circ \sim 63^\circ$ at 90% C.L. with no limitation for the Δm^2 .

Contents

1	Introduction	1
1.1	Neutrino Oscillation	3
1.1.1	Vacuum Oscillation	3
1.1.2	Neutrino Oscillations in Matter (MSW Effect)	5
1.1.3	CP violation in the lepton sector	7
1.1.4	Consideration of the Neutrino Mass	8
1.2	Solar Neutrino Anomaly	10
1.2.1	First observation of solar neutrino at Homestake	10
1.2.2	Standard Solar Model (SSM)	11
1.2.3	Kamiokande, real time solar neutrino observation	11
1.2.4	Observation of pp neutrino, SAGE and GALLEX	12
1.3	Discovery of Neutrino Oscillation	13
1.3.1	Anomaly of atmospheric neutrinos	13
1.3.2	Search for Neutrino Oscillation using Reactor Anti-Neutrinos	13
1.3.3	Evidence for oscillation of ν_μ	14
1.4	Solar Neutrino Flavor Changing	15
1.5	Motivation of this thesis	17
2	KamLAND Experiment	19
2.1	KamLAND Detector	22
2.1.1	Structure	22
2.1.2	Liquid scintillator and buffer oil	24
2.1.3	Target mass	25
2.1.4	Plastic balloon, balloon strap and acrylic plate	26
2.1.5	Purification system	27
2.1.6	PMT	28
2.1.7	Front-End Electronics (FEE)	30
2.1.8	Trigger system	31
2.2	Anti-Neutrino Detection	34
2.2.1	Delayed Coincidence Technique	34
2.2.2	Observed spectrum	36
2.2.3	Cross section of inverse β -decay	37
3	Event Reconstruction and Detector Calibration	40
3.1	Digital Waveform Analysis	41
3.1.1	Algorithm	41
3.1.2	Calibration of time bin width using clock test pulse	43
3.2	Single Photo-electron Charge Calibration (Gain Calibration)	45

3.3	Bad Channel Selection	45
3.4	Timing Calibration	47
3.5	Radioactive Source Calibration	50
3.6	Vertex Reconstruction	57
3.6.1	Fundamental algorithm	57
3.6.2	Tuning	57
3.6.3	Reconstruction uncertainty	58
3.7	Energy Reconstruction	61
3.7.1	Visible energy calculation	61
3.7.2	Correction for nonlinearity of visible energy	62
3.8	Muon Track Reconstruction	77
3.8.1	Selection criteria	78
3.8.2	Track reconstruction	78
3.8.3	Residual charge	81
3.9	Noise Event Selection (Noise Cut)	83
3.10	Flasher Event Selection (Flasher Cut)	86
4	Radioactivities in/into the Detector and Background	88
4.1	Study of Single Events	90
4.2	Measurement of ^{238}U and ^{232}Th	95
4.3	Spallation Study	99
4.3.1	Spallation neutron	99
4.3.2	Long life spallation products	104
4.3.3	^8He and ^9Li : neutron emitters	107
4.3.4	Spallation cut criteria and background estimation for $\bar{\nu}_e$ selection . . .	109
4.4	Fast Neutron	110
4.5	Accidental Coincidence for Anti-Neutrino Selection	112
4.6	Other $\bar{\nu}_e$ sources	116
5	Calculation of Reactor Anti-Neutrino	117
5.1	Calculation of Reactor $\bar{\nu}_e$ Flux	119
5.2	Calibration for the Delayed Coincidence	126
5.2.1	Comparison of Am-Be source calibration and MC simulation	126
5.2.2	Calibration for the time correlation	127
5.2.3	Calibration for the space correlation	127
5.3	Live Time Calculation	132
5.3.1	Deadtime	132
5.3.2	Detector veto time	134
5.3.3	Livetime calculation	135
6	Anti-Neutrino Event Selection	137
6.1	Selection Criteria	138
6.2	Event Reduction	138
6.3	Significance of Reactor Anti-Neutrino Disappearance	146

7	Oscillation Analysis	148
7.1	Hypothesis test using $\bar{\nu}_e$ Rate above 2.6MeV	149
7.2	Rate + Shape Analysis	152
7.2.1	The χ^2 and the Likelihood for Anti-Neutrino and Background Event Rate	152
7.2.2	Likelihood for Energy Spectrum Shape Distortion	153
7.2.3	Consideration of the Spectrum Uncertainty	154
7.2.4	Analysis results at 2.6 MeV threshold case	162
7.2.5	Analysis results at 0.9 MeV threshold case	165
7.3	Matter effects in reactor anti-neutrino analysis	169
7.4	Sensitivity for the 3 generation oscillation analysis	171
8	Summary	173
A	KamLAND collaboration	175
B	Trigger Types	176
C	Decay of ^{238}U, ^{232}Th and ^{40}K	180
C.1	^{238}U series	180
C.2	^{232}Th series	181
C.3	Level diagram for ^{40}K	181
D	Nuclear Level Diagrams of Calibration sources	184
D.1	^{68}Ge	184
D.2	^{65}Zn	185
D.3	^{60}Co	185

List of Tables

1.1	The relation between the electron density and the mixing angle in the matter.	6
2.1	Number of PMT in the detector	23
2.2	Liquid Scintillator Parameters	24
2.3	Parameters of mineral oils and pseudocumene	25
2.4	Buffer Oil Parameters	25
2.5	Rn permeability, solubility and diffusion constant of materials	26
2.6	Detector Parameters	27
2.7	Neutron capture nuclei	36
3.1	Simplified specifications of calibration sources	50
3.2	Correlation of calibration source energy with visible energy	62
4.1	Summary of Backgrounds for $\bar{\nu}_e$ (events / data-set)	89
4.2	Detection efficiency of Bi-Po coincidence event in U chain	97
4.3	Detection efficiency of Bi-Po coincidence event in Th chain	97
4.4	Spallation products (not neutron emitter)	104
4.5	Spallation products : neutron emitter	104
5.1	$\bar{\nu}_e$ detection efficiency	117
5.2	Systematic uncertainties of $\bar{\nu}_e$ detection	118
5.3	Contribution of thermal flux to KamLAND	120
5.4	Japanes and Korean reactors - part 1 -	121
5.5	Japanes and Korean reactors - part 2 -	122
6.1	Summary of the significance for reactor $\bar{\nu}_e$ disappearance	137
B.1	Trigger types as recorded by the trigger	179
C.1	Decay chain of ^{238}U	182
C.2	Decay chain of ^{232}Th	183

List of Figures

1.1	Feynman diagrams of neutrinos-electron reaction	5
1.2	MSW : resonance condition and flavor changing	7
1.3	Some models for the neutrino mass	9
1.4	SSM vs experiments[1]	10
1.5	SSM: pp-chain	12
1.6	Solar neutrino flux based on SSM [1]	12
1.7	Helioseismology: SSM vs measurement [1]	13
1.8	Correlation of data/MC with L/E_ν for atmospheric neutrinos. [2]	15
1.9	Flux of ^8B solar neutrinos deduced from the three neutrino reactions in SNO [3]	16
1.10	Oscillation parameters for electron neutrino before KamLAND [4]	17
1.11	Correlation of the sensitivity to observe the CP violation with Δm_{12}^2 at the long base-line experiment, JHF Hyper-Kamiokande [5]	18
2.1	Around KamLAND area	19
2.2	Contribution of each Japanese reactor	20
2.3	Japanese nuclear reactors map	21
2.4	Schematic diagram of the KamLAND detector	23
2.5	Purification system	27
2.6	Mechanical difference between 17" PMT and 20" PMT	28
2.7	Quantum efficiency of PMT which measure by Hamamatsu company.	28
2.8	Comparison of performance between 17" PMT and 20" PMT	29
2.9	ATWD : Analog Transit Waveform Digitizer	30
2.10	Digital waveform from FEE	31
2.11	Prompt trigger efficiency	32
2.12	Delayed trigger efficiency	33
2.13	Inverse β -decay & delayed coincidence technique	34
2.14	Kinematics in the inverse β -decay	35
2.15	The cross section of inverse β -decay ($\bar{\nu}_e p \rightarrow n e^+$) [6].	37
3.1	Data analysis and reduction flow.	40
3.2	Pedestals of digital waveform	43
3.3	Two photon pulse information is analyzed in the waveform analysis.	44
3.4	Periodic test pulse for time interval calibration between each samples.	44
3.5	Time variation of the 1p.e. charge	45
3.6	Charge, pulse area, histogram in low occupancy events.	46
3.7	Time variation for the number of bad-channels	47
3.8	Overview of the timing calibration	48
3.9	TQ-map : time-charge correlation of one channel	49
3.10	Time correlation of each channel, before and after the timing calibration	49

3.11	Layouts for calibration sources and deployment	50
3.12	$^{68}\text{Ge}(2\gamma, 0.511\times 2\text{MeV})$ calibration with deploying the center position	51
3.13	$^{68}\text{Ge}(2\gamma, 0.511\times 2\text{MeV})$ calibration at $z=-500\text{cm}$	52
3.14	$^{65}\text{Zn}(1\gamma, 1.11552\text{MeV})$ calibration at center	53
3.15	$^{65}\text{Zn}(1\gamma, 1.11552\text{MeV})$ calibration at $z=-500\text{cm}$	54
3.16	$^{60}\text{Co}(2\gamma, 1.173+1.333\text{MeV})$ calibration at center	55
3.17	$^{60}\text{Co}(2\gamma, 1.173+1.333\text{MeV})$ calibration at $z=-575\text{cm}$	56
3.18	Consideration of the vertex reconstruction	57
3.19	Tuning parameter of vertex reconstruction	58
3.20	Deviations of reconstructed vertex along z-axis for various radioactivities	59
3.21	Vertex distribution of 2.2 MeV neutron capture	60
3.22	Vertex distribution of β -decay events from $^{12}\text{B} / ^{12}\text{N}$ spallation products	60
3.23	Time properties of detected scintillation light	65
3.24	Singles spectra of nhits, charge sum and visible energy	65
3.25	Correlation of the total charge sum with reconstructed vertex	66
3.26	Tuning of the visible energy	66
3.27	Time variation of the energy for source calibration	67
3.28	Time variation of the energy scale for ^{40}K and ^{208}Tl	67
3.29	Time variation of the visible energy	68
3.30	Deviation of the visible energy at various positions along z-axis	69
3.31	Resolution of the visible energy at various positions along z-axis	70
3.32	Position dependences of visible energy for spallation neutron	71
3.33	Histograms of spallation neutron energy along to the radial direction	72
3.34	Histograms of spallation neutron energy along to z-axis	73
3.35	Correlation between the visible energy and deposited energy	74
3.36	Relation between visible energy and energy for ^{60}Co and ^{65}Zn	74
3.37	Uncertainty in the parameters for the energy scale correction	75
3.38	Nonlinearity correction (upper) and uncertainty of gamma-ray energy	75
3.39	Nonlinearity correction (upper) and uncertainty of electron energy	76
3.40	Nonlinearity correction (upper) and uncertainty of positron energy	76
3.41	Charge distribution of the muon event	77
3.42	Muon track reconstruction	79
3.43	Entrance point of the muon track	80
3.44	Exit point of the muon track	80
3.45	Correlation between total charge and reconstructed track length.	81
3.46	dQ/dX of muon track	82
3.47	Event display of usual event	84
3.48	Event display of typical noise event	84
3.49	Cut condition for noise events	85
3.50	Event display of successive events	85
3.51	Noise event rate for each run	86
3.52	Event display of a typical flasher PMT event	87
3.53	Cut criteria of flasher event	87
4.1	Energy spectra of single events in the whole volume	90
4.2	Vertex distributions of various energy events in the whole volume	91
4.3	Correlation of the energy spectrum with fiducial radius	92
4.4	Vertex distributions within 5 m radius in various energy	93

4.5	Single spectrum with the 4m fiducial radius without the 1.2 m radius cylindrical region along z-axis	94
4.6	$^{214}\text{Bi} \rightarrow ^{214}\text{Po} \rightarrow ^{210}\text{Pb}$	96
4.7	$^{212}\text{Bi} \rightarrow ^{212}\text{Po} \rightarrow ^{208}\text{Pb}$	98
4.8	NsumMax spectrum after muon within 1msec	99
4.9	Correlation between Nhit/NsumMax-1 and time difference from last muon and NsumMax	100
4.10	Time difference from last muons to spallation neutron capture events	101
4.11	Correlation between the multiplicity of spallation neutron and the residual charge of muon event	102
4.12	Time difference from last muon to spallation neutron capture event	102
4.13	Correlation between the reconstructed muon track and reconstructed vertex of neutron capture events	103
4.14	Energy spectra for 2msec and 10msec following muon	103
4.15	Correlations of spallation products with muons	105
4.16	Energy spectrum of single spallation events	106
4.17	^8He , ^9Li follows muon event	107
4.18	Time correlation between ^8He , ^9Li between non-energetic muon	108
4.19	Decay electron near the balloon edge	110
4.20	Fast neutron candidates	111
4.21	Distribution of accidental coincidence events within 5 m fiducial radius at 0.9 MeV threshold	112
4.22	Distribution of accidental coincidence events within 5 m fiducial radius at 2.6 MeV threshold	112
4.23	3D distribution of accidental coincidence events within 5 m fiducial radius at 0.9 MeV threshold	113
4.24	3D distribution of accidental coincidence events within 5 m fiducial radius at 2.6 MeV threshold	113
4.25	Distribution of the accidental coincidence events with the 5 m fiducial radius and with the cylindrical cut at 0.9MeV threshold	114
4.26	Distribution of the accidental background events with the 5 m fiducial radius and with the cylindrical cut at 2.6MeV threshold	114
4.27	Flat time distribution of accidental coincidence	114
4.28	Prompt energy spectrum of accidental coincidence	114
4.29	Distribution of the accidental background events within 5.2 m fiducial radius . .	115
4.30	Prompt energy spectrum of Geo $\bar{\nu}_e$	116
5.1	Nuclear power stations in Asia	123
5.2	Nuclear power stations in the world	123
5.3	Energy spectra of $\bar{\nu}_e$ flux from each nuclear fission, ^{235}U , ^{238}U , ^{239}Pu and ^{241}Pu	124
5.4	Uncertainty of neutrino energy spectrum for no oscillation case. The uncertainties of number of reactor $\bar{\nu}_e$ derived from this spectrum uncertainty are 2.48% for 2.6 MeV analysis threshold (2.25% for 0.9 MeV analysis threshold) in case of no oscillation.	124
5.5	Fission rate of each isotopes	124
5.6	Time variation of $\bar{\nu}_e$ flux from reactors	125
5.7	$\bar{\nu}_e$ energy spectra from long life nuclei(Ce144 , Ru106) and general reactor $\bar{\nu}_e$ spectrum for no oscillation case	125

5.8	Geometry of Am-Be source moderator	126
5.9	Visible energy spectrum of Am-Be calibration source	128
5.10	Time distribution of the neutron capture on proton and mean capture time	128
5.11	MC simulation of the recoil neutron	129
5.12	Diffusion of the positron and γ 's in the MC	130
5.13	Detection efficiencies of the neutron capture event within 160cm at various z position	131
5.14	Time intervals between each history event	133
5.15	Time interval of noise event after last muon	133
5.16	Unknown deadtime percentage for each run	133
5.17	Ratio of livetime/runtime for each run	135
6.1	Correlation of the event reduction with total charge sum	139
6.2	Correlation of the energy spectrum and fiducial radius, and delayed coincidence	140
6.3	Flow chart of $\bar{\nu}_e$ selection	141
6.4	Distribution of events after delayed-coincidence selection	142
6.5	Profiles of $\bar{\nu}_e$ candidates	143
6.6	Space & time correlation with delayed energy	144
6.7	Correlations with prompt energy	145
6.8	Detected and expected event rate of $\bar{\nu}_e$	146
6.9	History of reactor $\bar{\nu}_e$ disappearance searches	147
7.1	Excluded region of neutrino oscillation parameters by using rate analysis	149
7.2	KamLAND excludes SMA, LOW, VAC and a part of LMA solutions [4]	150
7.3	χ^2 projections to Δm^2 and $\sin^2 2\theta$ axis in rate analysis	151
7.4	Energy spectrum distortion follows energy dependent vertex correction	156
7.5	Energy spectrum distortion follows energy resolution	156
7.6	Generated points of Geo $\bar{\nu}_e$ simulation	157
7.7	Affection of the spectrum distortion of Geo $\bar{\nu}_e$ based on "standard distribution model"	158
7.8	Affection of the spectrum distortion of Geo $\bar{\nu}_e$ based on "mantle rich distribution model"	159
7.9	Affection of the spectrum distortion of Geo $\bar{\nu}_e$ based on "crust rich distribution model"	160
7.10	χ^2 difference with/without Geo $\bar{\nu}_e$ spectrum distortion	161
7.11	χ^2 difference with/without 3 types of Geo $\bar{\nu}_e$ spectrum distortion	161
7.12	Allowed region from shape only analysis above 2.6 MeV data set	162
7.13	Prompt energy spectra of data and best fit parameters of "rate+shape" analysis above 2.6 MeV data set	163
7.14	Allowed region of "rate+shape" analysis above 2.6 MeV data set	163
7.15	$\Delta\chi^2$ projection to Δm^2 axis and $\sin^2 2\theta$ axis above 2.6 MeV data set	164
7.16	Allowed region from shape only analysis above 0.9 MeV data set	165
7.17	Prompt energy spectra of data and best fit parameters of "rate+shape" analysis above 0.9 MeV data set	166
7.18	Allowed region of "rate+shape" analysis above 0.9 MeV data set	166
7.19	$\Delta\chi^2$ projection to Δm^2 axis and $\sin^2 2\theta$ axis above 0.9 MeV data set	167
7.20	Contour plots for oscillation parameters	168
7.21	Matter effects in KamLAND reactor $\bar{\nu}_e$ analysis	169

7.22	Affection of the matter effects for “rate” analysis	170
7.23	Affection of the matter effects for “rate + shape” analysis	170
7.24	Sensitivity for θ_{13}	171
7.25	Sensitivity for Δm_{12}^2 and $\sin^2 2\theta_{12}$	172
C.1	Decay chain of ^{238}U series	180
C.2	Decay chain of ^{232}Th series	181
C.3	Level diagram for ^{40}K	181
D.1	Level diagram for ^{68}Ge	184
D.2	Level diagram for ^{65}Zn	185
D.3	Level diagram for ^{60}Co	185

Chapter 1

Introduction

The neutrino which was predicted by W. Pauli in 1930 to explain the continuum spectrum of β decay, the existence of it was discovered by F. Reines and C.L. Cowan in 1956 [7]. They detected anti-neutrino ($\bar{\nu}_e$) from a nuclear reactor using liquid scintillator via the inverse β -decay reaction,

$$\bar{\nu}_e + p \rightarrow e^+ + n \quad (1.1)$$

KamLAND, which is a large volume liquid scintillator detector, follows this technique. On the other hand, R. Davis Jr. and his colleagues succeeded in detecting neutrinos from the Sun in 1968 [8]. But the number of detected neutrinos is much less ($\sim 1/3$) than theoretical predictions based on the solar model. This was the first measurement of the solar neutrino anomaly.

Results from various solar neutrino experiments gave the same answer as lack of the solar neutrino though accuracy of the solar model was improving by Helioseismology and so on. The neutrino oscillation, which was suggested by Maki, Nakagawa and Sakata in 1962 [9], well explains for this anomaly. The neutrino oscillation predicts flavor changing of neutrinos as in the quark sector, where transition probability depends on energy, flight distance, mixing angle, and the mass difference between the different flavor neutrinos.

Atmospheric neutrinos also exhibit such an anomaly. The ratio between the electron type neutrino and the muon type, is inconsistent with 1 : 2 which is predicted as follows,

$$\pi^+(\pi^-) \rightarrow \mu^+(\mu^-) + \nu_\mu(\bar{\nu}_\mu) \quad (1.2)$$

$$\mu^+(\mu^-) \rightarrow e^+(e^-) + \bar{\nu}_\mu(\nu_\mu) + \nu_e(\bar{\nu}_e) \quad (1.3)$$

The Super-Kamiokande (SK) group discovered that the atmospheric neutrino anomaly is in fact caused by neutrino oscillations in 1998 [2]. They measured the correlation of the number of muon type neutrino with various zenith angle (various flight distance), and they observed the disappearance of the muon type neutrino at various flight distances. This was very strong evidence for neutrino oscillations.

Moreover, the flavor changing from ν_e to ν_μ or ν_τ was reported based on the measurement of the charged current (CC), the neutral current (NC) and elastic scattering (ES) of solar neutrinos, which were measured by the SNO and SK groups,

$$\nu_e + d \rightarrow p + p + e^- \quad (\text{CC : SNO}), \quad (1.4)$$

$$\nu_{e,(\mu,\tau)} + d \rightarrow p + n + \nu_{e,(\mu,\tau)} \quad (\text{NC : SNO}), \quad (1.5)$$

$$\nu_{e,(\mu,\tau)} + e^- \rightarrow \nu_{e,(\mu,\tau)} + e^- \quad (\text{ES : SK and SNO}). \quad (1.6)$$

Yet, oscillation parameters for the solar neutrinos had not been determined because there were four candidate solutions and their maximum is 1,000,000 higher than their minimum for Δm^2 . These solutions are called 'Large Mixing Angle solution' (LMA), 'Low Δm^2 solution for Large Mixing Angle' (LOW), 'Small Mixing Angle solution' (SMA) and 'Vacuum Oscillation solution' (VAC). The LMA solution is favored from the global analysis which combine measurement results of all solar neutrino experiments but there was no experiment to determine the LMA is the solution by itself. The determination of oscillation parameters is the last subject for the solar neutrino anomaly.

KamLAND is the experiment to test the LMA directly via the observation of electron anti-neutrinos from nuclear reactors. Due to the ambiguity associated with Geo $\bar{\nu}_e$ below 2.49 MeV for the prompt energy, the analysis of reactor $\bar{\nu}_e$ is performed above 2.6 MeV prompt energy usually (HAT: higher energy analysis threshold). Analysis with lower energy region (≥ 0.9 MeV) is used for the consistency check of analysis (LAT: lower energy analysis threshold). Study of oscillation parameters for electron anti-neutrino is described in this thesis. This thesis is organized as follows,

Chapter 1 :

Neutrino oscillation and historical review of experiments for the neutrino oscillation are described in this chapter. The motivation of this thesis is described in the last section of this chapter.

Chapter 2 :

It is described as KamLAND detector. Delayed coincidence selection which is the method of $\bar{\nu}_e$ detection is also described.

Chapter 3 :

The event reconstruction and calibration of it. Systematic uncertainties of reconstruction are also discussed in this chapter.

Chapter 4 :

Selection criteria of $\bar{\nu}_e$ except for the delayed coincidence are decided from the viewpoint of background rejection. Fiducial volume cut criteria are decided from the study of accidental coincidence background. Muon veto and spallation cut criteria are decided from the study of correlated background from muon spallation products. The other internal and external background studies are also described in this chapter.

Chapter 5 :

For observation of the reactor $\bar{\nu}_e$ disappearance, calculation of the reactor $\bar{\nu}_e$ flux and calibration of the detection efficiency are essential. Detection efficiency of $\bar{\nu}_e$ and systematic uncertainties are summarized at the beginning of this chapter. The calculation of reactor $\bar{\nu}_e$ flux and calibration for the delayed coincidence are also described in this chapter.

Chapter 6 :

Selection of reactor $\bar{\nu}_e$ candidates is shown in this chapter. It is also described about the significance for the reactor $\bar{\nu}_e$ disappearance which could be caused by neutrino oscillations.

Chapter 7 :

Measurement for the oscillation parameters using the detected event rate and the energy spectrum shape distortion are described in this chapter.

Chapter 8 :

Summary and conclusion.

1.1 Neutrino Oscillation

1.1.1 Vacuum Oscillation

If neutrinos have a mass, the theory up to the present has to be modified. For massive neutrinos, the flavor eigenstates, ν_e, ν_μ, ν_τ , are not the same as the mass eigenstates, ν_1, ν_2, ν_3 , and their relation is written by the mixing matrix which is similar to the Cabibo-Kobayashi-Masukawa (CKM) matrix [10] for quarks.

$$|\nu_\alpha\rangle = \sum_{j=1}^3 U_{\alpha j} |\nu_j\rangle \quad (\alpha = e, \mu, \tau), \quad (1.7)$$

where, U is defined with mixing angle $\theta_{12}, \theta_{23}, \theta_{13}$ and a CP phase δ ,

$$U = \begin{pmatrix} 1 & 0 & 0 \\ 0 & c_{23} & s_{23} \\ 0 & -s_{23} & c_{23} \end{pmatrix} \begin{pmatrix} c_{23} & 0 & s_{13}e^{-i\delta} \\ 0 & 1 & 0 \\ -s_{13}e^{i\delta} & 0 & c_{13} \end{pmatrix} \begin{pmatrix} c_{12} & s_{12} & 0 \\ -s_{12} & c_{12} & 0 \\ 0 & 0 & 1 \end{pmatrix} \quad (1.8)$$

$$= \begin{pmatrix} c_{12}c_{13} & s_{12}c_{13} & s_{13}e^{-i\delta} \\ -s_{12}c_{23} - c_{12}s_{23}s_{13}e^{i\delta} & c_{12}c_{23} - s_{12}s_{23}s_{13}e^{i\delta} & s_{23}c_{13} \\ s_{12}s_{23} - c_{12}c_{23}s_{13}e^{i\delta} & -c_{12}s_{23} - s_{12}c_{23}s_{13}e^{i\delta} & c_{23}c_{13} \end{pmatrix} \quad (1.9)$$

where, $s_{ij} = \sin \theta_{ij}$, $c_{ij} = \cos \theta_{ij}$ ($i, j = 1, 2, 3$). This relation allows for the possibility that one neutrino (ν_α) converts to another flavor (ν_β). This phenomenon is known as neutrino oscillation.

Time evolution of the states obeys the Shrödinger equation,

$$i \frac{d}{dt} |\nu_j\rangle = E_j |\nu_j\rangle \quad (1.10)$$

where, E_j is the energy of ν_j , and so the wave function can be written as,

$$|\nu_j(t)\rangle = e^{-iE_j t} |\nu_j(0)\rangle. \quad (1.11)$$

For flavor eigenstates, using Eq.(1.7) and Eq.(1.10), (1.11),

$$i \frac{d}{dt} |\nu_\alpha\rangle = \sum_{j=1}^3 U_{\alpha j} E_j U_{j\alpha}^\dagger |\nu_\alpha\rangle \quad (1.12)$$

$$|\nu_\alpha(t)\rangle = \sum_{j=1}^3 U_{\alpha j} e^{-iE_j t} U_{j\alpha}^\dagger |\nu_\alpha(0)\rangle. \quad (1.13)$$

If ν_α is produced at $t = 0$, the probability of detecting this neutrino at $t = t$ is

$$P(\nu_\alpha \rightarrow \nu_\beta) = |\langle \nu_\beta(t) | \nu_\alpha(0) \rangle|^2 \quad (1.14)$$

$$= \sum_{j=1}^3 \left| \langle \nu_\beta(t) | U_{\alpha j} e^{-iE_j t} U_{j\alpha}^\dagger | \nu_\alpha(0) \rangle \right|^2 \quad (1.15)$$

$$= \delta_{\alpha\beta} - 4 \sum_{i>j} \text{Re} (U_{\alpha i}^* U_{\beta i} U_{\alpha j} U_{\beta j}^*) \cdot \sin^2 \Phi_{ij} \\ \pm 2 \sum_{i>j} \text{Im} (U_{\alpha i}^* U_{\beta i} U_{\alpha j} U_{\beta j}^*) \cdot \sin^2 \Phi_{ij} \quad (1.16)$$

where

$$\Phi_{ij} \equiv \frac{\Delta m_{ij}^2 l}{4E_\nu} = \frac{1.27 \Delta m_{ij}^2 [\text{eV}^2] l [\text{km}]}{E_\nu [\text{GeV}]} \quad (1.17)$$

$\Delta m_{ij}^2 = m_i^2 - m_j^2$, l is the flight distance, and E_ν is the neutrino energy. The sign in the third term of Eq.(1.16) is the CP violation effect, - for neutrinos and + for anti-neutrinos. Because $\Delta m_{12}^2 + \Delta m_{23}^2 + \Delta m_{31}^2 = 0$, there exist only two independent Δm^2 for three species of neutrinos. Thus 3 generation neutrino oscillation can be described by two Δm^2 , three angles ($\theta_{12}, \theta_{23}, \theta_{13}$) and one phase (δ).

To simplify the problem, only two flavors are considered,

$$U = \begin{pmatrix} \cos \theta_V & \sin \theta_V \\ -\sin \theta_V & \cos \theta_V \end{pmatrix} \quad (1.18)$$

where θ_V is the mixing angle in vacuum between ν_e and ν_x . And the survival probability Eq.(1.16) is simplified,

$$P(\nu_\alpha \rightarrow \nu_\beta) = \sin^2 2\theta_V \sin^2 \Phi \quad (1.19)$$

$$= \sin^2 2\theta_V \sin^2 \left(\frac{1.27 \Delta m^2 [\text{eV}^2] l [\text{m}]}{E [\text{MeV}]} \right)^2 \quad (1.20)$$

Therefore, the probability of $\nu_\alpha(\bar{\nu}_\alpha) \rightarrow \nu_\alpha(\bar{\nu}_\alpha)$ is

$$P(\nu_\alpha \rightarrow \nu_\alpha) = 1 - \sin^2 2\theta_V \sin^2 \left(\frac{1.27 \Delta m^2 [\text{eV}^2] l [\text{m}]}{E [\text{MeV}]} \right) \quad (1.21)$$

$$= 1 - \sin^2 2\theta_V \sin^2 \left(\frac{\pi l}{L_V} \right) \quad (1.22)$$

where Δm^2 is the mass square difference between ν_i and ν_j ($\Delta m^2 = |m_i^2 - m_j^2|$, $i, j=1, 2, 3$), l is the propagation length in the time interval of t , and L_V is the oscillation length in vacuum which is defined as

$$L_V \equiv \frac{4\pi E}{\Delta m^2} \quad (1.23)$$

For $\bar{\nu}_\alpha \rightarrow \bar{\nu}_\alpha$, this can be written a similar expression.

From the above equations, it is clear that $P_{\nu_e \rightarrow \nu_e}(t) < 1$, so that the number of observed $\nu_e(\bar{\nu}_e)$ events is less than that of generated $\nu_e(\bar{\nu}_e)$ events if $\nu_e(\bar{\nu}_e)$ and $\nu_x(\bar{\nu}_x)$ have finite different masses and there is a non-zero mixing angle between them.

On the other hand, the Shrödinger equation for two generations is

$$i \frac{d}{dt} \begin{pmatrix} \nu_e \\ \nu_x \end{pmatrix} = U \begin{pmatrix} E_1 & 0 \\ 0 & E_2 \end{pmatrix} U^\dagger \begin{pmatrix} \nu_e \\ \nu_x \end{pmatrix} \quad (1.24)$$

$$= \left[\frac{E_1 + E_2}{2} \begin{pmatrix} 1 & 0 \\ 0 & 1 \end{pmatrix} + \frac{E_2 - E_1}{2} \begin{pmatrix} -\cos 2\theta_V & \sin 2\theta_V \\ \sin 2\theta_V & \cos 2\theta_V \end{pmatrix} \right] \begin{pmatrix} \nu_e \\ \nu_x \end{pmatrix} \quad (1.25)$$

$$= \left[\frac{E_1 + E_2}{2} \begin{pmatrix} 1 & 0 \\ 0 & 1 \end{pmatrix} + \frac{\pi}{L_V} \begin{pmatrix} -\cos 2\theta_V & \sin 2\theta_V \\ \sin 2\theta_V & \cos 2\theta_V \end{pmatrix} \right] \begin{pmatrix} \nu_e \\ \nu_x \end{pmatrix} \quad (1.26)$$

$$\equiv (\hat{H}_0 + \hat{H}_V) \begin{pmatrix} \nu_e \\ \nu_x \end{pmatrix} \quad (1.27)$$

where \hat{H}_V is

$$\hat{H}_V \begin{pmatrix} \nu_e \\ \nu_x \end{pmatrix} \equiv \frac{\pi}{L_V} \begin{pmatrix} -\cos 2\theta_V & \sin 2\theta_V \\ \sin 2\theta_V & \cos 2\theta_V \end{pmatrix} \begin{pmatrix} \nu_e \\ \nu_x \end{pmatrix} \quad (1.28)$$

This Hamiltonian \hat{H}_V is derived assuming the Vacuum Oscillations.

1.1.2 Neutrino Oscillations in Matter (MSW Effect)

General Equations of the MSW Effect

Neutrino oscillations in matter were first proposed by S.P. Mikheyev and A.Yu. Smirnov based on the theory advocated by L. Wolfenstein. Therefore, it is often called the MSW effect.

When neutrinos propagate through matter, ν_e and ν_μ (or ν_τ) feel different potentials because ν_e scatters off electrons via both neutral and charged currents, whereas ν_μ (ν_τ) scatters only via the neutral current (Figure 1.1). The electron neutrino receives an extra contribution of $\sqrt{2}G_F n_e$ which derived from the charged current interaction, where n_e is the electron number density in the matter.

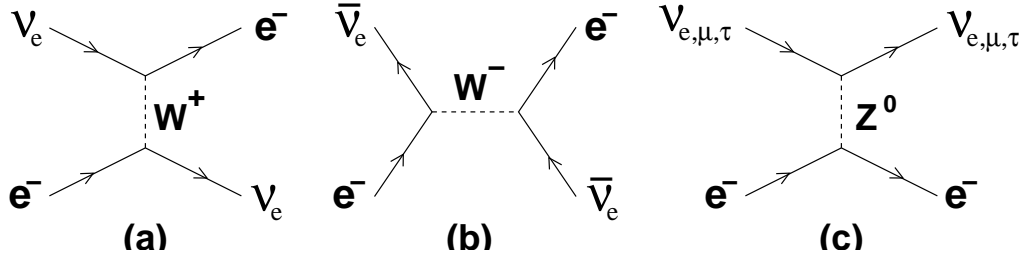


Figure 1.1: Feynman diagrams of the neutrino scattering with electron, (a) is a charged current interaction of ν_e , (b) is a charged current interaction of $\bar{\nu}_e$, and (c) is a neutral current interaction of ν_e, ν_μ, ν_τ ($\bar{\nu}_e, \bar{\nu}_\mu, \bar{\nu}_\tau$).

From these effective potentials, the Hamiltonian in the matter (\hat{H}_M) is written as

$$\hat{H}_M \begin{pmatrix} \nu_e \\ \nu_x \end{pmatrix} = \left(\hat{H}_0 + \hat{H}_V + \hat{H}_e + \hat{H}_{\mu,\tau} \right) \begin{pmatrix} \nu_e \\ \nu_x \end{pmatrix} \quad (1.29)$$

$$= \alpha \begin{pmatrix} 1 & 0 \\ 0 & 1 \end{pmatrix} \begin{pmatrix} \nu_e \\ \nu_x \end{pmatrix} \quad (1.30)$$

$$+ \frac{\pi}{L_V} \begin{pmatrix} \pm \frac{L_V}{\pi} \cdot \frac{G_F n_e}{\sqrt{2}} - \cos 2\theta_V & \sin 2\theta_V \\ \sin 2\theta_V & \mp \frac{L_V}{\pi} \cdot \frac{G_F n_e}{\sqrt{2}} + \cos 2\theta_V \end{pmatrix} \begin{pmatrix} \nu_e \\ \nu_x \end{pmatrix} \quad (1.31)$$

$$\equiv \alpha \begin{pmatrix} 1 & 0 \\ 0 & 1 \end{pmatrix} \begin{pmatrix} \nu_e \\ \nu_x \end{pmatrix} \quad (1.32)$$

$$+ \frac{\pi}{L_V} \begin{pmatrix} \pm \frac{L_V}{L_e} - \cos 2\theta_V & \sin 2\theta_V \\ \sin 2\theta_V & \mp \frac{L_V}{L_e} + \cos 2\theta_V \end{pmatrix} \begin{pmatrix} \nu_e \\ \nu_x \end{pmatrix}, \quad (1.33)$$

where the first term is a common phase¹, The sign '+' ('-') indicates for ν_e ($\bar{\nu}_e$) in ' \pm ' (The sign '-' ('+') indicates for ν_e ($\bar{\nu}_e$) in ' \mp '). and L_e is the neutrino-electron interaction length

¹A common phase can be omitted for the neutrino oscillation, because it doesn't influence on the oscillation.

which is defined as

$$L_e = \frac{\sqrt{2}\pi}{G_F n_e} \quad (1.34)$$

Now, the oscillation length and the mixing angle in matter are defined as L_M and θ_M , respectively.

$$\frac{\pi}{L_M} \begin{pmatrix} -\cos 2\theta_M & \sin 2\theta_M \\ \sin 2\theta_M & \cos 2\theta_M \end{pmatrix} \equiv \frac{\pi}{L_V} \begin{pmatrix} \pm \frac{L_V}{L_e} - \cos 2\theta_V & \sin 2\theta_V \\ \sin 2\theta_V & \mp \frac{L_V}{L_e} + \cos 2\theta_V \end{pmatrix} \quad (1.35)$$

Assuming that $|left\ side| = |right\ side|$ in the above equation, L_M , and $\sin^2 2\theta_M$ can be written as

$$L_M \equiv \frac{L_V}{\sqrt{\sin^2 2\theta_V + \left(\pm \frac{L_V}{L_e} - \cos 2\theta_V\right)^2}} \quad (1.36)$$

$$\sin^2 2\theta_M \equiv \frac{\sin^2 2\theta_V}{\sin^2 2\theta_V + \left(\pm \frac{L_V}{L_e} - \cos 2\theta_V\right)^2} \quad (1.37)$$

Generally, n_e is defined as $n_e = \rho(\text{g/cm}^3)/2 \times N_A$ ($N_A = 6.022 \times 10^{23} \text{mol}^{-1}$). Where the ρ is the density of matter, the density around Kamioka-mine is $\rho = 2.7 \text{ g/cm}^3$ for example. Therefore, $L_V = 2.48 \times E_\nu(\text{MeV})/\Delta m^2(\text{eV}^2)$ and $L_V/L_e = 7.63 \times 10^{-8} \rho(\text{g/cm}^3) \times E_\nu(\text{MeV})/\Delta m^2(\text{eV}^2)$.

From the above equations, a larger electron density (n_e) provides a larger mixing angle (θ_M) in the matter, as shown in Table 1.1. Here, $n_e^{\text{resonance}}$ is called ‘‘MSW Resonance Density’’, and the oscillation is maximum(‘‘Resonance Condition’’) at that density.

$$\frac{L_V}{L_e} = \cos 2\theta_V \quad (1.38)$$

$$n_e^{\text{resonance}} = \frac{\Delta m^2}{2\sqrt{2}G_F E} \cos 2\theta_V \quad (1.39)$$

Table 1.1: The relation between the electron density and the mixing angle in the matter.

n_e	0	...	$n_e^{\text{resonance}}$...	∞
θ_M	θ_V	...	$\pi/4$...	$\pi/2$

Neutrino Oscillations in the Sun

The flavor eigenstates in matter are written as

$$|\nu_e\rangle = \cos \theta_M |\nu_1\rangle + \sin \theta_M |\nu_2\rangle \quad (1.40)$$

$$|\nu_x\rangle = -\sin \theta_M |\nu_1\rangle + \cos \theta_M |\nu_2\rangle \quad (1.41)$$

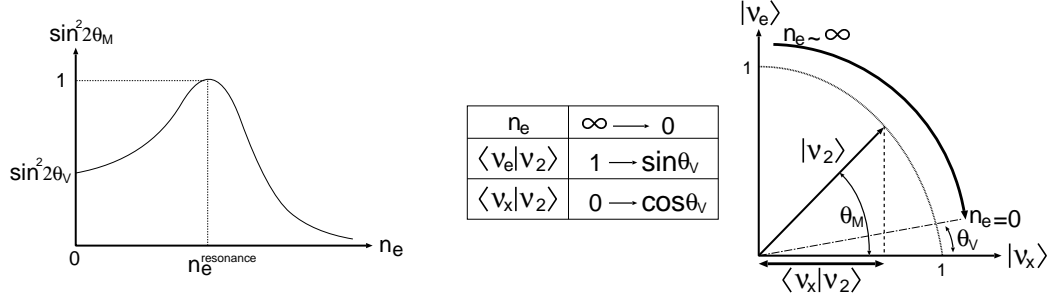


Figure 1.2: left: The definition of the resonance condition and resonance density.
 right: As the electron density decreases slowly, the flavor eigenstate remains close to the mass eigenstate $|\nu_2\rangle$. Upon emerging from the Sun to an essentially vacuum environment, the original $|\nu_e\rangle$ is close to the vacuum flavor eigenstate $|\nu_x\rangle$.

The neutrino flavor created in the Sun is the electron type neutrino (ν_e), and the electron density at the center of the Sun is very high, $n_e \sim \infty \Rightarrow \theta_M \sim \pi/2$. Therefore, the neutrino which is created in the Sun is almost ν_2 , and the flavor eigenstates of the solar neutrinos are written as

$$|\nu_e\rangle = \sin \theta_M |\nu_2\rangle \quad (1.42)$$

$$|\nu_x\rangle = \cos \theta_M |\nu_2\rangle \quad (1.43)$$

In the end, part of the electron neutrinos which are created at the center of the Sun ($n_e \sim \infty$) changes into another flavor when it goes out from the Sun ($n_e : \infty \rightarrow 0$). Figure 1.2 illustrates how a solar neutrino can change its flavor completely when the electron density varies slowly.

Regeneration in the Earth

Electron neutrinos which are converted to ν_x while passing through the Sun may be reconverted to ν_e on their way to a neutrino detector on the opposite side of the Earth from the Sun. If the MSW explanation is correct, electron neutrinos created in the Sun have had their flavor changed by interactions with matter. Therefore, regeneration in the Earth will on the average produce more ν_e from ν_x rather than vice versa and may make the Sun appear to shine brighter in electron neutrinos at night (Day-Night effect).

1.1.3 CP violation in the lepton sector

According to Eq. (1.16), CP violation can be observed only with appearance experiments, since $\text{Im}(U_{\alpha i}^* U_{\beta i} U_{\alpha j} U_{\beta j}^*) = 0$ for $\alpha = \beta$. There may be a chance in measuring the CP asymmetry in lepton sector if the oscillation $\nu_\mu \rightarrow \nu_e$ is observable in the future.

The $\nu_\mu \rightarrow \nu_e$ transition probability can be written from Eq. (1.16) and the matrix 1.9,

$$\begin{aligned}
 P(\nu_\mu \rightarrow \nu_e) = & 4c_{13}^2 s_{13}^2 s_{23}^2 \sin^2 \Phi_{31} \\
 & + 8c_{13}^2 s_{12} s_{13} s_{23} (c_{12} c_{23} \cos \delta - s_{12} s_{13} s_{23}) \cos \Phi_{32} \cdot \sin \Phi_{31} \cdot \sin \Phi_{21} \\
 & - 8c_{13}^2 c_{12} c_{23} s_{12} s_{13} s_{23} \sin \delta \cdot \sin \Phi_{32} \cdot \sin \Phi_{31} \sin \Phi_{21} \\
 & + 4s_{12}^2 c_{13}^2 (c_{12}^2 c_{23}^2 + s_{12}^2 s_{23}^2 s_{13}^2 - 2c_{12} c_{23} s_{12} s_{23} s_{13} \cos \delta) \sin^2 \Phi_{21} \\
 & - 8c_{13}^2 s_{13}^2 s_{23}^2 (1 - 2s_{23}^2) \frac{aL}{4E_\nu} \cos \Phi_{32} \cdot \sin \Phi_{31}. \quad (1.44)
 \end{aligned}$$

The first term has the largest contribution. The second $\cos \delta$ term is generated by CP phase δ and is CP conserving. The third $\sin \delta$ term is CP violation term. The fourth term, which is the solar neutrino term, is suppressed by $\sin \frac{\Delta m_{21}^2 L}{4E_\nu}$. The matter effect in the fifth term is given by

$$a = 2\sqrt{2}G_F n_e E_\nu = 7.6 \times 10^{-5} \cdot \underbrace{\rho}_{[\text{g/cm}^3]} \cdot \overbrace{E_\nu}^{[\text{GeV}]} [\text{eV}^2], \quad (1.45)$$

where G_F is the Fermi constant, n_e is the electron density and ρ is the earth density. The lower the energy gives the smaller the matter effect because the matter effect is proportional to neutrino energy. The probability $P(\bar{\nu}_\mu \rightarrow \bar{\nu}_e)$ is obtained by the replacing $a \rightarrow -a$ and $\delta \rightarrow -\delta$,

$$\begin{aligned} P(\bar{\nu}_\mu \rightarrow \bar{\nu}_e) = & 4c_{13}^2 s_{13}^2 s_{23}^2 \sin^2 \Phi_{31} \\ & + 8c_{13}^2 s_{12} s_{13} s_{23} (c_{12} c_{23} \cos \delta - s_{12} s_{13} s_{23}) \cos \Phi_{32} \cdot \sin \Phi_{31} \cdot \sin \Phi_{21} \\ & + 8c_{13}^2 c_{12} c_{23} s_{12} s_{13} s_{23} \sin \delta \cdot \sin \Phi_{32} \cdot \sin \Phi_{31} \sin \Phi_{21} \\ & + 4s_{12}^2 c_{13}^2 (c_{12}^2 c_{23}^2 + s_{12}^2 s_{23}^2 s_{13}^2 - 2c_{12} c_{23} s_{12} s_{23} s_{13} \cos \delta) \sin^2 \Phi_{21} \\ & + 8c_{13}^2 s_{13}^2 s_{23}^2 (1 - 2s_{23}^2) \frac{aL}{4E_\nu} \cos \Phi_{32} \cdot \sin \Phi_{31}. \end{aligned} \quad (1.46)$$

The CP asymmetry in the absence of the matter effect is,

$$A_{CP} = \frac{P(\nu_\mu \rightarrow \nu_e) - P(\bar{\nu}_\mu \rightarrow \bar{\nu}_e)}{P(\nu_\mu \rightarrow \nu_e) + P(\bar{\nu}_\mu \rightarrow \bar{\nu}_e)} \quad (1.47)$$

$$\simeq \frac{\Delta m_{12}^2 L}{4E_\nu} \cdot \frac{\sin 2\theta_{12}}{\sin \theta_{13}} \cdot \sin \delta, \quad (1.48)$$

because θ_{13} is small ($\sin^2 \theta_{13} < 0.12$ for $\Delta m_{23}^2 \sim 3 \times 10^{-3} \text{eV}^2$ at 90% C.L. [11]), $\Phi_{32} \simeq \Phi_{31}$, and $\sin \Phi_{21} \sim \Phi_{21}$. For small θ_{13} , CP asymmetry increases as $1/\sin \theta_{13}$, but the statistics decrease as $\sin^2 \theta_{13}$. Therefore, CP sensitivity does not depend strongly on the value of θ_{13} , but it strongly depend on Δm_{12}^2 .

1.1.4 Consideration of the Neutrino Mass

The standard model, which is the theory of elementary particles and of their interactions, explains almost all of the experimental results at present. The helicity of a massive particle is able to reverse because its velocity less than c (light velocity). So, there must be a right-handed neutrino (ν_R) if the neutrino mass is non-zero if neutrinos are Dirac-neutrino. A right-handed particle doesn't have $SU(2)_L$ interactions. Moreover, a hyper charge (Y) of ν_R is zero from $Q=I_3+Y$ because the charge (Q) and the iso-spin (I_3) are zero, so that ν_R doesn't have $U(1)_Y$ interaction. In other words, ν_R is sterile particle which cannot be detected, and neutrino masses are treated as 0 for simplicity in the standard model. Therefore, there is no theoretical reason why neutrino masses should be 0. For example, $L \sim g \bar{\nu}_L \nu_R \phi$ type interaction is permitted in the $SU(2)_L \times U(1)_Y$ gauge theory, where ϕ is the Higgs field and g is the coupling constant. It is the same reason why quarks are massive. It is same meaning that ν_R exists and neutrino mass is not 0. The strength of this interaction is proportional to the mass of the individual particle because it is mediated by a higgs particle. Therefore, it is very difficult to know ν_R exists or not if its mass is very small (Figure 1.3-(a)). It is impossible to explain why neutrino masses are very small compared with other leptons or quarks within the context of the standard model.

In other words, there is a possibility that the discovery of the neutrino mass is the discovery of the phenomenon beyond the standard model.

There is also the possibility that neutrinos are Majorana particles because they do not have charge. Majorana-particle is the particle which has no difference between particle and anti-particle. It is assumed that Majorana-neutrino is only left-handed[12], which cannot interact with the normal higgs particle(iso-spin 1/2) in the standard model. So, there must be another higgs particle whose iso-spin is 1(Figure 1.3-(b)) or another charged particle whose iso-spin is 1(Figure 1.3-(c)) if neutrinos have masses. Here, an iso-spin 1 charged particle violates lepton number conservation and an iso-spin 1 higgs particle does not exist in the standard model. As a result, the existence of the massive Majorana-neutrino means beyond standard model.

If Majorana-neutrinos can be left-handed and right-handed, the see-saw mechanism[13, 14, 12, 15] explains that neutrinos have very small mass(Figure 1.3-(d)). In this model, the relation between the masses of the left-hand neutrino(m_{ν_L}), right-hand neutrino(m_{ν_R}) and lepton(m_l) is;

$$m_{\nu_L} \cdot m_{\nu_R} \simeq m_l^2$$

m_{ν_L} can be very small if m_{ν_R} is very big $\sim 10^{16}\text{GeV}$ [15]. This is beyond the standard model energy scale, and iso-spin 1 higgs particles are not needed.

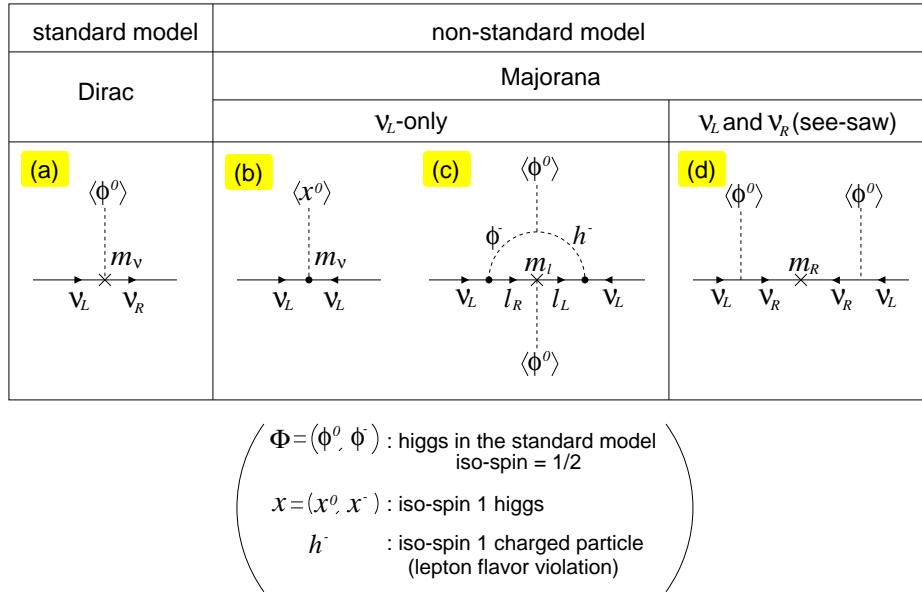


Figure 1.3: Mechanisms in which neutrinos have mass. (a) shows massive Dirac-neutrinos coupled with a higgs particle (ϕ^0). There must be an iso-spin 1 higgs particle(χ^0) or iso-spin 1 charged particle(h^-) because only left-handed Majorana-neutrinos have masses. Those interactions are shown in (b) and (c). In (d), it is shown the see-saw mechanism [13, 14, 12, 15].

The reason why neutrinos have small masses may be easy to explain if neutrinos are Majorana-neutrinos, while it looks unnatural for the existence of the Dirac-neutrinos. In either case, the discovery of lepton number violation or double beta decay or the exclusion of one of them is needed to determine the type.

1.2 Solar Neutrino Anomaly

The first phenomenon implying neutrino oscillation is the “solar neutrino anomaly”. This comes from the inconsistency of the observed neutrino event rate from the Sun between all experiments and theoretical prediction based on the SSM (Figure 1.4).

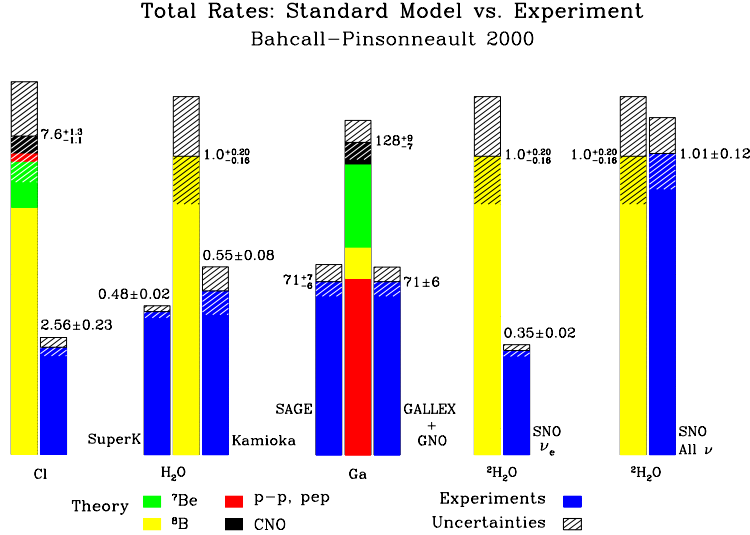


Figure 1.4: Comparisons of neutrino event rate between SSM prediction and experimental measurements [1].

Supposing neutrino oscillations, four regions of oscillation parameter space are given from the solar neutrino experiments. These solutions are called ‘Large Mixing Angle solution’ (LMA), ‘Low Δm^2 solution for Large Mixing Angle’ (LOW), ‘Small Mixing Angle solution’ (SMA) and ‘Vacuum Oscillation solution’ (VAC), as shown in Figure 1.10 and their maximum is 1,000,000 higher than their minimum for Δm^2 .

1.2.1 First observation of solar neutrino at Homestake

The first measurement of the solar neutrinos was performed by R. Davis Jr. and his associates using a chlorine ^{37}Cl radiochemical detector starting in 1968 [8]. They observed the solar neutrino by using the interaction;

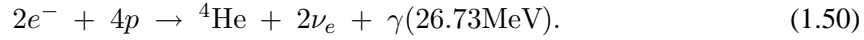
$$\nu_e + {}^{37}\text{Cl} \rightarrow {}^{37}\text{Ar} + e^- \quad (\text{energy threshold : } E_\nu > 0.81\text{MeV}). \quad (1.49)$$

Observed solar neutrinos are ^8B and ^7Be neutrinos (see Section 1.2.2). Their system was located 1,620 m underground (4,400 m w.e.) in the Homestake gold mine at Lead, South Dakota to reduce the cosmic ray muon flux. The detector was surrounded with a water for protection from spallation neutron background. They put 615 ton C_2Cl_4 into the cylindrical tank, and count ^{37}Ar several months later. ^{37}Ar decays to ^{37}Cl via the electron capture interaction with X-ray emission (2.82 KeV), and half-life is 34.8 days. The number of detected neutrinos was counted using X-ray emission. Their observed rate (2.6 ± 0.2 SNU) was much less than the theoretical prediction (7.9 ± 2.6 SNU) based on the Standard Solar Model (SSM) [16]. Here, SNU is the solar neutrino unit, [10^{-36} neutrino-capture/atom/sec]. The value is the product of

the solar neutrino flux [$\text{cm}^{-2}\text{s}^{-1}$] and cross section of the atom [cm^2]. This lower detection rate was the beginning of the solar neutrino anomaly, a problem unsolved for more than 30 years.

1.2.2 Standard Solar Model (SSM)

The Sun shines by burning hydrogen fuel. As the fuel is consumed, the star evolves. Stellar evolution is accompanied by nuclear fusion, which incidentally produces neutrinos,



The main sequence fuses protons to gain energy via the proton-proton chain (pp-chain) or CNO cycle, two distinct set of nuclear reactions. 98.5% of solar energy is derived from the pp-chain and remaining 1.5% is created by another. All processes in the pp-chain are shown in Figure 1.5. pp, pep, ${}^7\text{Be}$, ${}^8\text{B}$, and hep neutrinos are produced by these reactions. The flux of these neutrinos are shown in Figure 1.6.

The intensity of the neutrino flux is calculated by using solar models. The calculation of a model begins with the description of a main sequence that has a homogeneous composition. Hydrogen burns in the stellar core, supplying both the radiated luminosity and the thermal pressure that supports the star against the force of gravity. Successive models are calculated by allowing for composition changes caused by nuclear reactions, as well as the mild evolution of other contribution inside the star. A satisfactory solar model is a solution of the evolutionary equations that satisfies boundary conditions in both space and time. SSM gives a satisfactory account of what is known about the Sun from photons.

Accuracy of the SSM is explained by Helioseismology. Helioseismology [17], like terrestrial seismology, provides information about the interior of the body under study by using observations of slight motions on the surface. The comparison between observed and calculated helioseismological sound speeds is precise ($\sim 0.1\%$ RMS) [18] (see Figure 1.7 shows it).

1.2.3 Kamiokande, real time solar neutrino observation

Secondary solar neutrino observation was performed by Kamiokande [19] in 1987. Kamiokande was a water Čerenkov detector, previously located at the KamLAND site, 1,000 m underground (2,700 m w.e.) from the top of Mt. Ikenoyama in Kamioka. It consisted of 3,000 tons of water in a cylindrical tank. Solar neutrinos were detected via elastic electron scattering Eq.(1.6). The real time detection of the Čerenkov light from this recoil electron enables real time observation of the solar neutrino. The energy threshold was 7 MeV due to the radioactive impurities, and the main solar neutrino source was the ${}^8\text{B}$ neutrino.

The electron recoils in the same direction as the neutrino because of its light mass (0.511 MeV), and it indicates the direction and energy of the neutrino. The correlation of the neutrino direction with the Sun shows the existence of the solar neutrino clearly. This intelligent technique was succeeded by the Super-Kamiokande (SK) which is also a water Čerenkov detector, but with a much larger volume (50,000 ton) and a lower energy threshold (5 MeV).

The Kamiokande measured flux $(2.80 \pm 0.19(\text{stat}) \pm 0.33(\text{syst}) \times 10^6 \text{ cm}^{-2}\text{s}^{-1})$ is also lower than the SSM prediction $(5.05^{+1.01}_{-0.81} \times 10^6 \text{ cm}^{-2}\text{s}^{-1})$, $\sim 1/2$. The measurement result of SK is shown in latter Section 1.4.

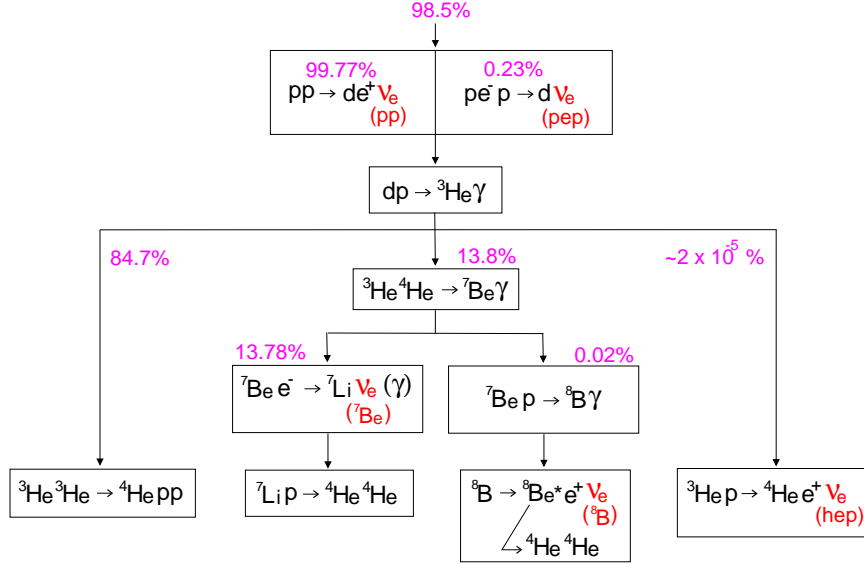


Figure 1.5: pp-chain of SSM.

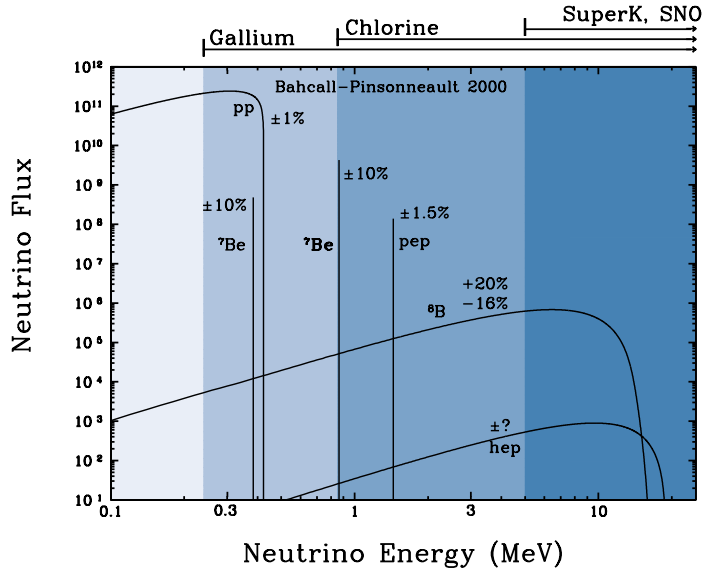


Figure 1.6: Solar neutrino flux based on SSM [1]. “Gallium”, “Chlorine”, and “SuperK,SNO” denote the sensitivity region of each experiment.

1.2.4 Observation of pp neutrino, SAGE and GALLEX

^8B and ^7Be neutrinos are only about 0.01% and 14% of the total of the solar neutrino flux. Their uncertainties are 20% and 10% respectively due to their low contribution to solar radiation. It is important to see pp neutrino with lower energy, because more than 85% of the total flux is pp neutrinos and its uncertainty is much lower than for other neutrinos ($\sim 1\%$).

The measurement of pp neutrinos has been performed in the ^71Ga isotope, SAGE [20] (in Russia) and GALLEX [21] (in Italy) experiments. The detection method is same as with the

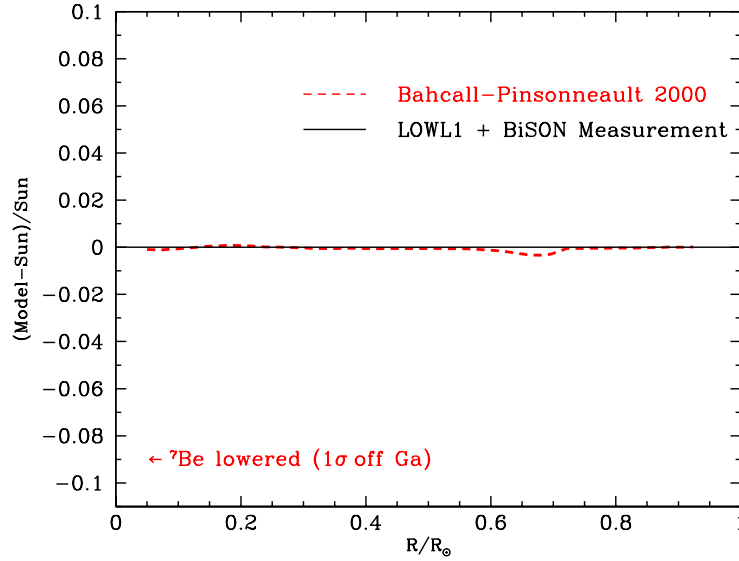


Figure 1.7: Predicted versus measured sound speeds [1]. It is the excellent agreement between the SSM prediction and the measurement with a fractional difference of 0.1% RMS for all sound speeds measurement from $0.05R_{\odot}$ to $0.95R_{\odot}$.

^{37}Cl experiment, in that they observe solar neutrinos by using the interaction;

$$\nu_e + {}^{71}\text{Ga} \rightarrow {}^{71}\text{Ge} + e^- \quad (\text{energy threshold : } E_{\nu} > 0.233\text{MeV}) \quad (1.51)$$

and the half-life time of ^{71}Ge is 11.4 days. Their results, SAGE: $69.9^{+8.0}_{-7.7}(\text{stat})^{+3.9}_{-4.1}(\text{syst})$ SNU and GALLEX: $76.4 \pm 6.3(\text{stat})^{+4.5}_{-4.9}(\text{syst})$ SNU, are lower than the SSM prediction 129^{+9}_{-7} SNU, ($\sim 1/2$).

1.3 Discovery of Neutrino Oscillation

1.3.1 Anomaly of atmospheric neutrinos

The atmospheric neutrino flux also exhibits an anomaly. Primary cosmic rays are high energy protons, which interact with atoms in the atmosphere and produce π or K particles. The atmospheric neutrinos are produced from the decay of these secondary cosmic rays. The production ratio between $\nu_e(\bar{\nu}_e)$ and $\nu_{\mu}(\bar{\nu}_{\mu})$ is calculated from Eq.(1.2) and Eq.(1.3), i.e. $N(\nu_{\mu} + \bar{\nu}_{\mu})/N(\nu_e + \bar{\nu}_e) \simeq 2$. The observation results of Kamiokande in 1988 were also lower than the theoretical prediction,

$$R = \frac{(\nu_{\mu} + \bar{\nu}_{\mu})/(\nu_e + \bar{\nu}_e)|_{\text{DATA}}}{(\nu_{\mu} + \bar{\nu}_{\mu})/(\nu_e + \bar{\nu}_e)|_{\text{MC}}} = 0.61 \pm 0.03(\text{stat}) \pm 0.05(\text{syst}) \quad (1.52)$$

where MC denotes Monte Carlo prediction [22]. If there are neutrino oscillations, $\Delta m^2 = 10^{-3} \sim 10^{-2} \text{ eV}^2$.

1.3.2 Search for Neutrino Oscillation using Reactor Anti-Neutrinos

$\nu_e \rightarrow \nu_{\mu}$ oscillation should be observed if the atmospheric neutrino anomaly is caused by the $\nu_{\mu} \rightarrow \nu_e$ oscillation, and such an observation was attempted by looking for reactor anti-

neutrino ($\bar{\nu}_e$) disappearance assuming CPT invariance. Two experiments carried out for this purpose were CHOOZ [11] and Palo Verde [23]. Both experiments detect $\bar{\nu}_e$ via the inverse β -decay reaction. Both detectors contain Gd-loaded (0.1%) liquid scintillator, and scintillation light is detected by PMT (Photomultiplier Tubes).

The CHOOZ power station located near Chooz village in France has two nuclear reactors with a total thermal power output of 8.5 GW_{th}. The CHOOZ detector looks for $\bar{\nu}_e$ 1,115 m and 998m distant from each reactor, and contains 5 tons of liquid scintillator. Its measurement result for (number of detected $\bar{\nu}_e$)/(number of expected $\bar{\nu}_e$) is,

$$\text{CHOOZ} \quad : \quad 1.01 \pm 2.8\%(stat) \pm 2.7\%(syst). \quad (1.53)$$

The experiment didn't observe the disappearance of reactor $\bar{\nu}_e$'s, and a $\Delta m^2 > 7 \times 10^{-4} \text{eV}^2$, $\sin^2 2\theta > 0.1$ region was excluded at 90% C.L. for $\bar{\nu}_e$ oscillations.

The Palo Verde Nuclear Generating Station is located west of Phoenix, Arizona. The Palo Verde detector used two reactors whose thermal power was in total 11.6GW_{th}. Flight distances of $\bar{\nu}_e$ are 890 m and 750 m and the target mass of the scintillator is 11.35 ton. The measurement result for (number of detected $\bar{\nu}_e$)/(number of expected $\bar{\nu}_e$) is also consistent with no-disappearance,

$$\text{Palo Verde} \quad : \quad 1.04 \pm 3\%(stat) \pm 8\%(syst), \quad (1.54)$$

and a $\Delta m^2 > 1.1 \times 10^{-3} \text{eV}^2$, $\sin^2 2\theta > 0.17$ region was excluded at 90% C.L. for the $\bar{\nu}_e$ oscillations.

Neither result shows that $\nu_e \leftrightarrow \nu_\mu$ oscillations are the answer of the atmospheric neutrino anomaly.

1.3.3 Evidence for oscillation of ν_μ

Subsequently, the Super-Kamiokande (SK) group discovered that the atmospheric neutrino anomaly was caused by neutrino oscillations in 1998 [2]. The zenith angle distribution of atmospheric neutrinos should be almost uniform because the distribution of the primary cosmic rays is almost uniform. SK measured the correlation of the number of neutrinos with various zenith angle (various flight length L), and they observed the correlation of the disappearance of the muon type neutrino with L/E_ν (E_ν : neutrino energy). In other words, a survival probability consistent with Eq.(1.21) was observed. This is strong evidence for neutrino oscillation behavior $\nu_\mu \rightarrow \nu_x$. On the other hand, such a correlation was not observed for electron type neutrinos, consistent with CHOOZ [11] and Palo Verde [23].

Moreover, $\nu_\mu \rightarrow \nu_s$ oscillation (ν_s is sterile neutrino) is rejected as a hypothesis at the 99% C.L. by the study of the neutral current interaction [24], [25]. Currently, $\nu_\mu \rightarrow \nu_\tau$ oscillation is reasonable, and the measured oscillation parameters Δm_{atm} and $\sin^2 2\theta_{atm}$ in the 90% C.L. range [26] are,

$$1.6 \times 10^{-3} \text{eV}^2 \leq \Delta m_{atm} \leq 3.9 \times 10^{-3} \text{eV}^2, \quad \sin^2 2\theta_{atm} > 0.92. \quad (1.55)$$

The muon type neutrino oscillation has been studied by the K2K (KEK to Kamioka) long-baseline (270km) experiment. This experiment produces a ν_μ beam using an accelerator, and measures its intensity and energy distribution at the near side (KEK) and far side (Kamioka, SK) detectors, and then compare each measurement. The latest result is 52 events observed, 80 events expecting corresponding to disappearance at the 99% C.L. [27].

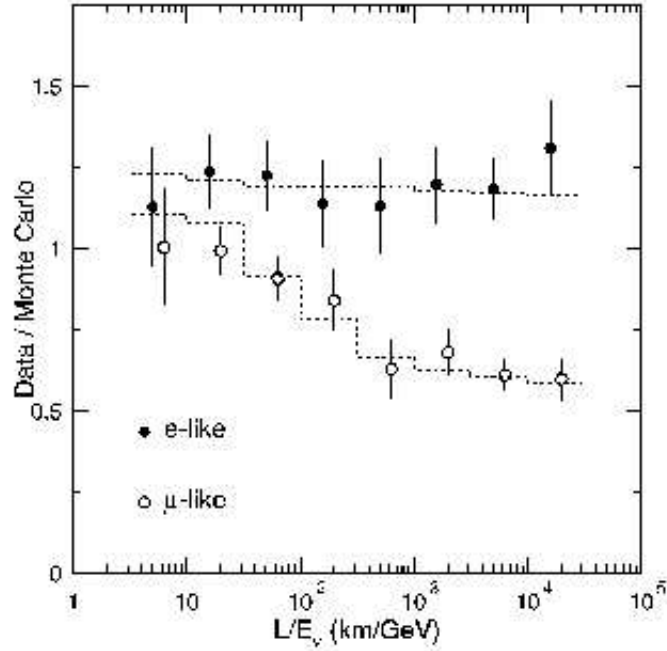


Figure 1.8: Correlation of data/MC with L/E_ν at the measurement of atmospheric neutrinos by Super-Kamiokande [2]. This is the evidence for oscillation of atmospheric neutrinos.

1.4 Solar Neutrino Flavor Changing

There was no conclusive evidence for solar neutrino oscillation until 2001, while the evidence for the neutrino oscillation of ν_μ was reported. In 2001, the Sudbury Neutrino Observatory (SNO) group reported their measurement results of the solar neutrino flux via charged current (CC) reaction on deuterium, Eq.(1.4), and the elastic scattering (ES) of electrons, Eq.(1.6). the SNO detector is located at the depth of 6,010 m of water equivalent in the INCO, Ltd. Creighton mine near Sudbury, Ontario in Canada. Its main goal is ^8B neutrino detection using the Čerenkov light in 1,000 metric tons of heavy water (D_2O). The CC reaction (Eq.(1.4)) is sensitive exclusively to electron-type neutrinos, while the NC (Eq.(1.5)) is sensitive to all active neutrino flavors (ν_e, ν_μ, ν_τ). The ES reaction (Eq.(1.6)) is sensitive to all flavors as well, but with reduced sensitivity to ν_μ and ν_τ . The CC reaction should directly determine the energy spectrum of the detected ν_e . The incident neutrino energy (E_ν) is related to the energy of the electron (E_e) by the expression $E_\nu = E_e + 1.442\text{MeV}$. The angular distribution of CC scattering is $(1-1/3\cos\theta)$. The CC reaction is distinguished from the ES by this angular distribution. The NC reaction threshold is 2.2 MeV and it is detected by the 6.25 MeV γ -ray from neutron capture on deuterium. Sensitivity to these three reactions allows for the determination of the electron and non-electron active neutrino components of the solar flux. The SNO solar neutrino flux observation results in 2001 [28] are;

$$\phi_{SNO}^{CC}(\nu_e) = 1.75 \pm 0.07(stat)_{-0.11}^{+0.12}(syst) \pm 0.05(theory) \times 10^6 \text{ cm}^{-2}\text{s}^{-1}, \quad (1.56)$$

$$\phi_{SNO}^{ES}(\nu_x) = 2.39 \pm 0.34(stat)_{-0.14}^{+0.16}(syst) \times 10^6 \text{ cm}^{-2}\text{s}^{-1} \quad (x = e, \mu, \tau). \quad (1.57)$$

The significance of the difference between CC and ES is at about 90% C.L., not conclusive, but more precise measurement of ES by SK [29], [30] is

$$\phi_{SK}^{ES}(\nu_x) = 2.32 \pm 0.03(stat)_{-0.07}^{+0.08}(syst) \times 10^6 \text{ cm}^{-2}\text{s}^{-1} \quad (x = e, \mu, \tau). \quad (1.58)$$

Both measurements for ES are consistent. The significance of the difference between $\phi_{SNO}^{CC}(\nu_e)$ and $\phi_{SK}^{ES}(\nu_x)$ is 99.96% C.L., and almost conclusive evidence for solar neutrino flavor changing.

The SNO group reported a more conclusive result in 2002. The flux via the NC reaction was reported in addition to CC and ES data updates [3]. The results are;

$$\phi_{SNO}^{CC}(\nu_e) = 1.76_{-0.05}^{+0.06}(\text{stat})_{-0.09}^{+0.09}(\text{syst}) \times 10^6 \text{ cm}^{-2}\text{s}^{-1}, \quad (1.59)$$

$$\phi_{SNO}^{ES}(\nu_x) = 2.39_{-0.23}^{+0.24}(\text{stat})_{-0.12}^{+0.12}(\text{syst}) \times 10^6 \text{ cm}^{-2}\text{s}^{-1}, \quad (1.60)$$

$$\phi_{SNO}^{NC}(\nu_x) = 5.09_{-0.43}^{+0.44}(\text{stat})_{-0.43}^{+0.46}(\text{syst}) \times 10^6 \text{ cm}^{-2}\text{s}^{-1}, \quad (1.61)$$

where, $x = e, \mu, \tau$. The NC result is consistent with the SSM prediction,

$$\phi_{SSM} = 5.05_{-0.81}^{+1.01} \times 10^6 \text{ cm}^{-2}\text{s}^{-1}, \quad (1.62)$$

and removes the constraint which tends to distort the solar neutrino energy spectrum. A simple change of variables resolves the data directly into electron (ϕ_e) and non-electron ($\phi_{\mu,\tau}$) components, [3],

$$\phi_e = 1.76_{-0.06}^{+0.05}(\text{stat})_{-0.09}^{+0.09}(\text{syst}) \times 10^6 \text{ cm}^{-2}\text{s}^{-1}, \quad (1.63)$$

$$\phi_{\mu,\tau} = 3.41_{-0.45}^{+0.45}(\text{stat})_{-0.45}^{+0.48}(\text{syst}) \times 10^6 \text{ cm}^{-2}\text{s}^{-1} \quad (\text{SNO only}), \quad (1.64)$$

$$\phi_{\mu,\tau}^{+SK} = 3.45_{-0.62}^{+0.65} \times 10^6 \text{ cm}^{-2}\text{s}^{-1} \quad (\text{SNO} + \text{SK}), \quad (1.65)$$

assuming the standard ^8B shape. This is the evidence for neutrino flavor transformation. The significance of the existence of a $\nu_{\mu,\tau}$ flux from the Sun is 5.3σ ($>99.9999\%$ C.L.). Figure 1.9 shows the flux of non-electron flavor active neutrinos vs the flux of electron neutrinos deduced from the SNO data. Three flux bands from their measurement meet at one point, this shows the reliability of the experiment.

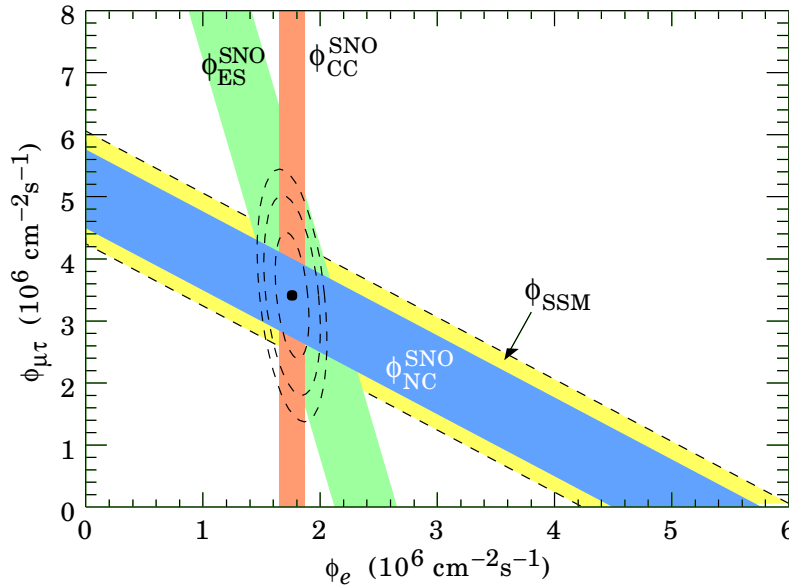


Figure 1.9: Flux of ^8B solar neutrinos which are μ or τ flavor vs flux of electron neutrinos deduced from the three neutrino reactions in SNO [3].

1.5 Motivation of this thesis

The validity of the SSM is proved by result of NC, and the most convincing reason for the lack of solar neutrinos is the neutrino oscillation. Yet, the oscillation parameter for the solar neutrinos has not been determined as there are four candidate solutions and their maximum is 1,000,000 higher than their minimum for Δm^2 . These solutions are called 'Large Mixing Angle solution' (LMA), 'Low Δm^2 solution for Large Mixing Angle' (LOW), 'Small Mixing Angle solution' (SMA) and 'Vacuum Oscillation solution' (VAC), as shown in Figure 1.10. The LMA solution is the most favored from the global analysis which combine measurement results of all solar neutrino experiments but there was no experiment to determine the LMA is the solution by itself. **Therefore, the determination of ν_e oscillation parameter set is the last subject of the solar neutrino anomaly. The motivation of this thesis is direct measurement of oscillation parameters via observing the reactor $\bar{\nu}_e$.**

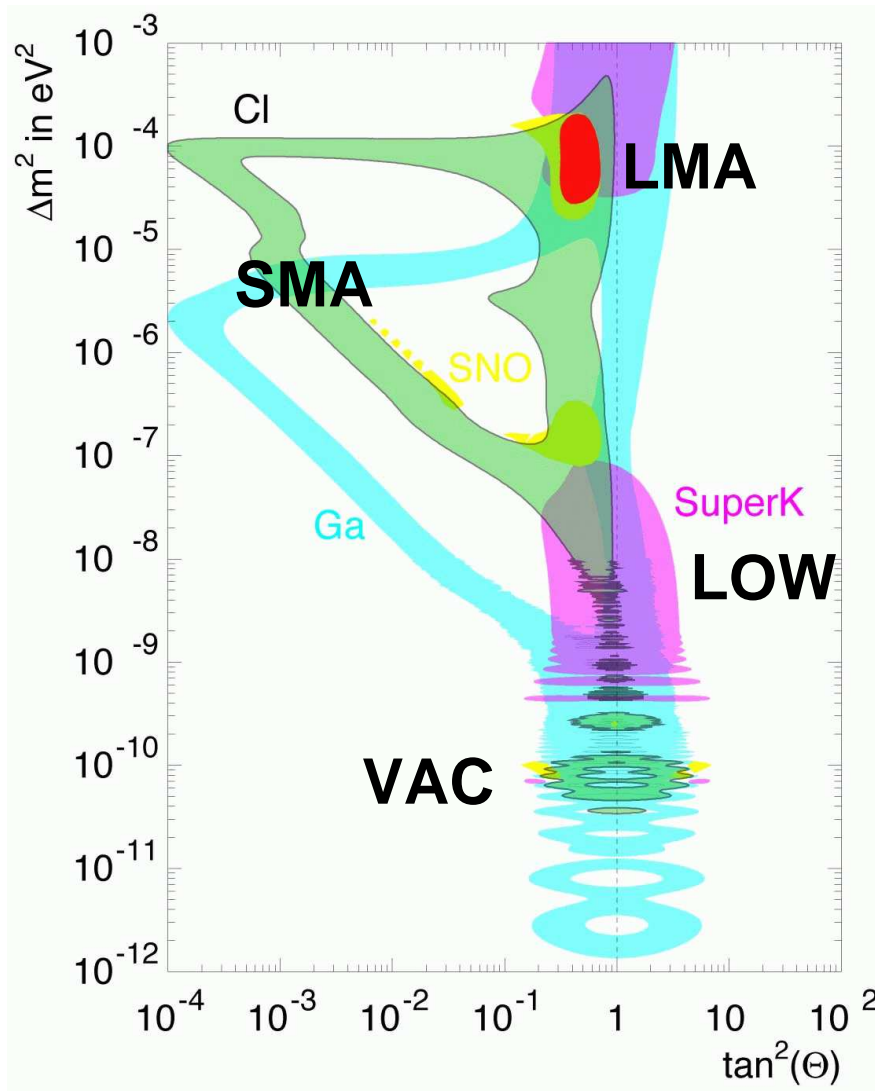


Figure 1.10: Oscillation parameters for electron neutrino before KamLAND [4]. The LMA solution is the most favored from the global analysis based on all solar neutrino experiments.

A more precise measurement of the oscillation parameter set, especially Δm_{12}^2 , may enhance the sensitivity of measurements of the CP-violating phase by the future long base-line experiments (for example, JHF to Hyper-Kamiokande 295 km base-line [5]). According to Eq. (1.48), the CP asymmetry is enhanced as $1/E$ by choosing a low energy neutrino beam. Figure 1.11 shows the sensitivity for CP violation at various values of Δm_{12}^2 . The sensitivity is,

- $\Delta m_{12}^2 = 3 \times 10^{-5} \text{eV}^2 \rightarrow |\delta_{CP}| \text{ or } |\delta_{CP} - 180^\circ| > 20^\circ (90\% C.L.)$
- $\Delta m_{12}^2 = 5 \times 10^{-5} \text{eV}^2 \rightarrow |\delta_{CP}| \text{ or } |\delta_{CP} - 180^\circ| > 10^\circ (90\% C.L.)$
- $\Delta m_{12}^2 = 10 \times 10^{-5} \text{eV}^2 \rightarrow |\delta_{CP}| \text{ or } |\delta_{CP} - 180^\circ| > 7^\circ (90\% C.L.)$

for the case of $\theta_{12} = \pi/8, \theta_{23} = \pi/4, \Delta m_{23}^2 = 3 \times 10^{-3} \text{eV}^2, \sin^2 2\theta_{13} = 0.01$, and $E_\nu \sim 0.75 \text{GeV}$.

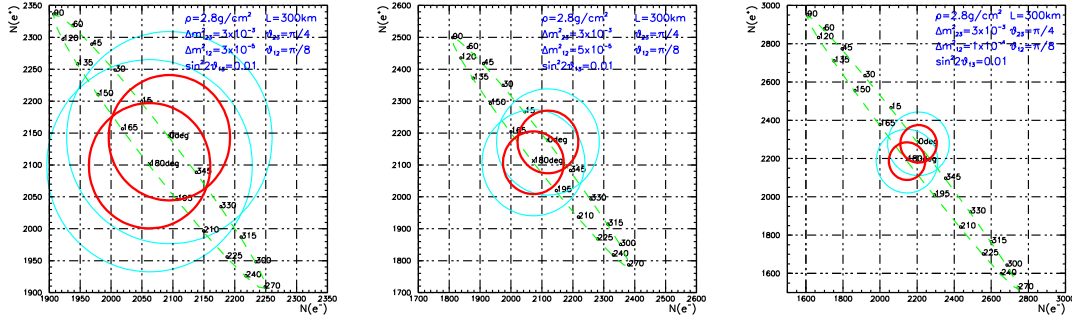


Figure 1.11: Correlation of the sensitivity for CP violation with Δm_{12}^2 at the long base-line experiment JHF Hyper-Kamiokande [5]. Higher Δm_{12}^2 gives better sensitivity to observe the CP violation.

Chapter 2

KamLAND Experiment

KamLAND is the Kamioka Liquid Scintillator Anti-Neutrino Detector. It is located at the site of the former Kamiokande experiment in a mine, 1,000 meters under the top of Mt. Ikenoyama.

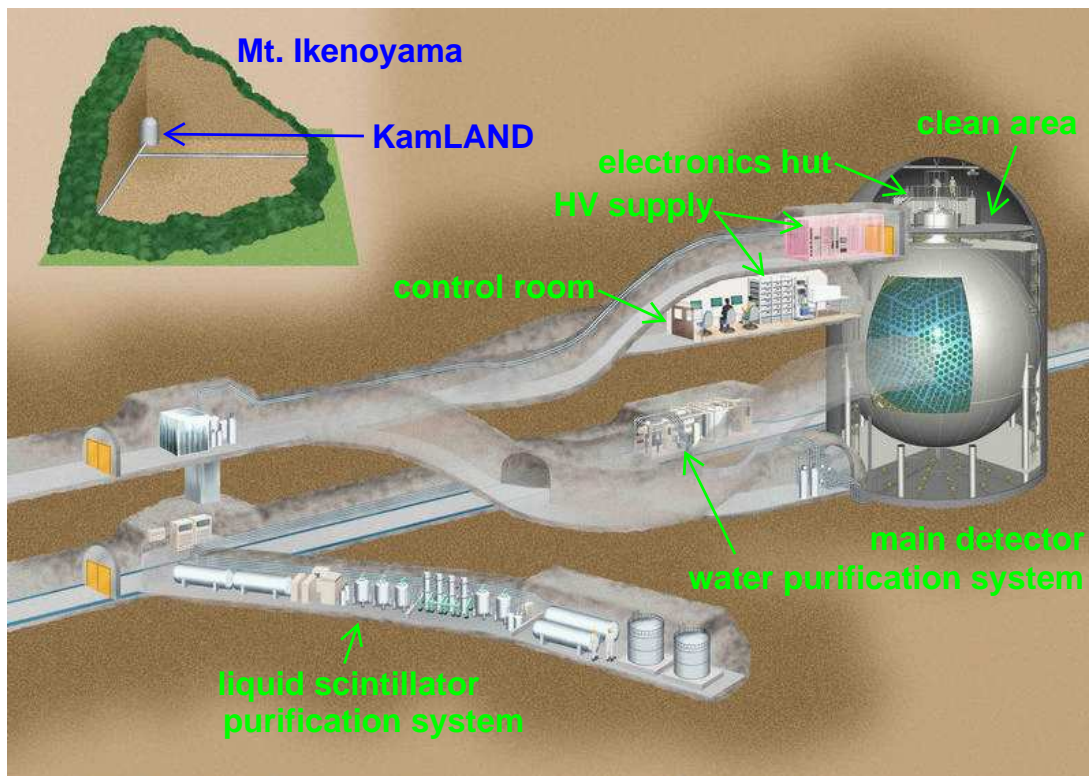


Figure 2.1: Around the KamLAND area

It is designed to detect very rare and significant interactions for the particle physics as follows,

- Anti-neutrino(neutrino) detection via inverse beta decay, $\bar{\nu}_e p \rightarrow n e^+$, or electron scattering, $\nu_x(\bar{\nu}_x) e^- \rightarrow \nu_x(\bar{\nu}_x) e^-$.
 - Anti-neutrinos from nuclear reactors $\rightarrow 1\sim 2$ events/day

- Terrestrial anti-neutrinos (Geo-neutrinos) $\rightarrow \sim 70$ events/year
- Neutrinos from the Sun
- Anti-neutrinos from the past Supernova.
- Anti-neutrinos synchronized with gamma-ray burst
- Decay of the stable nuclei, for example proton, ^{12}C .
 $\rightarrow < 2$ events/year (from current limit [31])

The main goal of the KamLAND experiment is the search for the oscillation of $\bar{\nu}_e$'s emitted from distant power reactors. Although the $\bar{\nu}_e$ flux at the location of KamLAND is due to many nuclear reactors at a variety of distances, it is dominated by a few reactors at the average distance of ~ 180 km (Figure 2.2 and 2.3). More than 79% of the computed flux arises from 26 reactors within the distance range 138-214 km. One reactor at 88 km contributes an additional 6.7% to the flux and the other reactors are more than 295 km away. The flux of $\bar{\nu}_e$ from a reactor at a distance L from KamLAND is approximately proportional to the thermal power flux $P_{th}/4\pi L^2$, where P_{th} is the reactor thermal power. This relatively narrow band of distances implies that for some oscillation parameters KamLAND can observe a distortion of the $\bar{\nu}_e$ energy spectrum. The most sensitive region is $\Delta m^2 = (1/1.27) \cdot (E[\text{MeV}]/L[\text{m}]) \cdot (\pi/2) \sim 3 \times 10^{-5} \text{eV}^2$, which means KamLAND is well tuned to verify the LMA solution. Electron anti-neutrinos are detected by using the inverse β -decay reaction, $\bar{\nu}_e + p \rightarrow e^+ + n$, which is used to detect $\bar{\nu}_e$'s with energy above 1.8 MeV in the liquid scintillator. The detection of the e^+ (≥ 1.022 MeV detected energy) and the 2.22 MeV neutron capture γ -ray in delayed coincidence is a powerful tool for reducing background. Moreover, the detector is designed to have an extremely low background.

This chapter describes the detector and delayed coincidence technique to detect $\bar{\nu}_e$'s via inverse β -decay.

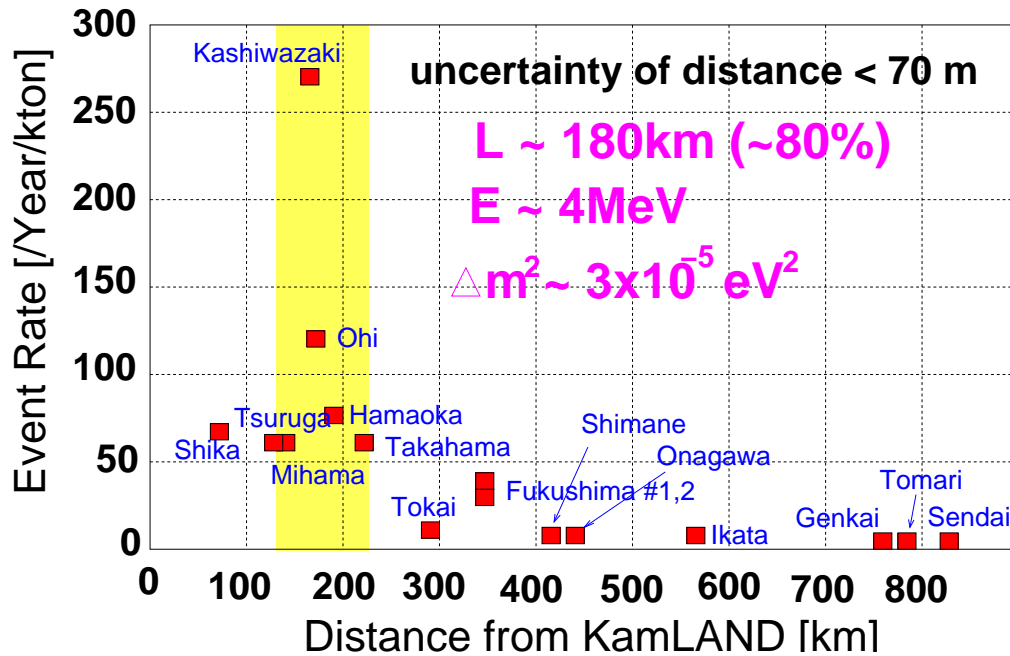


Figure 2.2: Expected $\bar{\nu}_e$ contribution from each Japanese reactor. The $\bar{\nu}_e$ flux is dominated by a few reactors at an average distance of ~ 180 km.

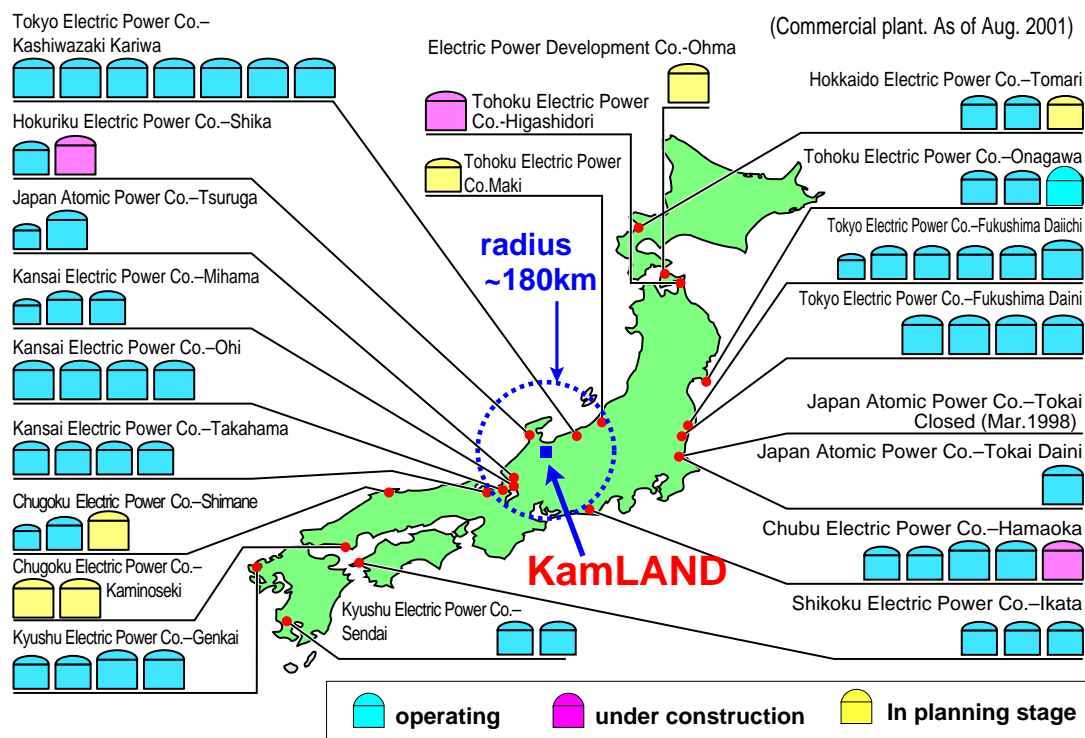


Figure 2.3: The map of Japanese nuclear reactors and KamLAND. Dashed line shows 180km radius from the KamLAND.

2.1 KamLAND Detector

2.1.1 Structure

Background events for the $\bar{\nu}_e$ detection are caused by undesired radioactive particles which come into the scintillator from the outside or inside of the detector. The detector itself is surrounded by 1,000m of rock (2,700m water equivalent). Which acts as a shield to significantly decrease the cosmic ray muon flux incident on the detector ($\sim 0.34\text{Hz}$). The less cosmic ray muon flux is better because it makes unstable isotopes in the detector and the decays of them cause background (fake) events for $\bar{\nu}_e$. The liquid scintillator is located at the center of the detector and covered with multiple layers of spherical materials to guard the external radioactivities. (Figure 2.4). Total weight (volume) of the scintillator is 1,000ton ($1,200\text{m}^3$). The scintillator is filled in a plastic spherical balloon ($\phi=13\text{m}$) made of 135- μm -thick transparent nylon/EVOH (Ethylene vinyl alcohol copolymer) composite film. It is suspended with Kevlar ropes to keep the spherical shape. The scintillator and its vessel are surrounded by the buffer of dodecane and isoparaffin oils, whose specific gravity is adjusted to be 0.04% lower than that of the scintillator. This is surrounded by the spherical stainless steel tank whose diameter is 18m. The scintillator and the buffer oil are purified to reduce internal radioactivities. The buffer layer shields the scintillator from external radiations and the fast neutron. External γ -rays are come from contained isotopes in detector materials or rock, especially ^{208}Tl and ^{40}K . The fast neutron is generated by the interaction of the cosmic ray muons at outside or inside the detector. The buffer oil region is divided into two regions by the transparent 3-mm-thick acrylic barrier whose radius is 8.3m. This acrylic barrier also prevents to permeance of the Rn generated from the decay of the radioactive isotopes which included in materials of PMT and stainless. The stainless tank is also surrounded by the water in the cylindrical cavity in the mine. This water wall is not only the buffer for the fast neutron but also the veto counter to the cosmic ray muon.

Regions at the top and bottom of the stainless sphere are cylindrical shape not spherical shape. The bottom region is just a space of scintillator circulation lines from the vessels to the purification system. The top region, which is called 'chimney', supports the balloon straps. It is also the route to put the calibration devises into the scintillator. There are various special veto counters around the chimney because the water shield is not enough or nothing. The detector is roughly divided into three region, the inside of the spherical stainless steel (inner detector; ID), the water tank region(outer detector; OD) and the chimney region.

The fluore in the scintillator is excited by the energy loss of the radiation generated from particle interactions, and emits light (*scintillation light*). This light is detected by an array of 1,879 photomultiplier tubes (PMTs), mounted on the surface of the containment stainless vessel. This array includes 1,325 specially developed fast PMTs with 17-inch-diameter photo-cathodes (17" PMT) and 554 former Kamiokande 20-inch PMTs (20" PMT) [32]. The distance from the center of the balloon to the sensitive surfaces of the PMTs is 8.3m. While the total photo-cathode coverage is 34%, the 17" PMTs cover 22%. At the outer detector, Čerenkov light, which is generated by cosmic ray muon, is detected by 225 of 20" PMTs which are placed on the wall, top and bottom of the cylindrical water tank. In the chimney region, 16 of 8" PMTs and 6 of 5" PMTs are used as a light detector for the veto.

Detected light is converted to an analog electric signal by the PMT and this analog signal information is converted to digital waveform information in the front-end electronics (FEE). Trigger is issued with PMT hit information (Nsum) at the electronics. The primary ID trigger threshold is set at 200PMT hits which corresponds to about 0.7MeV. The trigger efficiency for the reactor $\bar{\nu}_e$ detection is 99.998% (Section 2.1.8). This threshold is lowered to 120hits for

1msec after the primary trigger to observe lower energy delayed activity like Bi-Po correlated decay in ^{238}U and ^{232}Th . The OD trigger threshold is set to provide 99% efficiency for the detection of cosmic-ray muon. The DAQ (*Data Acquisition*) system reads out the waveforms with the trigger issues, and the Event Builder constructs the event using the time information (time-stamp) of each waveform and the trigger information.

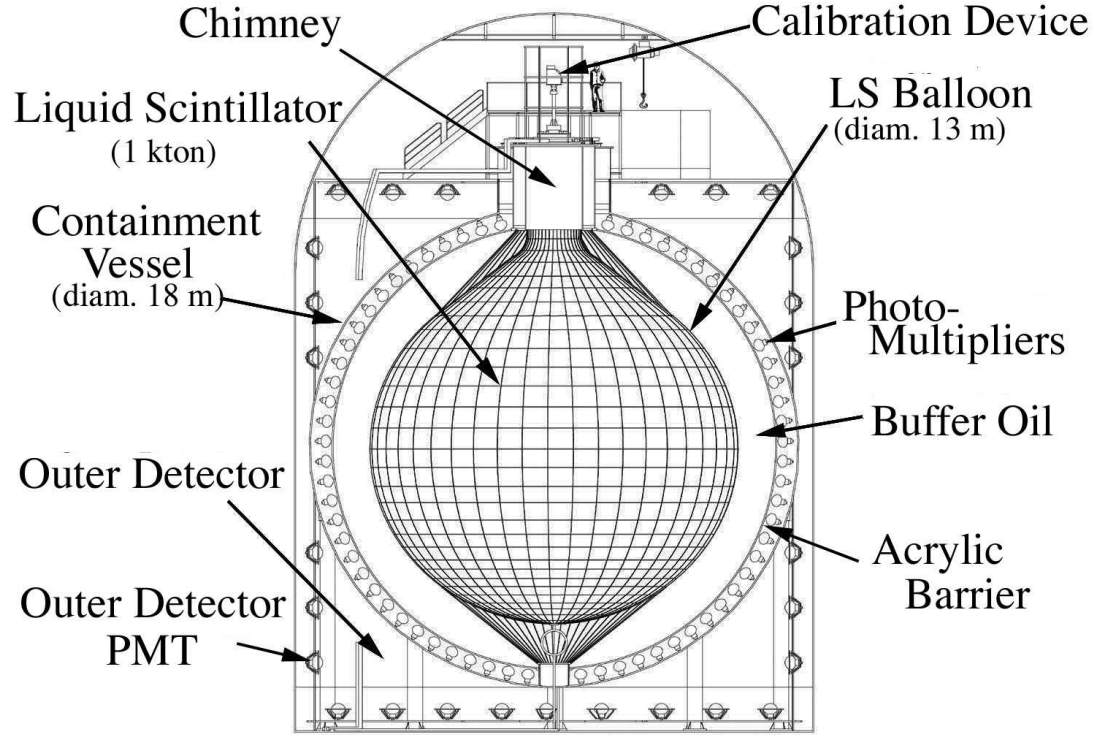


Figure 2.4: Schematic diagram of the KamLAND detector. Its layered structure rejects external radioactivity. The target scintillator is covered with transparent plastic balloon to guard it from penetration of ^{222}Rn gas. This balloon is also covered with the buffer oil, acrylic plate which acts as a barrier against external radiation. The water Čerenkov counter surrounds them as a muon veto counter. Moreover, 1,000m thickness rock surrounds all of them as a shield against cosmic ray muons.

Table 2.1: Number of PMT in the detector

PMT-type	inner detector	outer detector	chimney region	sum / PMT-type
20"	554	225	—	779
17"	1,325	—	—	1325
8"	—	—	16	16
5"	—	—	6	6
sum / region	1,879	225	22	2126

2.1.2 Liquid scintillator and buffer oil

One kton of liquid scintillator is necessary in KamLAND because high statistics is essential to the observation of reactor $\bar{\nu}_e$ disappearance. In addition, the sensitivity for Δm^2 strongly depends on the observed $\bar{\nu}_e$ energy according to Eq.(1.16). Therefore, better energy resolution as well as a low background environment is essential for the experiment. To realize this,

- very low radioactive impurities for the low background experiment
- high light yield for the good energy resolution
- discriminability between the light particle and the heavy particle, for example β and α , to reject background events.
- long term stability
- less toxicity and a lower flash point for safety
- inexpensive as possible

Hand-made scintillator was selected because it was cheap. Its composition is

$$\text{Normalparaffin}(80.2\%) + \text{Pseudocumene}(19.8\%) + \text{PPO}(1.52\text{g/l})$$

Normalparaffin($\text{C}_{12}\text{H}_{26}$) is a mineral oil. Pseudocumene(1,2,4-Trimethyl Benzene) is a popular solvent for liquid scintillator. PPO(2,5-Diphenyloxazole: $\text{C}_{15}\text{H}_{11}\text{NO}$) is one of the popular solutes(fluorescent substances) used on scintillator.

Table 2.2: Liquid Scintillator Parameters

parameter	design value	actual value
temperature [$^{\circ}\text{C}$]	~ 12	11.5
specific density @ 15°C [g/cm^3]	0.778	0.77754 ± 0.00010
H/C ratio	1.902	1.969
refractive index @ $\lambda=590\text{nm}$, 14°C	1.44	1.44087 ± 0.00015
light yield [p.e./MeV]		
(i) 17inch PMT only	~ 250	~ 300 @ center
(ii) 17inch + 20PMT	~ 400	—
time response parameters (unit is nsec) $R(t) = a/\tau_a \exp(-t/\tau_a) + b/\tau_b \exp(-t/\tau_b)$		
a	0.86	0.69
b	0.14	0.31
τ_a	6.9	4.0
τ_b	8.8	8.6
neutron capture time [μsec]	~ 212	212.5 ± 8.1
radiation length [cm]	18	—
flash point [$^{\circ}\text{C}$]	64	—
thermal expansion coefficient [$^{\circ}\text{C}$]	-0.00095	—
kinetic viscosity @ 30°C [cSt]	1.4	—

Table 2.3: Parameters of Liquid Scintillator / Buffer Oil Components

parameter	Pseudocumene	Normalparaffin	Isoparaffin
molecular structure	C_9H_{12}	$C_{12}H_{26}$	C_nH_{2n+2} ($n \sim 15$)
specific gravity (@ 15°C)	0.8796	0.7526	0.7958
flash point [°C]	54	83	78
melting point [°C]	-43.8	-7.5	<-50
refractive index (@ 15°C, $\lambda=589\text{nm}$)	1.5049	1.4217	1.4410
kinetic viscosity (mm^2/sec @ 15°C)	1.108	2.379	4.754

Radioactive impurities are very low in the mineral oil by nature. The less light gives worse energy resolution. The light yield depends on the light transparency of the scintillator as well as the light output because of its detector size. Therefore, the KamLAND scintillator is diluted with mineral oil to maintain high light transparency. The light transparency of the normal paraffin is much better than that of the pseudocumene. The composition ratio of the scintillator is adjusted to get the maximum light yield for central events [33], and the actual light yield is about 300 p.e./MeV. The measured light attenuation length of the scintillator is about 10 m at 400 nm wavelength, measured using a dye-laser [33], and the light output is 49% Anthracene (8,300 photons/MeV). 100 % Anthracene corresponds to 17,000 photons. Moreover, diluting with mineral oil lowers the flash point of the scintillator to 64 °C as well as the toxicity. Design parameters and actual values are shown in Table2.2.

To keep the spherical shape of the balloon, the specific gravity of the buffer oil is adjusted to be 0.04% lower than the scintillator. For this purpose, the buffer oil is a mixture of mineral oils, Normalparaffin($C_{12}H_{26}$) and Isoparaffin(C_nH_{2n+2} , $n \sim 14$). The mixture ratio of Normalparaffin to Isoparaffin, is 53/47. Design parameters and actual values are also shown in Table2.4.

Table 2.4: Buffer Oil Parameters

parameter	design value	actual value
specific density @ 15°C [g/cm^3]	0.778	0.77732 ± 0.00010
density difference from scintillator [%]	<0.1	<0.03
refractive index @ $\lambda=590\text{nm}$, 14°C	1.44	1.43532 ± 0.00013
flash point [°C]	≥ 78	—

2.1.3 Target mass

The scintillator density is $0.780 \text{ g}/\text{cm}^3$ at 11.5°C and the expected hydrogen-to-carbon ratio $H/C=1.969$ was verified by elemental analysis to within $\pm 2\%$. The specific gravity is measured to within 0.01% precision and an additional 0.1% error is assigned from the uncertainty in the temperature. Therefore, 408.48 ton fiducial mass contains 3.46×10^{31} free target protons.

2.1.4 Plastic balloon, balloon strap and acrylic plate

plastic balloon (scintillator vessel)

The spherical plastic balloon(the scintillator vessel) is the last barrier to guard the scintillator from the external radioactivities, especially ^{222}Rn generated from the radioactive isotopes ^{238}U in the materials of the PMTs and the stainless tank. Therefore, low permeability against the ^{222}Rn is required for its purpose as well as the mechanical strength to maintain the spherical shape of the central scintillator. The balloon is made of fivefold layer film,

$$\text{EVOH}(25\mu\text{m}) / \text{Nylon}(15\mu\text{m}) / \text{Nylon}(15\mu\text{m}) / \text{Nylon}(15\mu\text{m}) / \text{EVOH}(25\mu\text{m}),$$

of $135\mu\text{m}$ thickness. EVOH is an effective material because it prevents the permeation of ^{222}Rn . Nylon is used as a strength reinforcement. Rn permeability of the balloon and other materials are summarized in Table 2.5. The ^{222}Rn density ratio between inside and outside the balloon is 1.8×10^{-6} . The mechanical strength of the balloon was tested by pressure test with 1/1 scale and 1/4 scale models in water.

Table 2.5: Rn permeability, solubility and diffusion constant of materials. The 'permeability' is defined as '(diffusion constant) \times (solubility)'. PET means Poli-Ethylene Terephthalate.

material	diffusion constant [$\times 10^{-10}\text{cm}^2/\text{sec}$]	solubility	permeability [$\times 10^{-10}\text{cm}^2/\text{sec}$]
Teflon	500	~ 10	$\sim 5,000$
PET	~ 1	~ 10	~ 10
Nylon	~ 1	~ 10	~ 10
EVOH	0.001	~ 10	~ 0.01
balloon film	0.5	3.9	1.95

balloon strap

The plastic balloon is supported by 44-longitudinal and 30-lateral Kevlar braid ropes to maintain its spherical shape. Its structure looks like a cargo net. The Kevlar is made of para-amid fiber whose excellent features are suitable for KamLAND. Its chemical stability was tested by long term soaking test with oil in a high temperature room. Mechanical strength was also checked by pressure test with the 1/1 scale and 1/4 scale balloon. Moreover, it was washed with the alcohol to remove the radioactive impurities. However, the Kevlar still contains 8.3×10^{-10} g/g of ^{40}K whose decay rate corresponds to 21.6 Bq (2.3Bq for 1.46 MeV γ -ray).

acrylic plate

Three mm thickness acrylic plates are placed in the inner detector in front of the inner PMTs to prevent ^{222}Rn coming into the inner buffer oil region. Radioactive isotopes, ^{238}U and ^{232}Th , are included in materials of PMT and stainless tank. ^{222}Rn is generated from the decay of these isotopes.

2.1.5 Purification system

The liquid scintillator and buffer oil in the detector are purified by the purification system. The purification system is connected to the detector so that scintillator and buffer oil can be circulated throughout. Radio active impurities (^{238}U , ^{232}Th , ^{40}K , ^{222}Rn and so on) are removed by this system. Current quantities of radioactive impurities are summarized in Table 2.6.

The purification system is divided into two systems, one the system for scintillator and the other is for buffer oil. Each system consists of three filters, a water extraction tower and nitrogen purge tower. Figure 2.5 shows the flow chart of purification. The filters are used for removing dust in the scintillator and buffer oil. The solid elements, ^{238}U , ^{232}Th and ^{40}K , are removed by water extraction. These solid elements are ionized in the liquid and captured by the water. Pure water is used for this extraction, being supplied from the water purification system. Since the light output of the scintillator is quenched by oxygen, the nitrogen purge removes oxygen gas as well as the radioactive ^{222}Rn gas and water from the scintillator.

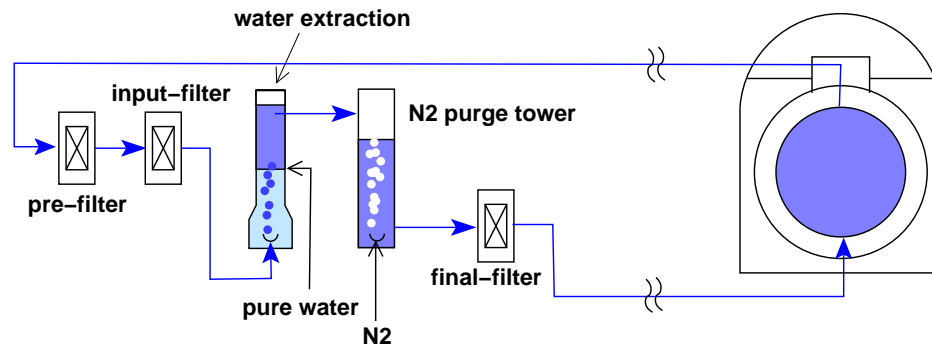


Figure 2.5: Purification system

Table 2.6: Detector Parameters

parameter	design value	actual value
scintillator volume	1,200 m ³	1,178±10 m ³
buffer oil volume	1,800 m ³	1,806±20 m ³
trigger threshold		
higher threshold (prompt trigger)	<1MeV	700KeV(50% efficiency)
lower threshold (delayed trigger)	—	425KeV(50% efficiency)
vertex resolution @ central 1MeV event	10 cm	~25 cm
fiducial volume for $\bar{\nu}_e$ event	600 ton	408.48 ton
energy resolution (σ/\sqrt{E})	<10 %	~7.5 % (for E_{visible})
contained U in the scintillator	$\leq 10^{-14}$ g/g $\leq 100\mu\text{Bq/m}^3$	$(3.5\pm 0.5)\times 10^{-18}$ g/g $(0.034\pm 0.005)\mu\text{Bq/m}^3$
contained Th in the scintillator	$\leq 10^{-14}$ g/g $\leq 100\mu\text{Bq/m}^3$	$(5.2\pm 0.8)\times 10^{-17}$ g/g $(0.16\pm 0.03)\mu\text{Bq/m}^3$
contained ^{40}K in the scintillator	$\leq 10^{-14}$ g/g	$<2.7\times 10^{-16}$ g/g

2.1.6 PMT

The light output from the scintillator is proportional to the event energy, and the energy resolution depends on the number of detected photons. Good timing resolution is also essential for vertex reconstruction. The new PMTs with a sensitive area of 17 inches in diameter (17" PMT) was developed especially for good timing resolution, and the 20" PMT were designed to detect the maximal number of photons. Due to this large sensitive area, the total detector coverage is 34% with 1,879 PMTs, and it is 22% counting only 17" PMTs.

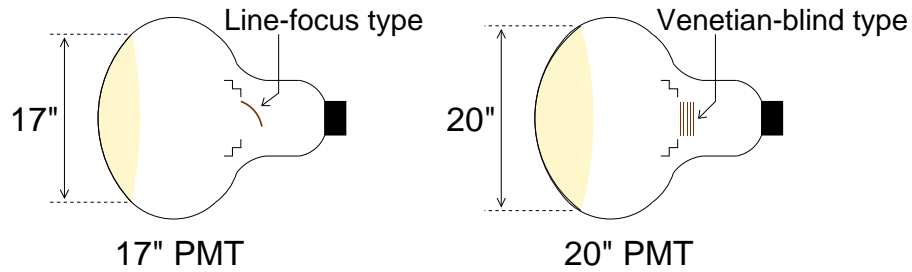


Figure 2.6: Mechanical difference between 17" PMT and 20" PMT. Their sizes are same but diameters of the photon detectable area are different (17 inch and 20 inch). Moreover dynode shape is different, "Line-focus" type for 17" PMT and "Venetian-blind" type for 20" PMT. Time resolution and 1p.e. resolution of 17" PMT are better than 20" PMT through reducing photon detectable area and dynode change.

By limiting the photon acceptance area to the central 17 inches and replacing the original Venetian-blind dynode with a line-focus type, the transit time spread (TTS) is significantly improved from ~ 5.5 nsec (FWHM) to ~ 3 nsec (FWHM), and the peak-to-valley ratio (P/V ratio) is improved from ~ 1.5 to ~ 3 . Figure 2.6 and 2.8 show a comparison of the shape and qualities between 17" PMTs and 20" PMTs which are used in Super-Kamiokande.

Variation of the 1p.e. pulse height in magnetic fields below 50 mGauss is less than 20%. A set of compensating coils will be installed in the cavern to cancel the magnetic field of the earth (~ 500 mGauss) to a level well below the limit of the 50 mGauss necessary for proper operation of the photomultipliers.

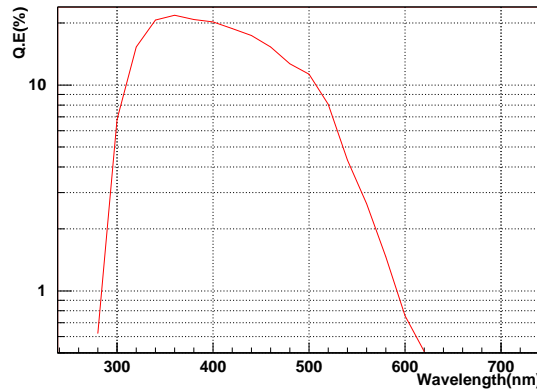


Figure 2.7: Quantum efficiency of PMT which measure by Hamamatsu company.

The correlation of quantum efficiency (Q.E.) with the wavelength of light is shown in Figure 2.7. It depends mainly on the material of the photo-cathode, bialkali, although individual differences exist because of variation in the thickness of the material .

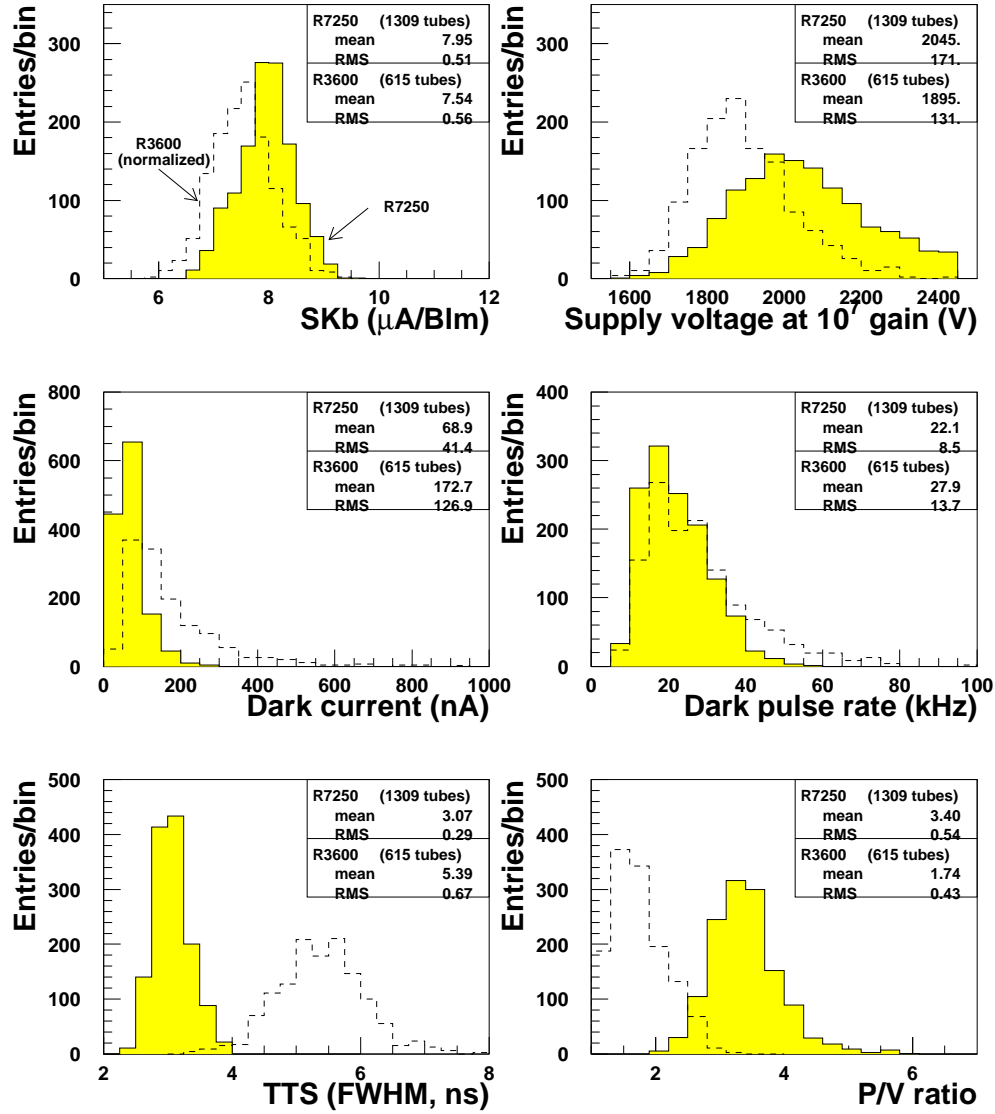


Figure 2.8: Performance difference between 17''PMT(shaded histogram) and 20''PMT. SKb means sensitivity of cathode to blue. TTS means Transit Time Spread. P/V ratio is Peak-to-Valley ratio in the pulse height spectrum for 1p.e. signals and dark current. P/V ratio is bigger if 1p.e. resolution is better and dark current is lower. Performance of the 17''PMTs are better than that of the 20''PMTs, especially TTS and P/V ratio.

2.1.7 Front-End Electronics (FEE)

The KamLAND front end electronics (FEE) system (Figure 2.9) is based on the Analog Transient Waveform Digitizer (ATWD). The ATWD simultaneously can capture four channels of independent signals at about 670MHz sample speeds. The sampling action is generated internally without high-speed external clocks. The ATWD is equipped with a common-ramp parallel Wilkinson 10-bit ADC, permitting the direct conversion on-chip of the captured analog signal. Digitization and readout of the entire 128-sample waveform requires about $25\ \mu\text{sec}$ at 40 MHz for the 10-bit range. The time interval between each sample is about 1.49nsec. It is well calibrated for each channel with frequent (daily) calibration at the beginning of of run using an internal 40 MHz test pulse. Each ADC gate width is 4 sample time intervals ($1.49 \times 4 \sim 6\ \text{nsec}$). The dual-ATWD ping-pong scheme which requires channel A and B realizes very short dead times ($< 0.4\ \mu\text{sec}$), and each PMT channel has two ATWD channels, A and B. The FEE is designed for the use of multiple ATWD channels to extend the dynamic range. Thus the four channels of one ATWD are addressed as follows,

- High gain channel
capture 20 times amplified waveform to detect 1p.e. level signals
- Medium gain channel
capture 4 times amplified waveform
- Low gain channel
capture attenuated, 1/2, waveform for the study of muon.
- Time interval calibration channel
The input for 40 MHz test pulse.

A lower gain waveform is acquired when higher gain is saturated (Figure 2.10). The discriminator threshold is adjusted to about 1/3 p.e. pulse height. Each PMT hit information is kept for 125nsec. Trigger decisions are based on this PMT hits information (Nsum).

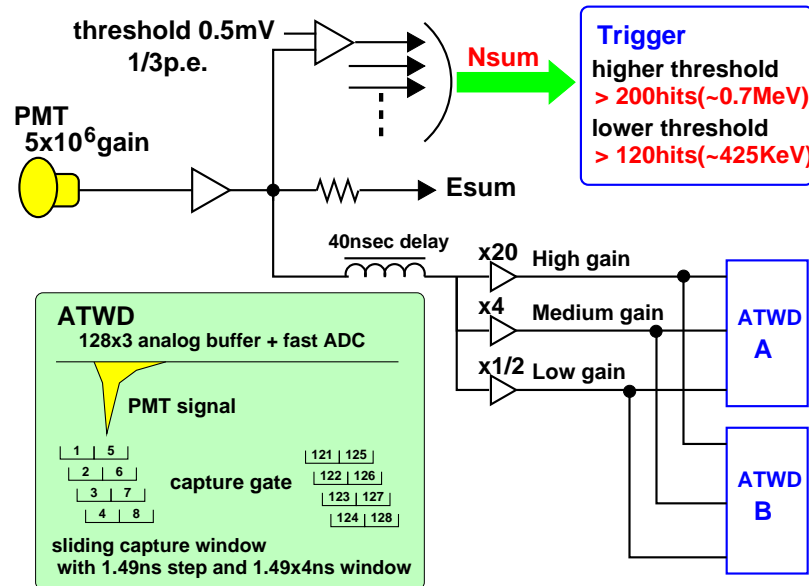


Figure 2.9: Dual $\times 3$ gain $\times 10$ bits $\times 128$ depth Analog Transit Waveform Digitizer sliding capture with 1.49nsec step and 1.49×4 nsec width

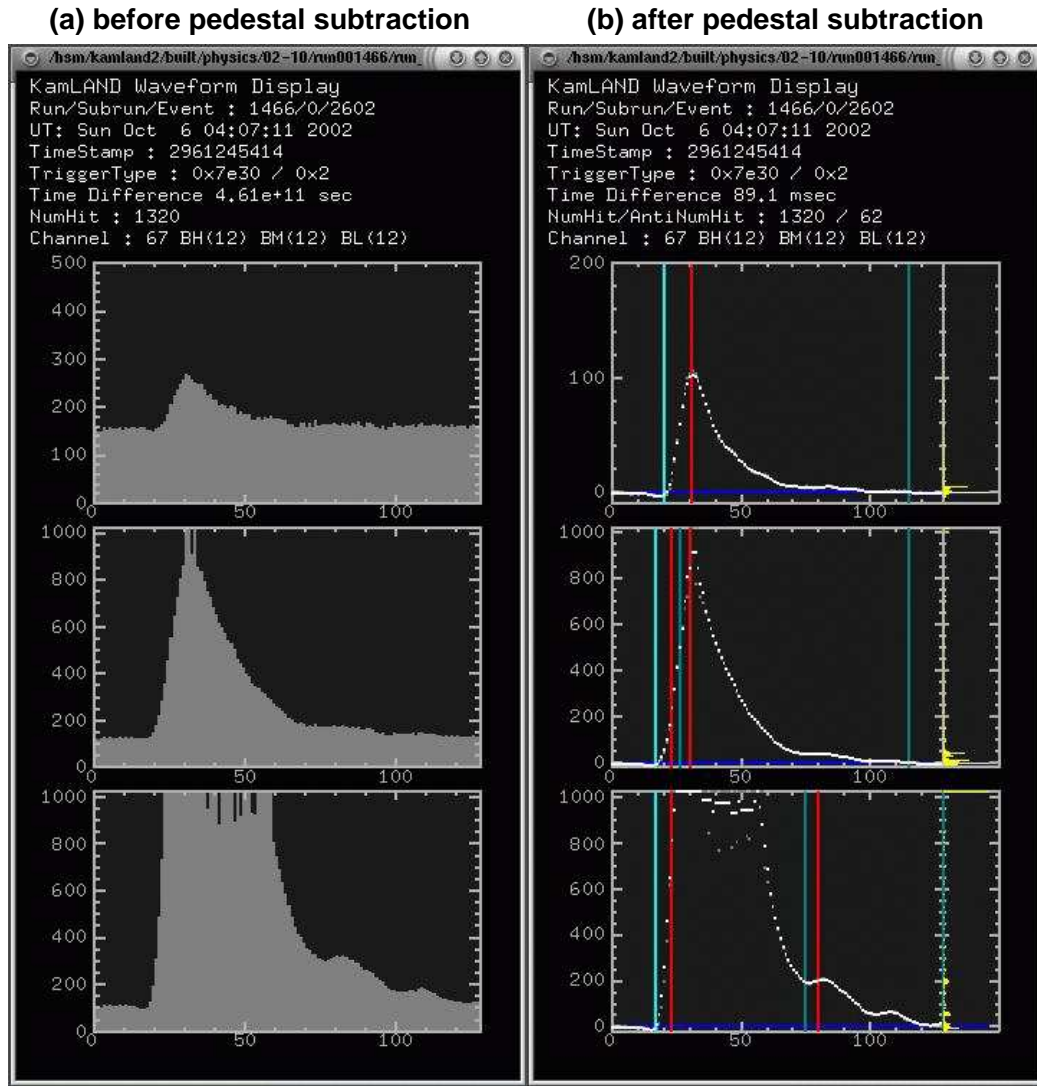


Figure 2.10: Digital waveform from FEE before pedestal subtraction (a) and after subtraction (b) in a muon event. Lower gain waveform is acquired when higher gain is saturated. These are high, medium and low gain from bottom to top figures.

2.1.8 Trigger system

The primary ID (inner detector) trigger threshold is set at 200PMT hits which corresponds to about 0.7MeV. This threshold is lowered to 120hits for 1msec after the primary trigger to observe lower energy delayed activity. Thus, the primary ID trigger is called the prompt (global) trigger and the later one is called the delayed trigger. The OD (outer detector) threshold is set to 6, 5, 6 and 7 hits respectively for the top, upper, lower and bottom region in the outer detector, and it has a 99% efficiency. Moreover, a “history” trigger is issued every 25 nsec while PMT hits exceed the lower threshold up to a maximum of 200nsec. The maximum value of Nsum in this history information for an event is called NsumMax.

The trigger issues a 5 bit trigger command to the FEE. The inner detector crates (numbers 1 to 5 & 7 to 10) and outer crate (OD; crate number 6) can receive different trigger commands.

Issuing of a trigger command is based on the different conditions described in Appendix B. All triggers are decided by the 4 bit Nsum received from each FEE card (4bit represents the number of PMTs connected to that card whose signal went above the discriminator level), a trigger signal from a calibration device such as a laser, or input from the data acquisition system (DAQ). For each trigger, a record of the trigger condition is kept. The format of this record is described in the Table B.1.

The correlation of the trigger efficiency with energy is calculated using NsumMax. The efficiency curve for the prompt trigger is defined as the ratio,

$$\frac{(\text{number of delayed trigger events with } N_{\text{sumMax}} \geq 200)}{(\text{number of delayed trigger events})} \quad (2.1)$$

The efficiency curve within 5m fiducial radius is shown in Figure 2.11. The efficiency is 99 %

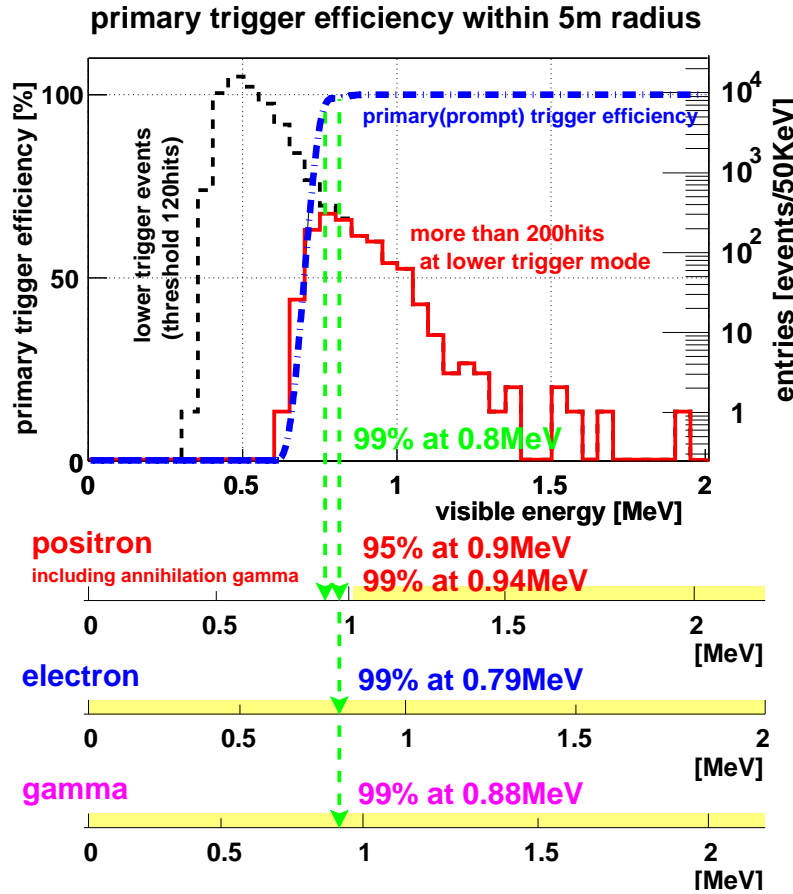


Figure 2.11: The primary(prompt) trigger efficiency curve within 5m fiducial radius is shown in dash-dot line. Trigger threshold is set at 200 PMT hits within 125nsec for this trigger, and it is set at 120 PMT hits for lower(delayed) trigger. The energy spectrum of lower trigger events within 5m radius is shown in dashed line, and ≥ 200 hits one is shown in solid line. The efficiency curve is defined as the ratio of these spectra for each energy $\Delta N_{\geq 200\text{hits}}/\Delta N$. A 99% efficiency is given at 0.8MeV visible energy and it is also given at 0.94, 0.79 and 0.88MeV for each particle, e^+ , e^- and γ . Deposit energy of positron is $\geq 1.022\text{MeV}$ because of pair annihilation with electron, but detected energy is less than 1.022MeV sometimes because of the energy resolution. The efficiency at 0.9MeV is 95% for positron.

at 0.8MeV visible energy and at 0.94, 0.79 and 0.88MeV true energy for each particle, e^+ , e^- and γ respectively. The difference is due to the quenching and Čerenkov light contribution of each particle (See section 3.7). The positron energy deposition is $\geq 1.022\text{MeV}$ because of pair annihilation with electron, but the detected energy is sometimes less than 1.022MeV because of the energy resolution. More than 99.998% efficiency is given for the reactor $\bar{\nu}_e$ detection in the case of no oscillation.

The delayed trigger efficiency within a 5m fiducial radius is also shown in Figure 2.12. This efficiency was evaluated using a special “prescaled” run. The trigger threshold of prescaled run is set at 50 PMT hits within any 125nsec and the trigger is active only periodically to reduce data size. The efficiency curve is defined as the ratio,

$$\frac{(\text{ number of prescaled trigger events with } N_{\text{hit}} \geq 120)}{(\text{ number of prescaled trigger events })} \quad (2.2)$$

The efficiency is 99% at 490KeV visible energy and at 500 and 570KeV for electron and gamma respectively.

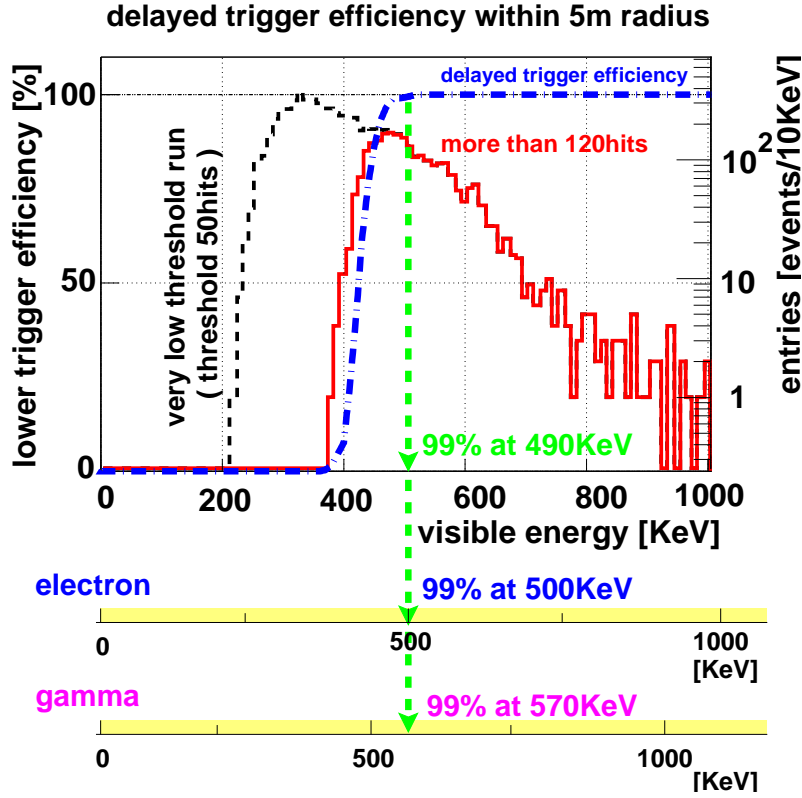


Figure 2.12: The lower(delayed) trigger efficiency curve within a 5m fiducial radius is shown as a dash-dot line. Trigger threshold is set at 120 PMT hits within 125nsec for this trigger. This efficiency was evaluated using a special “prescaled” run in which the trigger threshold was set at 50 PMT hits within 125nsec and the trigger is active only periodically to reduce data size. The energy spectrum of the run within a 5m radius is shown as a dashed line, and $\geq 120\text{hits}$ is shown as a solid line. The efficiency curve is defined as the ratio of these spectra for each energy $\Delta N_{\geq 120\text{hits}} / \Delta N$. The efficiency is 99% at 490KeV visible energy and at 500 and 570KeV for electron and gamma respectively.

2.2 Anti-Neutrino Detection

2.2.1 Delayed Coincidence Technique

Detection of $\bar{\nu}_e$ is performed via the inverse β -decay reaction in the scintillator,

$$\bar{\nu}_e + p \rightarrow e^+ + n \quad (E_{\text{threshold}} = \Delta m_{np} + m_e = 1.804\text{MeV}) \quad (2.3)$$

$$n + p \rightarrow d + \gamma(2.22457\text{MeV}). \quad (2.4)$$

The energy threshold of this interaction is calculated with the mass difference of the neutron and the proton ($\Delta m_{np}=1.293\text{MeV}$) and positron (electron) mass ($m_e=0.511\text{MeV}$).

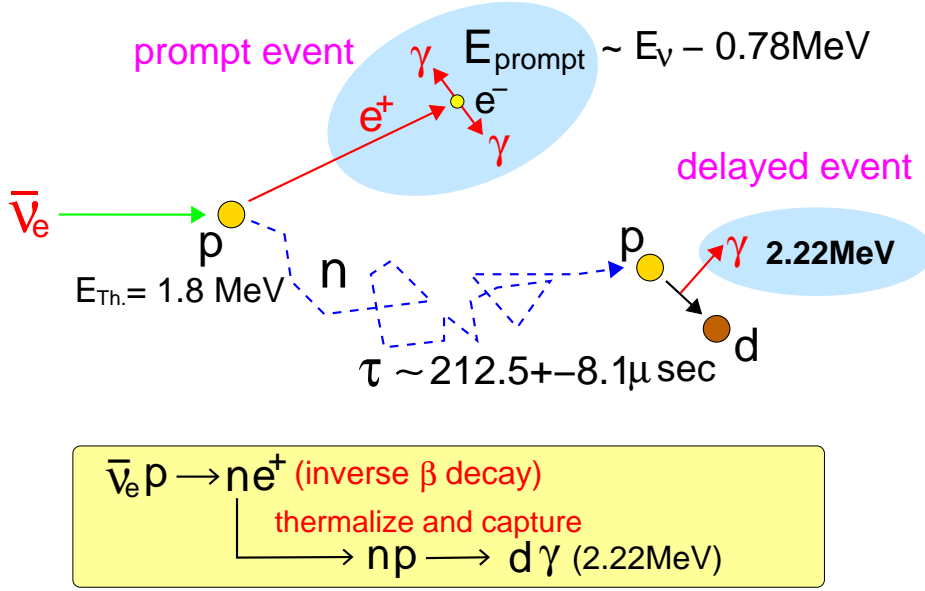


Figure 2.13: Electron anti-neutrino is detected as two correlated events. Positron event (“prompt” event) which is produced via $\bar{\nu}_e p \rightarrow e^+ n$ and a neutron capture gamma (“delayed” event) whose energy is 2.22457MeV . The energy threshold of inverse β -decay is $E_{\bar{\nu}_e}=1.806\text{MeV}$ and the prompt energy is more than 1.022MeV . These two events are correlated by vertex position and time difference.

The positron deposits its energy by ionization and then produces 2 γ -ray via pair annihilation: $e^+ + e^- \rightarrow 2\gamma$ ($2 \times 0.511\text{MeV}$). Therefore, the energy deposition $E_{\text{deposition}}$ in the scintillator is;

$$E_{\text{deposition}} = E_{\bar{\nu}_e} - (\Delta m_{np} + m_e) - T_n(\theta) + 2m_e \quad (2.5)$$

$$= E_{\bar{\nu}_e} - 0.782\text{MeV} - T_n(\theta), \quad (2.6)$$

where T_n is the kinetic energy of recoil neutron and its related with the scattering angle of positron θ (\leftrightarrow recoil angle of neutron). The prompt event is this energy deposition of the positron.

The kinematics in inverse β -decay is [34],

$$A = 4(E_{\bar{\nu}_e} + Mp + E_{\bar{\nu}_e} \cos \theta)(E_{\bar{\nu}_e} + Mp - E_{\bar{\nu}_e} \cos \theta) \quad (2.7)$$

$$B = 2(m_e^2 + M_p^2 - M_n^2 + 2M_p E_{\bar{\nu}_e}) E_{\bar{\nu}_e} \cos \theta \quad (2.8)$$

$$C = 4m_e^2(E_{\bar{\nu}_e} + M_n)^2 - (2M_p E_{\bar{\nu}_e} + M_p^2 - M_n^2 - m_e^2) \quad (2.9)$$

$$p_e = \frac{B + \sqrt{B^2 - A \cdot C}}{A} \quad \dots \quad \text{momentum of positron} \quad (2.10)$$

$$T_e = \sqrt{p_e^2 + m_e^2} - m_e \quad \dots \quad \text{kinetic energy of positron} \quad (2.11)$$

$$p_n = \sqrt{p_e^2 + E_{\bar{\nu}_e}^2 - 2p_e E_{\bar{\nu}_e} \cos \theta} \quad \dots \quad \text{momentum of neutron} \quad (2.12)$$

$$T_n = \sqrt{p_n^2 + M_n^2} - M_n \quad \dots \quad \text{kinetic energy of neutron} \quad (2.13)$$

$$\cos \varphi = \frac{E_{\bar{\nu}_e} - p_e \cos \theta}{p_n} \quad \dots \quad \varphi : \text{recoil angle of neutron} \quad (2.14)$$

where M_p, M_n are the mass of the proton and neutron, θ, φ are the recoil angles of the positron and neutron, and $E_{\bar{\nu}_e}$ is the $\bar{\nu}_e$ energy. The correlation of the kinetic energy of the neutron with the $\bar{\nu}_e$ energy is shown

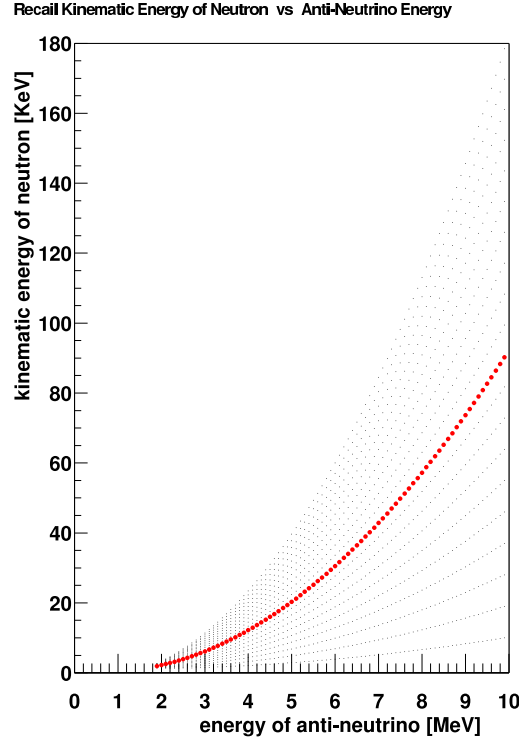


Figure 2.14: Correlation between kinetic energy of recoil neutron and $\bar{\nu}_e$ is shown for various direction from -1 to 1 per 0.1 with small circle and for mean kinetic energy with big circle. This is a calculation based on [6]. For reactor $\bar{\nu}_e$ detection, effective recoil energy of neutron is about 10KeV.

The neutron gives ~ 2.22 MeV γ -ray from thermal neutron capture on a proton (delayed event), Its mean capture lifetime is $212.5 \pm 8.1 \mu\text{sec}$ (Section 5.2.2). The neutron is captured not only on proton, but also on various other isotopes (Table 2.7). 0.55% of the neutrons are captured on ^{12}C while 99.45% of them are captured on protons. This information is useful for the energy calibration. (Section 3.7 and 4.3.1).

Table 2.7: Neutron capture nuclei

Isotope	Natural Abundance [%]	σ_{capture} [barn]	number [/kton]	fraction [%]	energy [MeV]
$^1\text{H}(\text{p})$	99.985	0.332	8.469×10^{31}	99.45	2.22457
$^2\text{H}(\text{d})$	0.015	0.0005	1.271×10^{28}	2×10^{-7}	6.2574
^{12}C	98.693	0.0034	4.255×10^{31}	0.55	4.9463
^{13}C	1.107	0.0009	4.732×10^{29}	2×10^{-5}	8.1762
^{14}N	99.634	0.0750	2.593×10^{28}	9×10^{-5}	10.8348
^{16}O	99.759	0.000178	6.047×10^{25}	5×10^{-9}	4.1425

Since the prompt and delayed events have characteristic correlations, such as vertex position, event time and monochromatic energy of the delayed event. Selection criteria for this delayed coincidence is;

- Time correlation $\cdots 0.5 \sim 660 \mu\text{sec}$ ($\sim 3\tau_{\text{capture}}$)
Calibration for this efficiency is described in Section 5.2.2.
- Space correlation $\cdots \leq 1.6 \text{ m}$
Calibration for this efficiency is described in Section 5.2.3.
- Delayed energy window $\cdots 1.8 \sim 2.6 \text{ MeV}$
Efficiency calculation is described in Section 3.7.

The delayed coincidence technique is a powerful tool for reducing background. Its reduction factor is $\sim 1/10,000$ (Chapter 6).

2.2.2 Observed spectrum

The number of reactor $\bar{\nu}_e$ (N_{expected}) is calculated as follows,

$$N_{\text{expected}} = \int n(E_e) dE_e, \quad (2.15)$$

$$n(E_e) = \int N_p [f(E_{\bar{\nu}_e}, t) \sigma(E_{\bar{\nu}_e})] \cdot \varepsilon_d dt, \quad (2.16)$$

where

E_e : positron energy

$f(E_{\bar{\nu}_e}, t)$: $\bar{\nu}_e$ flux

$\sigma(E_{\bar{\nu}_e})$: cross section of inverse β -decay

ε_d : detection efficiency ($\varepsilon_{\text{trigger}} \times \varepsilon_{\text{space-correlation}} \times \varepsilon_{\text{time-correlation}}$)

The recoil of the neutron should be considered because the observed positron energy is a little lower than in the no-recoil case. Therefore, the definition of $n(E_{\bar{\nu}_e})$ is changed by using the spectrum correction from [6], [35],

$$n(E_e) = \int N_p \left[f(E_{\bar{\nu}_e}, t) \sigma(E_{\bar{\nu}_e}) \frac{dE_{\bar{\nu}_e}}{dE_e} \right] \cdot \varepsilon_d dt, \quad (2.17)$$

$$\simeq \sum_i N_p \left[f_i(E_{\bar{\nu}_e}) \sigma(E_{\bar{\nu}_e}) \frac{dE_{\bar{\nu}_e}}{dE_e} \right] \cdot \varepsilon_d \Delta t_i \quad (i : \text{run number}), \quad (2.18)$$

$$\frac{dE_{\bar{\nu}_e}}{dE_e} = 1 + \frac{2E_e + \Delta}{M} \quad (2.19)$$

where $\Delta = M_n - M_p = 1.2933\text{MeV}$, $M = (M_n + M_p)/2 = 938.92\text{MeV}$, and Δt_i is the livetime of each run.

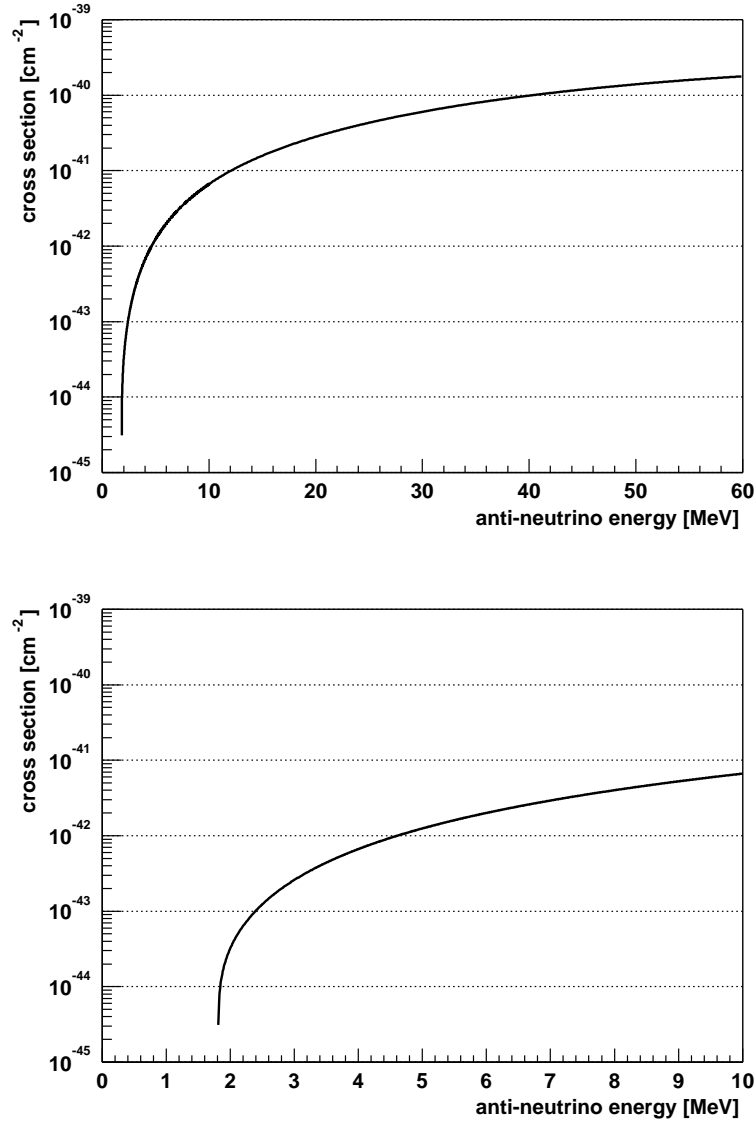


Figure 2.15: The cross section of inverse β -decay ($\bar{\nu}_e p \rightarrow n e^+$) [6].

2.2.3 Cross section of inverse β -decay

According to references [34], [6], and [36], the cross section of $\bar{\nu}_e p \rightarrow n e^+$ considered to the order of $O(1/M)$ is

$$\sigma(E_{\bar{\nu}_e}) = \left[\int_{-1}^1 \left(\frac{d\sigma(E_{\bar{\nu}_e})}{d\cos\theta} \right)^{(1)} d\cos\theta \right] \cdot (1 + \delta_{outer}^{rad}), \quad (2.20)$$

where $\left(\frac{d\sigma(E_{\bar{\nu}_e})}{d\cos\theta}\right)^{(1)}$ and δ_{outer}^{rad} are the differential cross section and outer radiative correction respectively. Figure 2.15 shows the correlation of cross section with energy.

differential cross section [34]

$$\begin{aligned} \left(\frac{d\sigma(E_{\bar{\nu}_e})}{d\cos\theta}\right)^{(1)} &= \frac{\sigma_0}{2} \left[(f^2 + 3g^2) + (f^2 - g^2)v_e^{(1)} \cos\theta \right] E_e^{(1)} p_e^{(1)} \\ &\quad - \frac{\sigma_0}{2} \frac{\Gamma}{M} E_e^{(0)} p_e^{(0)}, \end{aligned} \quad (2.21)$$

where

$$E_e^{(0)} = E_{\bar{\nu}_e} - \Delta \quad (\Delta = M_n - M_p = 1.2933\text{MeV}) \quad (2.22)$$

positron energy at zeroth order in $1/M_p$

$$E_e^{(1)} = E_e^{(0)} \left[1 - \frac{E_{\bar{\nu}_e}}{M_p} (1 - v_e^{(0)} \cos\theta) \right] - \frac{y^2}{M_p} \quad (2.23)$$

positron energy at first order in $1/M_p$

$$y^2 = \frac{\Delta^2 - m_e^2}{2} \quad (2.24)$$

$$p_e^{(j)} = \sqrt{\left(E_e^{(j)}\right)^2 - m_e^2} \quad (j = 0, 1) \quad (2.25)$$

$$v_e^{(j)} = \frac{p_e^{(j)}}{E_e^{(j)}} \quad (j = 0, 1) \quad (2.26)$$

$$f = 1.0 \quad \text{vector coupling constant} \quad (2.27)$$

$$g = 1.26 \quad \text{axial - vector coupling constant} \quad (2.28)$$

$$\sigma_0 = \frac{G_F^2 \cos^2 \theta_{cabibo}}{\pi} \left(1 + \delta_{inner}^{rad} \right) \quad (2.29)$$

G_F : Fermi constant

$\cos \theta_{cabibo} = 0.97$

$\delta_{inner}^{rad} = 0.024$ inner radiative correction

$$\begin{aligned} \Gamma &= 2(f + f_2)g \left[(2E_e^{(0)} + \Delta)(1 - v_e^{(0)} \cos\theta) - \frac{m_e^2}{E_e^{(0)}} \right] \\ &\quad + (f^2 + g^2) \left[\Delta(1 + v_e^{(0)} \cos\theta) - \frac{m_e^2}{E_e^{(0)}} \right] \\ &\quad + (f^2 + 3g^2) \left[(E_e^{(0)} + \Delta)(1 - \frac{1}{v_e^{(0)}} \cos\theta) - \Delta \right] \\ &\quad + (f^2 - g^2) \left[(E_e^{(0)} + \Delta)(1 - \frac{1}{v_e^{(0)}} \cos\theta) - \Delta \right] v_e^{(0)} \cos\theta, \end{aligned} \quad (2.30)$$

and $f_2 = \mu_p - \mu_n - 1 = 2.793 + 1.913 - 1.0 = 3.706$.

outer radiative correction [36]

The outer radiative correction consists of two parts, a virtual part ($g_v(E)$) and a bremsstrahlung part ($g_b(E)$),

$$\delta_{outer}^{rad} = \frac{\alpha}{\pi} [g_v(E_e) + g_b(E_e)], \quad (2.31)$$

where $\alpha = 1/137$ is the fine structure constant, and $g_v(E)$ and $g_b(E)$ are given by the following lengthy expressions,

$$\begin{aligned} g_v(E) = & 2 \ln \left(\frac{M_Z}{M_p} \right) + \frac{3}{2} \ln \left(\frac{M_p}{m_e} \right) \\ & + 2 \ln \left(\frac{E - m_e}{m_e} \right) \left(\frac{1}{2\beta(E)} \ln \left(\frac{1 + \beta(E)}{1 - \beta(E)} \right) - 1 \right) \\ & + \frac{3}{4} + \mathcal{A}(\beta(E)) - 0.57, \end{aligned} \quad (2.32)$$

$$\mathcal{A}(\beta) = \frac{1}{2} \beta \ln \left(\frac{1 + \beta}{1 - \beta} \right) - 1 - \frac{1}{\beta} \left[\frac{1}{2} \ln \left(\frac{1 + \beta}{1 - \beta} \right) \right]^2 + \frac{1}{\beta} L \left(\frac{2\beta}{1 + \beta} \right), \quad (2.33)$$

$$\beta(E) = \frac{\sqrt{E^2 + m_e^2}}{|E|}, \quad (2.34)$$

$$L(\beta) = \int_0^\beta \frac{\ln(|1 - x|)}{x} dx = - \sum_{k=1}^{\infty} \frac{\beta^k}{k^2} \quad (|\beta| \leq 1). \quad (2.35)$$

In the $\bar{\nu}_e p \rightarrow n e^+$ reaction, the first term in g_v is zero because $M_Z = M_p$. The quantities $\beta(E)$ and $L(\beta)$ also enter into the formula for $g_b(E)$,

$$\begin{aligned} g_b(E) = & \mathcal{C}(\beta(E)) + \frac{1}{2E^2\beta(E)} \int_{m_e}^E (E - x) \ln \left(\frac{1 + \beta(x)}{1 - \beta(x)} \right) dx \\ & + 4E \int_{m_e}^E \frac{x\beta(x)F(x) - E\beta(E)F(E)}{E - x} dx, \end{aligned} \quad (2.36)$$

$$F(E) = \frac{1}{2\beta(E)} \ln \left(\frac{1 + \beta(E)}{1 - \beta(E)} \right) - 1, \quad (2.37)$$

$$\begin{aligned} \mathcal{C}(\beta) = & 2 \ln 2 \times \left[\frac{1}{2\beta} \ln \left(\frac{1 + \beta}{1 - \beta} \right) - 1 \right] + 1 \\ & + \frac{1}{4\beta} \ln \left(\frac{1 + \beta}{1 - \beta} \right) \left[2 + \ln \left(\frac{1 - \beta^2}{4} \right) \right] + \frac{1}{\beta} [L(\beta) - L(-\beta)] \\ & + \frac{1}{2\beta} \left[L \left(\frac{1 - \beta}{2} \right) - L \left(\frac{1 + \beta}{2} \right) \right]. \end{aligned} \quad (2.38)$$

Chapter 3

Event Reconstruction and Detector Calibration

Interaction vertex position, energy, and muon track information are essential information for physics studies. Raw data from KamLAND contains just trigger information (run and event number, event time, number of hits) and digital waveforms with a huge amount of data (around 120 GB/day). Therefore, data reduction and event reconstruction must be done before any analysis.

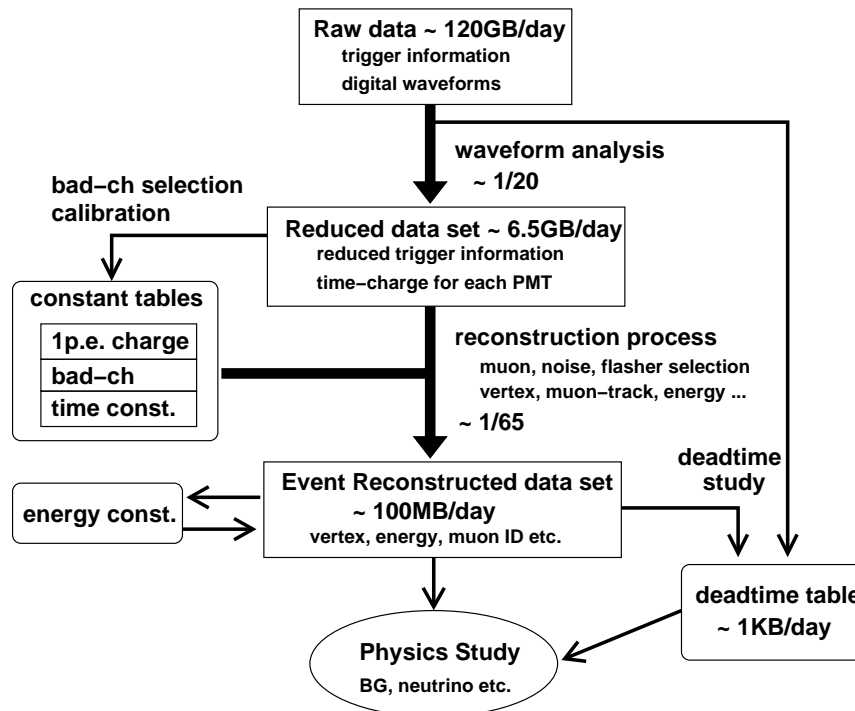


Figure 3.1: Data analysis and reduction flow.

First, the digital waveforms are analyzed and converted from their original format (10bits \times 128sample per channel) to time and charge information (64bits/channel), for a data reduction factor of about 20. Subsequently, various constants are created based on the detector calibration analysis. The event reconstruction process selects muon, noise, flasher and the other events, and reconstructs vertex, energy, and muon track. The data reduction factor is about 65. Finally, the various physics studies are performed using the reconstructed data set. Additionally, a deadtime table is created based on the deadtime study explained in Section 5.3.

3.1 Digital Waveform Analysis

Pulses coming from the PMTs are digitized inside a window of about 190 nsec. There are 128 samples with about 1.49 nsec between each sample. Waveform analysis is the process by which the arrival times and total charges of pulses within this time window are determined. The time relates the pulse to a specific physics event, while the charge associated with the incoming photon produced by an event can be related to the energy. The resolution and three gain channels (high-gain ~ 20 times, medium-gain ~ 2 times and low-gain ~ 0.5 times) of the electronics allow to analyze pulses created by highly energetic muons down to those created by single photons. Currently, all of the event reconstruction softwares use the time of the first pulse and the charge sum of all pulses in a given waveform, and also use the lower gain information in each channel, while multi pulse (like two, three photon) analysis is applied (Figure 3.3).

3.1.1 Algorithm

The analysis process can be described as follows, where w is pedestal subtracted sample, w' , w'' and w''' are derivatives of w , and sw is a smoothed one.

1. Pedestal subtraction

The ADC of each sample has unique offset. This fine structure is subtracted from the waveform before analysis. It is determined by acquiring 50 pedestal waveforms from each channel at the beginning of each run. Some pedestal waveforms contain noise or dark hit pulse, and these are rejected by the following cuts;

- the differential coefficient of every part of pedestal waveform should be less than 40 counts
- difference between maximum height and minimum height of the sample should be less than 50 counts
- no hit within 125nsec before trigger issue for the pedestal.
(the launch offset should be within 1 count from 0.)

There are two types of pedestal, “normal pedestal” and “pedestal only high gain which acquired forcibly” (FA pedestal). All three gain waveforms are taken for each PMT channel at “normal pedestal”, while only high gain waveforms are taken for on “FA pedestal”. The height of the normal pedestal sample is a few counts lower than that of the FA pedestal, and the FA pedestal sample is appropriate for the waveform of the high gain channel as shown in Figure 3.2.

2. Waveform smoothing

After pedestal subtraction, waveforms are smoothed to reduce the small statistical fraction in each ADC sample of high frequency noise. The smoothed sample can be written with first derivative,

$$sw_i = w_0 + \sum_{j=0}^{i-1} w'_j \quad (3.1)$$

3. Baseline adjustment

After pedestal subtraction, it is often found that the waveform baseline may not sit at zero ADC counts. The waveform is manually shifted so that its baseline is centered at

zero. This is important since the correct shifting will provide a more accurate value for pulse arrival time and charge. The baseline is readjusted with the difference between mean value of the original 128 samples and smoothed samples.

4. Pulse (peak) finding

The peak of the signal pulse is founded with the derivatives,

- $w'_{i-1} \cdot w'_{i+1} < 0$ & $w''_i \leq 0$ (looks like a peak)
find peak.
- $w'_{i-1} \cdot w'_{i+1} = 0$ & $w''_i \leq 0$ & $w_i > \text{previous} - \text{peak} - \text{hieght}$ (looks like a plateau)
find the edge whose right-side (latter timing samples) is higher than the left-side (faster timing samples) from a degenerate pulse consisting of multiple pulses.
- $w''_{i-1} \cdot w''_{i+1} < 0$ & $w'_i > 0$ & $w'''_i > 0$ (looks like a shoulder)
find an edge from a degenerate pulse consisting of multiple pulses.

5. Determination of pulse time and charge

The pulse time is defined as the leading edge (start time bin) of each pulse, and the resolution is the time interval between each sample. The ending time of each pulse is defined as bin just before the point of which smoothed sample height is negative after a peak. Charge is defined as the area of each pulse from the start time to the end time of the smoothed waveform. This area is normalized with the mean area of a single photon pulse.

Derivatives of waveform samples

In order to avoid high frequency noise in the derivatives, just a difference is not taken between neighboring samples, but over 5 samples. The exception to this is on the boundaries. If w_i is the waveform value where i takes values from 0 to 127, the first derivative as constructed by a 5 point running average,

$$w'_i = \frac{(w_{i+3} - w_{i-2})}{5}, \quad (3.2)$$

with exceptions at near the boundaries :

$$w'_0 = w_1 - w_0, \quad (3.3)$$

$$w'_1 = \frac{(w_3 - w_0)}{3}, \quad (3.4)$$

$$w'_{125} = \frac{(w_{127} - w_{124})}{3}, \quad (3.5)$$

$$w'_{126} = w_{127} - w_{126}, \quad (3.6)$$

The higher order derivatives are constructed in a similar fashion, but over 3-sample intervals of the previous derivative. A 3 point running average for the second derivative and a 3 point

running average for the third derivative are :

$$w''_i = \frac{(w'_{i+2} - w'_{i-1})}{3}, \quad (3.7)$$

$$w''_0 = w'_1 - w'_0, \quad (3.8)$$

$$w''_{125} = w'_{126} - w'_{125}, \quad (3.9)$$

$$w'''_i = \frac{(w''_{i+2} - w''_{i-1})}{3}, \quad (3.10)$$

$$w'''_0 = w''_1 - w''_0, \quad (3.11)$$

$$w'''_{125} = w''_{125} - w''_{124} \quad (3.12)$$

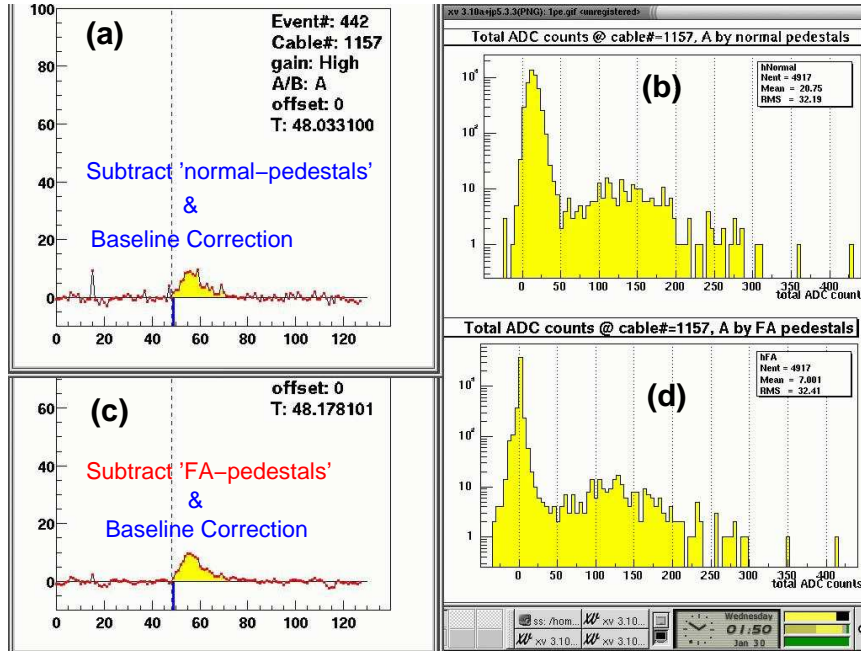


Figure 3.2: There are two types of pedestals, “normal pedestals” and “forced acquisition pedestals” (FA pedestal). All waveforms of all three gains are taken for each PMT channel when the pedestal is taken as “normal pedestal” mode. “FA pedestal” is taken only for high gain waveform. The height of a normal pedestal is a few counts lower than that of the FA pedestal and so an FA pedestal is appropriate for waveforms in the high gain channel. Digital waveforms which subtracted FA pedestal (c) look better than normal pedestal subtracted waveforms (a). Moreover, the 1p.e. peak looks better in the histogram of total ADC counts, (b) normal pedestal subtraction and (d) FA pedestal subtraction.

3.1.2 Calibration of time bin width using clock test pulse

The time interval between each sample is about 1.49nsec, and it is well calibrated for each channel with frequent (daily) calibration at the beginning of each run using an internal 40 MHz test pulse which is shown in Figure 3.4. The time bin width is written by the expression:

$$(\text{time bin width}) = 25\text{nsec}/(\text{peak} - \text{interval}) \quad (3.13)$$

The measurement result for each channel is iterated, and the time information of each channel is corrected.

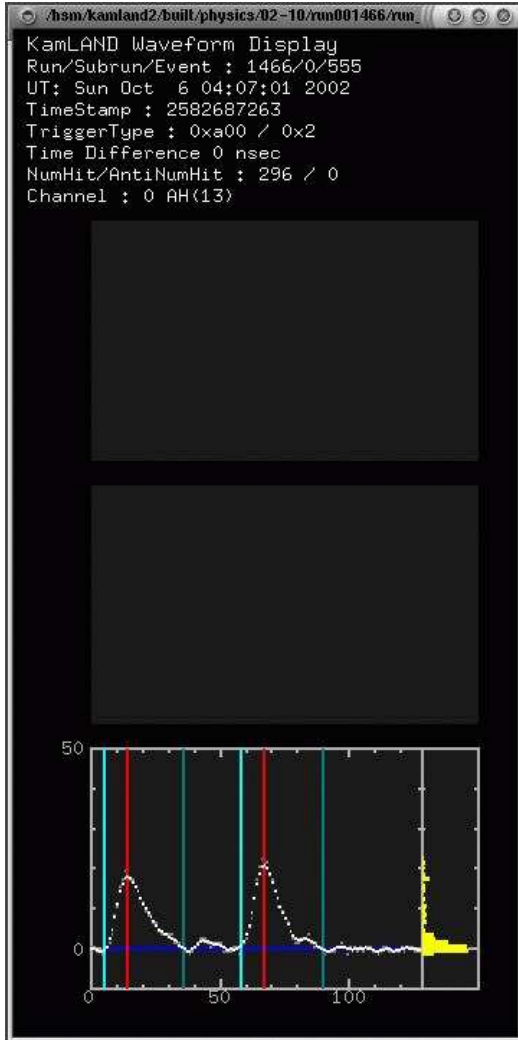


Figure 3.3: Two photon pulse information is analyzed in the waveform analysis.

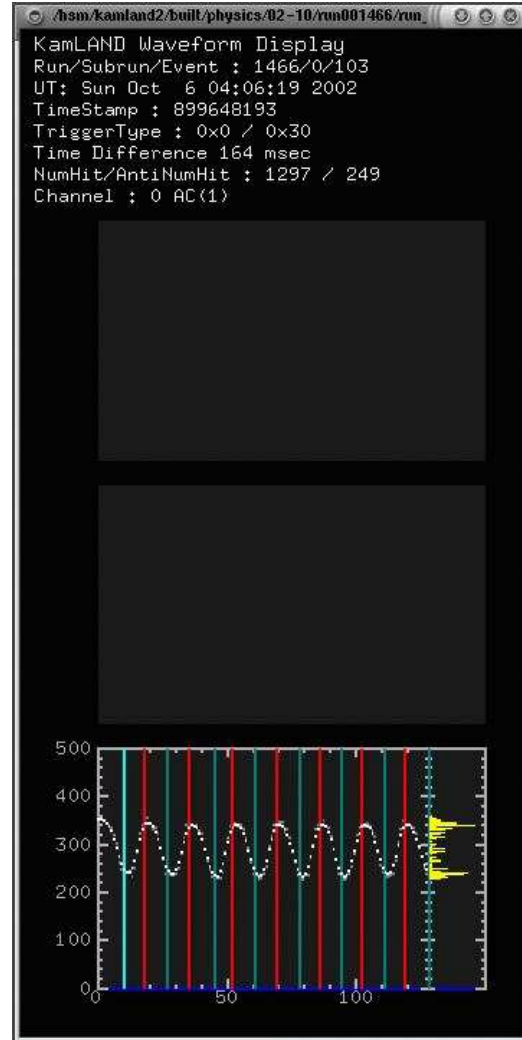


Figure 3.4: Periodic test pulse for time interval calibration between each samples.

3.2 Single Photo-electron Charge Calibration (Gain Calibration)

The charge of a single photo-electron (1p.e.), defined to be the area of a 1p.e. pulse, changed gradually over an ~ 8 month period (Figure 3.5). Thus, the pulse area of 1p.e for each channel must be calibrated, and the charge of each channel must be normalized channel by channel and run by run.

The mean 1p.e. charge is measured from the peak charge in selected events, which are chosen as follows;

- Muon veto for 2 msec
- Remove noise event
- Low occupancy ($9 \sim 14\%$) event ($120 \leq \text{NsumMax} \leq 180$)
- Distance from the reconstructed vertex to each PMT is more than 6 m.
- Single pulse for each PMT (waveform)

The histogram consisting the above mentioned events shows a clear 1p.e. peak (Figure 3.6). This peak value is used as the normalization constant for the charge. Therefore, the 1p.e. charge is defined as 1. This normalization constant is measured for each channel and for each run except for short runs of less than several hours. In such a case, the constants from a nearby run are used. The final result is that the charge of 1p.e. is exactly 1.

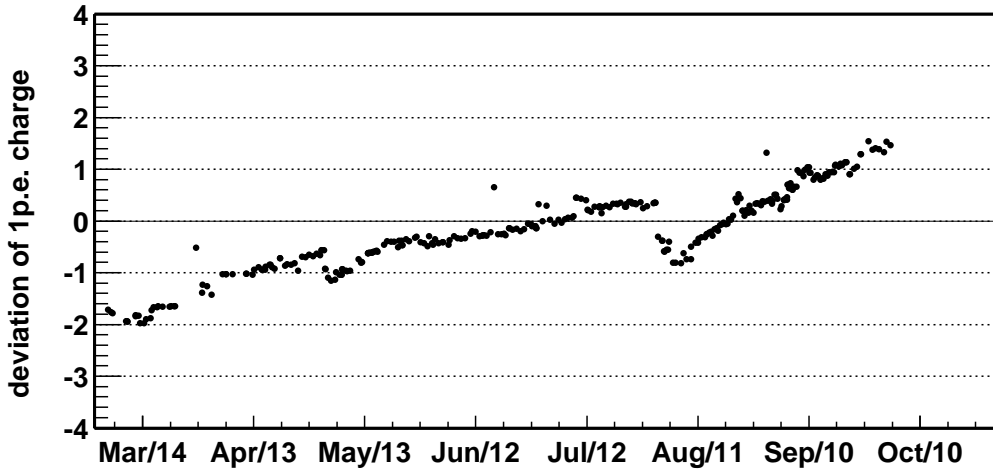


Figure 3.5: Time variation of the mean charge of single p.e., which is the pulse area of 1 p.e. pulse. Over approximately half a year, it has risen gradually by about 3.5%.

3.3 Bad Channel Selection

There were failed and unstable channels amounting to several in the inner detector and around 55 in the outer detector, the number of which has decreased for a half year period due to careful detector maintenance (Figure 3.7). These channels are referred to as “bad channels”

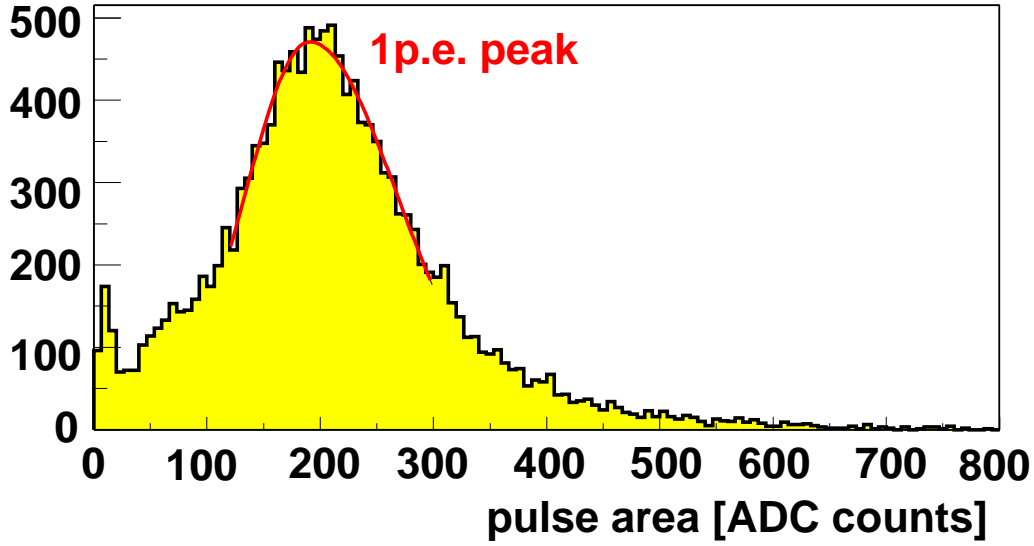


Figure 3.6: Charge, pulse area, histogram in low occupancy events.

(bad-ch) and are masked to prevent possibility of systematic biases affecting vertex and energy reconstruction.

Bad channels are found by observing each channel's hit rate and charge. The selection criteria for the inner detector are as follows;

1. Hit rate ($< 1,000\text{hits}/10,000\text{events}$)
Find low response channels coming from electronics failures.
2. No-hit rate ($> 1,000\text{no-hits}/10,000\text{events}$)
Find no response channels caused by PMT high voltage power outage etc.
3. Hit rate in high charge muon event, $Q_{ID} \geq 10^{5.5}$ p.e. ($< 80\text{hits}/100\text{high-charge-muon}$)
Find excessively low gain channel.
4. Difference of hit rate between A-ch and B-ch. ($> 22\%$ difference in 10,000 events sample)
Find bad-ch for which the ping-pong scheme in the FEE failed.
5. ADC counts for 1p.e. is too low ($< \bar{Q}_{adc} \times 1/4$) or too high ($> \bar{Q}_{adc} \times 4$).
Find very low gain or very high gain channels. The \bar{Q}_{adc} is the mean ADC counts corresponding to 1p.e. for each channel.
6. Charge difference in high charge muon events. ($Q_{ID} \geq 10^{5.5}$ p.e.)

$$\frac{1}{N_i} \sum_{j=1}^{N_i} \frac{(Q_i - Q_j)^2}{Q_j} > 400\text{p.e.} \quad (Q_j > 0, j : \text{neighbor PMT}) \quad (3.14)$$

Find channels with a large gain difference by a comparison of the gain between neighboring channels.

For the outer detector, only criterion #1 applies.

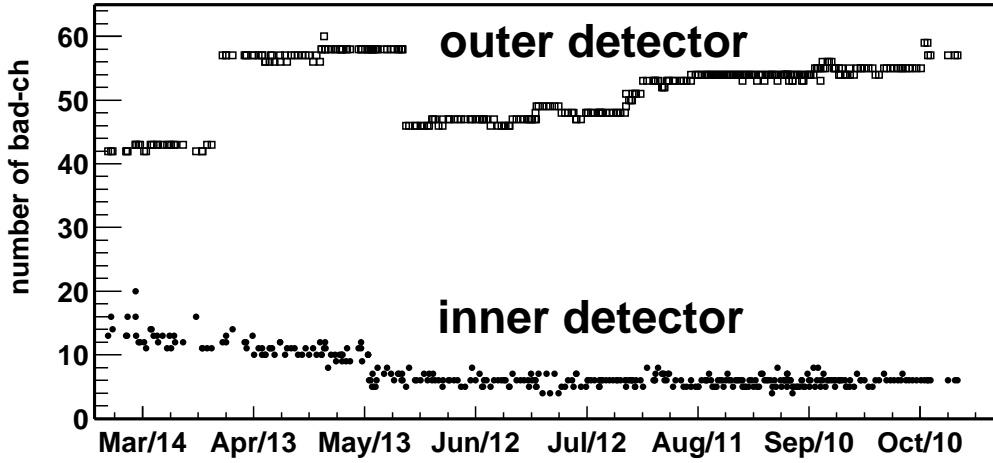


Figure 3.7: Time variation of bad channels. The dot marker indicates the number of bad channels in the inner detector, while the square marker indicates the outer detector.

3.4 Timing Calibration

Timing is not consistent from one PMT to another because the transit time of each PMT is not the same. Timing calibration was adapted to synchronize the timing for each channels. A pulsed dye-laser is used as the light source for this calibration (Figure 3.8). The 500 nm wavelength of the laser is much longer than the absorption wavelength ($<400\text{nm}$) of the scintillator, and its short pulse width ($\sim 1.2\text{ nsec}$) allows for precise timing measurement. The laser pulse is sent to the center of the inner detector via a quartz optical fiber, and illuminates the PMTs. A light attenuation filter (ND filter) and spherical diffuser provide uniform and variable light intensities from the single photo-electron level (a few percent occupancy) to about the 5,000 photo-electron level.

The time of acquired waveform has a 25nsec jitter due to the timing resolution of the trigger. This jitter is removed with a subtraction of the difference between the time the laser pulse is fired and time the trigger is issued. The laser pulse is detected with a 2inch monitor PMT and its time information is recorded to the local laser system via TDC and as a waveform via the FEE (Figure 3.8).

Moreover, each channel has different rise time caused by the different gain of each PMT, amplifier of the FEE. This means that each PMT has different correlation between the time and the charge (Figure 3.9). The time of each channel is corrected by considering this slewing effect. The correction table of the slewing effect is referred to as a “TQ-map”. Figure 3.10 shows the time distribution of all PMT hits for the 1 p.e. events during a time calibration run before and after the time correction is applied. It demonstrates the effectiveness of the calibration: $\sigma_t = 6\text{nsec} \rightarrow 2\text{nsec}$.

timing calibration system with dye-laser

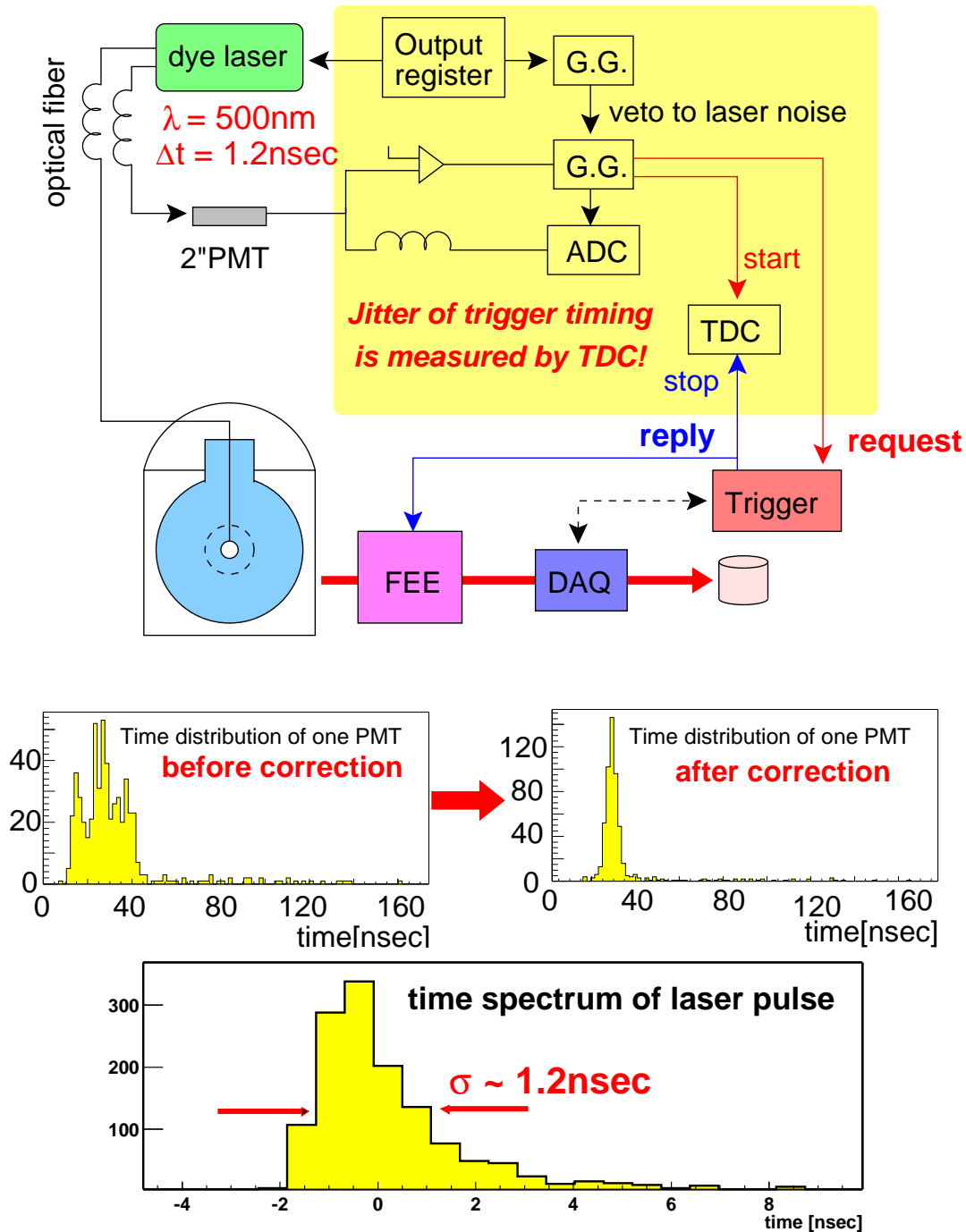


Figure 3.8: Overview of the timing calibration system. The wavelength of the dye-laser pulse is 500 nm, while the absorption wavelength is less than 400 nm. Therefore, there is no affection of the absorption in the scintillator. The short pulse width (~ 1.2 nsec) of the laser allows for the precise calibration of the PMT timing. The 25 nsec jitter of of the trigger issue is removed by the subtraction of the time difference between the “request” and “reply”.

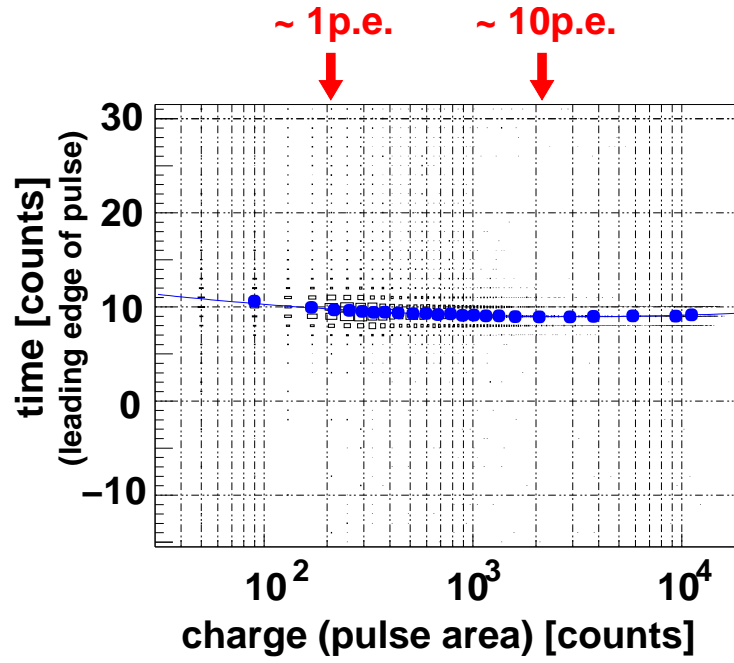


Figure 3.9: TQ-map: correlation between the time and charge in one channel from the timing calibration. The leading edge of the pulses corrected by this correlation for each channel.

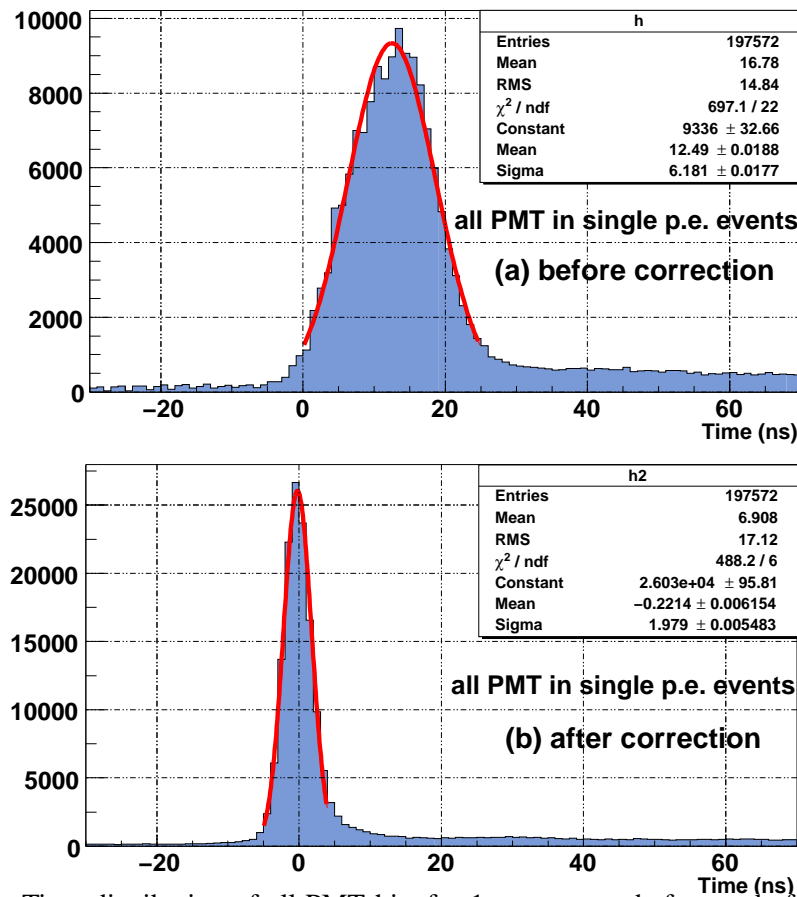


Figure 3.10: Time distribution of all PMT hits for 1 p.e. events before and after the timing calibration. The timing resolution is very good with $\sigma_t = 6\text{nsec} \rightarrow 2\text{nsec}$.

3.5 Radioactive Source Calibration

The understanding of the scintillator response in various energies is the very important. Currently, calibration with four radioactive sources, ^{68}Ge , ^{65}Zn , ^{60}Co and Am-Be, is on going. The calibration data are used for the tuning of the vertex reconstruction and the study of the energy response. Specifications of the sources and the device for the deployment are described in this section, but details of analysis and tuning are described in latter sections.

The simplified specifications of the calibration sources are summarized in Table 3.1, More

Table 3.1: Simplified specifications of calibration sources

^{68}Ge	2γ	$0.511 \times 2 = 1.022 \text{ MeV}$
^{65}Zn	1γ	1.11552 MeV
^{60}Co	2γ	$1.173 + 1.333 = 2.506 \text{ MeV}$
Am-Be	1γ	4.438 MeV
	1γ	7.653 MeV
	neutron	$T_n \sim 6 \text{ MeV}$

detail specifications for the calibration sources are summarized in Appendix D. Each source is encapsulated and hung with the stainless steel weights (Figure 3.11 and 5.8). The MC simulation predicts that shadowing effects from the weight are less than 0.2% and energy loss of the γ -rays in the capsule is less than 0.05% for ^{68}Ge , ^{65}Zn , ^{60}Co . But for Am-Be source, the value is $0.8 \sim 2.6\%$ (Section 5.2).

The vertex and energy reconstruction results in the source calibration are summarized in figures: Figure 3.12, 3.13 for ^{68}Ge , Figure 3.14, 3.15 for ^{65}Zn , and Figure 3.16, 3.17 for ^{60}Co . Detail tuning and calibration for the vertex and energy are described in the following sections. A study of the Am-Be source is described in Section 5.2.

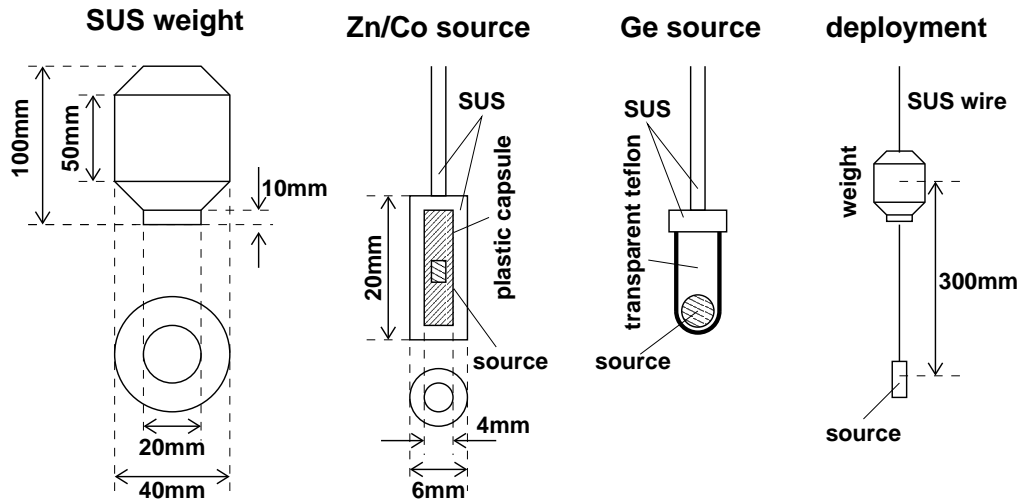


Figure 3.11: Layouts for calibration sources and deployment.

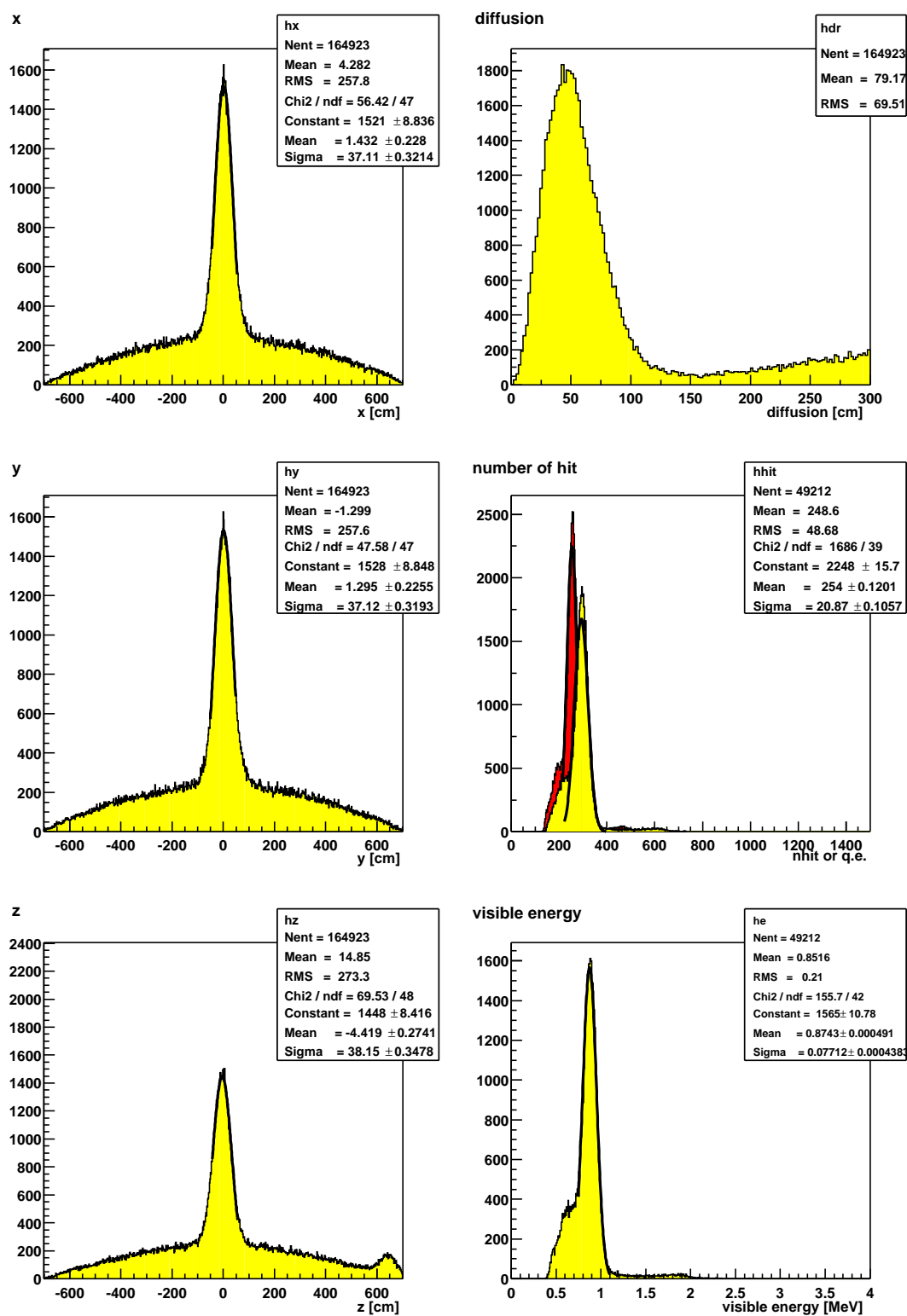
Ge at center : run001518

Figure 3.12: $^{68}\text{Ge}(2\gamma, 0.511 \times 2\text{MeV})$ with deploying the center position: reconstructed vertex, diffusion, the number of PMT hits in an event within a 125nsec time window (dark shaded histogram), and visible energy spectrum.

Ge at z=-5m : run001534

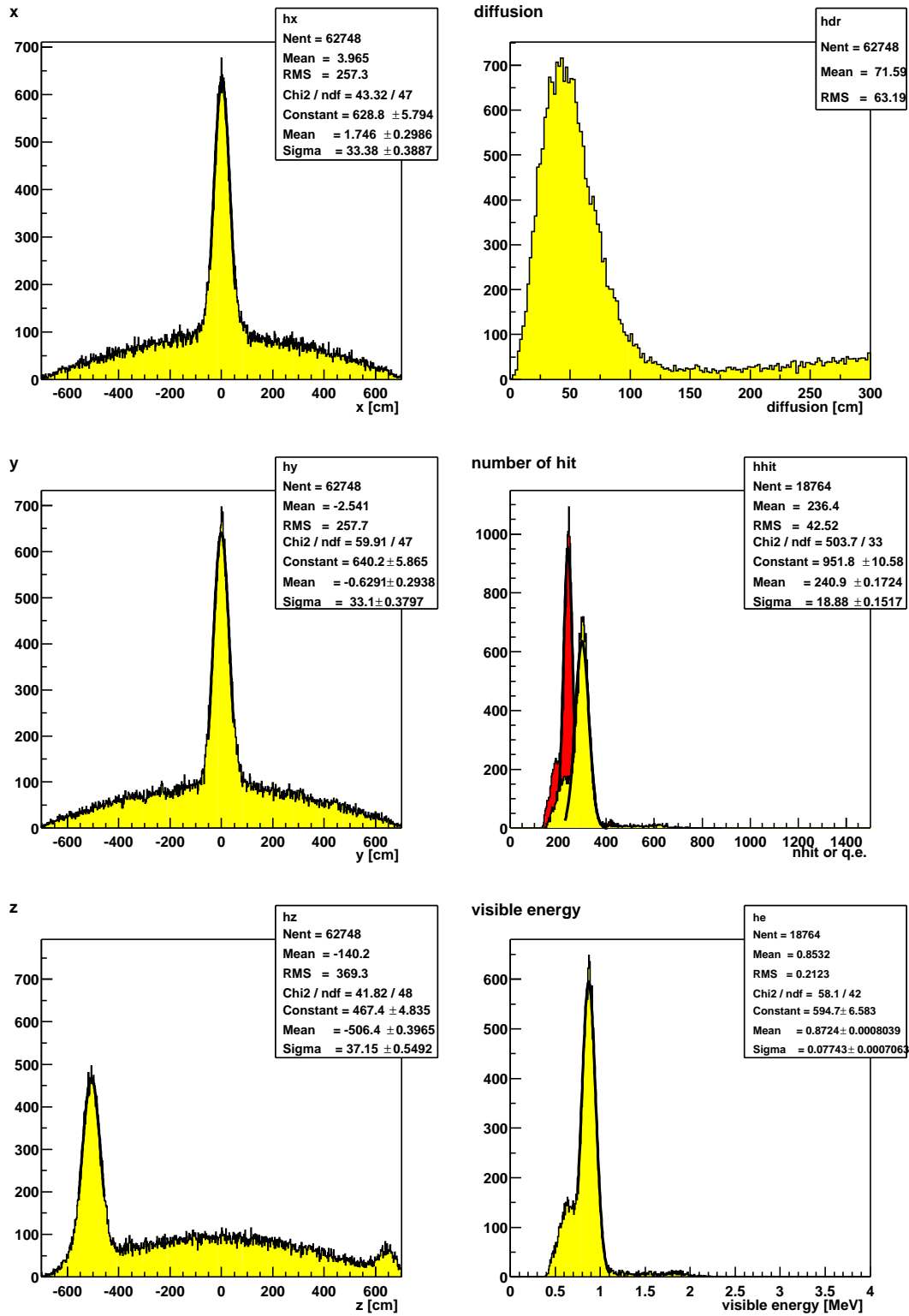


Figure 3.13: $^{68}\text{Ge}(2\gamma, 0.511 \times 2\text{MeV})$ at $z=-500\text{cm}$: reconstructed vertex, diffusion, number of PMT hits in an event within a 125nsec time window (dark shaded histogram), and visible energy spectrum.

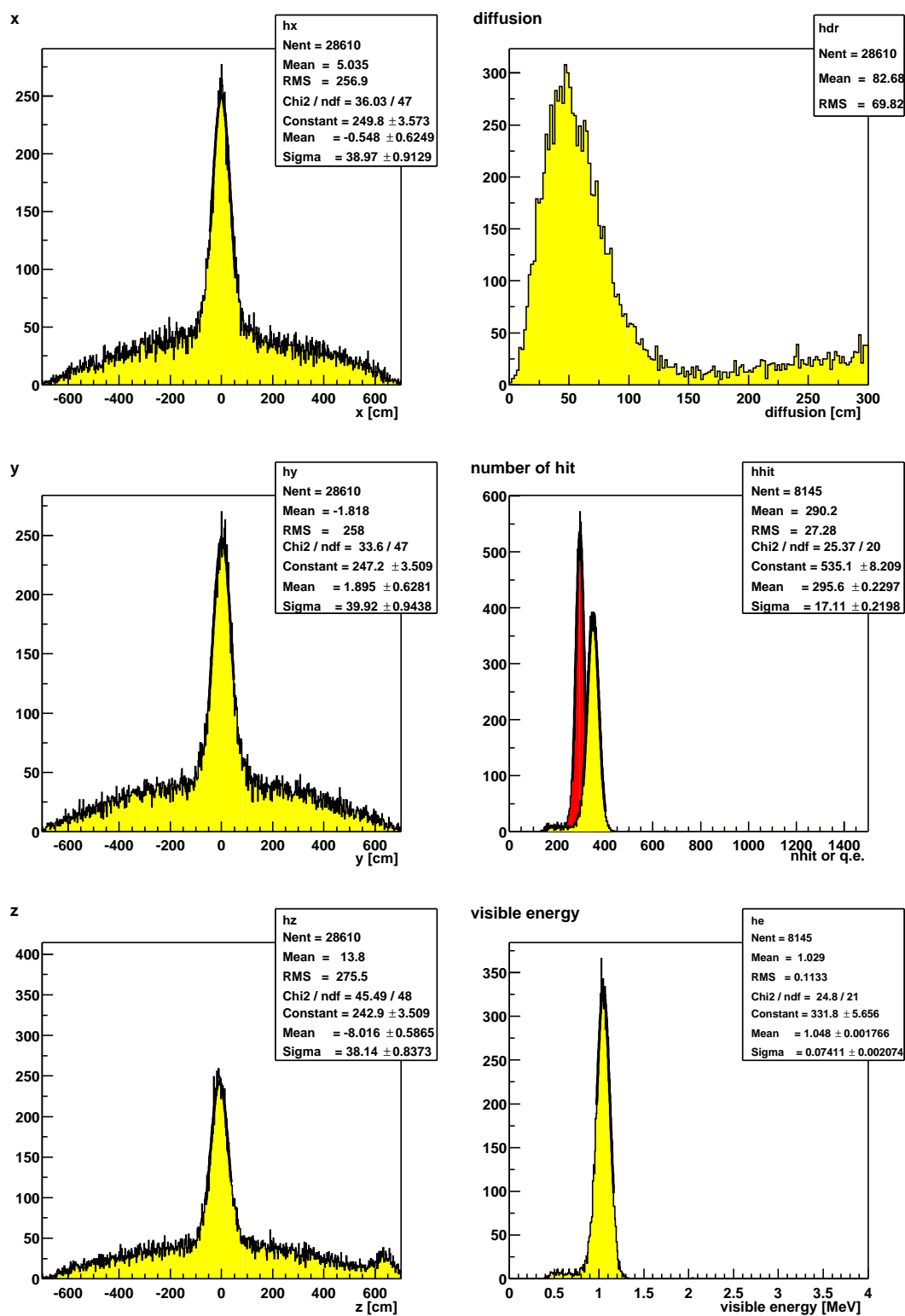
Zn at center : run000900

Figure 3.14: $^{65}\text{Zn}(1\gamma, 1.11552\text{MeV})$ at center: reconstructed vertex, diffusion, number of PMT hits in an event within a 125nsec time window (dark shaded histogram), and visible energy spectrum.

Zn at z=-5m : run000922

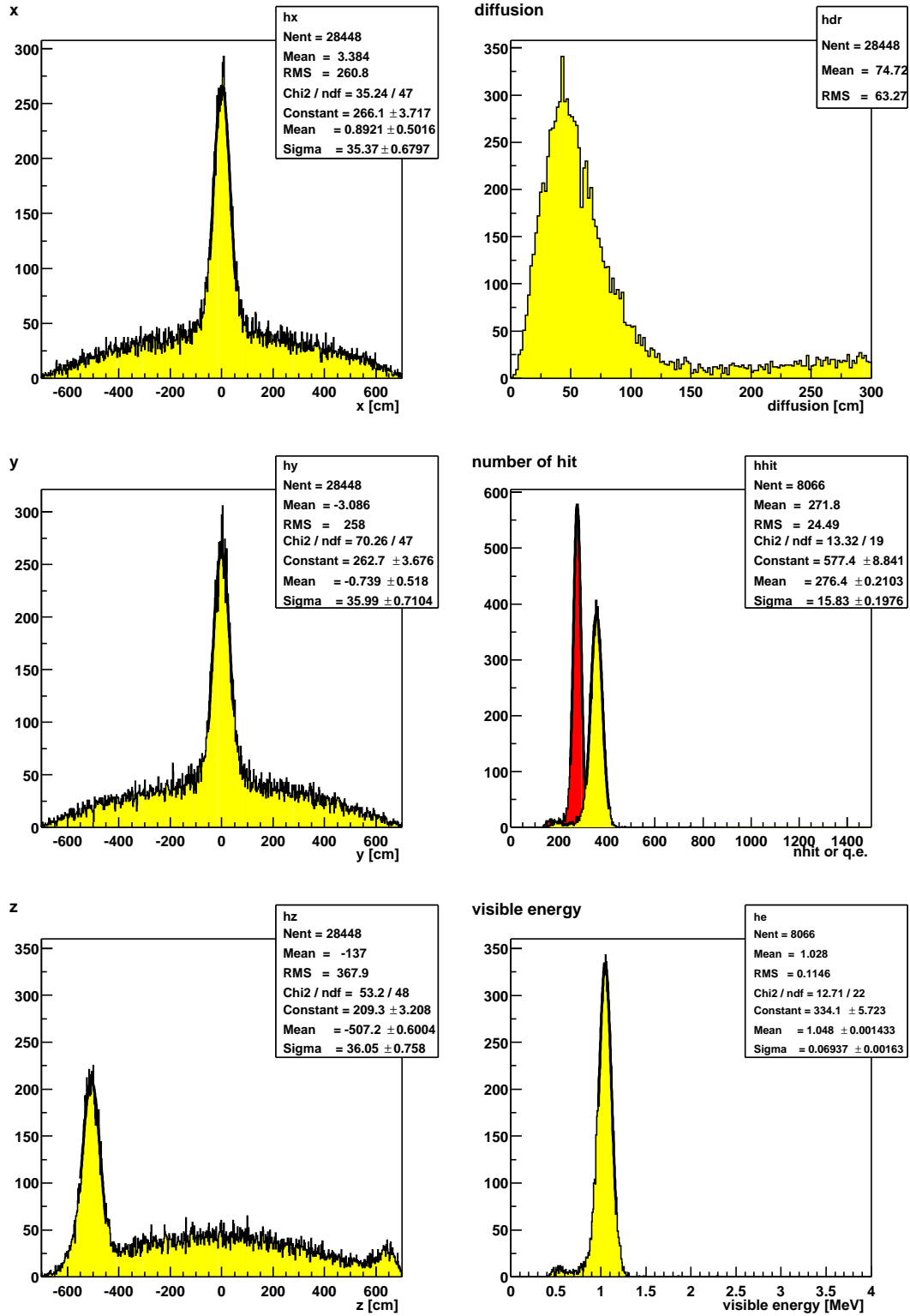


Figure 3.15: $^{65}\text{Zn}(1\gamma, 1.11552\text{MeV})$ at $z=-500\text{cm}$: reconstructed vertex, diffusion, number of PMT hits in an event within a 125nsec time window (dark shaded histogram) and visible energy spectrum.

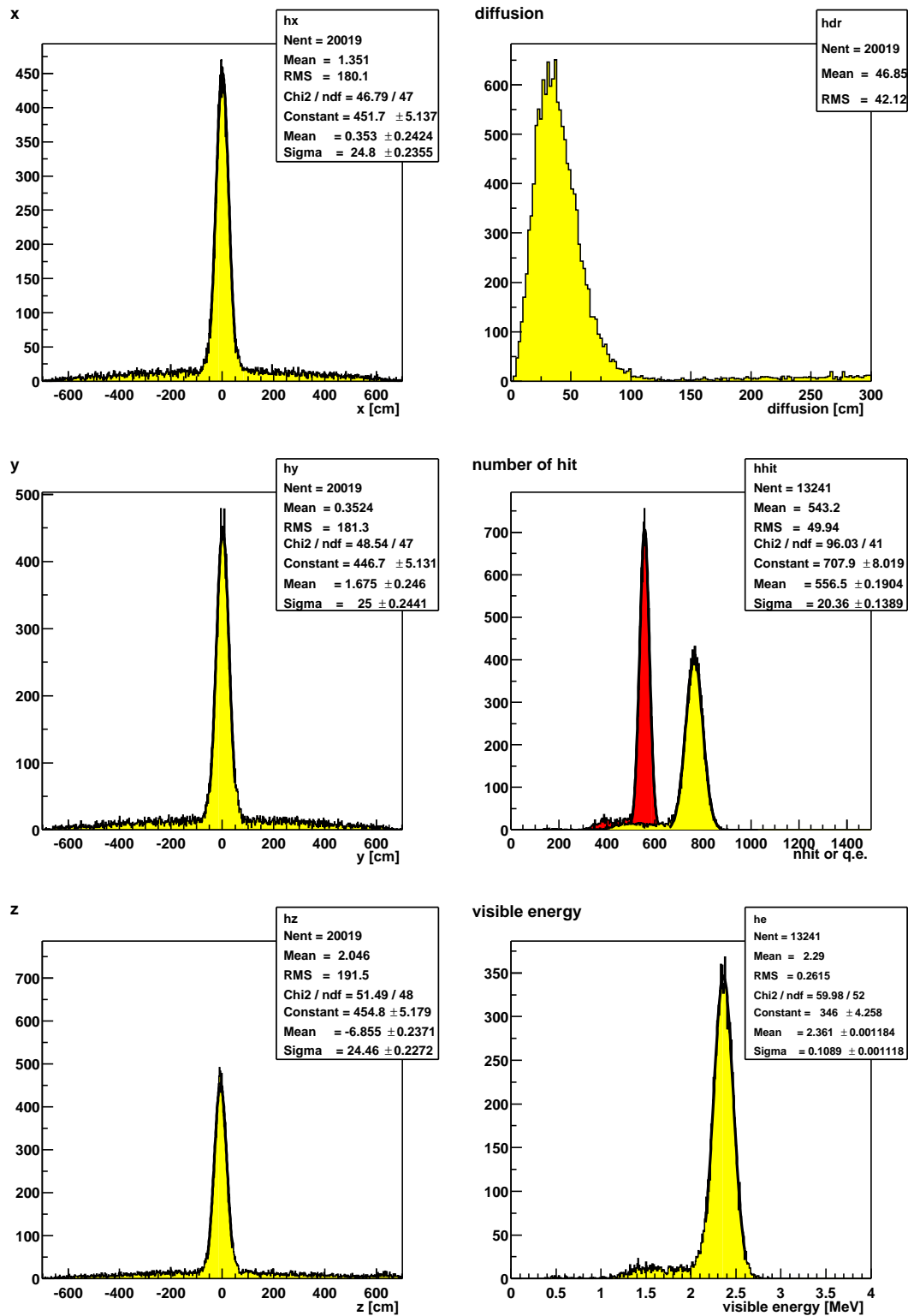
Co at center : run000891

Figure 3.16: $^{60}\text{Co}(2\gamma, 1.173+1.333\text{MeV})$ at center: reconstructed vertex, diffusion, number of PMT hits in an event within a 125nsec time window (dark shaded histogram) and visible energy spectrum.

Co at z=-5.75m : run000898

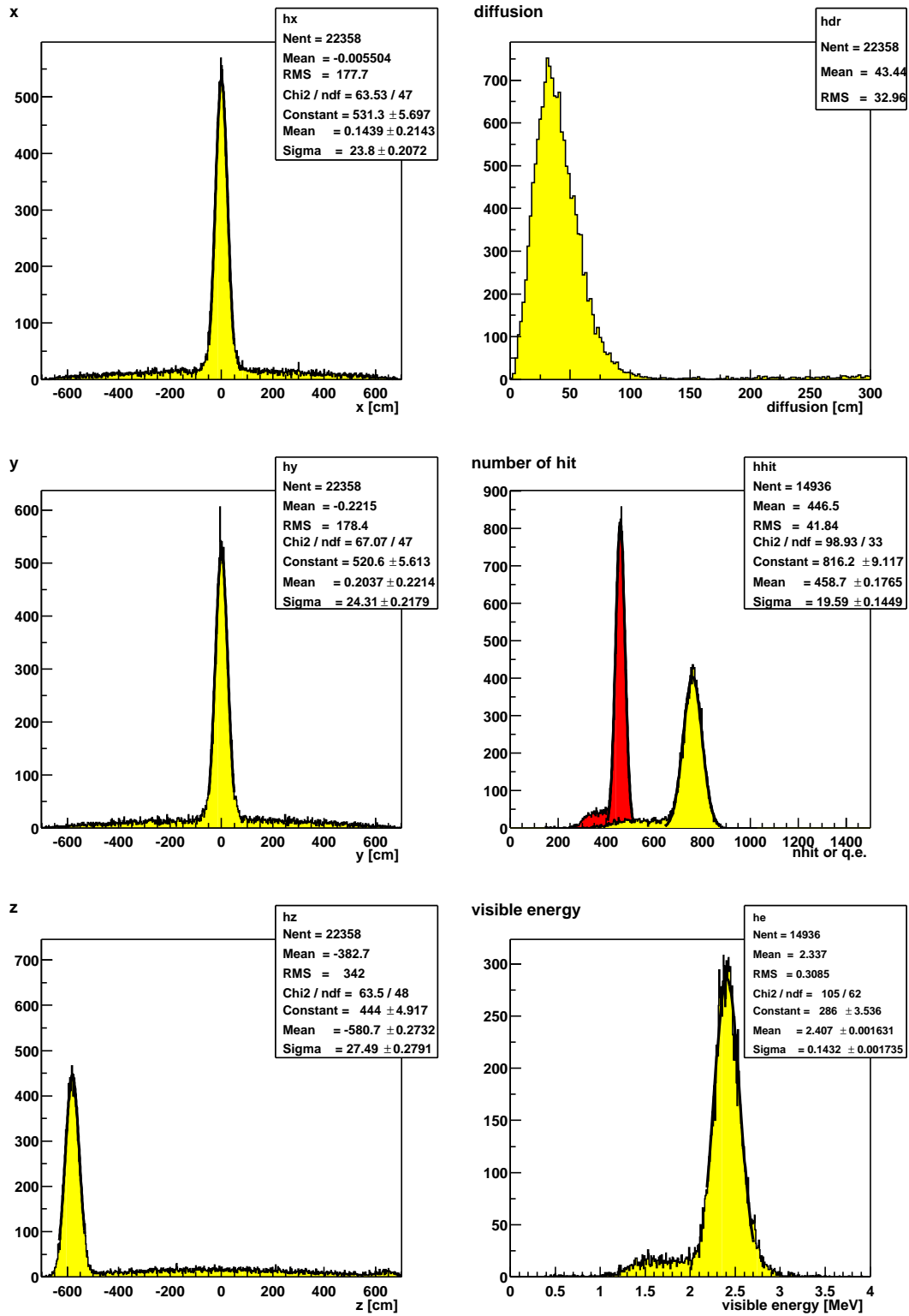


Figure 3.17: $^{60}\text{Co}(2\gamma, 1.173+1.333\text{MeV})$ at $z=-575\text{cm}$: reconstructed vertex, diffusion, number of PMT hits in an event within a 125nsec time window (dark shaded histogram) and visible energy spectrum.

3.6 Vertex Reconstruction

3.6.1 Fundamental algorithm

The interaction vertex is reconstructed by using the relative times of the PMT hits. Ideally, if a vertex position is assumed, the relative time (Δt_i) of each PMT is defined as follows;

$$\Delta t_i = t_i - l_i^{LS} / \left(\frac{c}{n_{LS}} \right) - l_i^{MO} / \left(\frac{c}{n_{MO}} \right) \quad (3.15)$$

where t_i is arrival (detected) time of the photon, l_i^{LS} and l_i^{MO} are the path length of the photon from the assumed vertex to each PMT, and n_{LS} and n_{MO} are the index of refraction of the liquid scintillator (LS) and the buffer oil (mineral oil: MO). The graphical explanation is contained in Figure 3.18-(a). The relative time distribution can be made more symmetric with a correction factor “tail weight” (w);

$$\Delta t'_i = \Delta t_i \times w \quad (3.16)$$

This weighted relative time distribution should be symmetrical and narrow for the true vertex position (Figure 3.18-(b)). The fundamental algorithm of the vertex reconstruction is a search for the most balanced vertex position. The calculation of tail weight is very complicated because each PMT’s transit time jitter should be incorporated, at the same time, the decay time of the scintillation light must be incorporated (Table 2.2). Therefore, the tail weight is defined as a tuning parameter to simplify the problem, and the source calibration determine it.

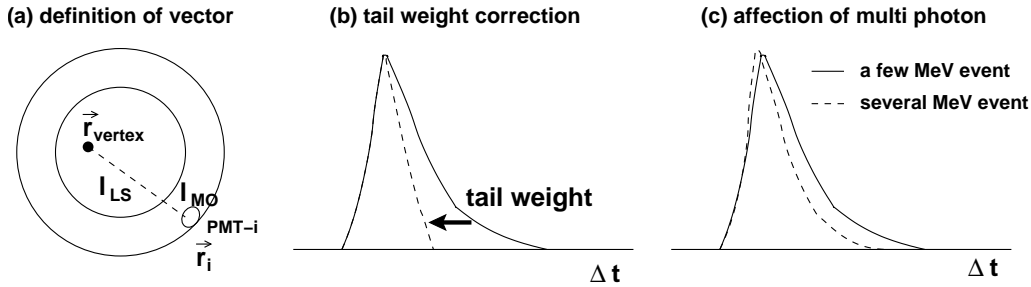


Figure 3.18: (a) Definition of terms for the vertex reconstruction. (b) Tail weight correction. (c) Relative time (Δt) distribution with multi photon changes.

3.6.2 Tuning

There isn't a precise measurement of n_{LS} and n_{MO} in the effective wavelength of the scintillation light (360 ~ 400 nsec), and the uncertainty of the scintillator balloon (vessel) radius is about 15 cm (locally about 20 cm around chimney). For simplicity, the Eq.(3.15) is converted to,

$$\Delta t_i = t_i - \frac{|\vec{r}_i - \vec{r}_{vertex}|}{v(r_{vertex})} \quad (r_{vertex} \equiv |\vec{r}_{vertex}|) \quad (3.17)$$

where v (effective speed of light) is also a tuning parameter which is determined by the source calibration. The tuning results of the v is shown in Figure 3.19, the v is a radius dependent value. And the tail weight is a constant: $w = 0.6$. The asymmetry between the top region (near the chimney) and the bottom region is due to missing PMTs (25 of 17inch PMTs at the top

and 5 of them at the bottom). The bottom direction data are addressed as $v(r_{vertex})$ for the application to radial direction.

An energy dependent bias still remains even if after the tuning for v and w (Figure 3.20-upper). The reason is that multi photon events change the relative time distribution (Figure 3.18-(c)). The energy-dependent radial adjustments are used to reproduce this systematic bias. The amplitude of this correction is conservatively defined as a systematic error related to the energy spectrum shape. The known source positions are calibrated within 5cm along z-axis in the fiducial radius (Figure 3.20-lower). On the other hand, the typical vertex reconstruction resolution is 25cm.

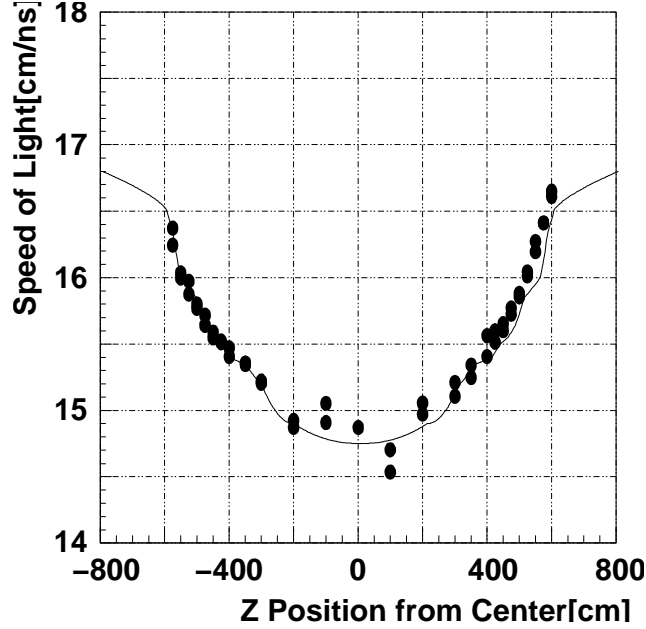


Figure 3.19: Z-axis dependence of the “effective” speed of light. There is no sensitivity around the center within a radius of 1m. The asymmetry between the top region (near the chimney) and the bottom region is caused by missing PMTs (25 of 17inch PMTs at the top and 5 at the bottom).

3.6.3 Reconstruction uncertainty

Reconstruction performance throughout the scintillator volume is verified by reproducing the uniform distribution of 2.2 MeV γ 's from spallation neutron capture, as shown in Figure 3.21.

$$\begin{aligned} \frac{N(R \leq 5m)}{N(\text{total} - \text{volume})} / \frac{V(R \leq 5m)}{V(\text{total} - \text{volume})} - 1 &= \frac{4,501}{10,219} / \frac{523.60\text{m}^3}{1171.12 \pm 25\text{m}^3} - 1 \\ &\rightarrow -1.48\% \pm 2.58\%(stat) \pm 2.13\%(volume) \\ &> -4.06\%(event) \pm 2.13\%(volume) \end{aligned}$$

The total systematic error on the reconstruction is the quadratic sum of the uncertainty of the fiducial mass ratio (4.06%) and the uncertainty of the total scintillator mass (2.13%), i.e. 4.58%. The fiducial mass ratio is the ratio between the number of neutron capture events in a 5 m fiducial radius and that in the total volume. The most of this large uncertainty comes from the statistical uncertainty of the number of neutron capture events. Some PMT hit information

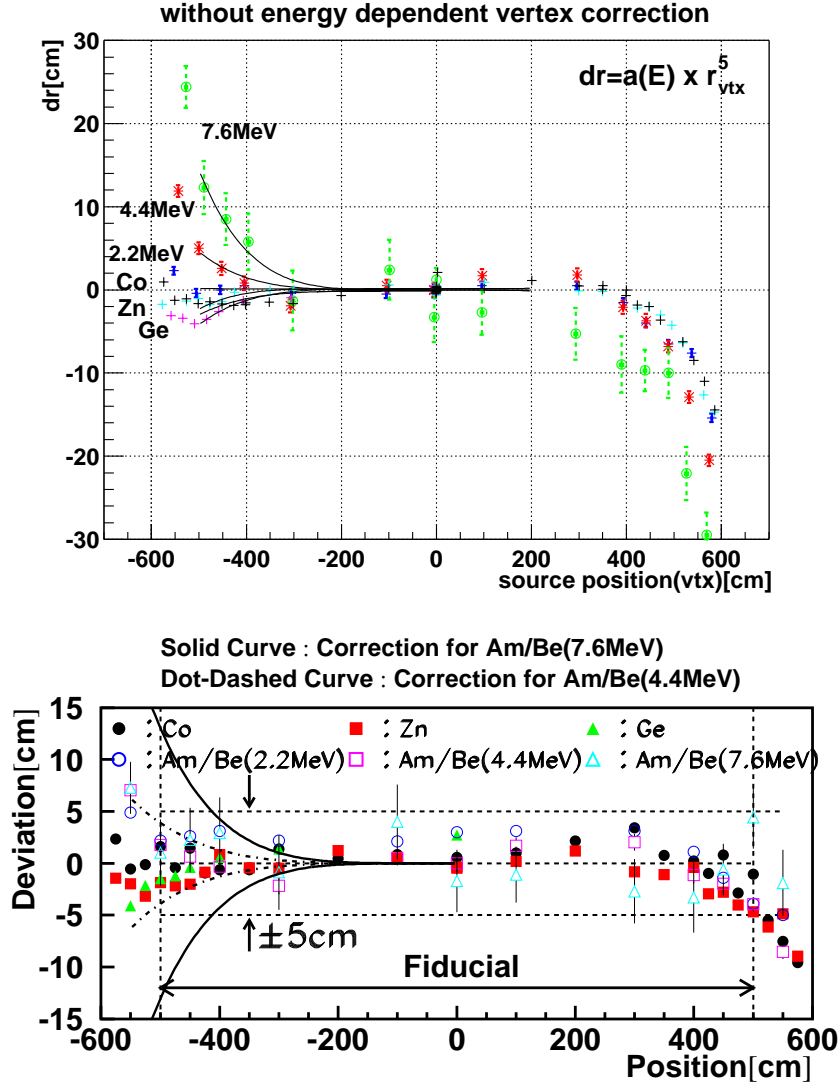


Figure 3.20: Deviations of reconstructed vertex along z-axis for various radioactivities, $^{68}\text{Ge}(2\gamma\ 0.511\text{MeV})$, $^{65}\text{Zn}(1\gamma\ 1.11552\text{MeV})$, $^{60}\text{Co}(2\gamma\ 1.1173+1.333\text{MeV})$ and AmBe(single $\gamma\ 2.22457, 4.438, 7.652\text{MeV})$. Reconstructed vertices have systematic bias related with the energy and the vertex radius. This is caused by time spectrum difference because its structure, especially tail structure, changes if one PMT detects multi photons. Upper figure shows deviations without the energy dependent radius correction. The correction along to radius direction, $(a_0 E_{\text{visible}} + a_1) \times r_{\text{vertex}}^5$, is applied to cancel this bias. Lower figure shows deviations with the energy dependent radius correction. Conservatively, the amplitude of this correction is adopted as its systematic error.

is unavailable within $\sim 1\text{msec}$ after muon due to electronics issues, and 1 msec veto is applied after muon to escape the unknown uncertainty of missing channels because. This is the reason for the low statistics.

The performance in several energy ranges is checked by looking at the β s from spallation products. The event distribution of spallation products, $^{12}\text{B}/^{12}\text{N}$, in terms of R^3 is shown in Figure 3.22. In the figure, $E > 4\text{MeV}$ and the time correlation with the muon is $2\sim 60\text{msec}$.

The accidental backgrounds are subtracted. Using the same ratio as above, it is found that $N(R < 500)/N(All) = 2472.8/5526.4 = 0.4478$, and the difference of number of events is found to be $+0.16 \pm 3.34\% < 3.5\%$. It follows, then, that the total error is $\sqrt{3.50^2 + 2.13^2} = 4.10\%$, which is less than in the case of spallation neutrons.

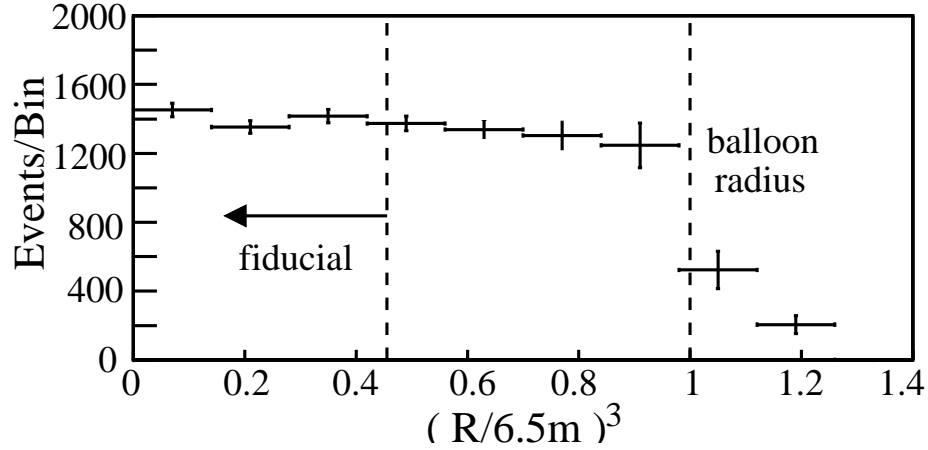


Figure 3.21: The R^3 vertex distribution of 2.2 MeV neutron capture γ 's. Vertex reconstruction performance is verified by reproducing this uniform distribution, and systematic error of vertex reconstruction is determined to the quadratic sum of the uncertainty of the fiducial mass ratio 4.06% (the ratio between number of neutron capture events in the fiducial volume and the total volume), and the uncertainty of the total scintillator mass 2.13%, i.e. 4.58%.

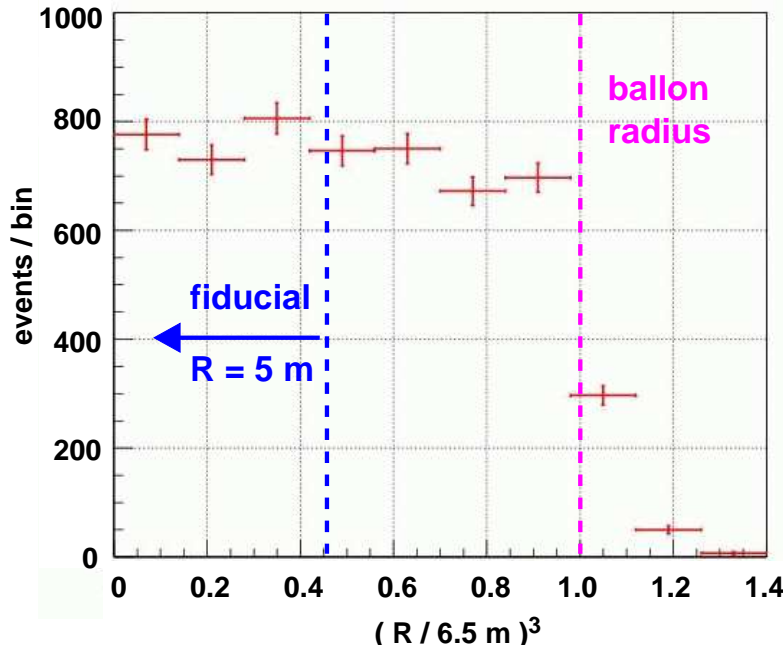


Figure 3.22: The R^3 vertex distribution of β -decay events from $^{12}\text{B} / ^{12}\text{N}$ spallation products above 4 MeV in visible energy.

3.7 Energy Reconstruction

3.7.1 Visible energy calculation

The observed energy is calculated using the detected charge information (light intensity). To account for time variation related to change in the detector status, various basic corrections are applied for each PMT charge and the total charge sum as follows,

- **Gain correction**
Each PMT charge is normalized by corresponding to ADC counts of 1p.e. run by run. The 1 p.e. ADC counts for each channel is measured from each run, using unnormalized charge information from low energy events (see section 3.2).
- **Bad Channel correction**
Bad channels are masked and whose charges are missing. All missing charge from each bad channel is corrected by adding the mean charge of neighboring PMTs.
- **Software Discriminator Threshold**
Software discrimination is applied at a 0.3 p.e. threshold for each PMT charge to account for noise reduction.
- **Real Hit PMT Selection**
Select real hit signals within a 150 nsec time window to reduce accidental (dark) hit signals and noise. Real hit signals are concentrated within the 150 nsec time interval as shown in Figure 3.23.
- **Shadow Effect Correction**
The charge of PMTs around the bottom and chimney regions are decreased due to the balloon rope shadow. This effect is corrected PMT by PMT and vertex position by vertex position since this effect is calculated using the PMT positions, event vertex, and rope geometry.

The total charge sum has the position dependence as shown in Figure 3.25 and 3.26-(a) because of the solid angle difference between each PMT, reflection on the surface of the PMT, and acrylic plate effects. First, the radial dependence is corrected using the correlation between the charge and radius in spallation neutron events (Figure 3.25). Yet, the position dependence of the charge sum along z-axis still remains even after the radius correction according to the calibration data as shown in Figure 3.26. This is caused by missing charge and less reflection than expected as 25 + 5 of the 17inch PMTs are missing at the top (chimney) and bottom regions of the detector, respectively. This missing charge is corrected with the mean charge of “close distant PMT” charges. Here, the “close distant PMT” means that the distance from the event vertex to the PMT is almost the same ($\leq 2\text{m}$) as the distance from the vertex to the missing PMT. On the other hand, another correction related to the effect of reflection on missing PMTs is adopted employing a 3 parameter function which results in a flat deviation (Figure 3.26-(b)). This is a function of the distance of the vertex from the chimney and the bottom, and is tuned with the ^{65}Zn source calibration along the z-axis. These charge corrections result in a clear energy spectrum which is shown in Figure 3.24. The visible energy is defined with the mean corrected charge sum in actual events, in this case the spallation neutron capture events on a proton which emits a 2.22 MeV single gamma-ray corresponding to the corrected charge is 710.8 p.e. in these events.

$$\text{visible energy} \equiv (\text{corrected charge sum}) / 710.8 \times 2.22 [\text{MeV}]$$

The time variation still remains for the visible energy even with basic corrections. It is observed in the source calibration (Figure 3.27), and in the peak of the ^{40}K and the edge of the ^{208}Tl in a single event spectrum (Figure 3.28). Fortunately, the ^{40}K peak and ^{208}Tl edge are measured in all of normal runs, and it is easy to fit the ^{40}K peak without short run less than several hours. Thus, the ^{40}K peak is fitted for every run and its variation is used of the correction factor to remove the time variation. (Another fit result of the close run is substitute for short runs.) This time dependent correction gives very stable energy information, and was found, with the ^{60}Co , ^{65}Zn source calibration and spallation neutron data, to be 0.6 % over seven months (Figure 3.29).

The reconstructed energy varies 0.8% for source calibration (Figure 3.30) during 7 months. But, for spallation neutrons, it varies by less than 0.5% within the 5.5 m radius. Local variations near the chimney region are 1.6% for $R \leq 5.5$ m and 1.39% for $R \leq 5$ m and the fitting error is 0.39%. Therefore, the systematic error for the visible energy reconstruction is:

$$\sqrt{0.6^2(\text{time} - \text{variable}) + 1.39^2(z - \text{axis}) + 0.39^2(\text{fitting} - \text{error})} = 1.56\%$$

Figure 3.33 and 3.34 show the energy spectra for selected spallation neutrons in various regions in the detector. Energy spectra for source calibrations are shown in Figure 3.12 and 3.13 for ^{68}Ge , Figure 3.14 and 3.15 for ^{65}Zn and Figure 3.16 and 3.17 for ^{60}Co . The correlation between the energy resolution and z-position is also shown in Figure 3.31 for source calibration and Figure 3.32 for spallation neutrons. In the bottom and top regions, the resolution is worse than in other radial regions because of fewer detected photons. The reconstructed visible energy for various sources and their resolutions are summarized in Table 3.2. According to this table, the selection efficiency of the delayed event energy cut (1.8~2.6 MeV visible energy) for $\bar{\nu}_e$ detection is,

$$\frac{1}{\sqrt{2\pi\sigma^2}} \int_{1.8}^{2.6} \exp\left(-\frac{(E - 2.22)^2}{2\sigma^2}\right) dE = 98.85\%. \quad (3.18)$$

The inconsistency between the visible energy and the deposited energy in the detector is explained in the following sub-section.

Table 3.2: Correlation of calibration source energy with visible energy. Resolution of neutron capture on ^{12}C has a large uncertainty because of its low statistics, and it is difficult to fit a Gaussian to the 7.652MeV γ from Am-Be.

source		energy[MeV]	$E_{vis}[\text{MeV}]$	$\sigma/\sqrt{E_{vis}(\text{MeV})}[\%]$
^{68}Ge	2γ	0.511×2	0.875	7.7
^{65}Zn	1γ	1.11552	1.049	7.4
^{60}Co	2γ	1.173+1.333	2.357	7.4
$\text{np} \rightarrow \text{d}\gamma$	1γ	2.22457	2.220	7.5
$\text{n}^{12}\text{C} \rightarrow ^{13}\text{C}\gamma$	1γ	4.9468	5.142	7.1~7.9
Am-Be	1γ	7.652	8.032	—

3.7.2 Correction for nonlinearity of visible energy

As described in the above Table 3.2, there is not a linear relationship between the visible energy and the deposited energy, also shown in Figure 3.35. There are nonlinear contributions and uncertainties contributing to this such as dark hit charge, single photo-electron detection efficiency, Čerenkov light, and the quenching effect;

- Dark hit charge

The accidental dark hit charge effect is reduced (but not to zero) during reconstruction of the visible energy. Thus, there is an uncertainty in the contribution of the dark hit charge which comes in as $E_{vis} = E_{deposit} + E_{dark}$. The sign of this contribution doesn't change and the maximum contribution is limited by the relative uncertainty of the visible energy between the ^{65}Zn and ^{60}Co calibration 0.6% (Figure 3.36). This means the contribution from dark hits is less than 6.7KeV ($\sim 2\text{p.e.}$).

- Single photo-electron (1p.e.) efficiency [37]

Probability of 1p.e. detection if there is no threshold effect

$$P(1) = \mu \exp(-\mu) \quad (3.19)$$

where μ is the mean number of photo-electrons,

$$\mu = \frac{1}{N_{PMT}} \times E \times \frac{dQ}{dE} \quad (3.20)$$

$$= \frac{1}{1325} \times E \times \frac{295\text{p.e.}}{1\text{MeV}} \quad (3.21)$$

The detection efficiency (ε) of 1p.e. is a concern, and the probability of 0p.e. and 1p.e. and $N\text{p.e.}(N > 2)$ detection efficiencies are,

$$P(0) = \exp(-\mu) + (1 - \varepsilon)\mu \exp(\mu) \quad (3.22)$$

$$= \exp(-\mu) [1 + (1 - \varepsilon)\mu] \quad (3.23)$$

$$P(1) = \varepsilon\mu \exp(-\mu) \quad (3.24)$$

$$P(N) = \frac{\mu^N}{N!} \exp(-\mu) \quad (N \geq 2) \quad (3.25)$$

The visible energy (E_{vis}) is calculated by adding up charges, so

$$E_{vis} = Q(1) \times P(1) + \sum_{N \geq 2} [Q(N) \times P(N)]. \quad (3.26)$$

Here, the normalization constant is omitted because it doesn't effect for the nonlinearity of energy. If there is no threshold effect, visible energy will be

$$\sum_{N \geq 1} [Q(N) \times P(N)] = \mu Q_1 \equiv E_{vis-no-th.} \quad (3.27)$$

where Q_1 is the mean charge of 1p.e. events with no threshold effect. Then, considering that only 1p.e events are affected by the threshold effect, E_{vis} is rewritten as

$$E_{vis} = \mu Q_1 - \mu \exp(\mu) Q_1 + Q(1) \varepsilon \mu \exp(-\mu) \quad (3.28)$$

$$= \mu Q_1 \left[1 - \exp(\mu) + \frac{Q(1)}{Q_1} \varepsilon \exp(-\mu) \right] \quad (3.29)$$

$$= E_{vis-no-th.} \left[1 - \exp(\mu) \left(1 - \frac{Q(1)}{Q_1} \varepsilon \right) \right] \quad (3.30)$$

Here, the $Q(1)$ is determined from the following relation.

$$Q_1 = Q(1) \varepsilon + Q_{loss}(1 - \varepsilon), \quad (3.31)$$

where Q_{loss} is the mean charge of the events under threshold, so, it should be less than 1/3 p.e.

Finally,

$$E_{vis} = E_{vis-no-th.}(1 - \exp(-\mu)\delta) \quad (3.32)$$

$$\delta \equiv \frac{Q_{loss}}{Q_1}(1 - \varepsilon), \quad (3.33)$$

This contribution is also only in one direction and the maximum contribution is limited by the relation of visible energy between the ^{65}Zn and ^{60}Co calibrations to be 0.6% (Figure 3.36). This corresponds to $\delta=0.05$.

- Contribution of Čerenkov light

The direct contribution of Čerenkov light can be ignored because the dominant wavelength is below the absorption wavelength of the scintillator. However, the scintillator re-emits absorbed Čerenkov light and this contribution has an energy dependence. Since its magnitude depends on the dE/dX of the charged particle, the contribution is related to the recoil energy of an electron for gamma-rays, and it is necessary to consider pair-annihilation. The limit and range of this contribution is tuned by altering the contribution of the quenching effect.

- Quenching effect

Strictly speaking, the response of the scintillator is a complex function of not only energy but the type of particle and its specific ionization. In organic materials, non-linearities are readily observed for electrons [38], although they are much smaller than the heavy particles such as alphas and protons. To estimate the contribution of the quenching effect, the most popular way is using Birk's formula,

$$\frac{dL}{dX} \propto \frac{\frac{dE}{dX}}{1 + kB \frac{dE}{dX}} \quad (3.34)$$

where the dL/dX is the emitted light intensity per unit length and kB is Birk's constant.

The contributions from the quenching and Čerenkov light are tuned with the 6 kinds of gamma ray data already mentioned in Table 3.2 and Figure 3.35. Here, it is natural to treat the 2γ 's of ^{68}Ge and ^{60}Co as 1γ whose energy is the effective mean of them. Results of a least square analysis is applied to the gamma data using 3 parameters, the parameters are Birk's constant, the Čerenkov intensity, and an absolute normalization factor (Figure 3.37). The recoil energies of electrons are calculated with a MC simulation.

The correction factor for the nonlinearity of the visible energy is tuned using only the Čerenkov and quenching contributions as the 1p.e. efficiency and dark hit contributions are negligible by comparison. The maximum contributions of the 1p.e. efficiency and the dark hit are addressed into the uncertainty of the energy scale instead.

The best fit result is shown in Figure 3.38, and calculations for electrons and positrons are shown in Figure 3.39 and 3.40. The uncertainty of the nonlinearity correction for positron contains

- Čerenkov/Birk's uncertainty : 0.98% at 2.6MeV
- Low energy cut off in MC for recoil electron calculation: 0.3% at 2.6MeV

- Dark hit and 1p.e. inefficiency : 0.4% at 2.6MeV

The correlation is shown in Figure 3.38, 3.39 and 3.40 for various energies and particles.

The total systematic error of the energy scale is calculated using the quadratic sum of visible energy uncertainties and the nonlinearity correction. For example, the systematic error at a 2.6 MeV analysis energy threshold is given by,

$$Sys.Error(E = 2.6\text{MeV}) = \sqrt{1.56^2 + 0.98^2 + 0.3^2 + 0.4^2} \quad (3.35)$$

$$= 1.91\%. \quad (3.36)$$

This corresponds to a 2.1% error in the number of the reactor $\bar{\nu}_e$ events for the no oscillation case.

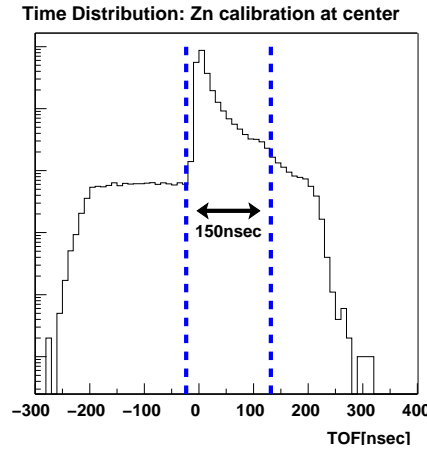


Figure 3.23: Time properties of detected scintillation light where
 $TOF = (\text{detected time}) - (\text{distance from center to each PMT})/(\text{light velocity})$
 Real hit signals are concentrated within a 150 nsec time interval.

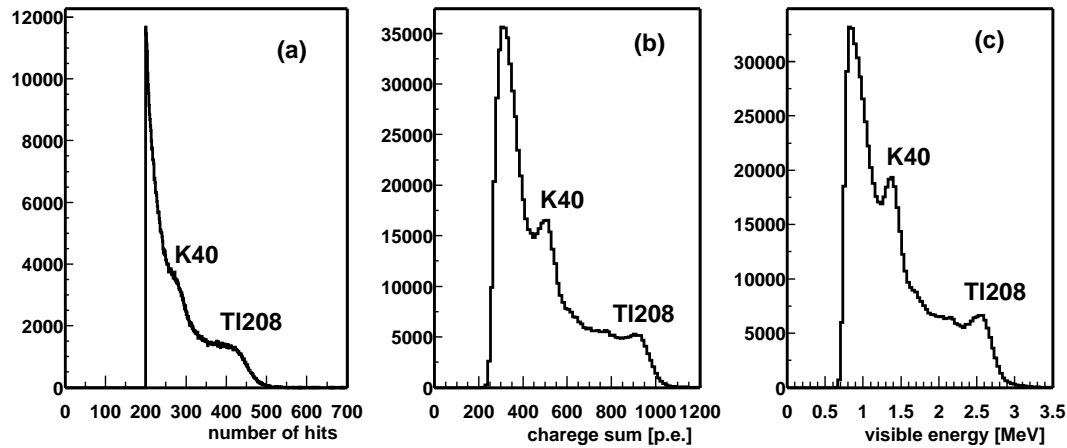


Figure 3.24: Singles spectra within a 6.5 m radius for (a) number of PMT hits, (b) charge sum with applied gain correction, and (c) visible energy. The visible energy provides much more accurate information, for example, the clear gamma ray peak in the ^{40}K and ^{208}Tl spectra.

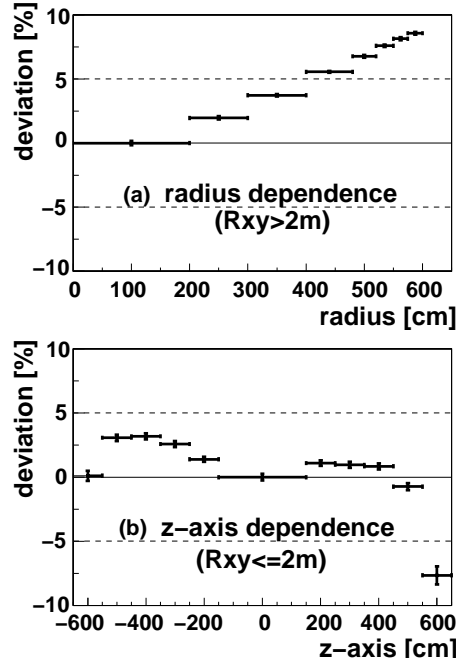


Figure 3.25: Correlation between event charge and vertex for proton captured spallation neutron events (1γ , 2.22457MeV). Upper figure (a) shows correlation between the deviation of total charge and vertex radius except around z-axis, $R_{xy} > 2\text{m}$, and lower one (b) shows z-axis dependence of the total charge, around z-axis $R_{xy} \leq 2\text{m}$.

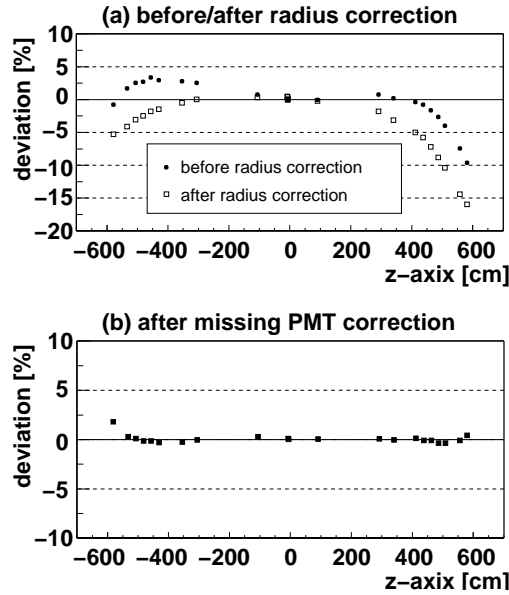


Figure 3.26: The position dependence of the event charge for the ^{65}Zn calibration during the day (run00901~run0924) is shown as dotted markers in the upper figure (a). The data of after radius correction are also shown by square markers in (a). Large deviations still remain around the chimney and bottom regions in the detector even though the above corrections were adopted. The reason is missing charges of missing PMTs around the chimney and bottom, as well as the effect of the reflections at the surface of the PMT and the acrylic plates. The missing charge from missing PMTs is corrected for with the mean charge of “same distance PMTs”. Yet, another correction related to the reflection parameterized as a 3 parameter function, flattens the deviation.

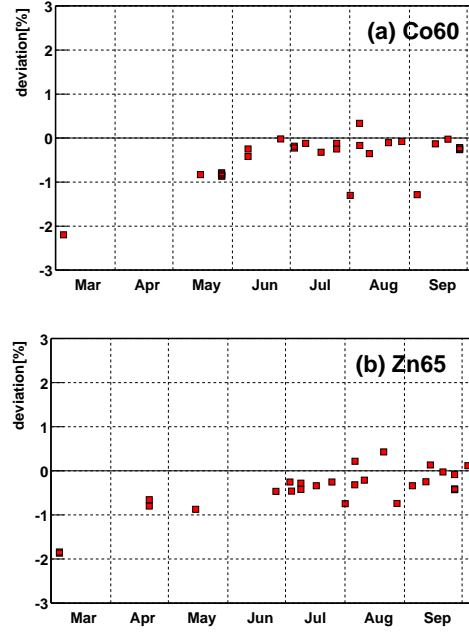


Figure 3.27: Time variation of the energy scale without the time dependent correction for (a) $^{60}\text{Co}(2\gamma, 1.173+1.333=2.506\text{MeV})$ and (b) $^{65}\text{Zn}(1\gamma, 1.11552\text{MeV})$ sources at the center position. The variation of the energy scale is a few percent for half year even though it is applied 1p.e. charge and bad channel corrections were applied. Each marker indicates the fitted mean value for the energy spectrum using a gaussian distribution. Fitting errors are $\sim 0.1\%$ and $\sim 0.5\%$ for Zn and Co respectively.

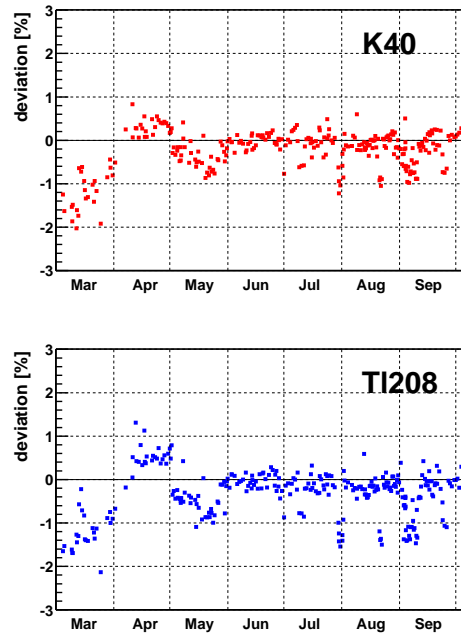


Figure 3.28: Time variation of fitted ^{40}K peak (1.46MeV) and ^{208}Tl edge ($\leq 2.616\text{MeV}$) without the time dependent correction. These reproduce the time variation of the source calibration. The time variation of the ^{40}K peak is adopted as the time dependent correction factor because it is easy to fit and more reliable than edge. This correction factor is defined run by run except for bad and short runs.

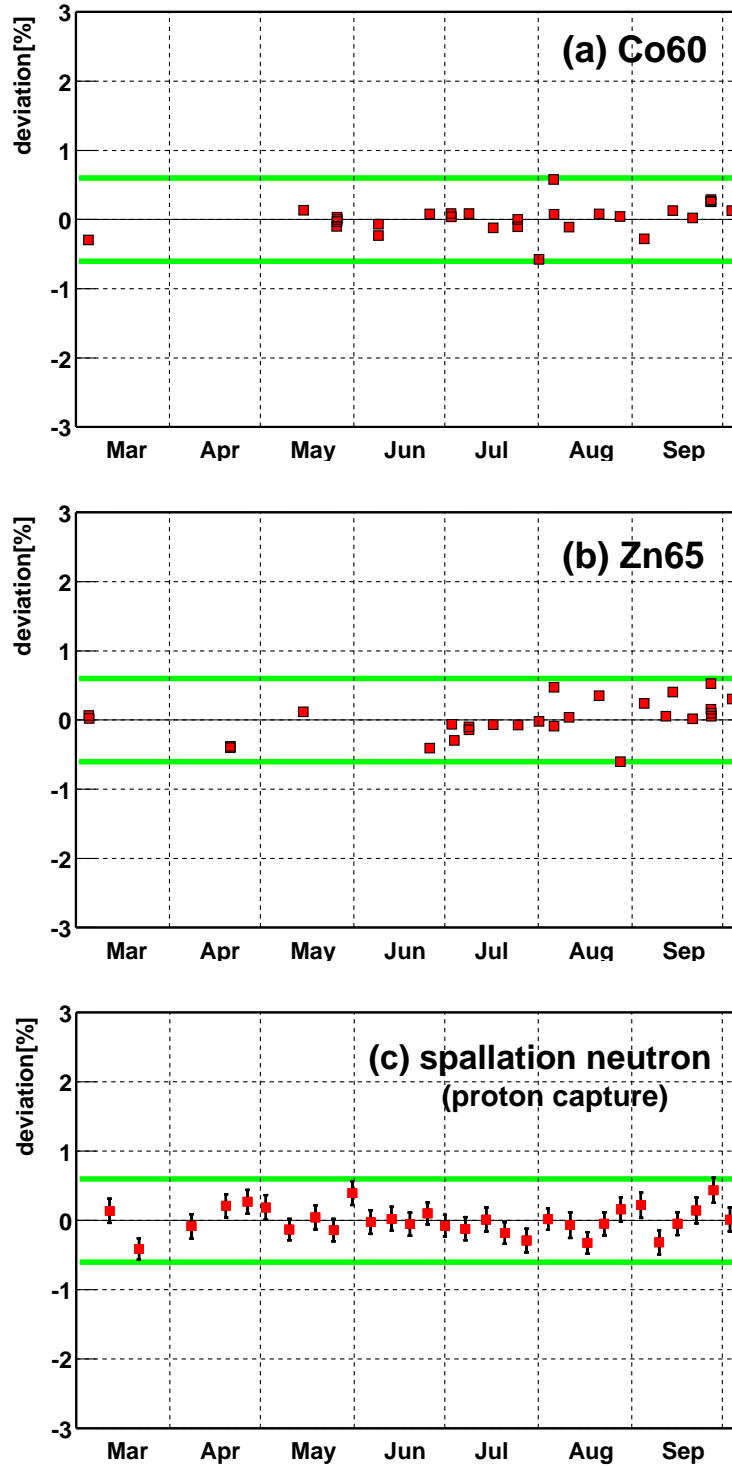


Figure 3.29: Time variation of the reconstructed energy for each source, (a) ^{60}Co (2 γ , 1.173+1.333=2.506 MeV), (b) ^{65}Zn (1 γ , 1.11552 MeV), and (c) spallation neutrons which were captured on protons (1 γ , 2.22457 MeV). The energy scale exhibits less than a 0.6% variation in time during the entire data set. Each marker is the fitted mean value for each energy spectrum using a gaussian distribution. Fitting errors are $\sim 0.1\%$ and $\sim 0.5\%$ for Zn and Co respectively.

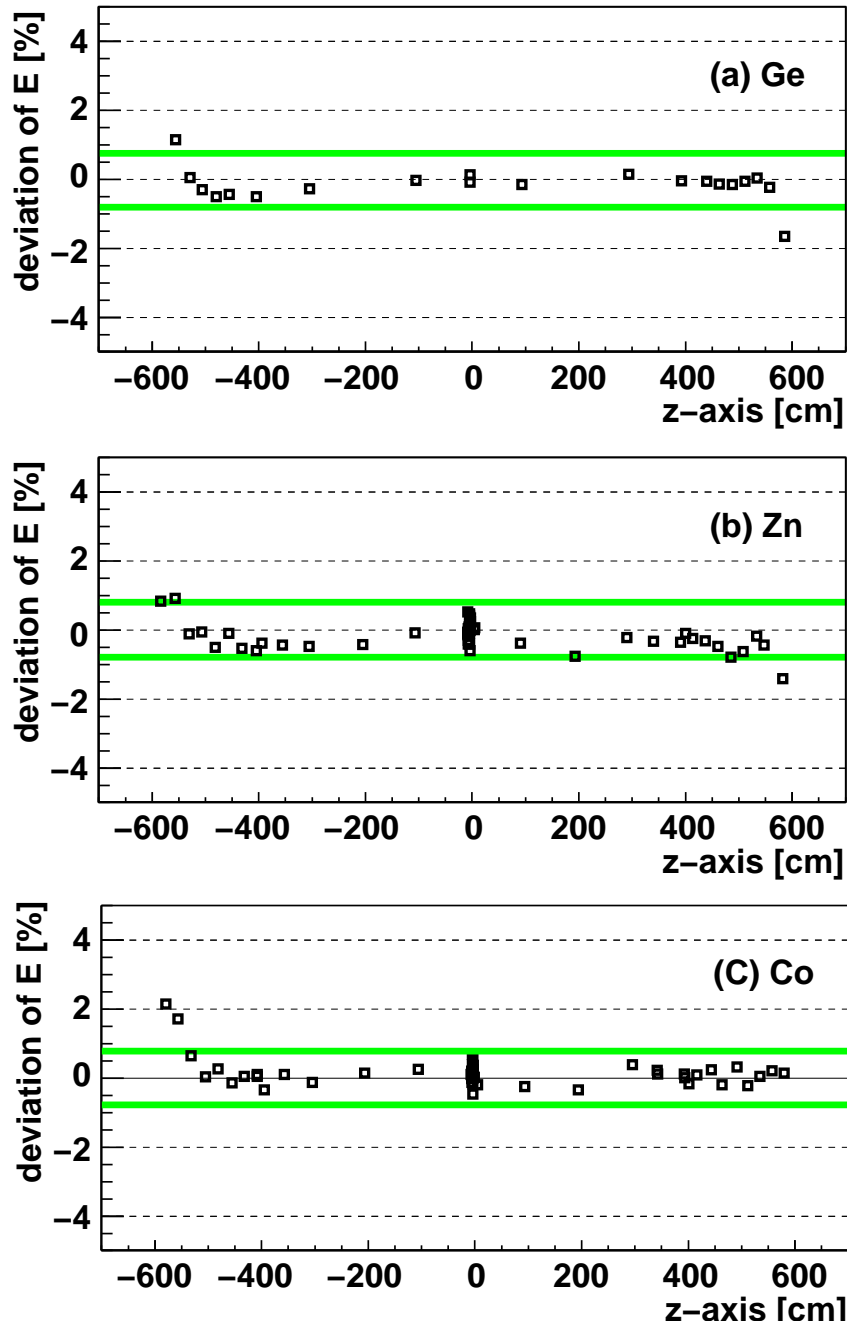


Figure 3.30: Deviation of reconstructed energy at various positions on z-axis for various sources, $^{68}\text{Ge}(2\gamma, 0.511 \times 2\text{MeV})$ $^{65}\text{Zn}(1\gamma, 1.11552\text{MeV})$ $^{60}\text{Co}(2\gamma, 1.173+1.333\text{MeV})$. Here, deviation means the difference from the mean energy of central calibrations for each source. Thus, this deviation includes both the uncertainty in position dependence and of time. Each deviation is less than 0.8% within a 5m distance from the center.

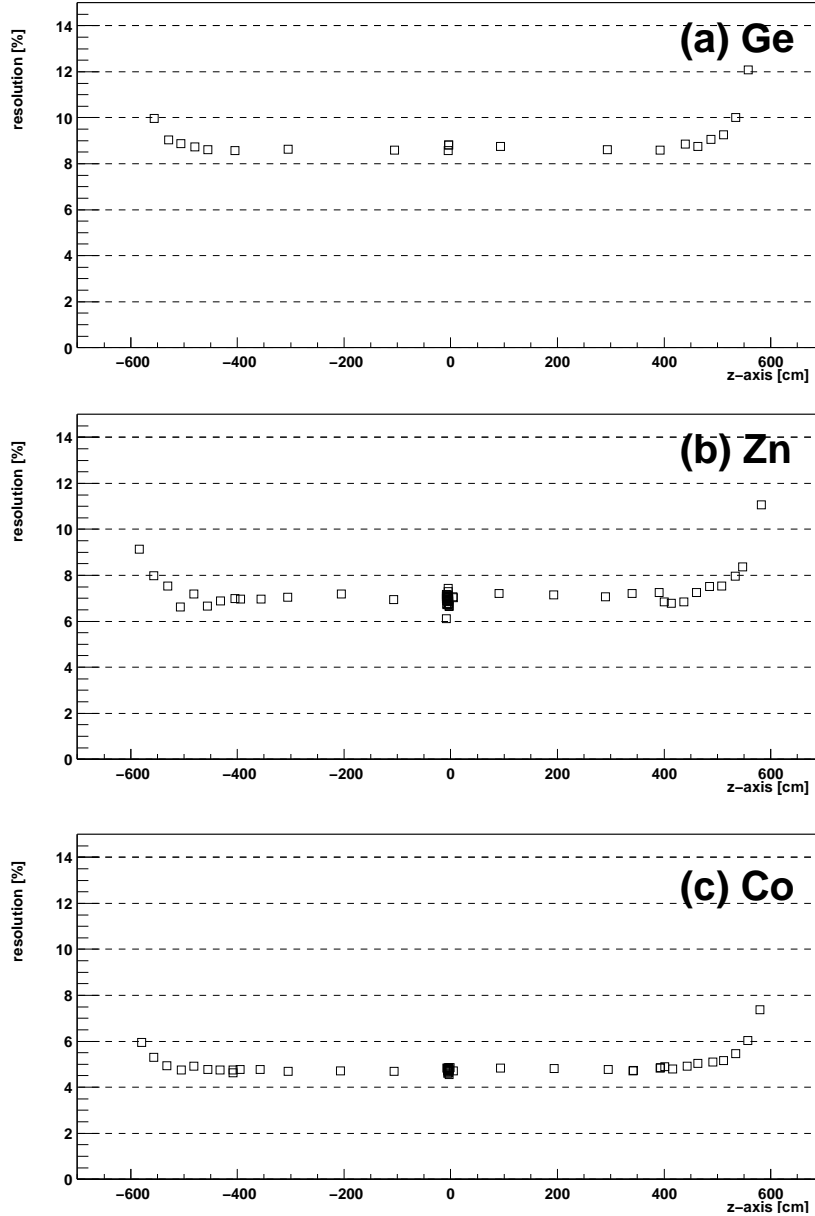


Figure 3.31: Correlation of the resolution σ/E with z-position for each calibration sources, $^{68}\text{Ge}(2\gamma, 0.511 \times 2\text{MeV})$, $^{65}\text{Zn}(1\gamma, 1.11552\text{MeV})$ and $^{60}\text{Co}(2\gamma, 1.173+1.333\text{MeV})$. At the bottom and top region, the resolution is worse than in the central region due to fewer detected photons.

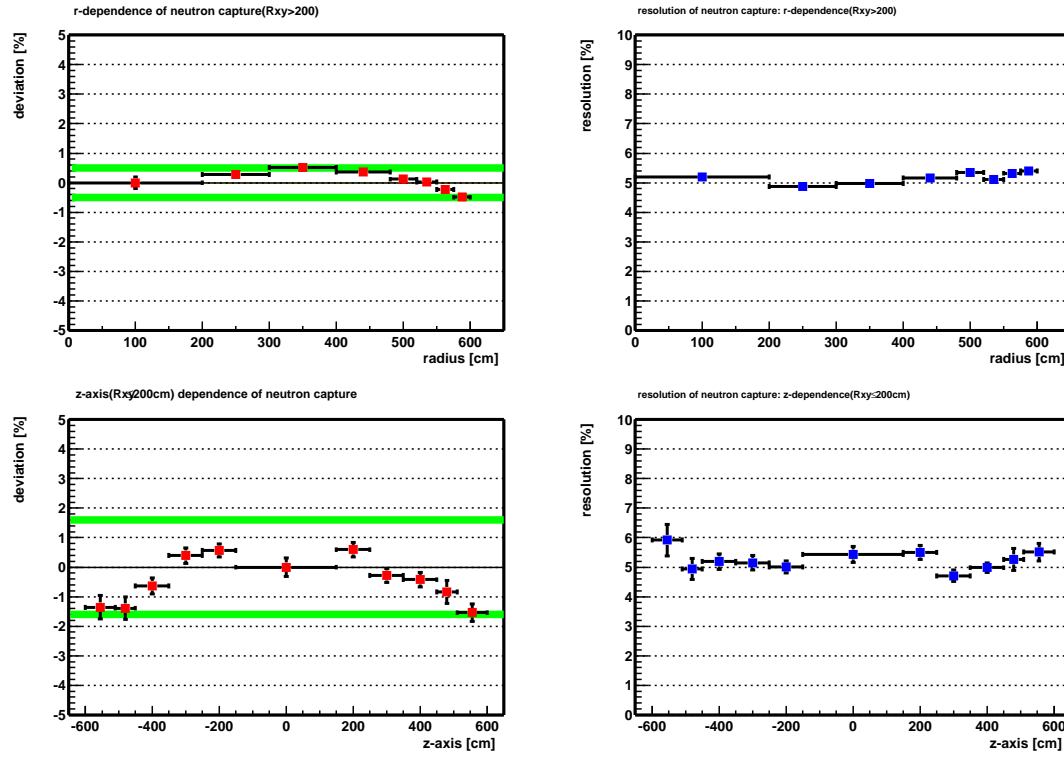


Figure 3.32: Position dependence of visible energy and its resolution for neutron capture gamma events (2.22457 MeV) are shown for various radii around the z-axis region (≤ 2 m). The reconstructed energy varies less than 0.5% within a 5.5 m radius; local variation near the chimney and bottom regions are 1.6% for $R \leq 5.5$ m and 1.39% for $R \leq 5$ m and the fitting error is 0.39%. Here, the energy resolution (σ/E) for each position is about 5%, corresponding to $\sigma/\sqrt{E(\text{MeV})} \sim 7.5\%$.

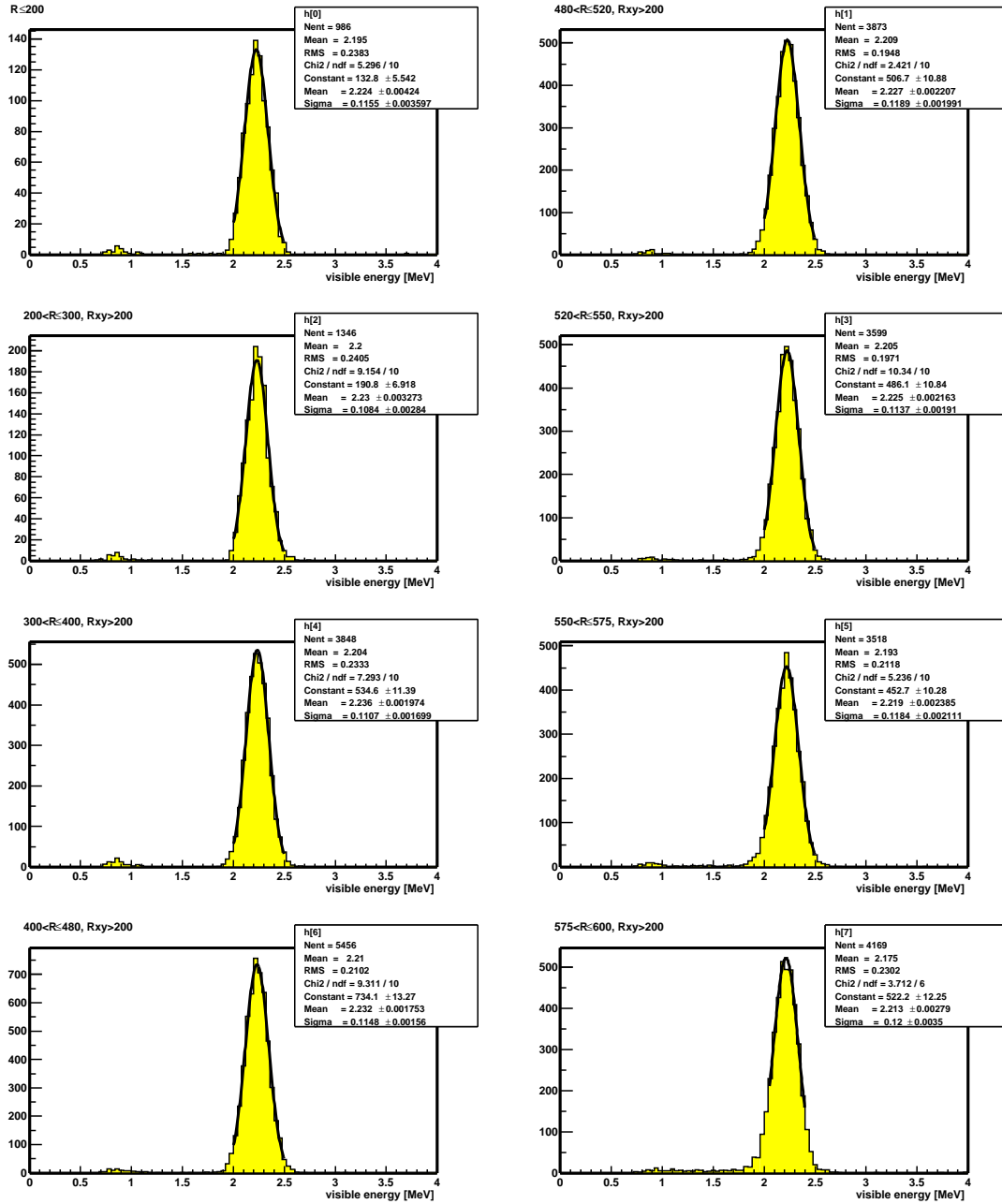


Figure 3.33: Visible energy spectrum of neutron capture gamma events (2.22457 MeV) for various radii except near the z-axis region (≤ 2 m).

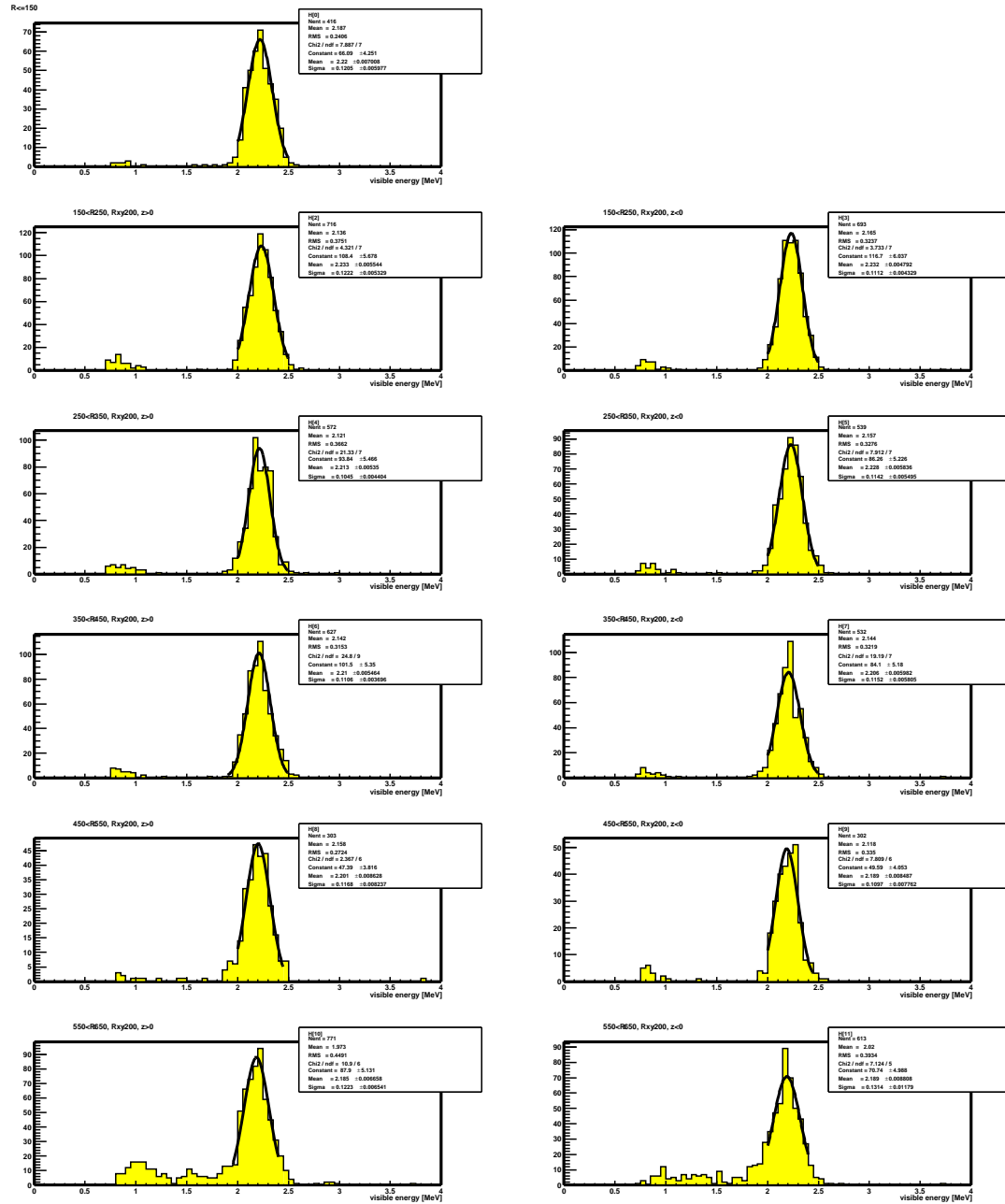


Figure 3.34: Visible energy spectrum of neutron capture gamma events (2.22457 MeV) for various radii around the z-axis region ($\leq 2m$).

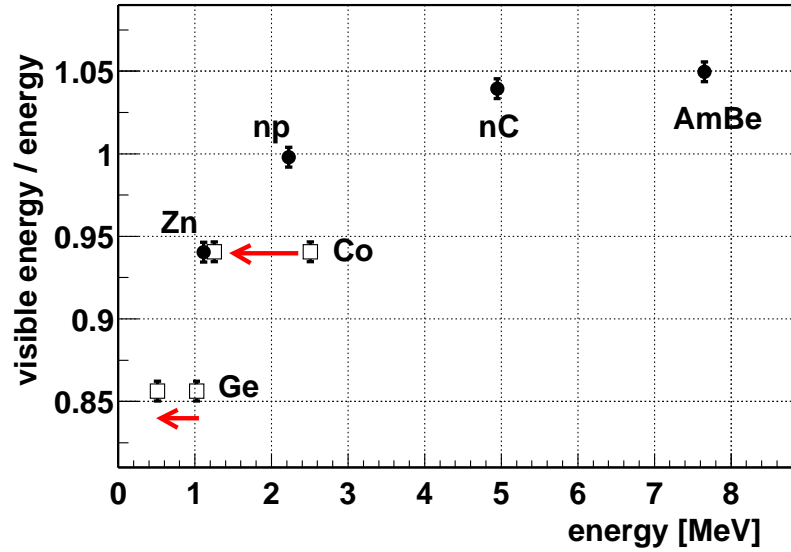


Figure 3.35: Correlation between the visible energy and deposited energy. The ratio of (visible energy)/(deposited energy) should be constant if the relation ship is linear. 1γ sources are indicated as a filled circle marker and 2γ sources with a square marker. It is natural to treat the 2γ of ^{68}Ge and ^{60}Co as 1γ whose energy is the mean of the two if contributions from Čerenkov and quenching effects are assumed.

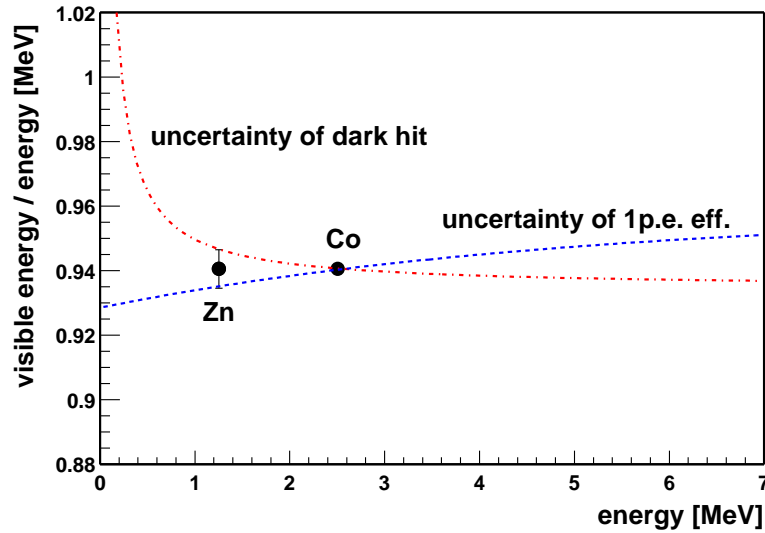


Figure 3.36: The relation between visible energy and energy for ^{60}Co and ^{65}Zn . The relative uncertainty is only time dependent uncertainty of 0.6% because both calibration points are at the detector center.

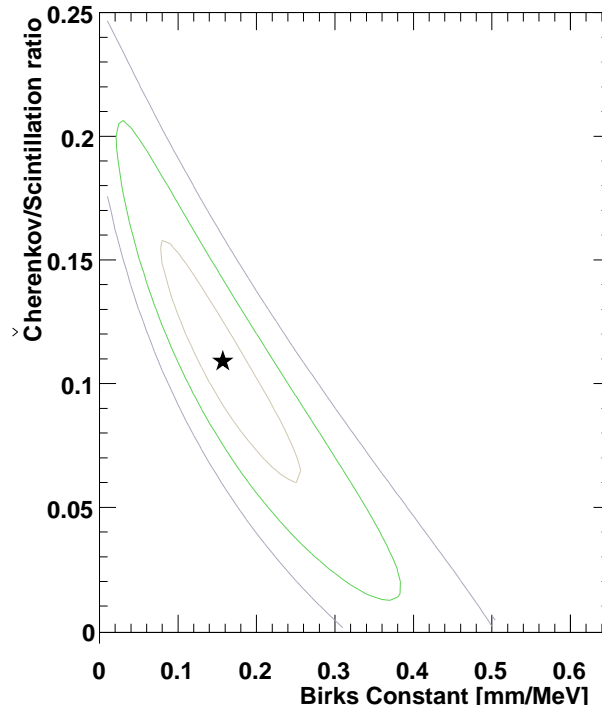


Figure 3.37: Uncertainty in the parameters for the energy scale correction. The star marker indicates the best fit parameters from various source calibration results. Elliptic lines mean 1σ , 2σ and 3σ region corresponding to the best fit parameters.

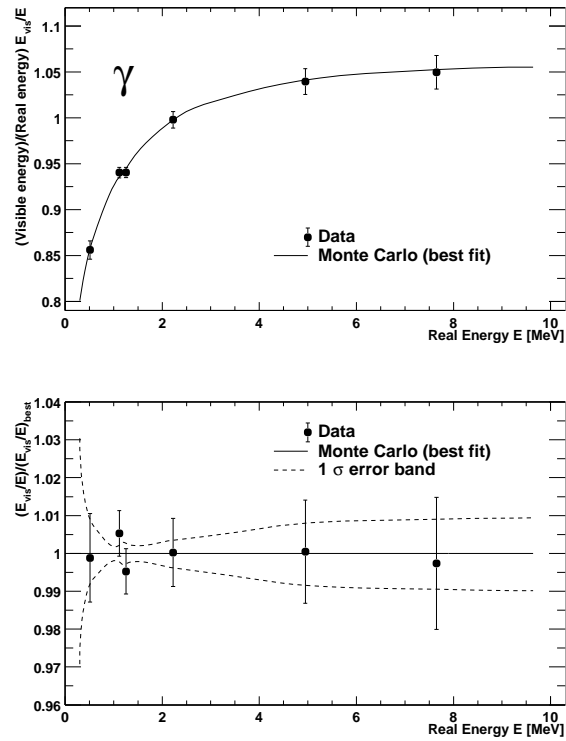


Figure 3.38: Tuned nonlinearity correction (upper) and uncertainty in the energy (lower) for gamma-rays.

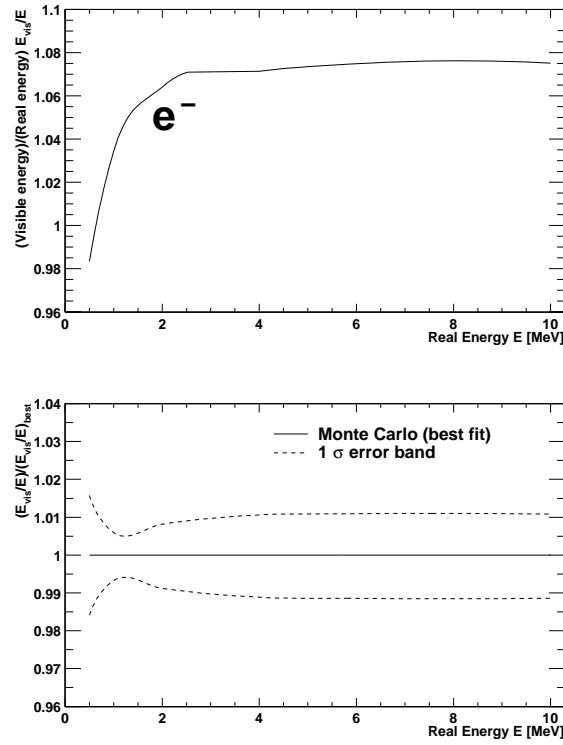


Figure 3.39: Nonlinearity correction (upper) and uncertainty in the electron energy. These correction factors are estimated by a 3 parameter fit using the MC for the 6 kinds of gamma data.

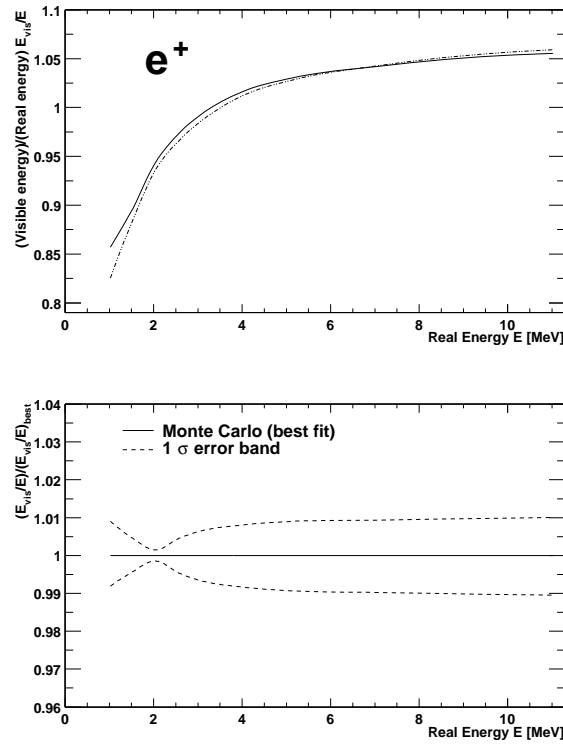


Figure 3.40: Nonlinearity correction (upper) and uncertainty in the positron energy. These correction factors are estimated by a 3 parameter fit using the MC for the 6 kinds of gamma data.

3.8 Muon Track Reconstruction

The cosmic ray muons passing into the detector make various spallation products via their interactions with scintillator materials. In particular, spallation neutrons, ^8He and ^9Li make correlated events similar to a $\bar{\nu}_e$. Thus, the selection of the cosmic ray muon events and reconstruction of their track and residual charge are essential to the study of spallation and spallation backgrounds of $\bar{\nu}_e$. The tracking information of the muon is very useful for the study of spallation products and for determining the spallation cut criteria to reject the background for the $\bar{\nu}_e$; for example, the correlation of spallation events with the reconstructed muon track. If the muon interacts with the scintillator materials and produces many spallation products, a higher energy deposition than usual occurs. The residual charge information reflects this energetic muon information very strongly. In this section, the selection criteria for muons, the track reconstruction algorithm and the definition of the residual charge are described. The study of spallation products and spallation cut criteria for $\bar{\nu}_e$ selection are described in Section 4.3.

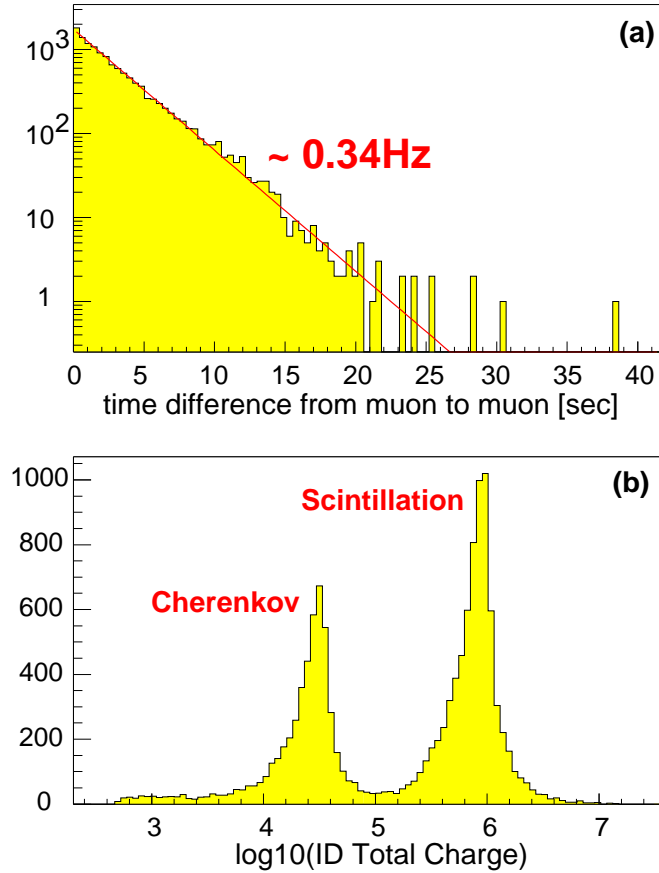


Figure 3.41: The muon event is selected with the following selection criteria, (I) PMT charge sum at ID is greater than 10,000 p.e. (II) PMT charge sum at ID is greater than 500 p.e. and the number of PMT hits in the OD is greater than 5hits. (a) Time difference between each muons, muon rate is about 3.4Hz. (b) Logarithm of PMT charge sum in the ID. There are two clear peaks, through going muons (scintillation light is dominant) and clipping muons (Cherenkov light only) respectively.

3.8.1 Selection criteria

Selection criteria for muon events are as follows,

- (A) $Q_{ID} \geq 10,000$ p.e. but not a noise event
Total charge sum in the inner detector is greater than 10,000 p.e.. The high energy event whose deposition energy is higher than about 33 MeV is selected. The event rate with this selection criteria is 0.31~0.32 Hz.
- (B) $Q_{ID} \geq 500$ p.e. and $N_{OD} \geq 5$ hits but not noise event
All of detected light is emitted Čerenkov light outside of the scintillator vessel. Detected light intensity from the Čerenkov light is about 1/23 that of the scintillation light (Section 3.8.3). Thus, the actual deposited energy is more than 37 MeV. The muon rate with this selection criteria is 0.027~0.028 Hz.

The selected muon rate is about 0.34 Hz, and the time interval between muon events and the spectrum of total charge in the inner detector is shown in Figure 3.41. The charge spectrum gives clear information for classification of the type of muon using the charge sum. The word “clipping muon” is often used in this thesis. It is defined to be a muon that passes through the inner detector but not through the scintillator balloon.

3.8.2 Track reconstruction

The muon track information is reconstructed via following steps,

1. Find the earliest hit PMT but which is not isolated in the time ordering (see Figure 3.43). The intersection with the balloon surface of the line drawn from the center of the detector to this PMT in question is defined as the primary entrance point.
The time information of PMT hits is the most clear information for distinguishing the entrance position of a cosmic ray muon. On the other hand, the charge information is not useful for find the actual entrance position because strong light intensity is emitted at the entrance into the scintillator balloon, and the closest PMT from the entrance of the scintillator balloon is not necessary the muons entrance point.
2. Find the most intense PMT hit which is not isolated in charge ordering and whose hit time is not earlier than that of the entrance PMT (see Figure 3.44). The intersection with the balloon surface of the line drawn from the center of the detector to this PMT in question is defined as the primary exit point.
The energy deposition along the muon track emits Čerenkov light as well as scintillation light, and it is forward of the muon track. Therefore, deposition is most intense at the exit position.
3. Correct the primary reconstructed track based on the correlation between the total charge sum and the track length.
For a clipping muon event, the correlation between the primary track length and the total charge sum is often unusual. The primary entrance or the primary exit or both are corrected to the most appropriate point, between the primary entrance to the earliest PMT and the primary exit to the most intensive PMT.
4. Check reconstruction quality and assign a degree of “badness” for each reconstruction. The “badness” of greater than 100 means a completely miss reconstruction.
Follows are check items,

- (a) Could the earliest PMT and the most intensive one be found ?
- (b) Is the mean time of the PMT hits at the inner detector (ID) around the entrance position earlier than around the exit position ?
- (c) Is the mean time of the PMT hits at the outer detector (OD) around the entrance direction earlier than around the exit direction ?

This quality check of the reconstruction is very important because mis-reconstruction of the muon track is very critical to the spallation background rejection.

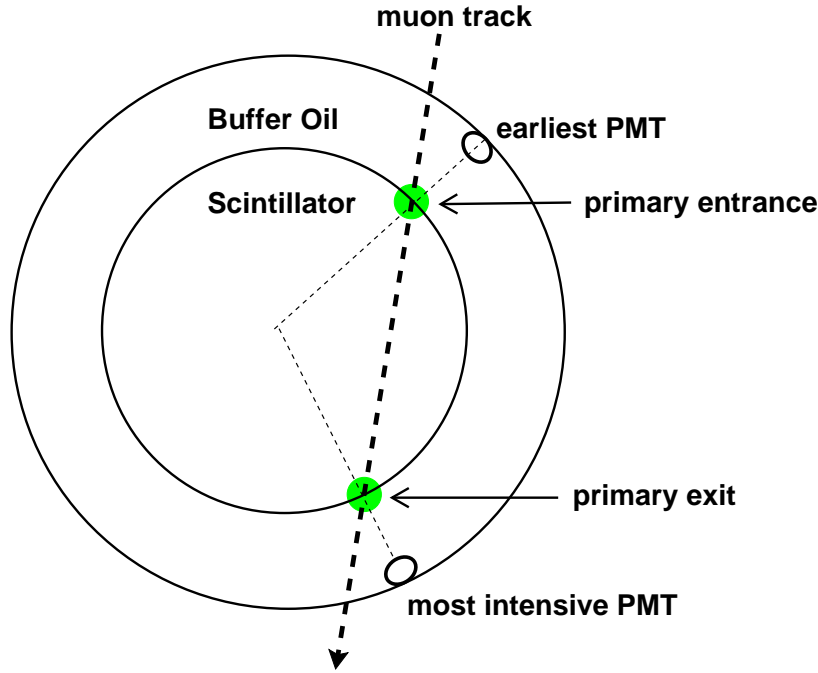


Figure 3.42: First, entrance and exit points are determined using time and charge information from hit PMT. Then the most appropriate positions are found using the correlation between the track length and the total charge sum.

Actually, above reconstruction algorithm is not appropriate for multi muon events or “stopping muons” which stop in the detector. About 11.6% of muons are miss-reconstructed of their tracks but the most of them are clipping muons, which do not enter the scintillator. Therefore, the effective mis-reconstruction rate is around 0.45% for all muon events.

Correlations between the total charge sum of muon events and the reconstructed track length of muons, the distance from the center of the detector to the reconstructed muon track (impact parameter) are shown in Figure 3.45 without mis-reconstructed muons. Moreover, Figure 4.13 shows the very good correlation between spallation neutrons and reconstructed muon tracks (89% efficiency within 2 m and 94% efficiency within 3 m). This is a very important value to estimate the number of the spallation background in $\bar{\nu}_e$ candidates. More details are described in Section 4.3.1.

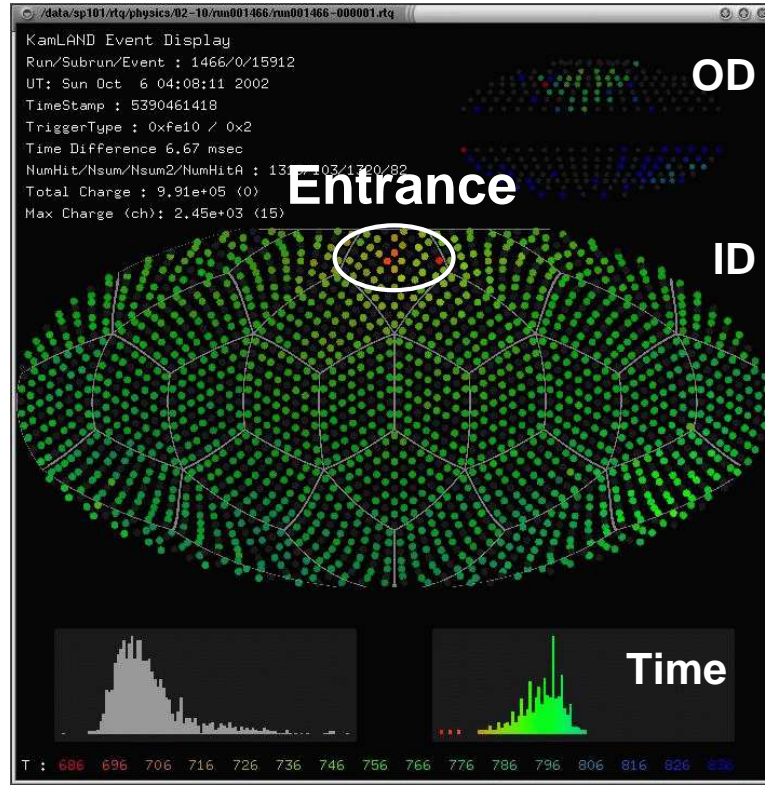


Figure 3.43: The entrance point of the muon track is decided with time information of PMT hits.

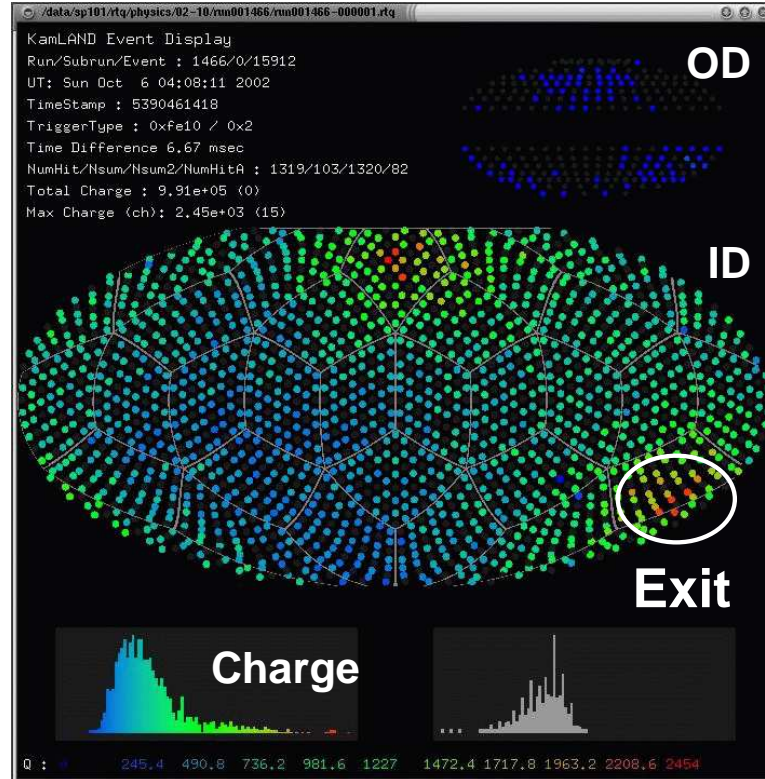


Figure 3.44: The exit point of the muon track is decided with charge information of PMT hits.

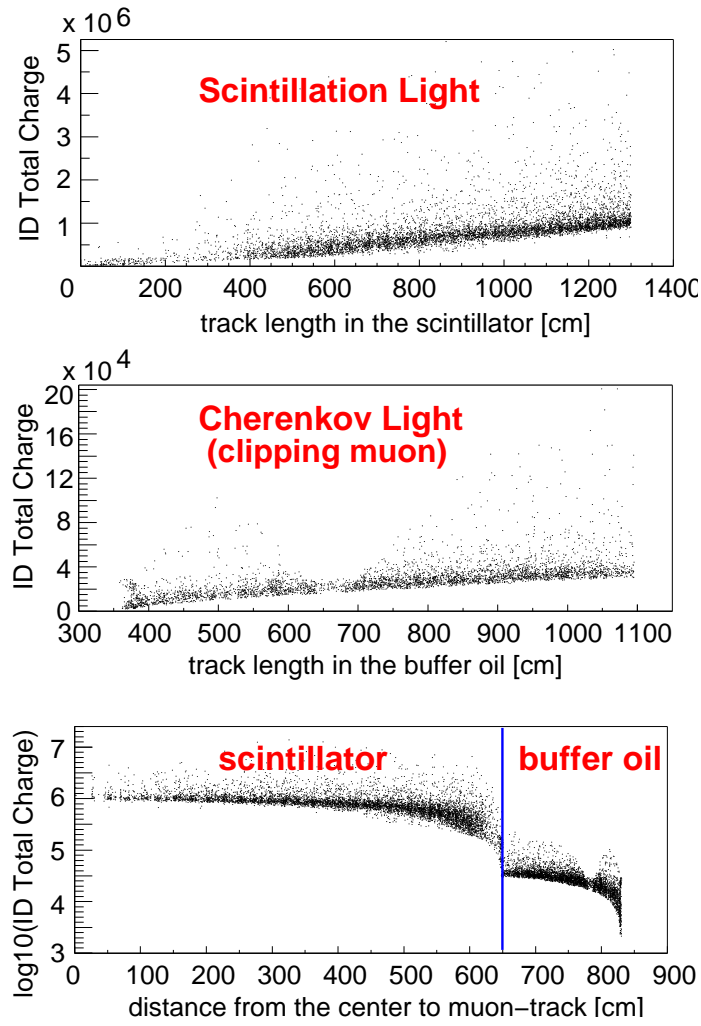


Figure 3.45: Correlation between total charge and reconstructed track length.

3.8.3 Residual charge

The correlation of the total charge sum with the track length (dQ/dX) is calculated as follows,

$$\left(\frac{dQ}{dX}\right)_{\check{C}herenkov} = \frac{Q_{ID}}{L} \quad (3.37)$$

$$\left(\frac{dQ}{dX}\right)_{Scintillation} = \frac{Q_{ID} - (dQ/dX)_{\check{C}herenkov}}{L - l_{scinti.}} \quad (3.38)$$

where Q_{ID} , L and $l_{scinti.}$ are the total charge sum of the inner detector, the track length of the muon track at the inner detector and the track length in the scintillator balloon respectively. Figure 3.46 shows dQ/dX distributions for the Čherenkov and the scintillation lights. The

peak values are the ideal dQ/dX for them,

$$\left(\frac{dQ}{dX}\right)_{\check{C}herenkov}^{ideal} = 32.45 \text{ p.e./cm} \quad (3.39)$$

$$\left(\frac{dQ}{dX}\right)_{Scintillation}^{ideal} = 738.4 \text{ p.e./cm} \quad (3.40)$$

The $(dQ/dX)_{Scintillation}$ is about 23 times higher than the $(dQ/dX)_{\check{C}herenkov}$. The residual charge ΔQ is calculated using these values,

$$\Delta Q = Q_{ID} - \left(L \times \left(\frac{dQ}{dX}\right)_{\check{C}herenkov}^{ideal} + l_{scinti.} \times \left(\frac{dQ}{dX}\right)_{Scintillation}^{ideal} \right) \quad (3.41)$$

The ΔQ has a good correlation with the production rate of spallation products as shown in Figure 4.11. This is also the essential information for the spallation study.

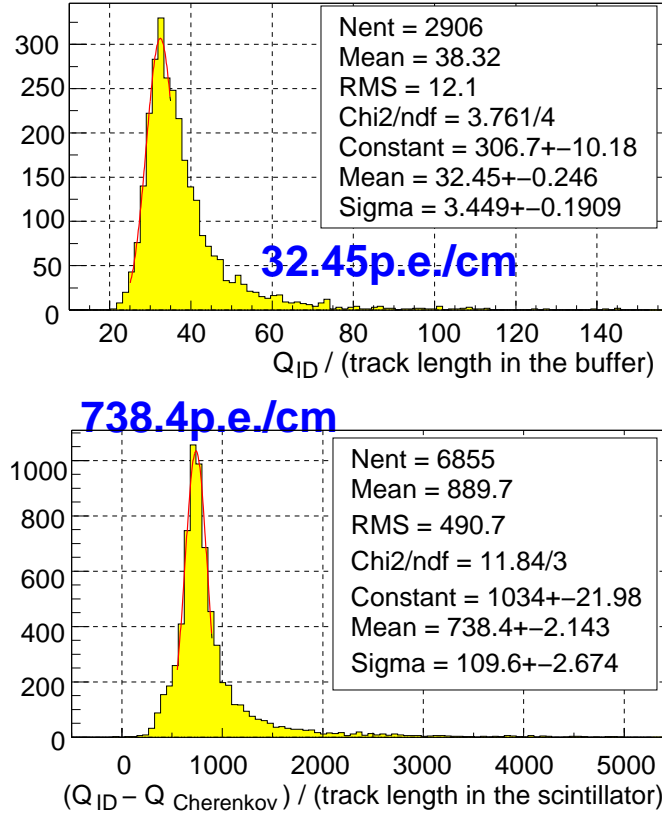


Figure 3.46: Normalized charge by track length of reconstructed muon, so called dQ/dX (similar to dE/dX). Upper figure is for clipping muons ($(dQ/dX)_{\check{C}herenkov}$) and lower is for through going muons ($(dQ/dX)_{scintillation}$).

3.9 Noise Event Selection (Noise Cut)

Real physics events have a timing correlation with PMT hits as in Figure 3.47. But, noise events have no time correlation with PMT hits as shown in Figure 3.48. The noise events created sometimes;

- After a muon event for about $150 \mu\text{sec}$
In this case, this is caused by the ringing in the front-end-electronics (FEE). This ringing creates fake PMT hits and these “fake” hits issue a trigger causing a fake event.
- Unstable network
The data taking network is busy and effected by unexpectedly large data transfers. For example, if a flasher PMTs causes a very high trigger rate. During this period, illegal time ordering of data packets occurs. This confuses the event building process and the data packet is ignored increasing that part (~ 100 ch) of the PMT information is ignored.
- After deadtime
Noise events occur when the detector revived after deadtime. This is caused by muons passing through the detector right before revival from the deadtime.

It is easy to select and to cut noise events through the timing correlation of PMT hits. Almost all PMT hits are clustered within a 100 nsec time interval as shown in Figure 3.47. The correlation between number of maximum PMT hits within the 100 nsec time interval (n_{100}) and the number of hit PMTs (n_{hit}) is a clear cut criterion for noise events (Figure 3.49),

$$\text{Noise Selection Criteria: } n_{100} \leq (n_{hit} + 50) / 2$$

Rare events, like $^{212}\text{Bi} \rightarrow ^{212}\text{Po}(T_{1/2} = 299\text{nsec}) \rightarrow ^{208}\text{Pb}$ in Th-chain, are occasionally selected by this criterion (Figure 3.50).

The accidental noise selection rate is easy to calculate using a low hit trigger rate in a special run, which recorded only the number of PMT hit. The event rate with a 100 hit threshold is about 250 Hz in contrast to the usual trigger threshold (200 hits) and about 21 Hz.

$$\text{accidental rate} = 250 \text{ Hz} \times 250 \text{ Hz} \times 100 \text{ nsec} \sim 6 \times 10^{-3} \text{ Hz}$$

The actual noise rate is almost consistent with this, but little bit lower than expectation at $5 \times 10^{-3} \text{ Hz}$ (Figure 3.51). The accidental noise selection rate for a normal event whose trigger threshold is 200 hits and about 21 Hz is,

$$\text{accidental rate (for usual event)} = 21 \text{ Hz} \times 21 \text{ Hz} \times 100 \text{ nsec} \sim 4.4 \times 10^{-5} \text{ Hz}.$$

The inefficiency caused by cuts on the noise events is

$$\text{inefficiency caused by noise cut} = (\text{accidental rate for usual event}) / 21 \text{ Hz} \sim 2 \times 10^{-4} \text{ \%}.$$

The inefficiency caused by the noise cut is negligible, and the systematic uncertainty related to the the noise cut is defined, conservatively, to the inefficiency of $2 \times 10^{-4} \text{ \%}$.

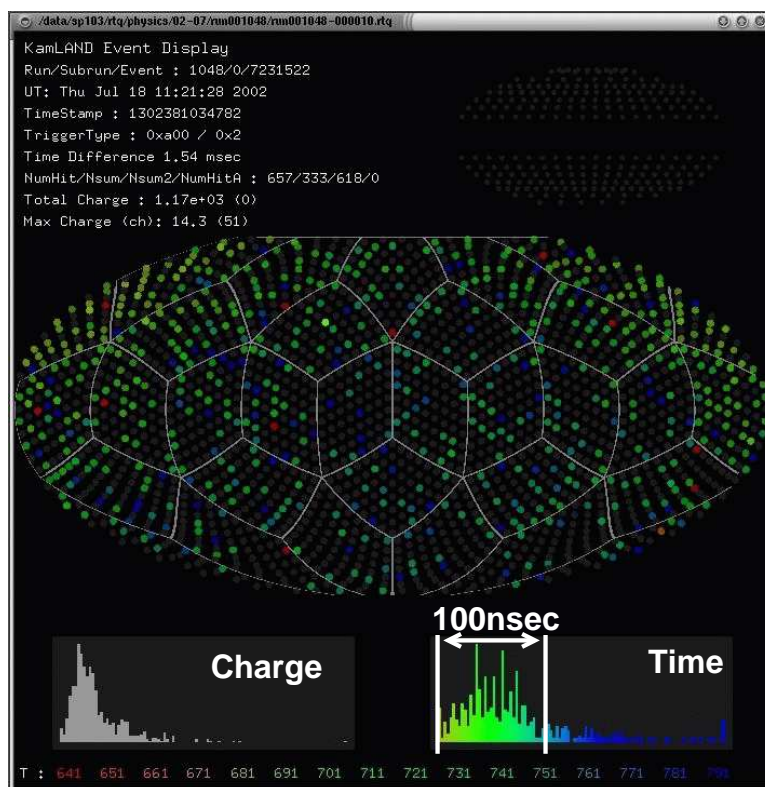


Figure 3.47: An event display of a typical low energy event. Almost all PMT hits are clustered within a 100nsec time window.

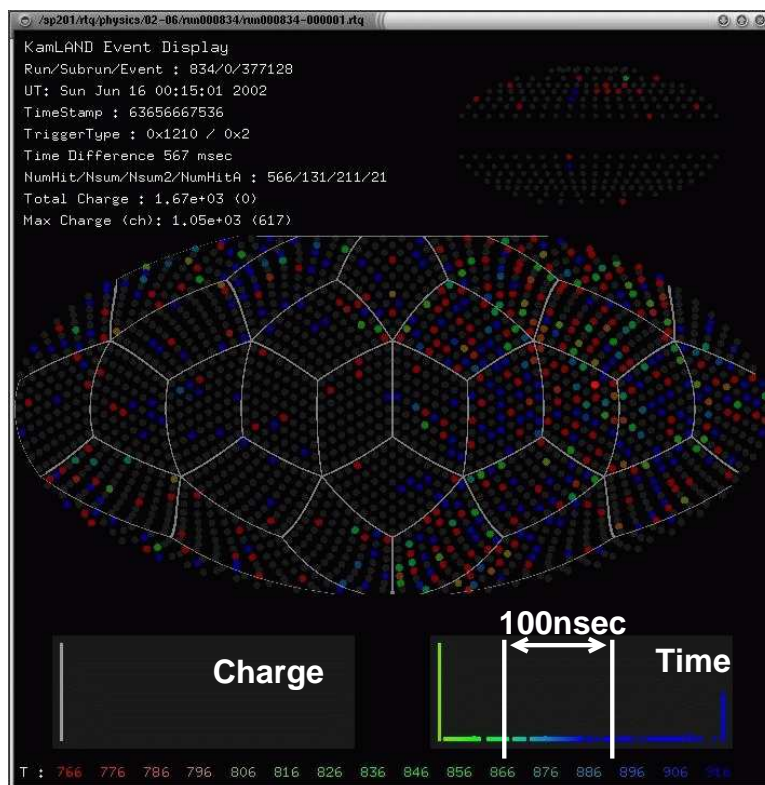


Figure 3.48: An event display of a typical noise event. There is no correlation between PMT hit times.

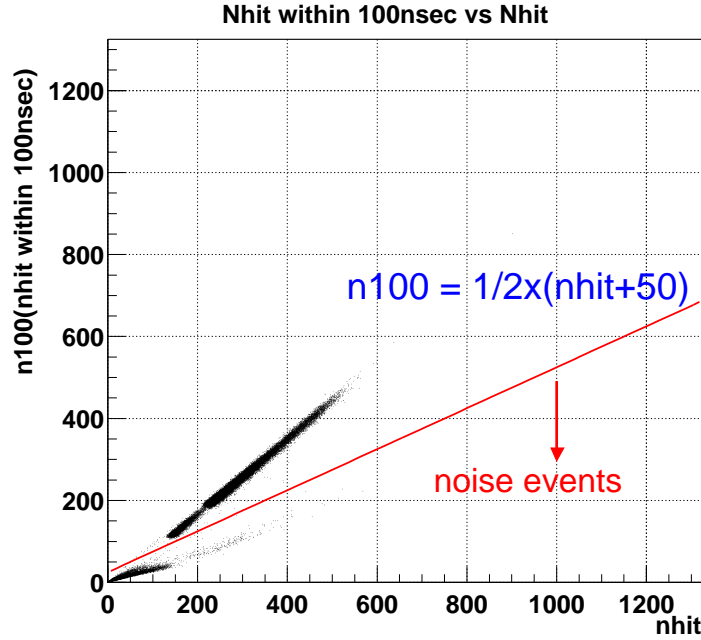


Figure 3.49: The cut condition for noise events is shown as a function, $n100 \leq (nhit+50)/2$. The “nhit” means the number of PMT hits in a event and the “n100” means the number of the maximum PMT hits within a 100nsec time window in a event.

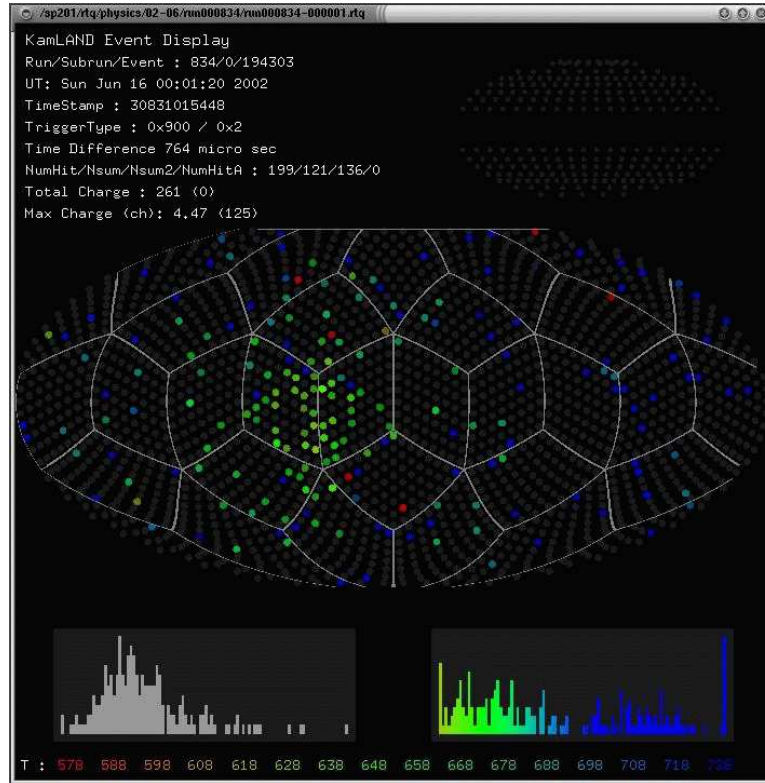


Figure 3.50: An event display of successive events defined as a noise event and cut based on the time correlation of the PMT hits. It looks as if there are two physics events from the time correlation, but the correlation looks flat if it is considered one physics event. This is also a candidate for a characteristic internal radioactivity event in the Th-chain, $^{212}\text{Bi} \rightarrow ^{212}\text{Po}(T_{1/2} = 299\text{nsec}) \rightarrow ^{208}\text{Pb}$.

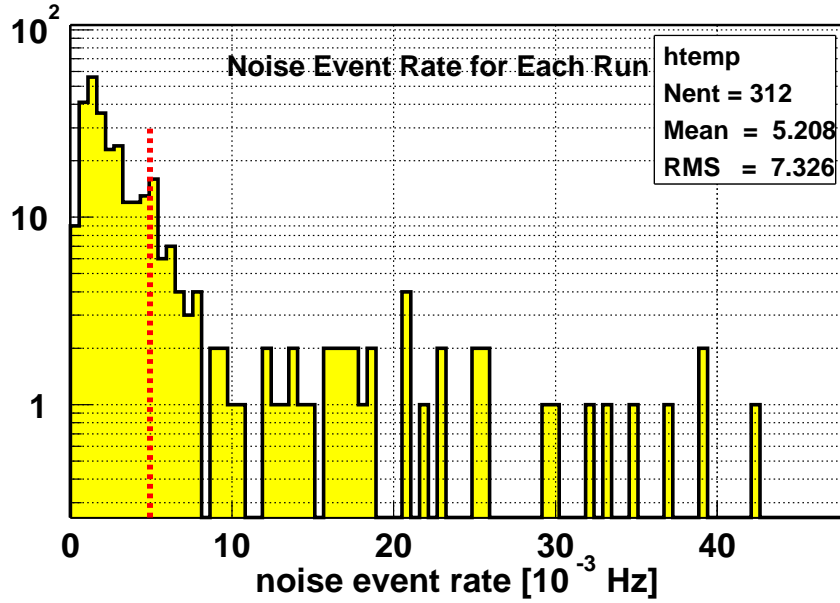


Figure 3.51: Noise event rate for each run. Expected accidental noise event rate ($\sim 5 \times 10^{-3}$ Hz) is shown with a dashed line. The noise rate in some runs is much higher than the expectation but which is caused by broken data packets when the network is busy. In this case, it is defined as “noisy period”.

3.10 Flasher Event Selection (Flasher Cut)

Flasher PMTs, which emit light and then detect it, create a fake signal for high energy events ~ 20 MeV with charge around 6,000 p.e. as in Figure 3.52. Since the flash light illuminates other PMTs, such events are not recorded as noise events. However, they are easy to select because of their high charge. The selection criteria are,

- Total charge in the inner detector is greater than 2,500 p.e. ($\sum_i q_i \geq 2,500 \text{ p.e.}$).
- The ratio of the maximum PMT charge in a event to the total charge sum is greater than 0.6 ($q_i / \sum_i q_i \geq 0.6$).

and their effectiveness is shown in Figure 3.53.

The selection probability is 0.0097% of all events, and so this value is defined as an inefficiency in the uncertainty of $\bar{\nu}_e$ detection.

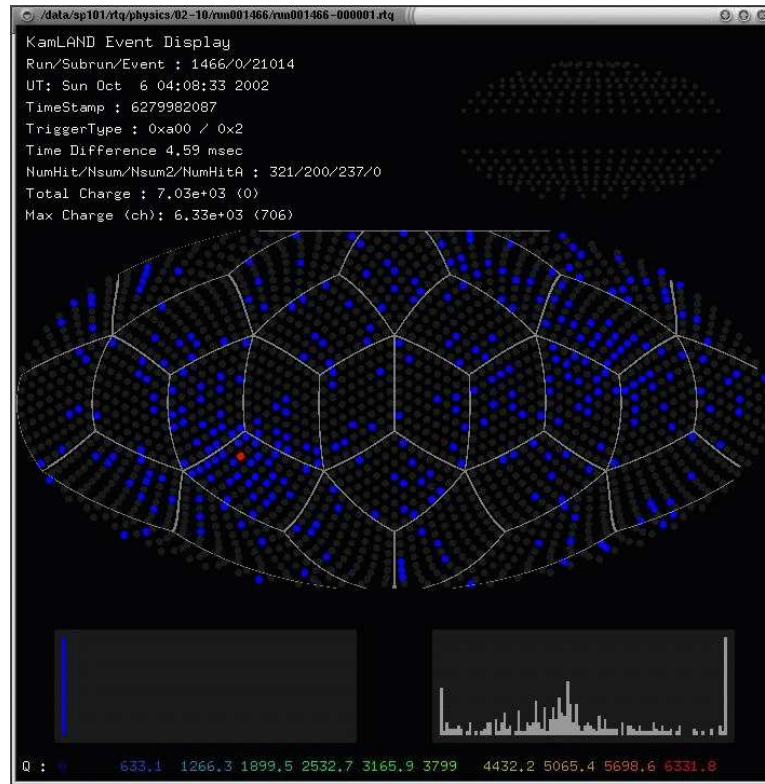


Figure 3.52: Event display of a typical flasher PMT event. One PMT's signal is very intense, and illuminates itself.

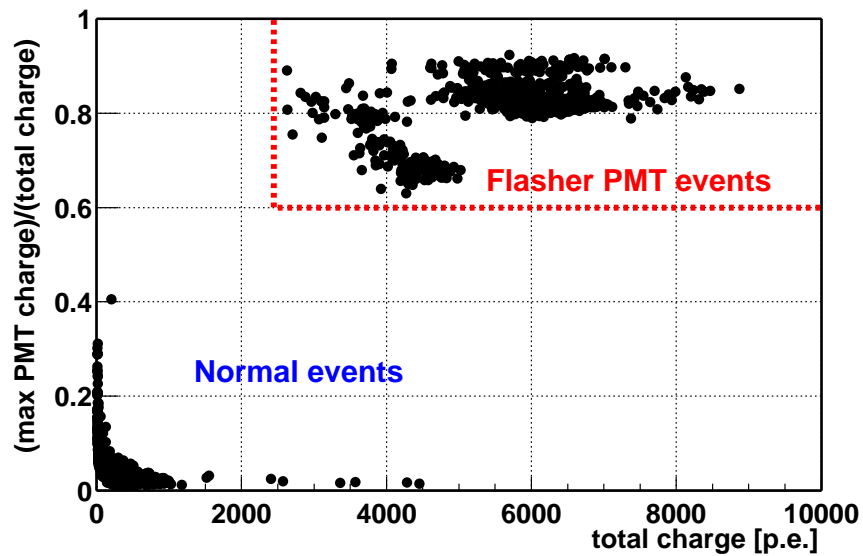


Figure 3.53: Flasher event can be cut with simple selection criteria requiring that the total charge in the inner detector be greater than 2,500 p.e. ($Q_{ID} \geq 2,500 \text{ p.e.}$) and that the ratio of the maximum PMT charge to the total event charge be greater than 0.6 ($q_{max.}/Q_{ID} \geq 0.6 \text{ p.e.}$).

Chapter 4

Radioactivities in/into the Detector and Background

There are various radioactivities in the detector, and some of them are coming into the detector from outside or produced by the spallation of cosmic-ray muon. Main radioactive impurities which contained in the scintillator are ^{238}U (including ^{222}Rn and ^{210}Pb), ^{232}Th , ^{40}K and ^{85}Kr . Incoming radioactivities are γ -ray of ^{40}K and ^{208}Tl , cosmic-ray muon, fast neutron. ^{40}K is mainly emitted from the rope of the scintillator balloon. ^{208}Tl is emitted from the surrounding rock or the surface of the PMTs. The cosmic-ray muons create various spallation products, neutron, ^{12}B , ^{12}N , ^9B , ^8B , ^8Li and neutron emitters (^8He and ^9Li). The fast neutron is produced in the rock or in the outer detector by the muon spallation and comes into the inner detector.

Some of their characteristic decay makes correlated events, and these are background (fake event) for the $\bar{\nu}_e$ event. The contribution of them is reduced by the cuts for background rejection, and remained number of them is estimated in this chapter.

- Multi neutrons capture of spallation neutrons (Section 4.3.1)
Whole volume veto for 2 msec following muon suppresses it efficiently. Remained number of events is negligible.
- Neutron emitted decay of ^8He and ^9Li (Section 4.3.3 and 4.3.4)
Spallation cut, whole volume veto for 2sec following energetic muon or track correlated cut (within 3 m only for delayed events) following non-energetic muon, reduces its contribution drastically ~ 1 event for 145days data set ($1 \sim 2\%$ of expected reactor $\bar{\nu}_e$).
- Recoil proton and neutron capture caused by fast neutron (Section 4.4)
Some of them which were produced in the outer detector are measured. The contribution from the surrounding rock is estimated by using the MC simulation based on the measurement and production rate of the spallation neutron. Conservative upper limit (<0.5 events) is given, currently ($\sim 1\%$ of reactor $\bar{\nu}_e$).
- Successive β -decay, $^{214}\text{Pb} \rightarrow ^{214}\text{Bi} \rightarrow ^{214}\text{Po}$, in Uranium chain (Section 4.2)
It is negligible because its quantity is very low ($3.5 \pm 0.5 \times 10^{-18}$ g/g).
- Correlated decays in Thorium chain (Section 4.2)
Due to its energy range and quantity, it is negligible ($5.2 \pm 0.8 \times 10^{-17}$ g/g).

On the other hand, accidental coincidence makes another type of background, uncorrelated background. Its contribution is estimated by using same selection criteria as $\bar{\nu}_e$ without the

condition for time window cut. Fiducial cut criteria are decided by the accidental background study (Section 4.5):

- Fiducial radius cut ($R \leq 5$ m)
- Cylindrical cut within 1.2 m along central vertical axis (z-axis) only for the delayed events. This cut eliminates the radiation from thermometers which are deployed along z-axis.

The fiducial cut reduces the accidental background to be 0.0089 events ($\sim 0.01\%$ of $\bar{\nu}_e$) above 2.6 MeV prompt energy (~ 3 events above 0.9 MeV prompt energy).

There are other $\bar{\nu}_e$ sources except for reactor $\bar{\nu}_e$'s, i.e. atmospheric neutrinos and Geo $\bar{\nu}_e$'s [39]. They are described in Section 4.6. Their contributions are also estimated though nobody knows precise contribution of Geo $\bar{\nu}_e$'s. Due to the ambiguity associated with Geo $\bar{\nu}_e$'s below 2.49 MeV for the prompt energy, the analysis of reactor $\bar{\nu}_e$ is performed above 2.6 MeV prompt energy usually (HAT). The analysis with lower energy region (≥ 0.9 MeV) is used for the consistency check of analysis (LAT). Therefore, the background is also classified to two types. The background for reactor $\bar{\nu}_e$ detection is summarized in Table 4.1.

Table 4.1: Summary of Backgrounds for $\bar{\nu}_e$ (events / data-set)

Background	0.9MeV analysis threshold (LAT)	2.6MeV analysis threshold (HAT)
Accidental	1.81 ± 0.08	0.0085 ± 0.0005
$^8\text{He}, ^9\text{Li}$	1.1 ± 1.0	0.94 ± 0.85
fast neutron	< 0.5	< 0.5
U	negligible	negligible
Th	negligible	negligible
Atmospheric $\bar{\nu}_e$	1.02×10^{-4}	1.02×10^{-4}
Geo $\bar{\nu}_e$		
(i) 0 TW	0	0
(ii) 16 TW	9.1	0.044
(iii) 30 TW	17.0	0.082
total		
w/o Geo $\bar{\nu}_e$	2.91 ± 1.12	0.95 ± 0.99

4.1 Study of Single Events

Figure 4.1 shows the energy spectrum of single events except for muon, noise and flasher events. There is a valley around 0.7 MeV in the spectrum of the single events, it is made by the lower contribution of the delayed trigger (lower trigger; see Section 2.1.8) events as the meshed histogram in Figure 4.1. Thermal neutron capture events on proton and ^{12}C are observed within 2 msec following muon (thick line in Figure 4.1), details are described in Section 4.3.1. Stop or clipping muon events are dominant above 15 MeV, which are concentrated around the equator because of thin water and no PMT in the outer detector. It can be well understood from Figure 4.2-(a).

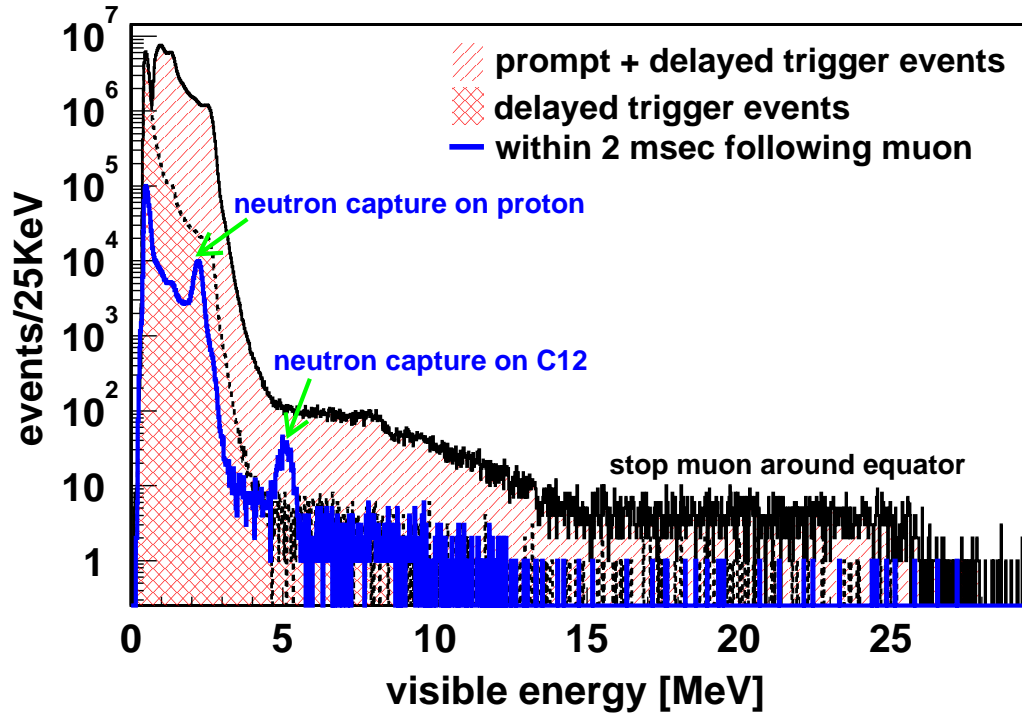


Figure 4.1: Energy spectra of single events in the whole volume. The hatched histogram is the energy spectrum without muon, noise and flasher events. The meshed one is only for the delayed (lower) trigger events. Its lower contribution makes valley around 0.7 MeV. The 2 msec veto following muon is adopted for the hatched and meshed histograms. The thick line indicates events within 2 msec following muons. Thermal neutron capture events on proton and ^{12}C are observed clearly.

The vertex distributions of events at various energy ranges are shown in Figure 4.2. The “muon veto” (veto for 2 msec following muons) has already applied for all plots in this figure. The most intensive region is the top of the detector around the chimney because there are various stainless steel materials to hang the scintillator balloon. The spallation products like ^{12}B , ^{12}N and so on are dominant above several MeV energy range. The life time of them is longer than 2 msec. The vertex distribution of them looks uniform, while there are small affection from the stop muons around the equator. From 1 to several MeV energy range, many events are observed near the balloon edge as shown in Figure 4.2-(c)~(e). The most probable explanation for Figure 4.2-(c) is the radiation from the dust on the surface of the balloon inside, for example $\beta + \gamma$ decay of ^{208}Tl (^{232}Th chain) gives about 5 MeV energy deposition in the

scintillator. Figure 4.2-(d), (c) indicate the attenuation of external radiations, γ -rays from ^{208}Tl (2.62 MeV) and ^{40}K (1.46 MeV). The most of 2.62 MeV γ -rays of ^{208}Tl are emitted from the outside of the detector, because many radioactive isotopes like ^{238}U and ^{232}Th are contained

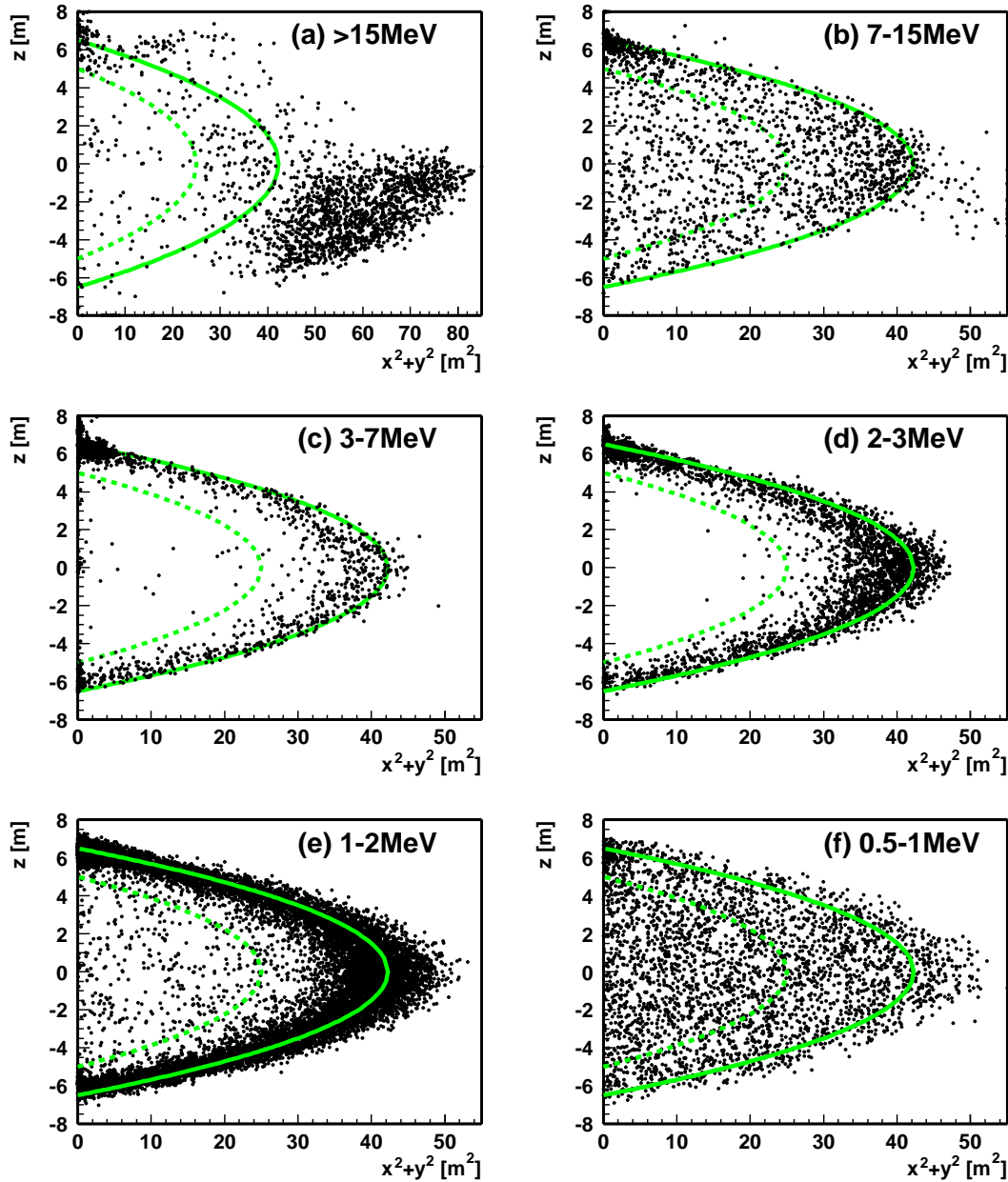


Figure 4.2: Vertex distributions of various energy events in the whole volume. Intensive region is exists around the equator and outside of the scintillator balloon in higher energy. Probably, these are stop or clipping muon events because there is no PMT in the outer detector around equator and the water buffer is thin. The most intensive region is the top of the detector around the chimney. The event distribution is uniform at long life ($>2\text{msec}$) spallation products energy region or below 1 MeV region. External radiations from ^{40}K and ^{208}Tl are dominant at MeV order energy region.

in the surrounding rock and the ^{208}Tl is the daughter isotope of the ^{232}Th . Its event rate is about 3 Hz. On the other hand, the most of 1.46 MeV γ -rays of ^{40}K are emitted from the inside of the balloon ropes. The balloon ropes contain $8.3 \times 10^{-10} \text{ g/g}$ of ^{40}K , and its decay rate is 21.6Bq(γ -ray 2.3Bq). Both external γ -rays are strongly suppressed by the fiducial radius cut. It is clearly observed in Figure 4.3. Especially, the 1.46 MeV γ -ray is almost rejected by the 5 m radius cut. Due to the energy resolution ($\sigma/\sqrt{E(\text{MeV})} \sim 7.5\%$), the observed energy of the 2.62 MeV γ -ray has the distribution. This must be the delayed event of the accidental background (Section 4.5) because the cut condition of the delayed energy is 1.8~2.6 MeV in $\bar{\nu}_e$ selection.

Below 1 MeV, the distribution of events is uniform as in Figure 4.2-(f). The most of them are ^{85}Kr and ^{210}Bi (^{210}Pb). The half-life time of ^{85}Kr is $T_{1/2}=10.756\text{y}$ and it decays to ^{85}Rb via β -decay (99.5%, $Q_\beta=687\text{KeV}$) or $\beta + \gamma$ (0.43%, $Q_\beta=173\text{KeV} + E_\gamma=514\text{KeV}$). The ^{210}Pb , which is the daughter isotope of ^{222}Rn (^{238}U), is contained in the detector. The half-life time of it is $T_{1/2}=22.3\text{y}$ and it decays to ^{210}Bi ($Q_\beta=64\text{KeV}$). The ^{210}Bi decays to ^{210}Po via β -decay ($T_{1/2}=5.013\text{d}$, $Q_\beta=1.163\text{MeV}$). Figure 4.4 shows the event distribution within 5 m fiducial radius. The vertex distribution is almost uniform in various energy range except for the 2.62 MeV γ -ray region. Moreover, another intensive region is observed in Figure 4.4-(d). Thermometers and its cables exist along the central z-axis, these are deployed at the center, $z=+5.5\text{ m}$ and $z=-5.5\text{ m}$. Their metal materials contain radioactive isotopes, this is the reason the center position is intensive. These affection is rejected by the cylindrical cut within 1.2 m along z-axis. Figure 4.3 indicates 1.5~4 MeV radiations are emitted around the thermometers.

Figure 4.5 is the single spectrum with the 4 m fiducial radius without the 1.2 m radius cylin-

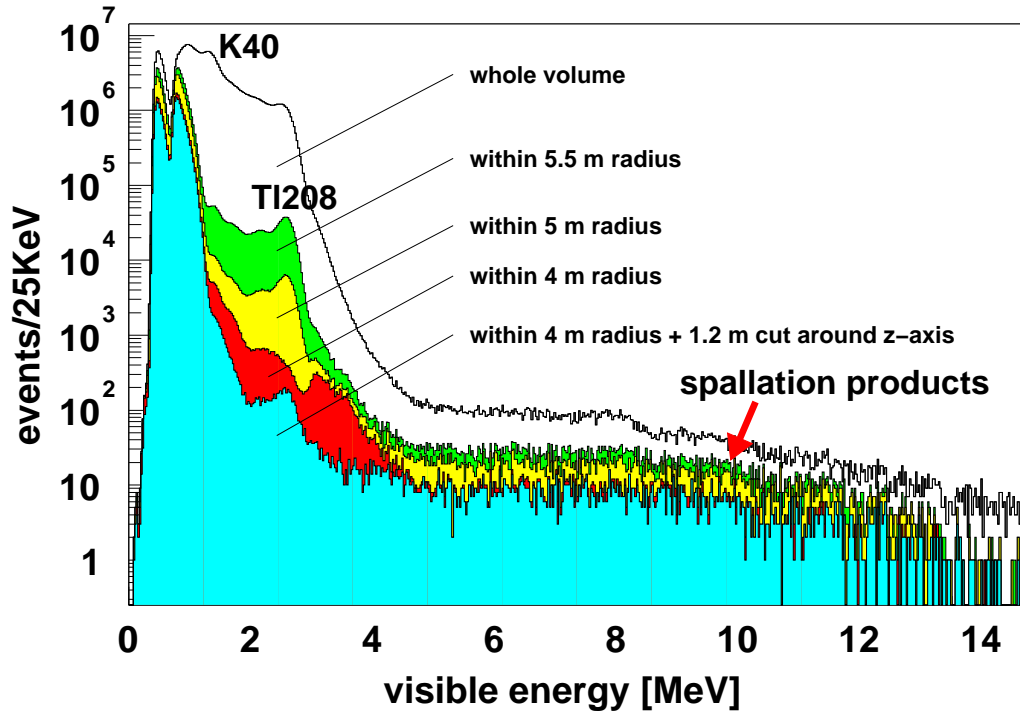


Figure 4.3: Correlation of the energy spectrum with fiducial radius. External radiations, γ -rays from ^{208}Tl (2.62 MeV) and ^{40}K (1.46 MeV) are strongly suppressed by the cut of the fiducial radius cut. Along the central z-axis (especially center) intensive radiations are observed around 1.5~4 MeV. These are emitted from the thermometers and their cables.

drical region along z-axis. The observed energy spectrum constrains the ^{40}K contamination to be less than about 2.7×10^{-16} g/g. Above several MeV region, the expected spectrum based on the measured event rate of ^{12}B in KamLAND (Section 4.3) and others in another experiment for the muon spallation [40] well agree with the observed spectrum in KamLAND. The expectation around 4 MeV region based on the measured ^{232}Th rate (Section 4.2) with spallations also agree with the observed spectrum.

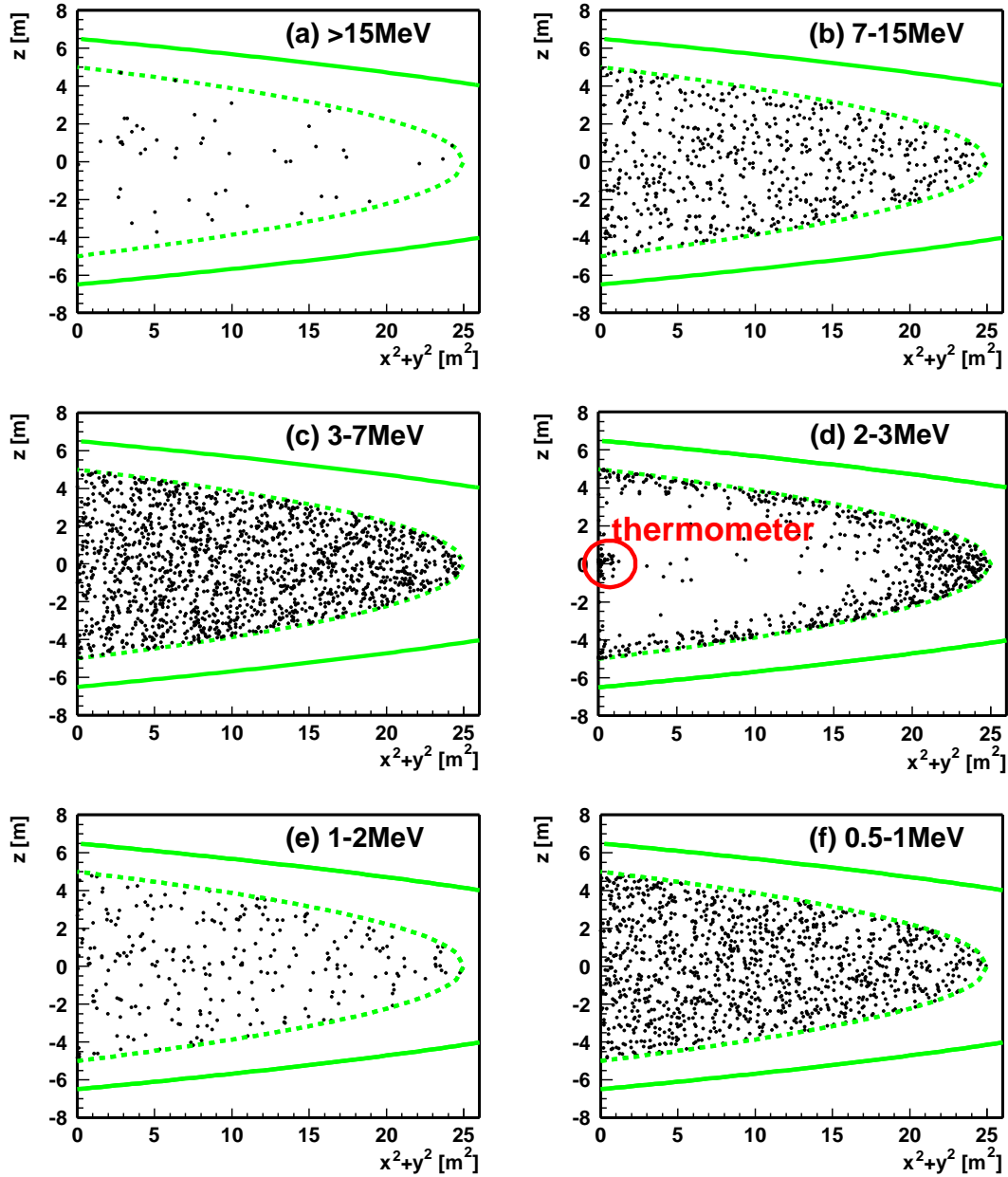


Figure 4.4: Vertex distributions within 5 m radius in various energy. The distribution of the single events is uniform without the 2.6 MeV γ -ray (^{208}Tl) energy region. The contribution of the radioactivities from the thermometer is observed as well as the external contribution of the ^{208}Tl .

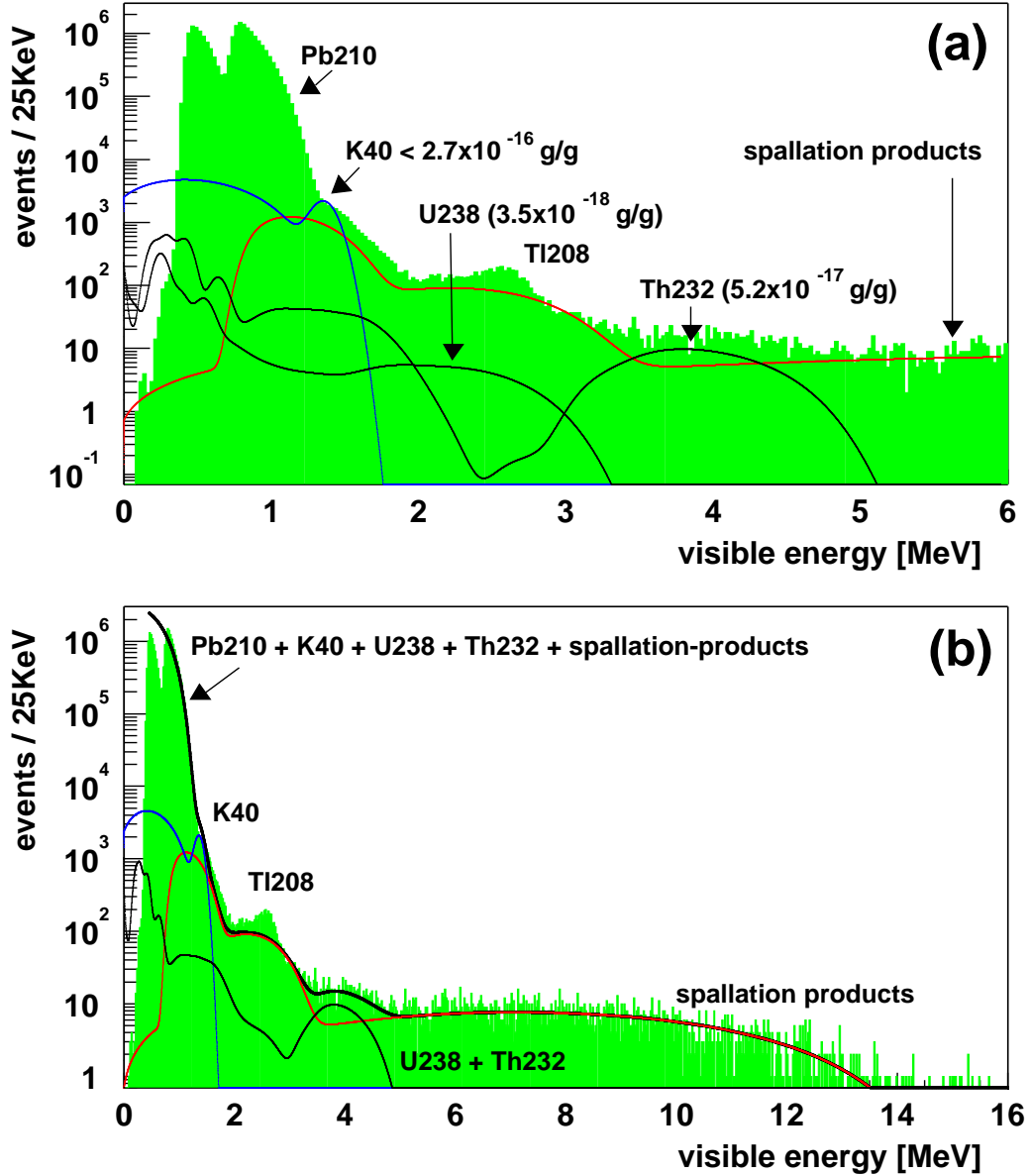
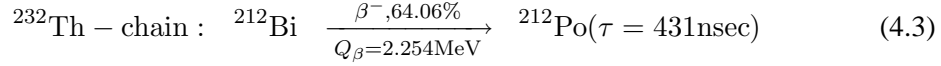
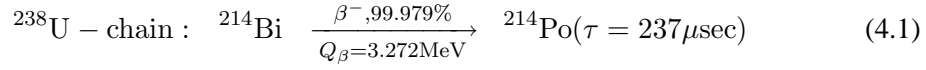


Figure 4.5: Single spectrum with the 4m fiducial radius without the 1.2m radius cylindrical region along z-axis. (a) shows lower energy range below 6 MeV, and (b) includes higher energy region. The measured spectrum is shown as shaded histogram, and each line shows the expected spectrum for each radioactivity. Two different threshold triggers makes a valley around 0.7MeV because of the difference of trigger rates. The upper limit of ^{40}K is evaluated from the event rate for 1.46~1.65MeV energy window: 2.7×10^{-16} g/g. The “spallation products” includes ^{12}B (63events/day/kton), ^9C (5.5events/day/kton), ^8Li (5events/day/kton), ^8B (8events/day/kton), $^8\text{He}+^9\text{Li}$ (2.4events/day/kton), ^6He (19events/day/kton), ^{11}C (1,039events/day/kton), and ^{10}C (139events/day/kton). These production rates are coming from [40] except for ^{12}B (which comes from Section 4.3). It is good agreement with single spectrum, especially in higher energy range $>5\text{MeV}$. Thick line in (b) is summed up one, where it is supposed 1.15Bq/m^3 for the decay rate of ^{210}Pb and 2.0×10^{-16} g/g for the quantity of ^{40}K . The ^{208}Tl is the external γ -rays, the event rate of it is strongly depends on the fiducial radius (see Figure 4.3).

4.2 Measurement of ^{238}U and ^{232}Th

There are characteristic decay in ^{238}U and ^{232}Th chain,



These events are selected using the delayed coincidence technique as shown in Figure 4.6 and 4.7. Selection criteria are as follows;

- Time correlation
 - ^{238}U chain: $5\mu\text{sec} \leq \Delta T \leq 1,000\mu\text{sec}$
For avoiding to incorporation of Bi-Po decay in Th chain, The veto for $5\mu\text{sec}$ should be applied following any prompt event. Time window of the delayed trigger is limited less than $1,000\mu\text{sec}$. It is the specification of the trigger.
 - ^{232}Th chain $0.4\mu\text{sec} \leq \Delta T \leq 1\mu\text{sec}$
For avoiding to incorporation of Bi-Po decay in U chain, time correlation window should be less than $1\mu\text{sec}$. Detection efficiency of very short time interval less than about 300nsec from previous event is too low abnormally. Therefore, it is veto within $0.4\mu\text{sec}$ when we calculated the quantity of it.
- Space correlation $\Delta R \leq 1\text{m}$
- Energy window cut
 - ^{238}U chain: $E_{\text{prompt}} \geq 1.3\text{MeV}$, $E_{\text{delayed}} \leq 1\text{MeV}$
 - ^{232}Th chain: $1\text{MeV} \leq E_{\text{prompt}} \leq 2\text{MeV}$, $E_{\text{delayed}} \leq 1\text{MeV}$
- Veto for 2 msec following muons to reject multiple neutron capture events
- Fiducial cut
 - ^{238}U chain: 4m of the fiducial radius to reduce the accidental coincidence.
 - ^{232}Th chain: 5m of the fiducial radius to reduce the accidental coincidence.

^{238}U

Very clear prompt and delayed energy spectra are observed in Figure 4.6-(a), (b), and good vertex correlation is also observed in Figure 4.6-(d). Fitted mean decay time ($232.3 \pm 7.2 \mu\text{sec}$) in Figure 4.6-(c) is good agreement with the value in Table of Isotopes ($237 \mu\text{sec}$). The detection efficiency is summarized in Table 4.2, and its decay rate is $1.4 \mu\text{Bq/m}^3$

According to Figure 4.6-(e), (f), the most of ^{214}Bi - ^{214}Po events are distributed along the central z-axis because ^{222}Rn comes into the detector sometimes with the calibration devices, and the accidental coincidence is dominant over 6 m radius. Therefore, actual quantity in the scintillator is measured with the 2 m cylindrical cut along central z-axis, and it is $0.034 \pm 0.5 \mu\text{Bq/m}^3$ ($\leftrightarrow 3.5 \pm 0.5 \times 10^{-18} \text{ g/g}$). In Figure 4.6-(a), (b), shaded histograms mean this cut is applied.

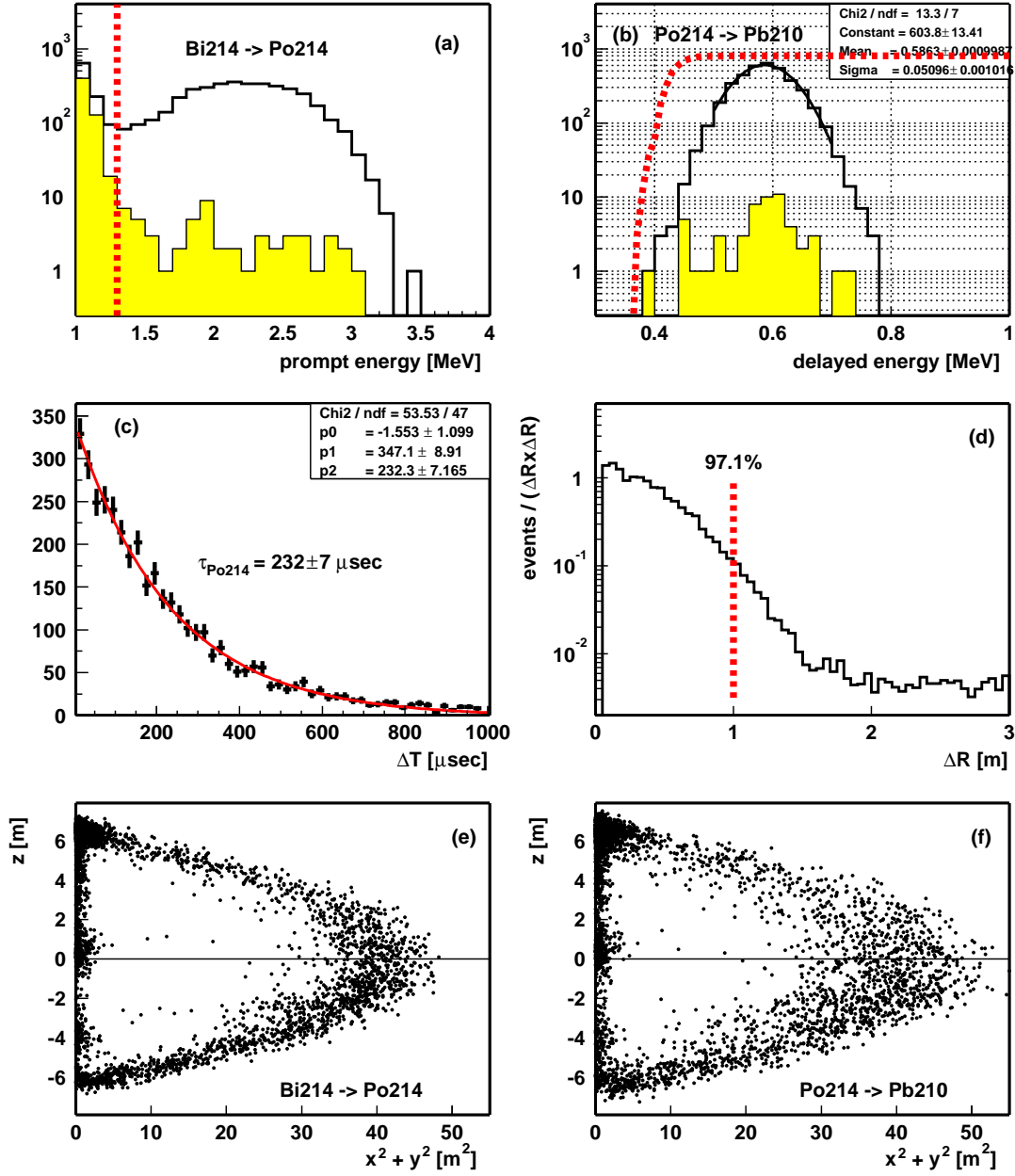


Figure 4.6: $^{214}\text{Bi} \rightarrow ^{214}\text{Po} \rightarrow ^{210}\text{Pb}$ in ^{238}U chain is observed. Shaded histogram means that the cylindrical region for 2 m radius along central z-axis is cut.

- (a) prompt energy spectrum
- (b) delayed energy spectrum
- (c) time correlation between the prompt and delayed events
- (d) space correlation between the prompt and delayed events
- (e) vertex distribution of prompt events
- (f) vertex distribution of delayed events

^{222}Rn exists along the central z-axis because it infects at the calibration.

Table 4.2: Detection efficiency of Bi-Po coincidence event in U chain

space correlation ($\Delta R \leq 1\text{m}$)	97.1%
time correlation ($5\mu\text{sec} \leq \Delta T \leq 1,000\mu\text{sec}$)	96.4%
prompt energy window ($\geq 1.3\text{MeV}$)	86.4%
delayed energy threshold ($\leq 1\text{MeV}$)	99.7%
total	80.6%

 ^{232}Th

In Figure 4.7, no fiducial cut sample is shown as non-shaded histograms. The shaded histograms mean that the 5m of the fiducial radius cut and the cylindrical cut for 2m radius along central z-axis are applied. The end point energy in Figure 4.7-(a) is consistent with it of the $^{212}\text{Bi} \rightarrow ^{212}\text{Po}$ decay. The peak of α in $^{212}\text{Po} \rightarrow ^{208}\text{Pb}$ decay is observed clearly in Figure 4.7-(b). There are good vertex correlation between the prompt and delayed events as shown in Figure 4.7-(d).

Fitted mean decay time in Figure 4.7-(c) (498 ± 34 nsec) is longer than the value in Table of Isotopes (431 nsec) because of the accidental coincidence around balloon edge and bottom and top along z-axis. Figure 4.7-(e), (f) help to understand these accidental coincidence. Detection efficiency is summarized in Table 4.3, and its decay rate in the scintillator is $(0.16 \pm 0.03) \mu\text{Bq/m}^3$ ($\leftrightarrow 5.2 \pm 0.8 \times 10^{-17}$ g/g).

Table 4.3: Detection efficiency of Bi-Po coincidence event in Th chain

space correlation ($\Delta R \leq 1\text{m}$)	97.8%
time correlation ($0.5\mu\text{sec} \leq \Delta T \leq 1\mu\text{sec}$)	29.7%
prompt energy widow ($1 \sim 2\text{MeV}$)	34.8%
delayed energy threshold ($\leq 1\text{MeV}$)	99.9%
total	10.1%

Correlated background estimation for $\bar{\nu}_e$ detection

The Bi-Po-Pb decay is negligible because its delayed energy is much lower than that of neutron capture gamma (2.22MeV). The $^{214}\text{Pb} \rightarrow ^{214}\text{Bi}$ decay in ^{238}U chain is more serious in case of 0.9 MeV lower analysis threshold (LAT) Its contribution is less than 1.0×10^{-5} events for LAT data set even if $1 \mu\text{Bq/m}^3$ of ^{222}Rn or ^{238}U . Anyway, the correlated background in ^{238}U and ^{232}Th chain is negligible due to the very low quantities of them and the cylindrical cut within 1.2m radius along z-axis for delayed event (Section 4.5).

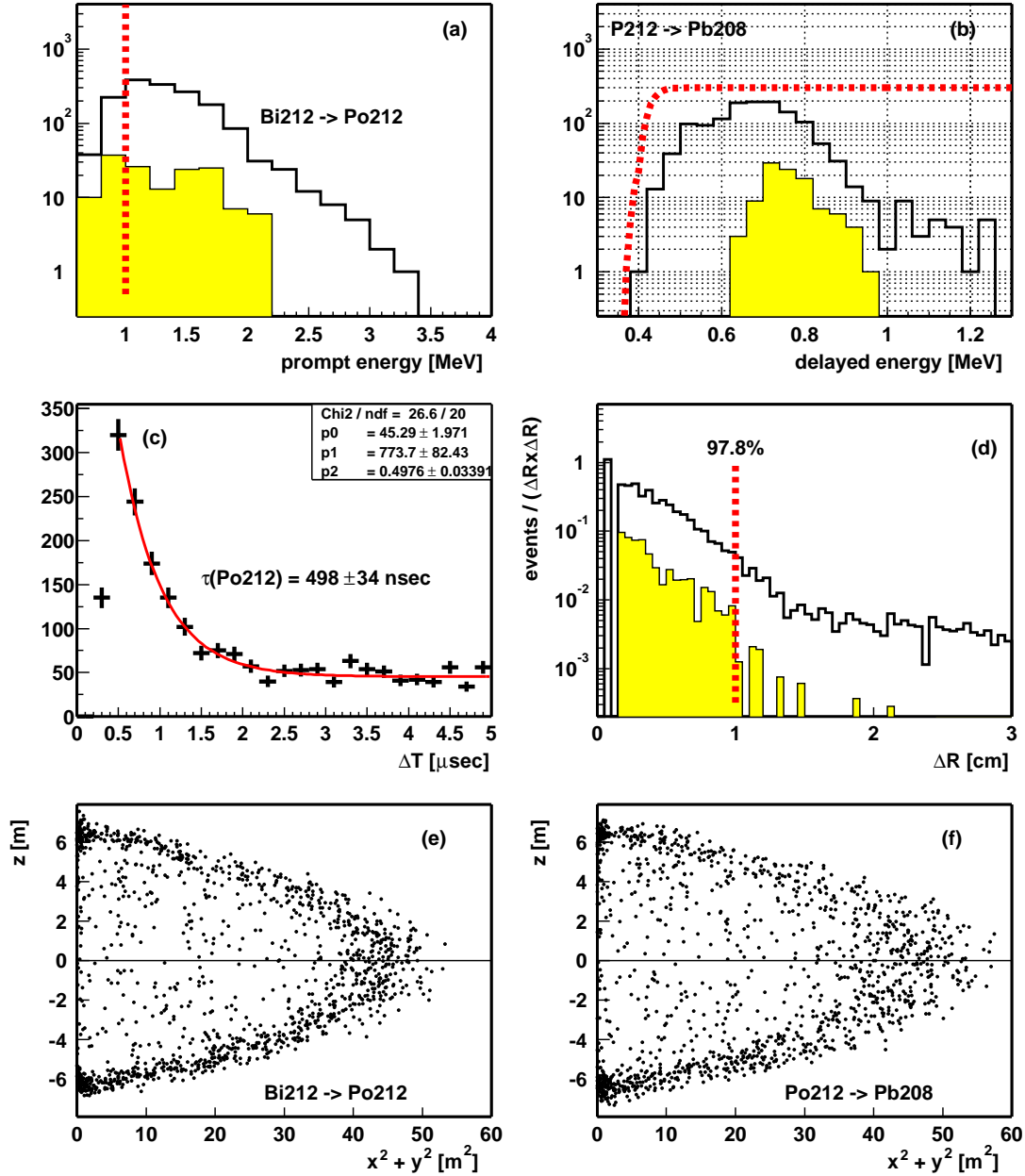


Figure 4.7: $^{212}\text{Bi} \rightarrow ^{212}\text{Po} \rightarrow ^{208}\text{Pb}$ in ^{232}Th chain is observed. Shaded histogram means fiducial cut is applied, radius $\leq 5\text{m}$ and the cylindrical cut for 2 m radius along central z-axis.

- (a) prompt energy spectrum
- (b) delayed energy spectrum
- (c) time correlation between the prompt and delayed events
- (d) space correlation between the prompt and delayed events
- (e) vertex distribution of prompt events
- (f) vertex distribution of delayed events

The top and bottom along z-axis are intensive because stainless steel materials exist to hang the scintillator balloon.

4.3 Spallation Study

4.3.1 Spallation neutron

The cosmic ray muon breaks ^{12}C in the scintillator, and many neutrons are produced. These neutrons are captured on proton or ^{12}C or the others within several hundred μsec from their production because the mean capture time of them is $212.5 \pm 8.1 \mu\text{sec}$ (Section 5.2.2). Very clear peaks of these capture γ -rays are observed in the NsumMax (number of hits when trigger was issued) spectrum by selecting 1msec events after muon (Figure 4.8). The ratio of (proton

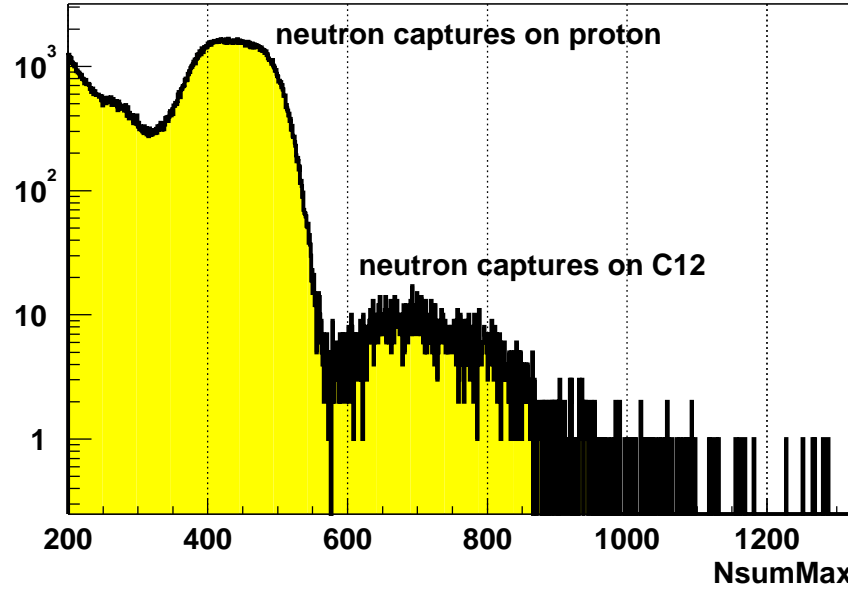


Figure 4.8: NsumMax spectrum after muon within 1msec, but first $150\mu\text{sec}$ was veto because of the deadtime of electronics. Thermal neutron capture on proton(γ , 2.22457MeV) and ^{12}C (γ , 4.9468) events make clear energy peak. It is easy to select neutron capture event on proton with a simple cut condition $350 < \text{NsumMax} < 550$.

captured)/(^{12}C captured) agrees with the predicted ratio 99.45%/0.55% (see Table 2.7). However, the number of acquired waveform information is less than actual number of PMT hits unfortunately because the ringing problem in FEE makes many busy channel in FEE for several hundreds μsec (Figure 4.9). This missing digital waveform problem is easy to check with “number of acquired digital waveforms should be larger than NsumMax”, and good events are selected easily. The correlation of good events with time is shown in Figure 4.10, 1 msec is needed for the recovery from this problem. The NsumMax has small affection, actually. But it is recovered within $300 \sim 400 \mu\text{sec}$ from last muons. It is caused by several multiple neutrons. Therefore, this problem is only for the energetic muons because the neutron multiplicity of the energetic muons is high (Figure 4.12).

The production rate and mean capture time of spallation neutrons are evaluated by the fitting of time distribution of neutron capture event after $500 \mu\text{sec}$. The mean capture time is fitted to $212 \pm 2 \mu\text{sec}$, and it is consistent with the prediction of the MC based on Am-Be calibration, i.e. $212.5 \pm 8.1 \mu\text{sec}$ (see Section 5.2.2). The production rate is fitted to $3,024 \pm 24$ events/day/kton, and it changes to $3,251 \pm 19$ events/day/kton or 2801 ± 16 events/day/kton if capture time is change to $212.5 - 8.1 = 204.4 \mu\text{sec}$ or $212.5 + 8.1 = 220.6 \mu\text{sec}$. Thus, the production

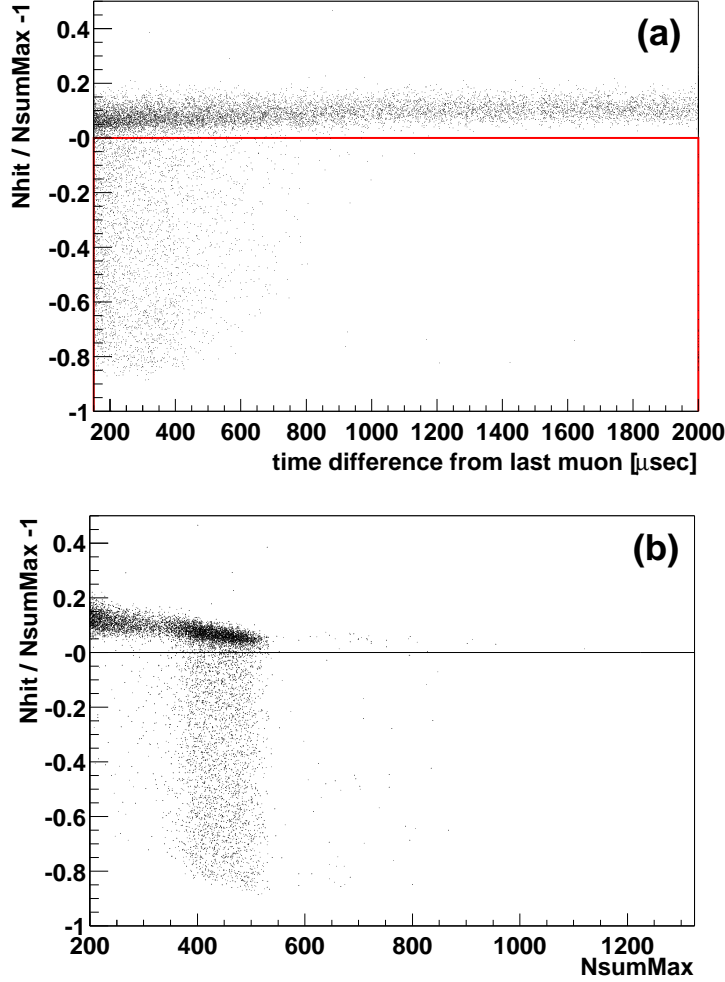


Figure 4.9: Correlation between $N_{hit}/N_{sumMax}-1$ and time difference from last muon (a) and N_{sumMax} within 1msec (b). The N_{hit} means number of digital waveform information from PMTs which detect photon.

(a) Parts of PMT hits information disappear within ~ 1 msec after muon.

(b) But N_{sumMax} information is not broken.

rate of the spallation neutron is $3,024 \pm 246$ events/day/kton, and $\sim 1,300$ events/day/kton of various unstable products are expected except for the neutron according to [40].

The multiplicity of neutron has good correlation with the residual charge of the muon track as shown in Figure 4.11. It indicates that the possibility of the muon spallation is higher if the residual charge is higher. The definition of the “energetic muon” is the muon whose residual charge is higher than 10^6 p.e., and the residual charge of the “non-energetic muon” is less than 10^6 p.e.. This is essential information for the study of the muon spallation. There is good correlation between the reconstructed muon track and the vertex of spallation neutrons for the non-energetic muons (Figure 4.13). The cut of the track correlated volume is adopted as the spallation cut for the $\bar{\nu}_e$ detection. Its rejection efficiency is calculated from this track correlation efficiency for the spallation neutrons (see Section 4.3.3 and 4.3.4).

Figure 4.14 shows visible energy spectrum after muon for good events. The neutron capture

γ -rays on proton and ^{12}C are good energy calibration sources (Section 3.7).

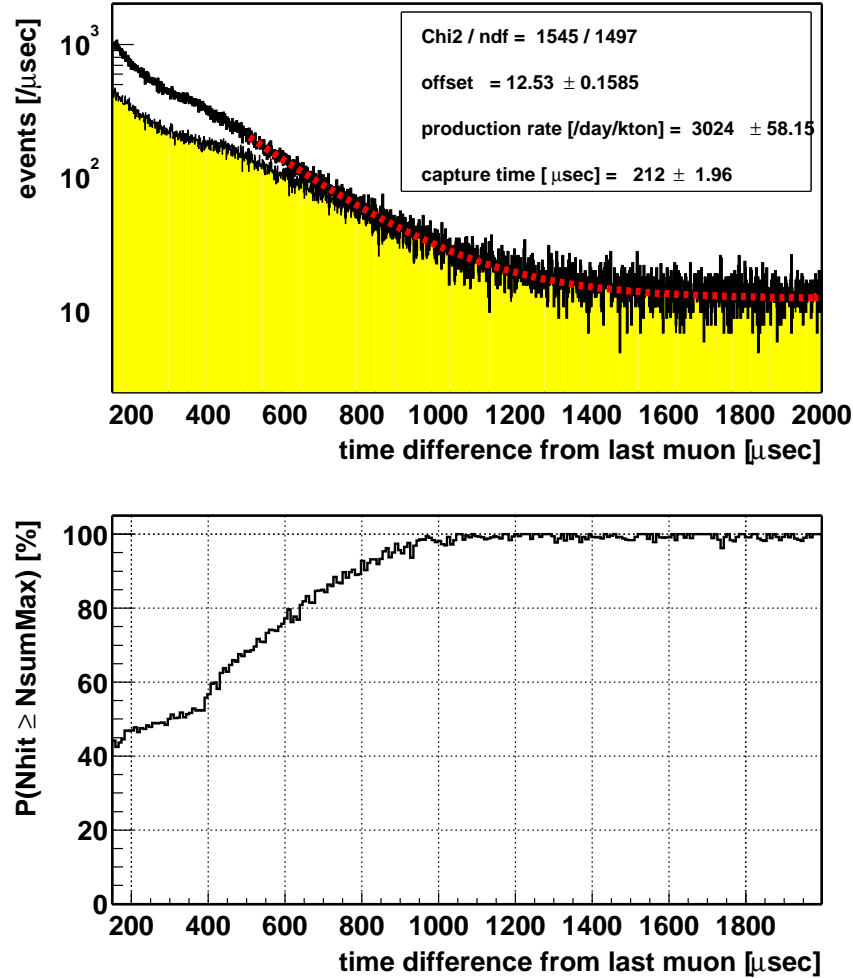


Figure 4.10: Time difference from last muons to spallation neutron capture candidates (upper figure). These events are selected with a simple cut, $350 < \text{NsumMax} < 550$ for the non-shaded histogram, and good event cut (number of waveform information should be rather than NsumMax) is adopted for the shaded histogram. The lower figure shows time variable for the percentage of good neutron event which defined as the ratio shaded-histogram to non-shaded-histogram in the upper figure. Parts of PMT hits (actually, waveform) information disappear within $\sim 1\text{msec}$ after muons. Moreover, the NsumMax has small affection of several multiple neutrons even though the NsumMax has no affection of this missing waveform problem. Thus, The production rate of spallation neutron is evaluated by the fitting with $n_{\text{offset}} + \frac{n_{\text{pr}}}{\tau} \exp(-\frac{t}{\tau}) / \langle \text{live-time} \rangle$, n_{offset} , n_{pr} and τ mean the number of constant background events, production rate and neutron capture time on proton, and fitting result is shown as the dashed line $n_{\text{offset}} = 12.5 \pm 0.2 \text{ events}$, $n_{\text{pr}} = 3,024 \pm 58 \text{ events/day/kton}$ and $\tau = 212.0 \pm 2.0 \mu\text{sec}$. Fitted capture time is consistent with the MC simulation based on Am-Be calibration ($212.5 \pm 8.1 \mu\text{sec}$).

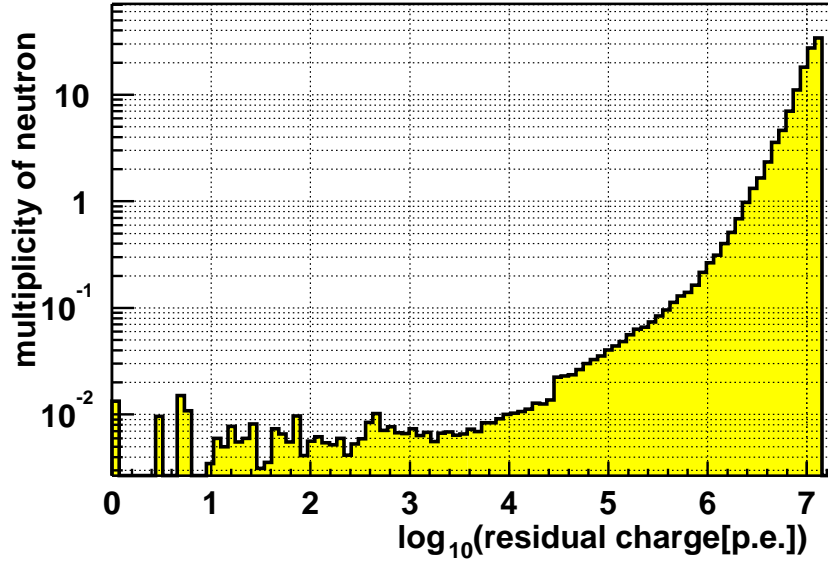


Figure 4.11: Correlation between the multiplicity of spallation neutron and the residual charge of muon events (see Section 3.8.3). Here, neutron event is selected with NsumMax information.

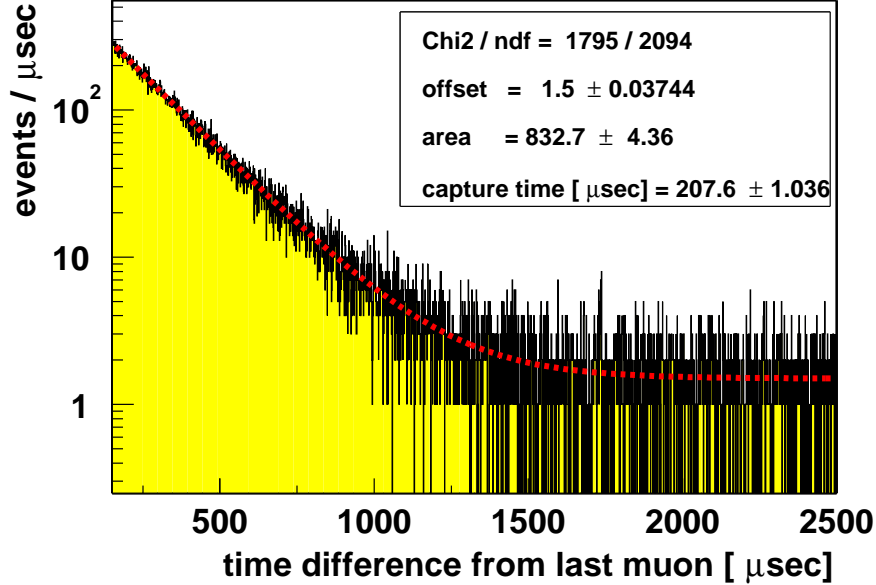


Figure 4.12: Time difference from last muon to spallation neutron capture candidates. In this figure, the residual charge of muon is less than $1,600,000 \text{ p.e.} (10^{6.2} \text{ p.e.})$ to reduce inefficiency caused by multiple neutrons and bigger than $100,000 \text{ p.e.}$ to reduce background events. The fitted capture time is $207.6 \pm 1.0 \mu\text{sec}$. This is still consistent with the prediction from the MC based on Am-Be calibration ($212.5 \pm 8.1 \mu\text{sec}$).

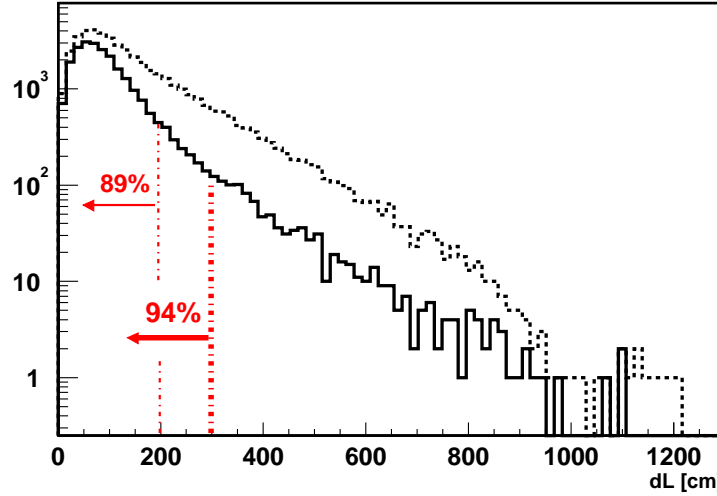


Figure 4.13: Correlation between reconstructed muon track and reconstructed vertex of spallation neutron capture events. The selection criteria are $\Delta T_{\text{muon}} \leq 2\text{msec}$, $1.8\text{MeV} \leq E \leq 2.6\text{MeV}$, the number of PMT hits is rather than the NsumMax and the fiducial radius is 5m. The “dL” means distance from the muon track to spallation neutron events. The dashed line indicates the correlation for all muon events. The solid line indicates the correlation for the non-energetic and good reconstructed muons (residual charge $< 1,000,000\text{p.e.}$, badness < 100 and total charge sum $> 40,000\text{p.e.}$). The 93.6% of spallation neutrons exists within 3m from that muon track. The track correlated spallation cut for the $\bar{\nu}_e$ detection is adopted for the non-energetic muon because the good track correlation with the vertex of spallation products is observed (see Section 4.3.3 and 4.3.4).

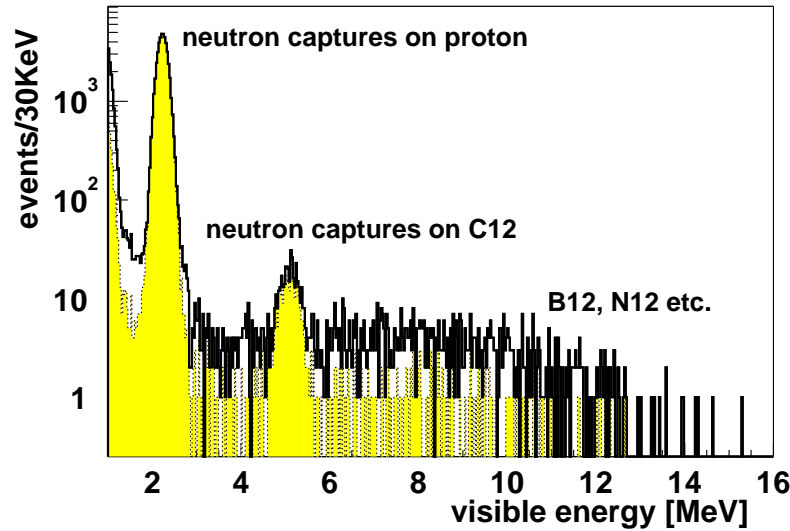


Figure 4.14: Energy spectra after muon within 2msec(dotted line and shaded area) and within 10msec(solid line) are shown, but first $150\mu\text{sec}$ was veto because of the deadtime of electronics. The good event selection cut (number of PMT hits should be rather than NsumMax) is adopted to reduce the affection of missing waveforms derived from the electronics deadtime. Thermal neutron capture on proton(γ , 2.22457MeV) and ^{12}C (γ , 4.9468) events make clear energy peak and other spallation products, ^{12}N and ^{12}B , make higher energy edge. The peak energy of capture event on ^{12}C looks slightly higher than actual energy because of the difference between visible energy scale and gamma energy scale.

4.3.2 Long life spallation products

There are nuclear spallation products as well as neutrons. Major products are summarized in Table 4.4 and 4.4 according to [40]. Neutron emitters, background for $\bar{\nu}_e$ detection, are summarized in the separate table. These products can be classified to four types;

- [A]: mean life time is less than 30 msec
- [B]: mean life time is 100~300 msec
- [C]: mean life time is about 1 sec
- [D]: very long mean life time (>10 sec)

It is easy to select [A], Figure 4.15-(a) shows time distribution after muon above 3.5MeV events within 300 msec and Figure 4.16-(a) and (c) show energy spectrum of this time window and background subtracted one. The good correlation of the track with spallation products is also observed in 4.15-(c). The production rate of ^{12}B and ^9C are evaluated from a fit with function, $\text{const.} + n_B/\tau_B \exp(-x/\tau_B) + n_C/\tau_C \exp(-x/\tau_C)$, here only ^{12}B is considered as [A] because the energy spectrum (Figure 4.16-(a) and (c)) indicates ^{12}B ($Q_{\beta^-}=13.4\text{MeV}$) is dominant. Fitted production rates are 60 ± 2 events/day/kton and 12 ± 46 events/day/kton for ^{12}B and ^9C .

Only energetic muons ($\Delta Q \geq 10^6$ p.e.) are used for the selection of longer lifetime products ([C]) because of background reduction. Time distribution and energy spectrum are also shown in Figure 4.15-(b) and Figure 4.16-(b) and (d). Supposing ^8Li is dominant in [C] because ^6He is below the energy threshold of this selection, production rates are 63 ± 2 events/day/kton and 34 ± 28 events/day/kton for ^{12}B and others ($^9\text{C} + ^8\text{Li}$). The production rates of [B] and [C] have already been measured in another experiment [40], (^8Li , ^8B , ^9C) = (5.0 ± 1.0 , 8.0 ± 1.4 , 5.5 ± 2.0) events/day/kton, and these sum is 18.5 ± 4.9 events/day/kton. The result is almost consistent with it.

Table 4.4: Spallation products (not neutron emitter)

	isotope	mean life time	energy
[A]	^{12}N	$\tau = 15.9$ msec	$Q_{EC} = 17.3$ MeV
	^{12}B	$\tau = 29.1$ msec	$Q_{\beta^-} = 13.4$ MeV
[B]	^9C	$\tau = 182.5$ msec	$Q_{\beta^+} = 16.0$ MeV
[C]	^8B	$\tau = 1.11$ sec	$Q_{\beta^+} = 13.7$ MeV
	^6He	$\tau = 1.16$ sec	$Q_{\beta^-} = 3.5$ MeV
	^8Li	$\tau = 1.21$ sec	$Q_{\beta^-} = 16.0$ MeV
[D]	^{11}Be	$\tau = 19.9$ sec	$Q_{\beta^-} = 11.5$ MeV
	^{10}C	$\tau = 27.8$ sec	$Q_{\beta^+} = 1.9$ MeV
	^{11}C	$\tau = 29.4$ min	$Q_{\beta^+} = 0.96$ MeV
	^7Be	$\tau = 76.9$ days	$Q_{EC} = 0.478$ MeV

Table 4.5: Spallation products : neutron emitter

isotope	mean life time	decay mode	energy
^8He	$\tau = 171.7$ msec	$\beta^- + ^8\text{Li}$ (84%)	$Q_{\beta^-} = 10.7$ MeV
		$\beta^- + n + ^7\text{Li}$ (16%)	
^9Li	$\tau = 257.2$ msec	$\beta^- + ^9\text{Be}$ (50%)	$Q_{\beta^-} = 13.6$ MeV
		$\beta^- + n + ^8\text{Be}$ (50%)	

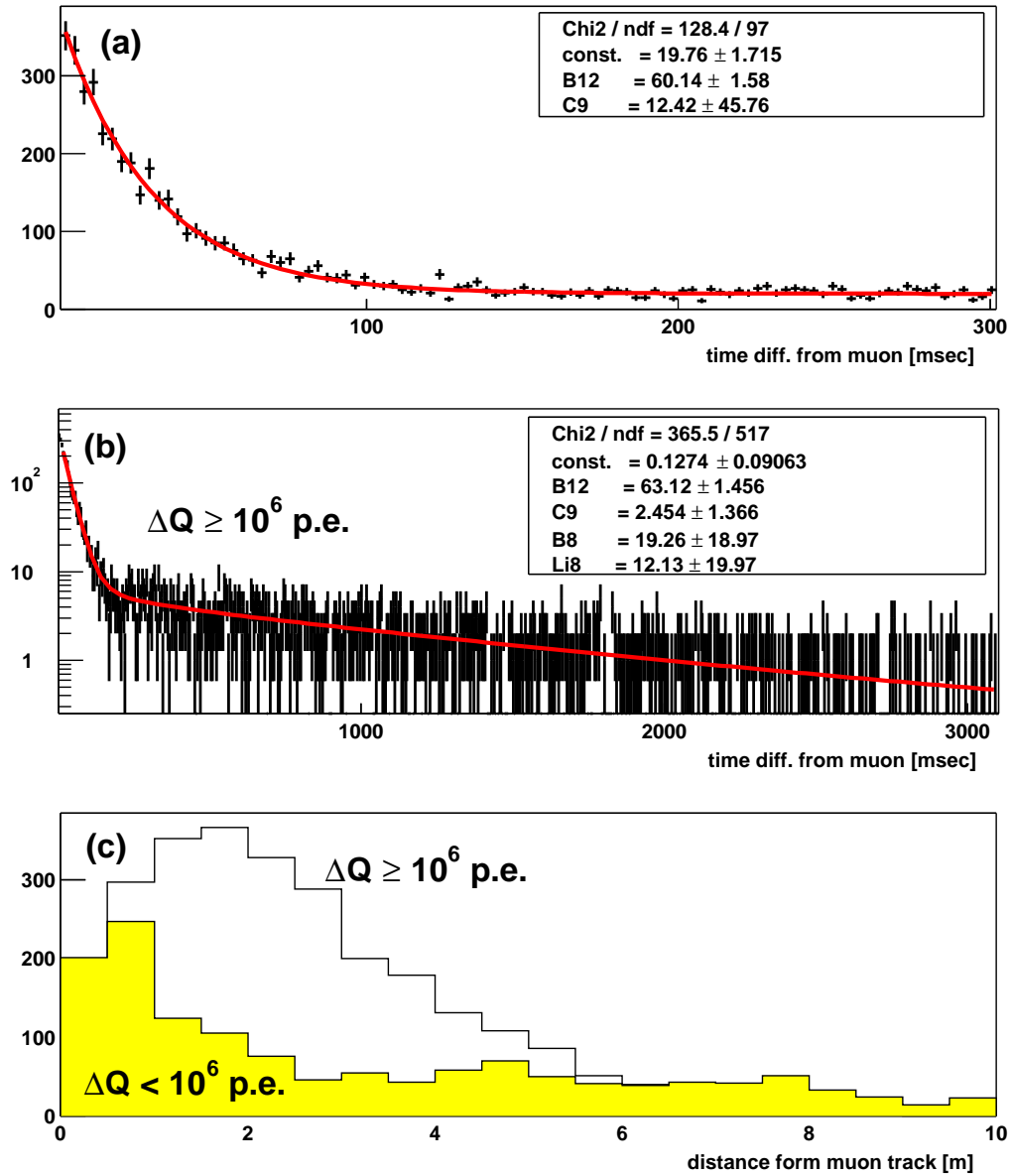


Figure 4.15: Correlations of spallation products with muons.

(a) Time distribution following muons above 3.5 MeV visible energy within 300 msec. Some events are overlapping to vanish the time structure of the muon rate. Short life spallation products like ^{12}B make the decay curve shape. Those production rate is evaluated by the fitting assuming each mean life.

(b) Time distribution following energetic muons above 3.5 MeV visible energy within 2 sec. Some events are also overlapping to vanish the time structure of the muon rate. Longer life time products are also evaluated using the same method.

(c) The correlation of reconstructed muon track and reconstructed event vertices within 100 msec following muons. Non-shaded histogram means the energetic muon case, and shaded one means the non-energetic muon case. The good correlation is also observed for the non-energetic muons as spallation neutrons.

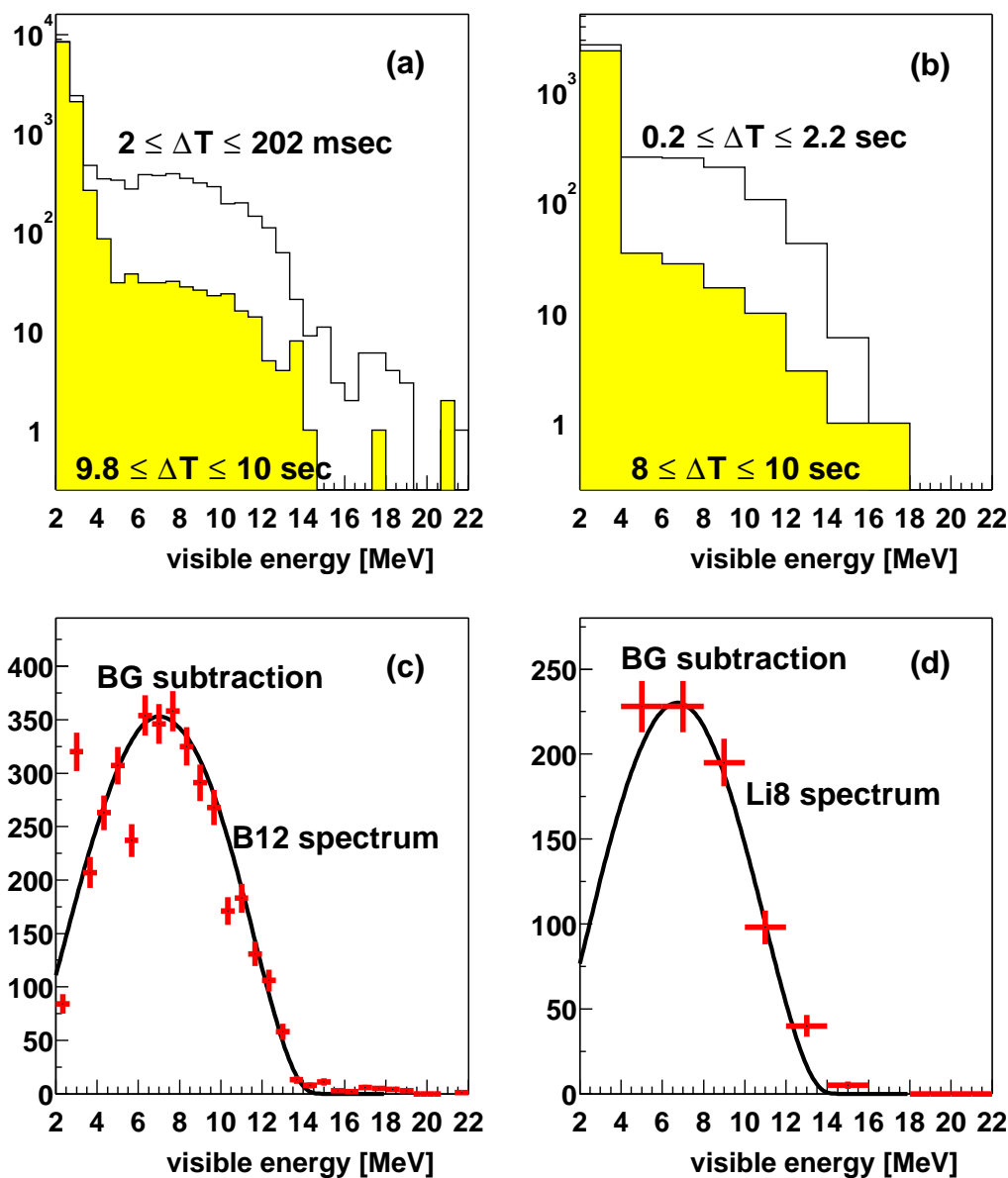


Figure 4.16: Energy spectrum of single spallation events.

(a) Energy spectrum after muons, 2msec-202msec (non-shaded) and 9.8sec-10sec (shaded). Shaded histogram indicates the background for the spallation products.

(b) Energy spectrum after energetic muons, 200msec-2.2sec (non-shaded) and 8sec-10sec (shaded). Shaded histogram also means the background spectrum for spallation products.

(c) Background subtracted energy spectrum from (a). This spectrum indicates that the ^{12}B is dominant.

(d) Background subtracted energy spectrum from (b). This spectrum indicates the ^8Li is dominant.

4.3.3 ^8He and ^9Li : neutron emitters

Nuclear spallation products are classified into single β -emitters and correlated β +neutron emitters. The former are eliminated by the delayed coincidence technique for the $\bar{\nu}_e$ event selection. But the latter creates the delayed coincidence event, the β is as the prompt event and neutron capture gamma is as the delayed event. ^8He and ^9Li are β +neutron emitters, which are selected using the delayed coincidence selection (Section 6.1),

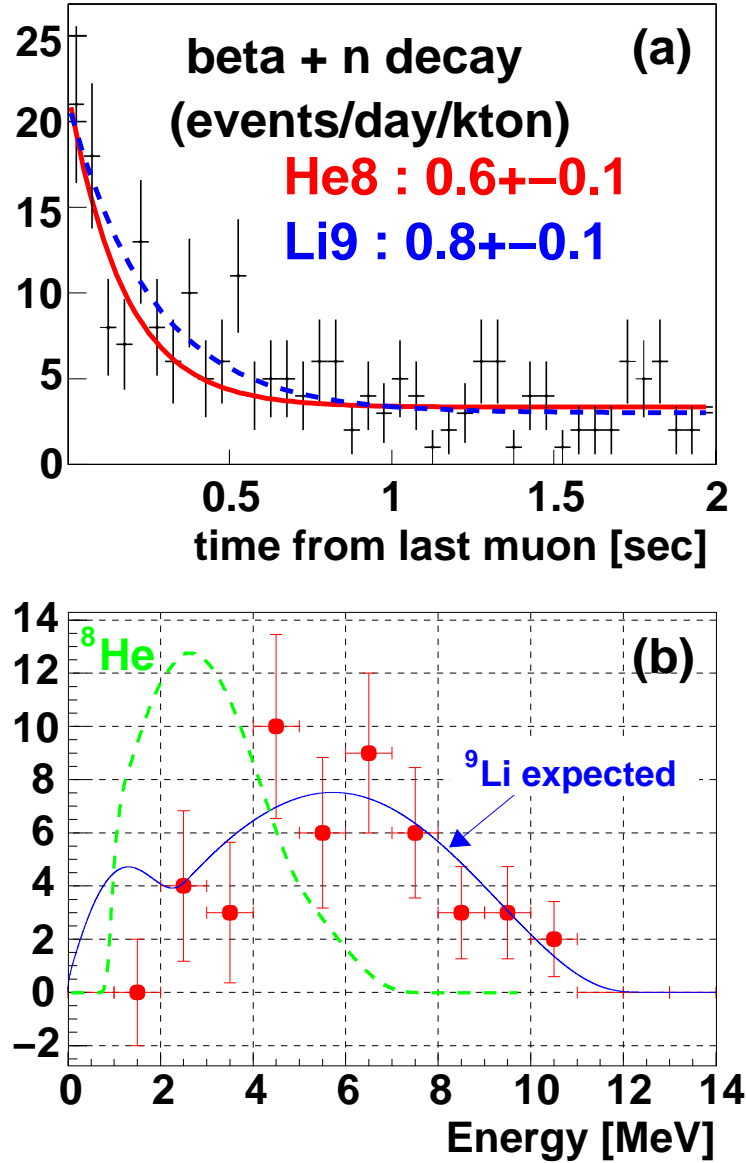


Figure 4.17: Profile of ^8He , ^9Li candidates. (a) Time correlation of ^8He , ^9Li candidate events with last muon event, some events are overlapping to vanish the time. Production rate are evaluated by supposing only one isotope, 3.8 ± 0.7 and 1.5 ± 0.2 events/day/kton for ^8He and ^9Li respectively. (b) Energy spectrum of prompt events within 500msec following energetic muon. Expected prompt energy spectra of ^8He , ^9Li are shown in dashed and solid lines. ^9Li events are favored according to the energy spectrum.

- Time correlation, $0.5 \mu\text{sec} \leq \Delta T \leq 660 \mu\text{sec}$
- Space correlation, $\Delta R \leq 1.6\text{m}$
- Delayed energy window, $1.8 \text{ MeV} \leq E_{\text{delayed}} \leq 2.6 \text{ MeV}$
- Fiducial radius, $R \leq 5 \text{ m}$
- Cylindrical cut within 1.2 m along central vertical axis (z-axis) only for the delayed events. This cut eliminates the radiation from thermometers which are deployed along z-axis.

Time correlation between these delayed coincidence events and muons are shown in Figure 4.17-(a), some events are overlapping to vanish the time structure of the muon rate. These backgrounds exist certainly. The number of ^8He is 63.3 ± 10.6 events using the exponential fitting supposing ^8He only, and the number of ^9Li events is 76.5 ± 11.9 events. These production rates are 3.8 ± 0.7 /day/kton and 1.5 ± 0.2 /day/kton for ^8He and ^9Li respectively. This is almost consistent with the predicted production rate $^8\text{He} + ^9\text{Li} = 2.4 \pm 0.5$ /day/kton from [40]. The prompt energy spectrum is also shown at (b) in the same figure. The ^9Li events are dominant, though selected events are low statistics.

For the non-energetic muons (residual charge $\Delta Q < 10^6 \text{ p.e.}$), no time correlation is observed in case the delayed event is 3 m outside from the muon track. Figure 4.18 shows time correlations between the non-energetic muons and the ^8He , ^9Li candidates whose vertex of delayed events is near or far from the muon track. The good time correlation is still observed for near the track ($\Delta L \leq 3\text{m}$). Therefore, the ^8He and ^9Li backgrounds are rejected by “Spallation Cut” which described in the following sub-section. The number of the ^9Li is 16.1 ± 14.6 events in case near the muon track. Remained number of the ^8He , ^9Li events after the spallation cut is

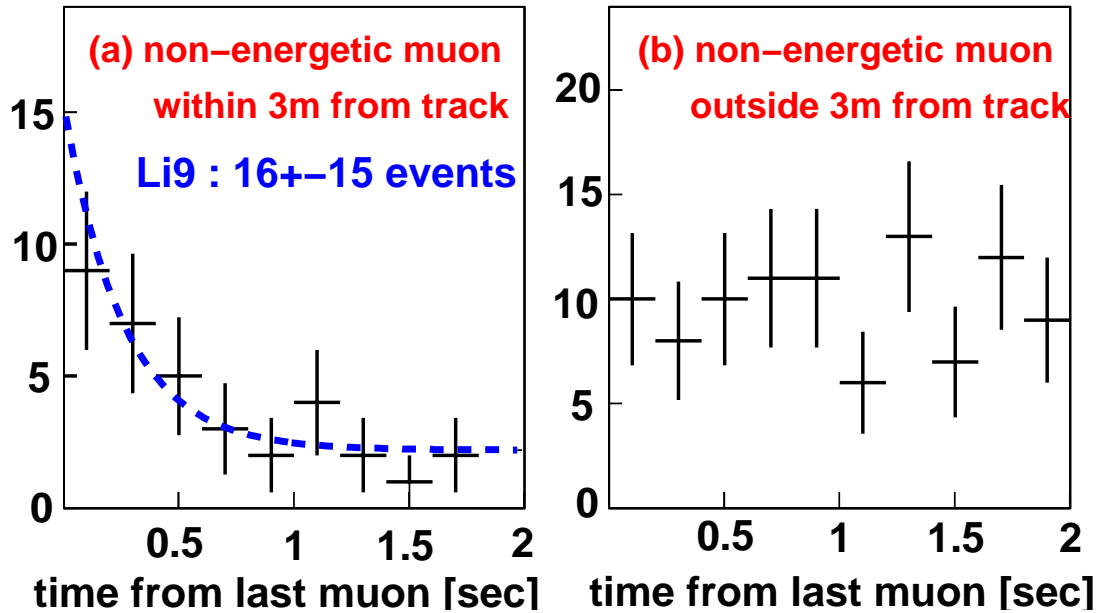


Figure 4.18: Time correlation between ^8He , ^9Li candidates between non-energetic muon. (a) The delayed events are within 3m from the muon track. (b) The delayed events are 3m outside from the muon track.

expected by using this number and the track correlation of the spallation neutron capture event (93.6% within 3m for ΔL), i.e. $(16.1 \pm 14.6 \text{ events}) \times \frac{100\% - 93.6\%}{93.6\%} = (1.1 \pm 1.0 \text{ events})$.

4.3.4 Spallation cut criteria and background estimation for $\bar{\nu}_e$ selection

The “spallation cut” to reject the spallation background is decided based on the study of spallation neutron and neutron emitters. Its criteria are as follows;

- Low charge muon ($Q \leq 40,000 \text{ p.e.}$)
Whole volume of the detector is veto for 2 msec.
The track of these muons is outside of the scintillator balloon.
- Energetic muon ($Q > 40,000 \text{ p.e.}$ & $\Delta Q \geq 10^6 \text{ p.e.}$)
Whole volume of the detector is veto for 2 sec.
- Miss reconstructed muon ($Q > 40,000 \text{ p.e.}$ & badness ≥ 100)
Whole volume of the detector is veto for 2 sec.
- Well reconstructed non-energetic muon ($Q > 40,000 \text{ p.e.}$ & badness < 100 & $\Delta Q < 10^6 \text{ p.e.}$)
Whole volume of the detector is veto for 2 msec. Veto 2 sec around around the muon track within 3 m (only for the delayed events).

The Q is the charge sum of each muon event, the ΔQ is the residual charge of each muon event ($\Delta Q = 10^6 \text{ p.e.} \sim 3 \text{ GeV}$ extra energy deposition), and the badness is the grade of muon track reconstruction.

The remained number of spallation background events is as follows;

- Neutron-neutron coincidence : negligible
This is negligible because 2 msec veto following a muon is sufficient to reject the thermal neutrons
 - ^8He and ^9Li , neutron emitters : 1.1 ± 1.0 and 0.94 ± 0.85 events for LAT and HAT data
 - energetic muon $\cdots < 0.03$ events
 $(76.5 \pm 11.9) \times \exp(-2 \text{ sec} / 257.2 \text{ msec}) \sim 0.03$
 - non-energetic muon and $\Delta L \leq 3 \text{ m} \cdots < 0.01$ events
 $(16.1 \pm 14.6) \times \exp(-2 \text{ sec} / 257.2 \text{ msec}) \sim 0.01$
 - non-energetic muon and $\Delta L > 3 \text{ m} \cdots 1.1 \pm 1.0$ events for LAT (see previous section)
- $\Rightarrow \text{LAT} : 1.1 \pm \sqrt{0.1^2 + 0.03^2 + 0.01^2} = 1.1 \pm 1.0$ events
 $\Rightarrow \text{HAT} : (1.1 \pm 1.0) \times 0.85 = 0.94 \pm 0.85$ events
 (apply the weight of ^9Li energy spectrum)

4.4 Fast Neutron

Most external fast neutrons are produced by muons which pass through both the outer detector and the surrounding rock. This background is studied by detecting delayed coincidence events which tagged with a muon which passed only in the outer detector. Decay electron (Michel electron following muon) which concentrates around the scintillator balloon edge is observed as well as the fast neutron (Figure 4.19), it can be separated with the fast neutron by cutting the short time interval cut less than $10\mu\text{sec}$. The observed mean life time of the muon is $2.03\pm0.14\mu\text{sec}$, and it is almost consistent with the precise measurement $2.197\mu\text{sec}$ [31].

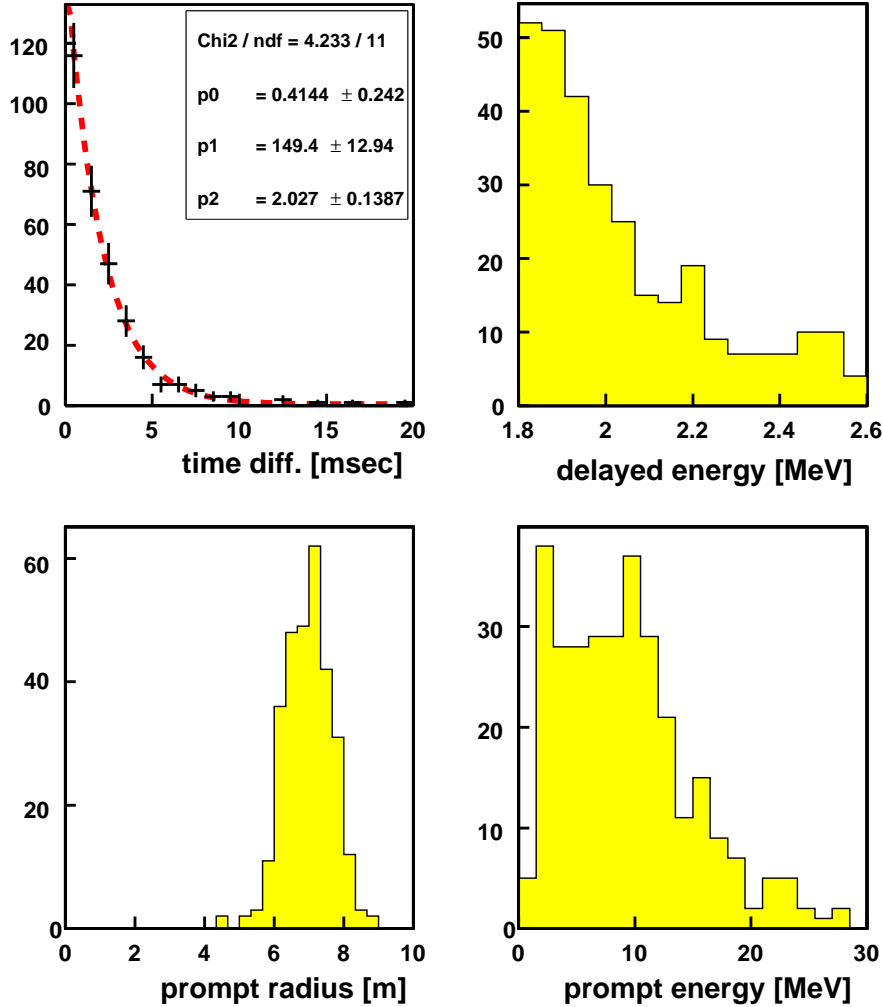


Figure 4.19: Decay electron is observed which follows the low charge (10,000 p.e.) muon. The mean lifetime of muon is $2.03\pm0.14\mu\text{sec}$, it is almost consistent with $2.197\mu\text{sec}$ from PDG [31].

The observed mean capture time of the thermal neutron is $200\pm31\mu\text{sec}$, it is also plausible. Events concentrate near the balloon edge, and there is no candidate in the 5 m fiducial radius. The $\bar{\nu}_e$ background in the fiducial volume is estimated by extrapolating the distribution of them. The attenuation length is $40\pm8\text{cm}$; 48cm (Figure 4.20). The number of events in the 5 m fiducial is estimated less than 2 events with this attenuation length. Therefore, upper limit

of background events due to fast neutrons from the outer detector is estimated by using the in-efficiency of the outer detector (8%), i.e. $2 \text{ events} \times 0.08 = 0.17 \text{ events}$. The number the surrounding rock is estimated from the MC simulation which calibrate with the measurement results of the contribution from the outer detector, neutron production rate and the shielding (attenuation) factor of the relevant materials. The MC gives also upper limit $<0.3 \text{ events}$. The total number of fast neutron background is less than 0.5 events in the entire data set.

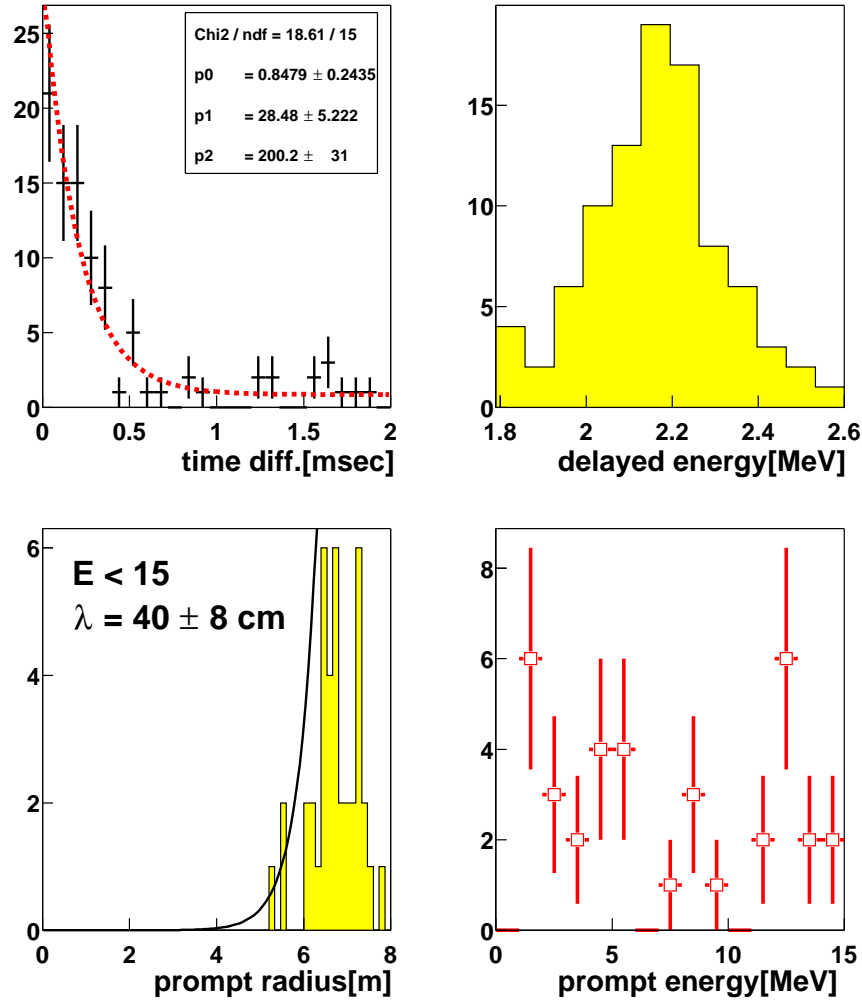


Figure 4.20: By using the delayed coincidence technique, fast neutron candidates which are almost generated in the outer detector. are observed, prompt event is supposed as recoil proton and delayed event is thermal neutron capture. There are good correlations between prompt and delayed events. Observed mean capture time is $191 \pm 26 \mu\text{sec}$, it is consistent with $212.5 \mu\text{sec}$ (Section 5.2.2). Delayed energy spectrum is good agreement with the energy of the thermal neutron capture on proton (2.22 MeV). The attenuation from outside to inside of the detector is observed for the distribution of this candidates. Its attenuation length is $40 \pm 8 \text{ cm}$ for the below 15 MeV candidates.

4.5 Accidental Coincidence for Anti-Neutrino Selection

The background from accidental coincidence is estimated with the number of events whose selection criteria is same as $\bar{\nu}_e$ selection without the time window cut. Selection criteria of $\bar{\nu}_e$ is described in section 6.2.

The fifth cut condition for $\bar{\nu}_e$ selection, the cylindrical cut along z-axis for the delayed event, is coming from the remarkable distribution of accidental coincidence events. Accidental rate is much higher than other region along z-axis, especially center and bottom as shown in Figure 4.21, 4.22, 4.23 and 4.24. The delayed signal has obvious clusters at center and along z-axis. At the $\bar{\nu}_e$ selection, the cylindrical cut within 1.2m along z-axis is adopted only for the delayed events. This cut eliminates the radiation from thermometers. The vertex distribution of the accidental background which applied this cylindrical cut is shown in Figure 4.25 and 4.26. For the prompt event, the cluster around the center is also reduced by this cut.

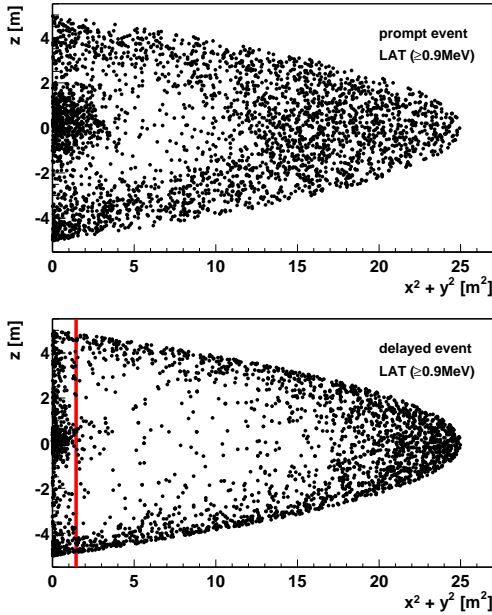


Figure 4.21: Distribution of accidental coincidence events within 5 m fiducial radius, upper figure shows for the prompt events and lower figure shows for delayed events. The analysis threshold for the prompt events is 0.9 MeV (LAT). It is high intensity around center, z-axis and edge of fiducial radius, especially for the delayed events. The solid line in the lower figure indicates the boundary of the cut around z-axis, <1.2 m.

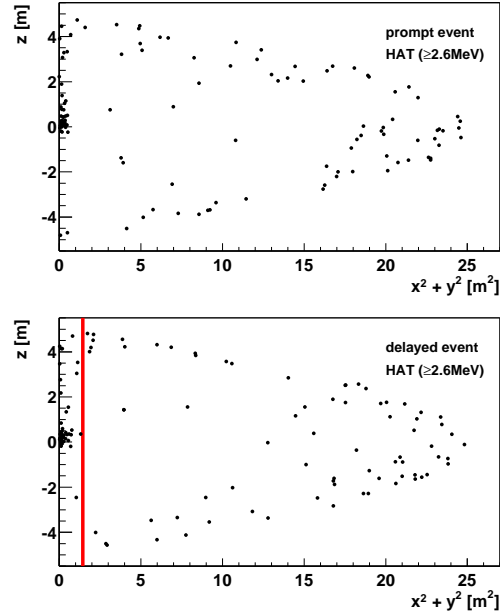


Figure 4.22: Distribution of accidental coincidence events within 5 m fiducial radius, upper figure shows for the prompt events and lower figure shows for the delayed events. The analysis threshold for the prompt events is 2.6 MeV (HAT). The center is high intensity region for both events. The solid line in the lower figure indicates the boundary of the cut around z-axis, <1.2 m.

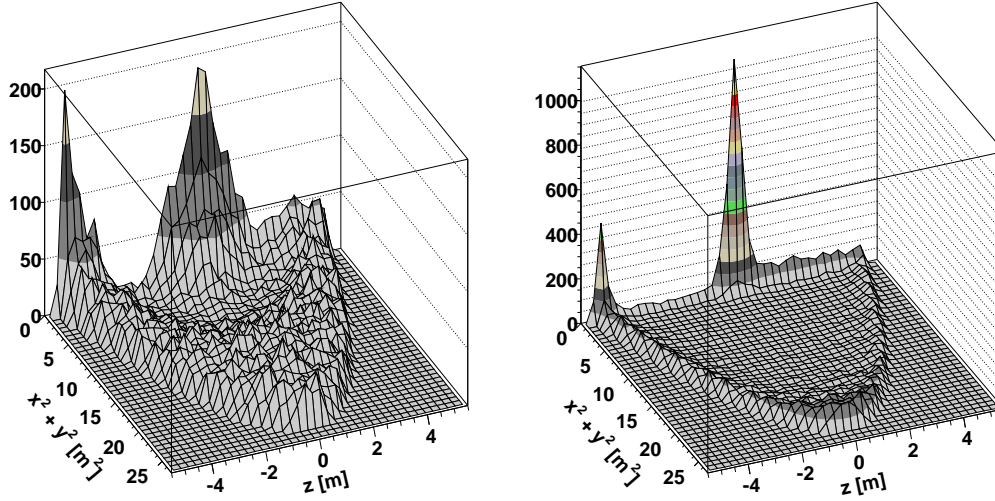


Figure 4.23: Correlation of the accidental background rate with vertex position of prompt (left side) and delayed (right side) event within the 5 m fiducial radius. The analysis threshold of the prompt events is 0.9 MeV (LAT). The accidental event rate at the center and the bottom region is much higher than other region because of radiations from a thermometer at center and a stainless steel flange at the bottom. Along central vertical axis (z-axis), the accidental background rate is higher because ^{222}Rn comes into the detector with calibration devices, or cables of the thermometers emit radiation. For the delayed events, around edge of fiducial radius is also high rate because the 2.62 MeV gamma (^{208}Tl) comes into the detector from the outside of the detector.

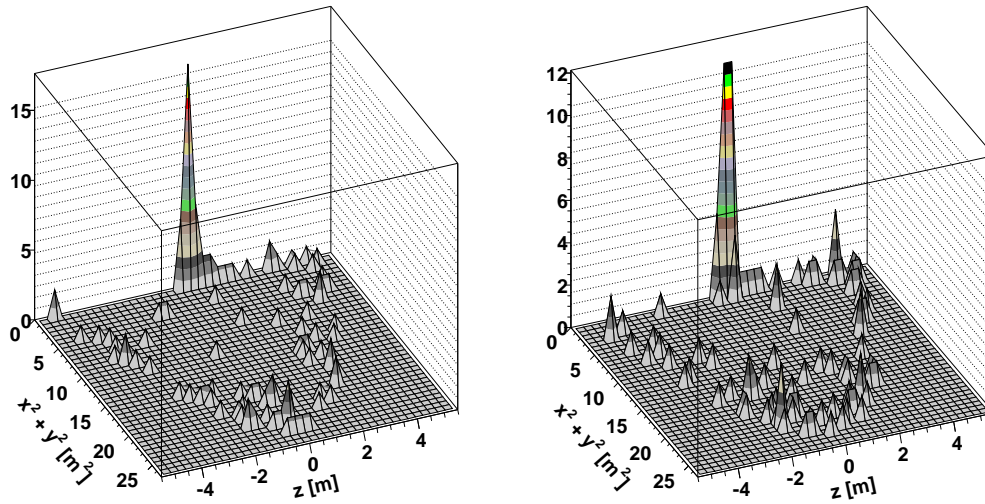


Figure 4.24: Correlation of the accidental background rate with vertex position of the prompt (left side) and the delayed (right side) events within the 5 m fiducial radius. The analysis threshold of the prompt events is 2.6 MeV (HAT). The accidental background rate at the center is much higher than other region because of radiations from a thermometer. There is almost no accidental background events except around edge of the fiducial radius and the equator.

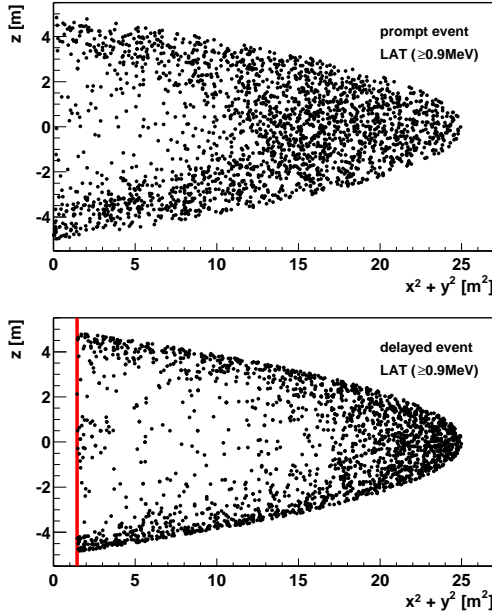


Figure 4.25: Distribution of the accidental coincidence events with the 5 m fiducial radius and with the cylindrical cut along z-axis (<1.2 m) only for delayed event. The upper figure indicates the prompt events, and the lower figure indicates the delayed events. The analysis threshold of the prompt event is 0.9 MeV (LAT). The accidental background around the center is rejected for the prompt events as well as the delayed events.

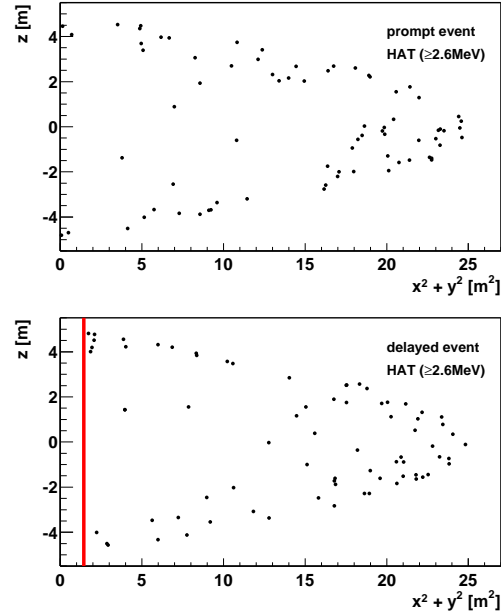


Figure 4.26: Distribution of the accidental background events with the 5 m fiducial radius with the cylindrical cut along z-axis (<1.2 m) only for delayed event. The upper figure indicates the prompt events and the lower figure indicates for the delayed events. The analysis threshold of the prompt events is 2.6 MeV (HAT). The accidental background around the center is reduced for the prompt events as well as the delayed events.

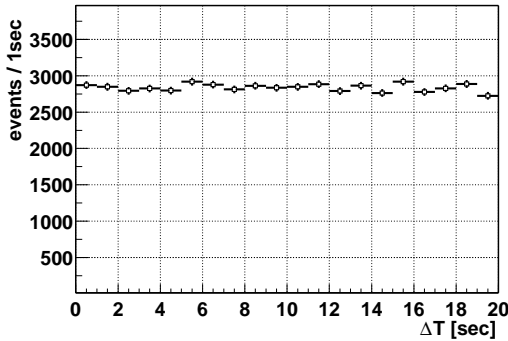


Figure 4.27: Time interval between prompt event to delayed event in accidental coincidence event. Time variation is consistent with statistical uncertainty.

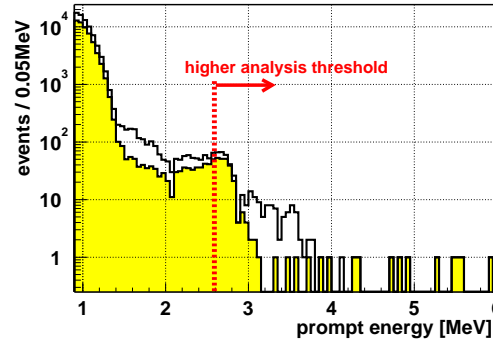


Figure 4.28: Prompt energy spectrum of the accidental background. The non-shaded histogram is not applied the cylindrical cut long z-axis within 1.2 m radius for the delayed events, and the shaded one means that it is applied. The accidental background rate is about 200 times different between 0.9 MeV analysis threshold and 2.6 MeV one.

The time distribution of the accidental background events is checked as a function of time in the off-time windows (10 msec \sim 20 sec), and also in the swap method which exchanges the treatment of the prompt and delayed events. These time distributions are fairly flat. The time spectrum of the accidental background in the off-time windows is shown in Figure 4.27. The variation at the different time window is included into the error of the accidental background rates. The prompt energy spectrum of accidental background is shown in Figure 4.28. The expected numbers are 1.81 ± 0.08 at 0.9 MeV threshold (LAT) and 0.0085 ± 0.0005 at 2.6 MeV threshold (HAT).

The accidental background rate is 2.1 (LAT) and 3.4 (HAT) times higher than it for 5 m of the fiducial radius case if the fiducial radius is expanded to 5.2 m. The distribution of accidental event also changes like Figure 4.29. The number of reactor $\bar{\nu}_e$ events is 124.40 event for LAT and 86.78 event for HAT, which is described in the latter Chapter 5. Signal/Noise ratio will be changed from $124.4/1.81 \sim 68.7$ to $124.4/1.81/2.1 \sim 32.7$ for LAT, and also change from $86.78/0.0086 \sim 10,000$ to $86.78/0.0086/3.2 \sim 3,000$ for HAT. Therefore, the 5 m fiducial radius is better than larger one to check a consistency of oscillation analysis between LAT and HAT. This is one of the strong motivation to decided the fiducial radius is 5m.

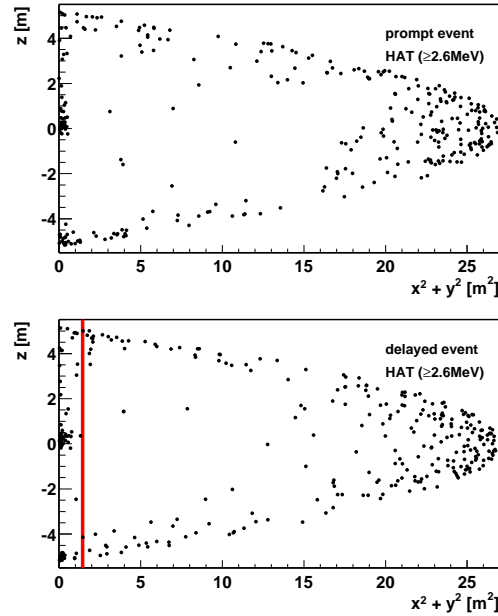


Figure 4.29: Distribution of the accidental background events within 5.2 m fiducial radius, the upper figure the distribution of the prompt events and the lower figure shows it for the delayed events. The analysis threshold of the prompt event is 2.6 MeV (HAT). The accidental background rate is higher than 5 m fiducial radius case, especially around the equator. The expected accidental background rate is 3.4 times higher than it for the 5 m fiducial radius case.

4.6 Other $\bar{\nu}_e$ sources

There are $\bar{\nu}_e$ sources except for the reactor $\bar{\nu}_e$, atmospheric $\bar{\nu}_e$, Geo $\bar{\nu}_e$ [39], relic $\bar{\nu}_e$ from the past supernovae. Observation of them are also interesting, but these are background for the the study of reactor $\bar{\nu}_e$. Almost all of them are negligible due to its energy range is higher than reactor $\bar{\nu}_e$ energy range (< 10 MeV) except for Geo $\bar{\nu}_e$ (Figure 4.30). Number of the atmospheric $\bar{\nu}_e$ events is 1.02×10^4 events by supposing the BGN flux model [41]. On the other hand, Geo $\bar{\nu}_e$ exists certainly, while nobody detected it. For example, it is expected to observe ~ 10 events below 2.49 MeV detected energy region (Table 4.1) according to the model Ia in [39]. Due to this unknown contribution, it will be classified to two types data sets for reactor $\bar{\nu}_e$ analysis, LAT (0.9 MeV analysis threshold) and HAT (2.6 MeV analysis threshold). Its contribution is less than 0.1 events for HAT data set even if the intensity of the Geo $\bar{\nu}_e$ is 40 TW.

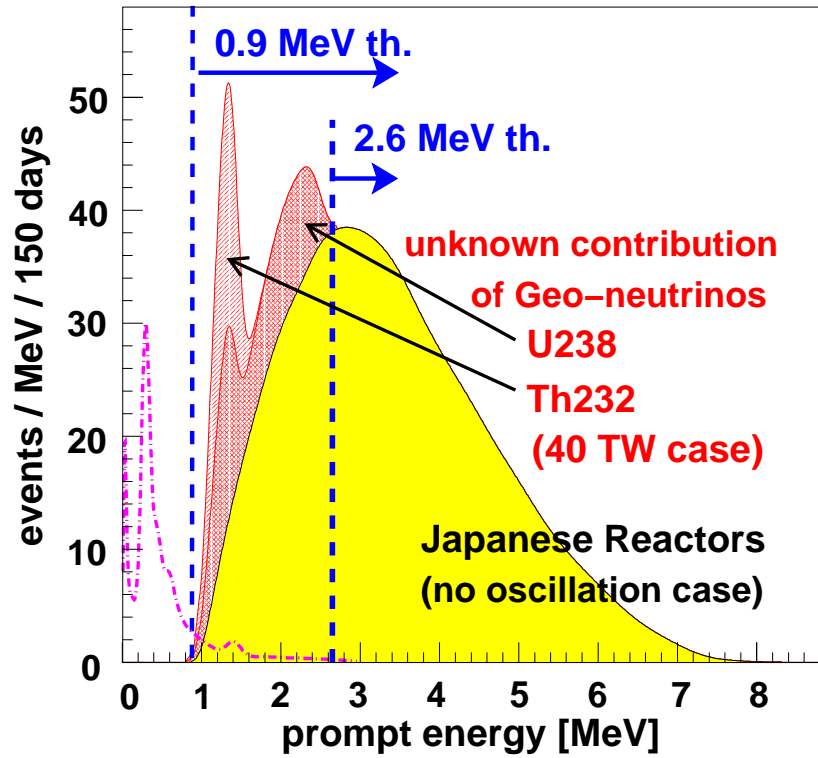


Figure 4.30: Prompt energy spectrum of reactor $\bar{\nu}_e$ (shaded area, no oscillation case) and Geo $\bar{\nu}_e$ (meshed and hatched area). In this figure, 40 TW intensity is assumed for Geo $\bar{\nu}_e$. Usually, the analysis threshold at 2.6 MeV prompt energy is addressed for the analysis of the reactor $\bar{\nu}_e$ because there is no limitation for the contribution of the Geo $\bar{\nu}_e$. The dash-dot line indicates the background spectrum from radioactive impurities in the scintillator in case ^{238}U , ^{232}Th and ^{40}K are 10^{-16} , 10^{-16} and 10^{-15} g/g respectively, but these background are negligible because the scintillator in the KamLAND is very clean as described in this chapter.

Chapter 5

Calculation of Reactor Anti-Neutrino

The calculation of expected neutrino event rate is essential for the neutrino disappearance experiment, like a KamLAND. The number of expected reactor $\bar{\nu}_e$ events is calculated by using Eq. (2.17). The number of protons is 3.46×10^{31} in 408.48 tons fiducial volume (Section 2.1.3), and Eq. (2.20) is adopted as a cross section of inverse β -decay ($10^{-43} \sim 10^{-42} \text{ cm}^2$). The reactor flux is calculable for each run (~ 24 hours) because the information of each reactor operation is given frequently, which is described in the first section. The flux is $\sim 10^{11} \bar{\nu}_e/\text{day}/\text{cm}^2$ in case of no oscillation, and the expected $\bar{\nu}_e$ event rate is roughly ~ 1 events/day/fiducial.

The detection efficiency and the livetime are also important values for this calculation. The trigger efficiency (Section 2.1.8), the probability of a thermal neutron capture on proton (Section 4.3) and the efficiency of the delayed energy window cut (Section 3.7) have been described previous sections. Calibrations for the space and time correlation efficiency of the delayed coincidence selection are described in the second section in this Chapter. The $\bar{\nu}_e$ detection efficiency is summarized in Table 5.1. At the third section, deadtime study and calculation

Table 5.1: $\bar{\nu}_e$ detection efficiency

	0.9MeV threshold (LAT)	2.6 MeV threshold (HAT)
Trigger efficiency	99.998%	—
Delayed Energy (1.8~2.6 MeV)	98.85 %	98.85 %
Space Correlation ($\Delta R \leq 160 \text{ cm}$)	83.61%	83.61%
Time Correlation ($0.5 \leq \Delta T \leq 660 \mu\text{sec}$)	95.29%	95.29%
Neutron Capture on Proton	99.48%	99.48%
Total	78.34%	78.35%

of the livetime for $\bar{\nu}_e$ detection are described. The livetime for $\bar{\nu}_e$ detection is 145.09 days of 163.80 days runtime (88.6%).

Systematic uncertainties for the reactor $\bar{\nu}_e$ detection and calculation are summarized in Table 5.2. In case of no oscillation, the expected number of $\bar{\nu}_e$ events is 86.78 ± 5.59 events above 2.6MeV prompt energy (124.40 ± 7.45 events above 0.9MeV). In the analysis of neutrino oscillations, $\bar{\nu}_e$ flux from each reactor is weighted by the survival probability at each oscillation parameter set using Eq.(1.21), and the number of $\bar{\nu}_e$ events is calculated using Eq.(2.16).

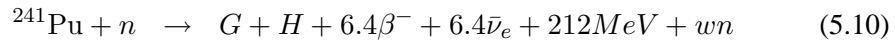
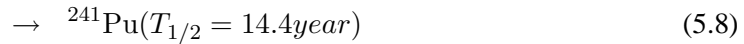
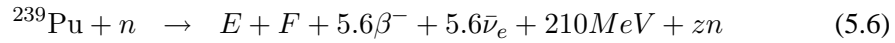
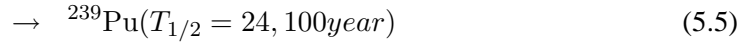
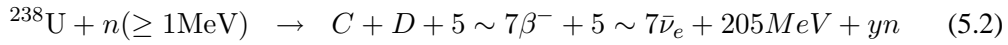
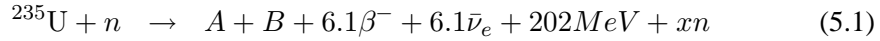
Table 5.2: Systematic uncertainties of $\bar{\nu}_e$ detection

	0.9MeV threshold (LAT)	2.6 MeV threshold (HAT)
number of target protons	<0.1%	<0.1%
cross section	0.2%	0.2%
$\bar{\nu}_e$ spectra	2.25%	2.48%
- reactor $\bar{\nu}_e$ flux -		
distance	<0.1%	<0.1%
thermal power		
Japanese reactors	2.0%	2.0%
Korean reactors	0.23%	0.23%
other reactors	0.34%	0.34%
chemical composition	<1.0%	<1.0%
time lag	0.28%	0.28%
long life nuclei	0.54%	0.0023%
- efficiencies -		
Trigger efficiency	0.002%	—
Time Correlation	0.57%	0.57%
($0.5 \leq \Delta T \leq 660 \mu\text{sec}$)	(0.54%/95.29%)	(0.54%/95.29%)
Space Correlation	2%	2%
($\Delta R \leq 1.6\text{m}$)	(1.67%/83.61%)	(1.67%/83.61%)
livetime calculation	0.069%	0.069%
- event selection (reconstruction) -		
flasher event cut	<0.01%	<0.01%
noise event cut	$< 2 \times 10^{-4}\%$	$< 2 \times 10^{-4}\%$
fiducial cut	4.58%	4.58%
analysis energy threshold	—	2.13%
Total	6.00%	6.43%

5.1 Calculation of Reactor $\bar{\nu}_e$ Flux

There are many nuclear reactors in Japan and Korea, and total thermal power of them is about 150 GW. Many of them are Boiling Water Reactor (BWR) or Pressurized Water Reactor (PWR), and there are two extra types for the study of Plutonium rich reactor, Advanced Thermal Reactor (ATR) and Fast Breeder Reactor (FBR). PWR and BWR are using enriched Uranium, which contains 3~4 % higher concentration ^{235}U , while the natural Uranium consists of 99.3 % of ^{238}U . Reactors in Japan and Korea are summarized in Table 5.4 and 5.5. Systematic error of the distance is addressed <0.1 % because its uncertainty is less than 70 m for Japanese reactors and about 1 km for Korean reactors. Figure 5.1 and 5.2 show the nuclear power stations in Asia and in the world.

Nuclear fission creates neutron rich isotopes and it converts to more stable isotope via β -decay, the anti-neutrino ($\bar{\nu}_e$) is emitted at this β -decay. The first fission is caused by the spontaneous fission of ^{238}U ($4.468 \times 10^9\text{y}$, $5.45 \times 10^{-5}\%$) or cosmic ray muon spallation and so on. The emitted neutrons cause nuclear fission or capture processes as follows,



The anti-neutrino flux is calculated with the fission rate of each isotope and $\bar{\nu}_e$ spectrum for each fission (Figure 5.3). Spectrum uncertainty for each isotope is shown in Figure 5.4. These spectra and uncertainties are coming from [42], [43] and [44], and the overall spectrum has been checked within 1.4 % accuracy by previous short-baseline reactor $\bar{\nu}_e$ experiment [45]. The uncertainties for the number of reactor $\bar{\nu}_e$ derived from this spectrum uncertainty are 2.25% and 2.48% for LAT (0.9MeV analysis threshold) and HAT (2.6MeV analysis threshold) in case of no oscillation.

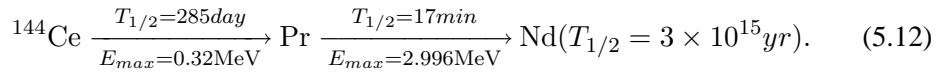
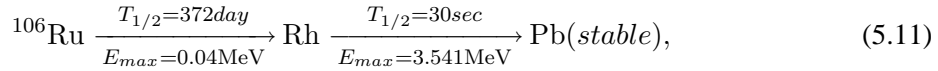
During a power cycle, the fuel's composition changes as Plutonium isotopes are bred and Uranium is depleted (burn-up effect). It causes variation of $\bar{\nu}_e$ production rate from each Isotope, and actual time variation of the energy spectrum of $\bar{\nu}_e$ flux is typically 4% to 10%. The total fission rates of each isotope in the core is therefore a function of both thermal power of the reactor and the total burn-up of the fuel in the core. The ideal way to know the composition is detailed simulation calculation of all reactor cores, where the accuracy of the detail calculation is checked less than 1% [46]. But, it is practically impossible with limited time. Therefore, simple modeling of burn-up is essential to know the flux variation from the time evolution of the chemical composition, and this model is constructed with some parameters;

- fraction of new fuel
- initial ^{235}U concentration of the fuel
- integrated thermal output
- current thermal output

This simple parameterization method is developed by Tokyo Electric Power Company (TEPCO). This method reproduces detailed calculation with 0.5% accuracy for all the existence fuel types except for very long term operation more than 2 years. Its accuracy is less than 1% even if the reactor operation term is 2 years, though there is no such a long term operation in Japanese reactors currently. Above information from each reactor is provided every hour in case of the starting or stopping, while it is provided every week usually (Figure 5.5 and 5.6). It's sufficient interval. By the way, ^{242}Pu , which doesn't emits $\bar{\nu}_e$, contributes for the thermal energy, but it is included in the 1% uncertainty, while its contribution is only $0.01 \sim 0.1\%$ actually. Therefore, uncertainty of the chemical composition for fission is addressed $<1\%$. Averaged over the present livetime period, the relative fission yields are $^{235}\text{U} : ^{238}\text{U} : ^{239}\text{Pu} : ^{241}\text{Pu} = 0.568 : 0.078 : 0.297 : 0.057$.

The systematic error assigned to the thermal power is conservatively taken as 2% from the regulatory specification for safe reactor operation ¹. The contribution ratio from all reactors is summarized in Table 5.3. The contribution from Korean reactors is estimated to be $2.29 \pm 0.23\%$ based on reported electric power generation. The 0.23% uncertainty is given as the 10% of contribution, which is the conversion error from electric power to thermal power. The contribution from other reactor is $0.68 \pm 0.34\%$ from an estimate using reactor specifications from the International Nuclear Safety Center (<http://www.insc.anl.gov/>). Its systematic error is addressed as a half of it.

The finite β -decay lifetimes of fission products introduce an additional uncertainty of 0.28% to the $\bar{\nu}_e$ flux, this is estimated from the difference of the total $\bar{\nu}_e$ yield associated with shifting the run time by one day. Another time-lag effect comes from long-lifetime beta-decay nuclei, such as ^{106}Ru and ^{144}Ce [47],



This contribution is calculated to be $0.68 \pm 0.34\%$ and $0.043 \pm 0.022\%$ for the LAT (0.9MeV

Table 5.3: Contribution of thermal flux to KamLAND

Site	thermal flux [MW/cm^2]	contribution ratio [%]
Japan	2.387×10^{-11}	97.03
Korea	5.640×10^{-13}	2.29
Japanese Research	2.500×10^{-11}	0.10
Europe	6.298×10^{-14}	0.26
Taiwan	2.916×10^{-14}	0.12
North America	2.894×10^{-14}	0.12
China	1.676×10^{-14}	6.8×10^{-2}
India	1.761×10^{-15}	7.2×10^{-3}
Africa	3.369×10^{-16}	1.4×10^{-3}
Pakistan	3.106×10^{-16}	1.3×10^{-3}
South America	2.428×10^{-16}	1.0×10^{-3}

¹From the private communication with the electricity company

analysis threshold) and HAT (2.6MeV analysis threshold) data sets, where 50% error to the contribution at equilibrium is assigned. Its energy spectrum of $\bar{\nu}_e$ is observed in Figure 5.7.

Table 5.4: Japanes and Korean reactors - part 1 -

company	reactor name	distance [Km]	type	thermal power [MW]	electricity [MW]
Chubu	Hamaoka-1	213.62	BWR	1593	540
	Hamaoka-2	213.70	BWR	2436	840
	Hamaoka-3	213.90	BWR	3293	1100
	Hamaoka-4	214.04	BWR	3293	1137
Chugoku	Shimane-1	401.07	BWR	1380	460
	Shimane-2	401.21	BWR	2436	820
Genden	Tokai2	295.36	BWR	3293	1100
	Tsuruga-1	138.43	BWR	1064	357
	Tsuruga-2	138.44	PWR	3423	1160
Hokkaido	Tomari-1	783.13	PWR	1650	579
	Tomari-2	783.02	PWR	1650	579
Hokuriku	Shika-1	87.77	BWR	1593	540
JapanNuclearCycle	Fugen	138.46	ATR	557	165
	Monju	141.46	FBR	714	280
Kansai	Mihama-1	145.67	PWR	1031	340
	Mihama-2	145.72	PWR	1456	500
	Mihama-3	145.78	PWR	2440	826
	Oh-1	178.70	PWR	3423	1175
	Oh-2	178.78	PWR	3423	1175
	Oh-3	178.99	PWR	3423	1180
	Oh-4	179.11	PWR	3423	1180
	Takahama-1	191.20	PWR	2440	826
	Takahama-2	191.23	PWR	2440	826
	Takahama-3	191.64	PWR	2660	870
	Takahama-4	191.67	PWR	2660	870
Kyusyu	Genkai-1	754.37	PWR	1650	559
	Genkai-2	754.48	PWR	1650	559
	Genkai-3	754.60	PWR	3423	1180
	Genkai-4	754.71	PWR	3423	1180
	Sendai-1	830.33	PWR	2660	890
	Sendai-2	830.25	PWR	2660	890
Shikoku	Ikata-1	560.74	PWR	1650	566
	Ikata-2	560.80	PWR	1650	566
	Ikata-3	560.66	PWR	2660	890
Tohoku	Onagawa-1	430.52	BWR	1593	524
	Onagawa-2	430.65	BWR	2436	825
	Onagawa-3	430.55	BWR	2436	825

Table 5.5: Japanes and Korean reactors - part 2 -

company	reactor name	distance [Km]	type	thermal power [MW]	electricity [MW]
Tokyo	Fukushima1-1	349.45	BWR	1380	460
	Fukushima1-2	349.40	BWR	2381	784
	Fukushima1-3	349.36	BWR	2381	784
	Fukushima1-4	349.32	BWR	2381	784
	Fukushima1-5	349.58	BWR	2381	784
	Fukushima1-6	349.61	BWR	3293	1100
	Fukushima2-1	345.36	BWR	3293	1100
	Fukushima2-2	345.42	BWR	3293	1100
	Fukushima2-3	345.46	BWR	3293	1100
	Fukushima2-4	345.49	BWR	3293	1100
	KashiwazakiKariwa-1	159.17	BWR	3293	1100
	KashiwazakiKariwa-2	159.29	BWR	3293	1100
	KashiwazakiKariwa-3	159.40	BWR	3293	1100
	KashiwazakiKariwa-4	159.60	BWR	3293	1100
	KashiwazakiKariwa-5	160.68	BWR	3293	1100
	KashiwazakiKariwa-6	160.58	BWR	3926	1356
	KashiwazakiKariwa-7	160.46	BWR	3926	1356
KHNP	Kori-1	734.52	PWR	1727	587
	Kori-2	734.52	PWR	1913	650
	Kori-3	734.52	PWR	2796	950
	Kori-4	734.52	PWR	2796	950
	Ulchin-1	711.81	PWR	2796	950
	Ulchin-2	711.81	PWR	2796	950
	Ulchin-3	711.81	PWR	2943	1000
	Ulchin-4	711.81	PWR	2943	1000
	Wolsong-1	708.58	PWR	1995	678
	Wolsong-2	708.58	PWR	2060	700
	Wolsong-3	708.58	PWR	2060	700
	Wolsong-4	708.58	PWR	2060	700
	Yonggwang-1	986.41	PWR	2796	950
	Yonggwang-2	986.41	PWR	2796	950
	Yonggwang-3	986.41	PWR	2943	1000
	Yonggwang-4	986.41	PWR	2943	1000
	Yonggwang-5	986.41	PWR	2943	1000

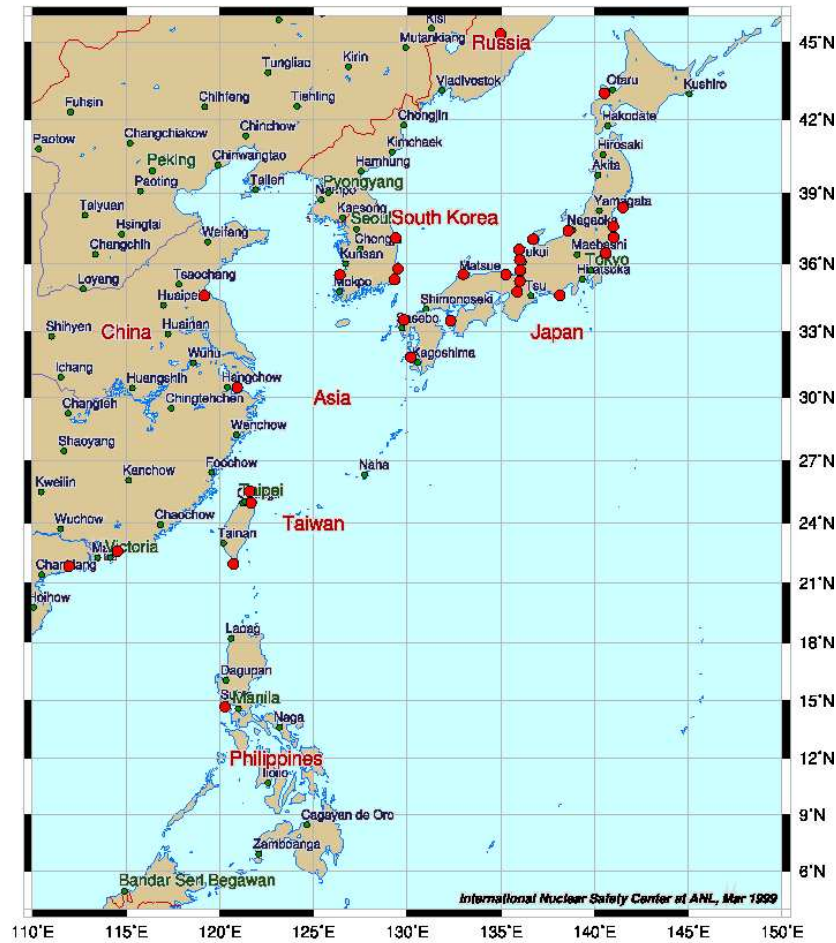


Figure 5.1: Nuclear power stations in Asia.

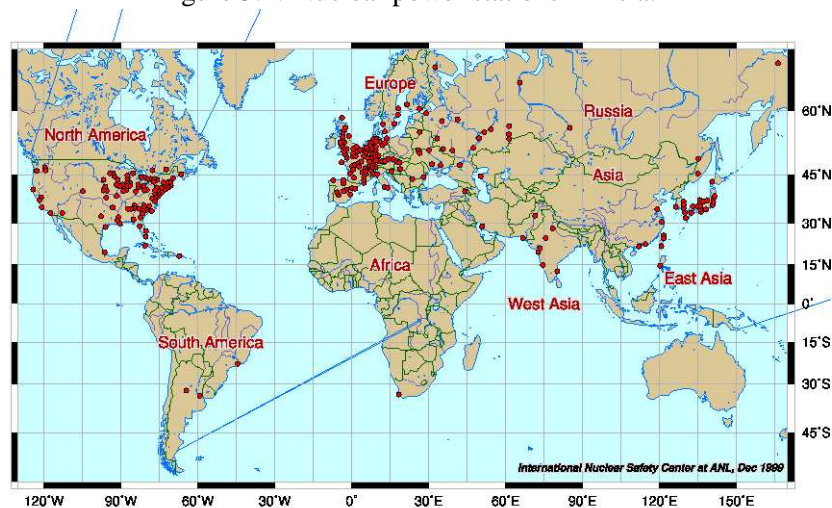


Figure 5.2: Nuclear power stations in the world.

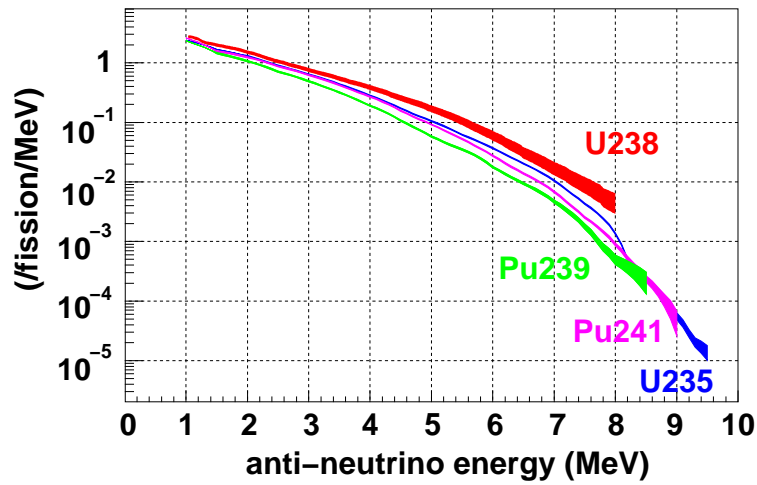


Figure 5.3: Energy spectra of $\bar{\nu}_e$ flux from nuclear fissions, ^{235}U , ^{238}U , ^{239}Pu and ^{241}Pu [42], [43], [44]. Overall spectrum is checked within 1.4 % accuracy by Bugey experiment [45].

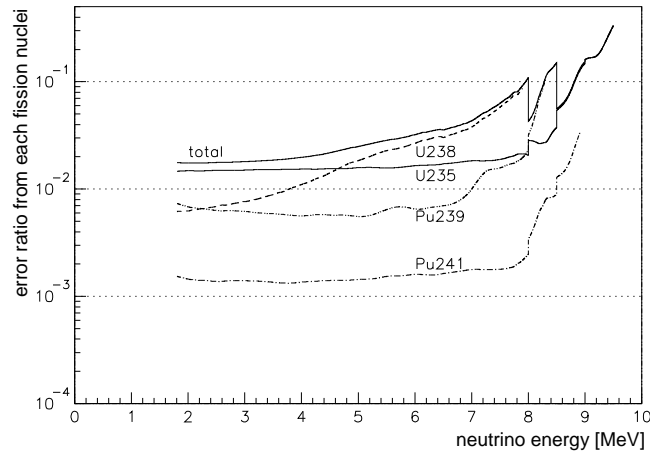


Figure 5.4: Uncertainty of neutrino energy spectrum for no oscillation case. The uncertainties of number of reactor $\bar{\nu}_e$ derived from this spectrum uncertainty are 2.48% for 2.6 MeV analysis threshold (2.25% for 0.9 MeV analysis threshold) in case of no oscillation.

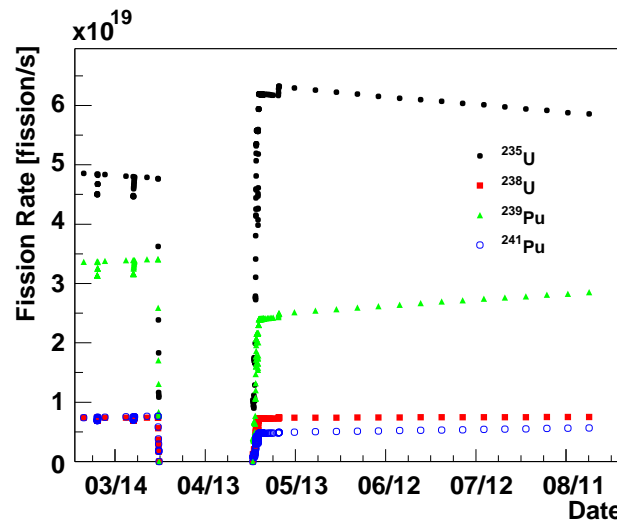


Figure 5.5: Fission rate of each isotopes, ^{235}U , ^{238}U , ^{239}Pu and ^{241}Pu , at one reactor.

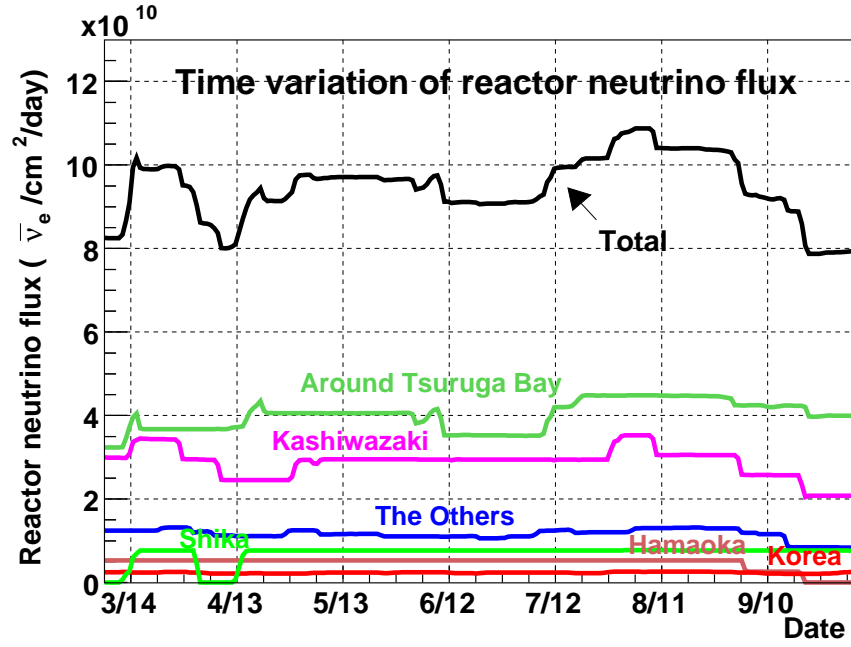


Figure 5.6: Time variation of $\bar{\nu}_e$ flux from reactors. The frequent information from each reactor provides 2.3 % accuracy for the intensity of reactor $\bar{\nu}_e$ flux for 2.6 MeV analysis threshold (2.4 % for 0.9 MeV analysis threshold).

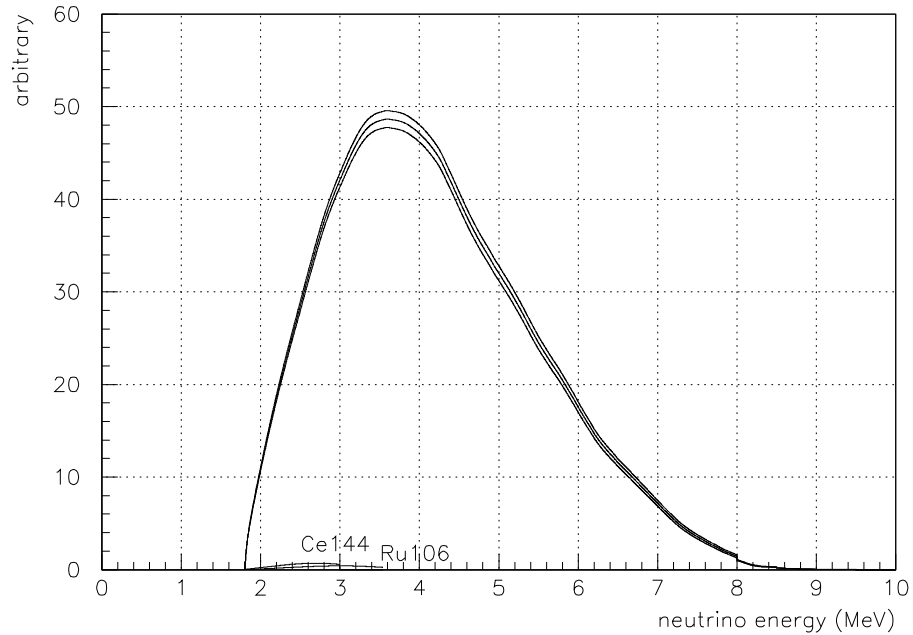


Figure 5.7: $\bar{\nu}_e$ energy spectra from long life nuclei (Ce144, Ru106) and general reactor $\bar{\nu}_e$ spectrum for no oscillation case. The band around reactor $\bar{\nu}_e$ spectrum means uncertainty of this spectrum. The contribution of long life nuclei is negligible for 2.6 MeV analysis threshold 0.043 ± 0.022 %, while 0.68 ± 0.34 % contribution for 0.9 MeV threshold case.

5.2 Calibration for the Delayed Coincidence

The $\bar{\nu}_e$ is detected via inverse β -decay, and it makes correlated double events, i.e. delayed-coincidence event. The delayed event is the single γ -ray event from neutron capture on nuclei, proton and ^{12}C and others, while only proton captured gamma event is analyzed in this thesis (Table 2.7).

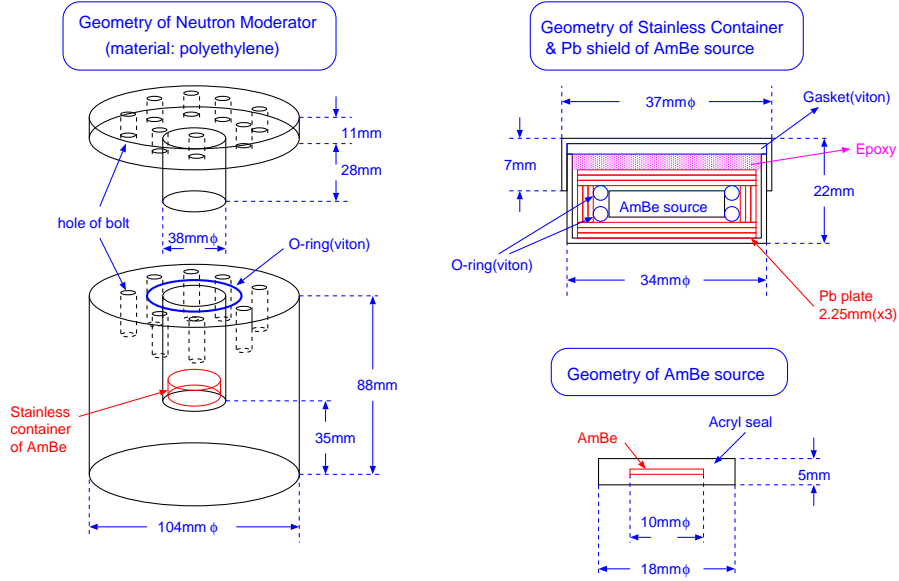


Figure 5.8: Geometry of Am-Be source moderator.

5.2.1 Comparison of Am-Be source calibration and MC simulation

Efficiencies of the time and space correlations are calibrated with Am-Be (neutron emission source), and it is compared with Monte Carlo (MC) simulation based on Geant4 [48]. Inside of the Am-Be source, the α particle is emitted from Am and it interacts with ^9Be and various γ and neutron are emitted,



Three states of $^{12}\text{C}^*$, i.e. 4.438, 7.653 MeV of the single gamma peak [49] and 9 MeV of the multi gamma peak [50] are observed in Figure 5.9. The neutron capture gamma on proton (2.22457 MeV) is also observed. The kinetic energy of the neutron is much higher than recoil neutron in the inverse β -decay (~ 10 KeV). These energy are 3 \sim 7 MeV for the 4.438MeV ^{12}C state and 1 \sim 3 MeV for the 7.653MeV state [49], and recoil proton by the neutron is observed as same event of γ -rays. The Am-Be source is packed in the polyethylene moderator to stop the recoil proton because the primary purpose of Am-Be calibration is the energy calibration for higher energy range with various γ -rays. The geometry of the moderator is 10 cm diameter and 10 cm height cylinder which is drawn in Figure 5.8. The difference between the calibration with the moderator and without it is estimated by using the MC simulation. The MC simulation predicts that the shadow of the moderator and loss of the energy in the moderator decrease visible energy (actually, number of photons) about 2.6, 1.4, 0.8 and 1.6% for the neutron capture, 4.438MeV, 7.653MeV and 9MeV levels respectively. Thus, peaks in Figure 5.9 correspond to 2.22, 4.66, 8.034 and 9.42MeV visible energy for each process, though measured peaks are 2.16, 4.60, 7.97 and 9.27MeV. The recoil proton contributes for 4.438MeV γ peak and it looks broad shape.

5.2.2 Calibration for the time correlation

The MC also predicts that the thermal neutron capture time is shorter than the without moderator case, this difference is coming from the difference of the proton density between the moderator and the scintillator. The time interval from prompt 4.43MeV γ event to neutron capture event is shown in Figure 5.10-(b), the selection criteria are 4~5.5MeV energy window cut for the prompt event and 1.5~2.6 MeV for the delayed event. The neutron capture time in Am-Be source calibration (τ_{AmBe}) is $189.5 \pm 2.5 \mu\text{sec}$ (Figure 5.10-(d)). On the other hand, Figure 5.10-(a) shows the time interval between the generated time of the neutron (6MeV) and the captured time in the MC simulation with the moderator. The capture time from the MC (τ_{mc}) is $194.2 \pm 1.0 \mu\text{sec}$ with the moderator (Figure 5.10-(c)). It is $212.5 \mu\text{sec}$ without moderator and 10KeV kinetic energy neutron case. Moreover, the correlation of the capture time with the kinetic energy is less than $1 \mu\text{sec}$ (Figure 5.11). Thus, the systematic error of the capture time is addressed with a sum of the difference between the MC and the measurement and the quadratic sum of each error for each evaluation,

$$\delta\tau(\text{moderator} - \text{geometry}) = |194.2 - 189.5| + \sqrt{1.0^2 + 2.5^2} \quad (5.14)$$

$$= 7.4\mu\text{sec}. \quad (5.15)$$

This should be scaled for no moderator case,

$$\tau \pm \delta\tau = 212.5 \pm (7.4 \times 212.5/194.2) \quad (5.16)$$

$$= 212.5 \pm 8.1\mu\text{sec}. \quad (5.17)$$

This is consistent with the value of the spallation neutron study (Section 4.3.1). Therefore, efficiency of the time correlation (0.5~660 μsec) is;

$$(\text{Efficiency of Time Correlation}) = \frac{1}{\tau} \int_{0.5\mu\text{sec}}^{660\mu\text{sec}} \exp(-\frac{t}{\tau}) dt \quad (5.18)$$

$$= 95.29 \pm 0.54\%. \quad (5.19)$$

5.2.3 Calibration for the space correlation

Diffusion of the delayed event can be also simulated with the MC. The diffusion of the neutron is simulated in 1, 10, 100KeV and 1MeV kinetic energy (Figure 5.11). And, diffusions of positron and γ -rays are also simulated as shown in Figure 5.12. Assuming the vertex resolution 25cm which derived from source calibration with ^{60}Co , the delayed γ event within 1.6m from the interaction point is 98.83%. This is consistent with the measurement results of the Am-Be calibration $98.79 \pm 0.06\%$ (Figure 5.13). Under $\bar{\nu}_e$ selection criteria, the fiducial radius ≤ 5 m, the cylindrical cut 1.2 m radius for the delayed event along z-axis and space correlation 1.6 m (Section 6.2), the efficiency of the space correlation is 83.61% using the MC diffusion data, while it is 1.67% smaller when the diffusion of the Am-Be calibration is used. The space correlation efficiency based on the MC is adopted for the reactor $\bar{\nu}_e$ calculation because the vertex reconstruction bias caused by the moderator shadow have not been estimated well, but its difference is addressed as the systematic error.

$$(\text{Efficiency of Space Correlation}) = 83.61 \pm 1.67\%$$

Moreover, the space correlation efficiency is consistent with 2% even if the vertex resolution is 10 cm better or worse.

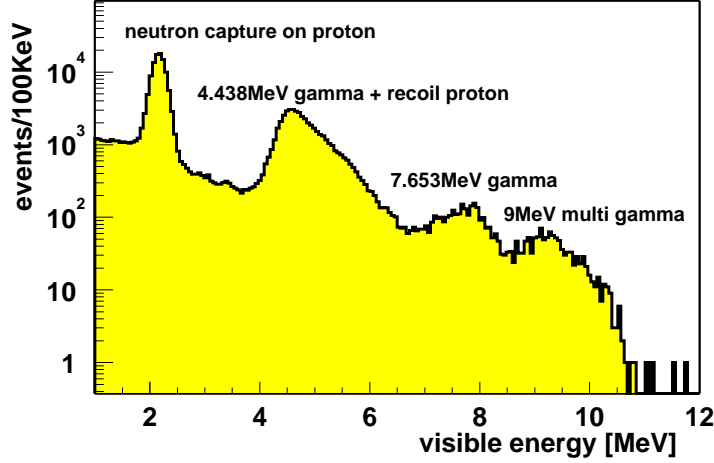


Figure 5.9: This is the visible energy spectrum of Am-Be calibration source. Three states of $^{12}\text{C}^*$, i.e. 4.438, 7.653 MeV single gamma peak [49] and 9 MeV multi gamma peak [50] are observed in Figure 5.9, and the neutron capture gamma on proton (2.22457 MeV) is also observed. The recoil proton contributes for 4.438MeV γ state. The MC simulation predicts that the shadow of the moderator and energy loss in the moderator decrease visible energy (actually, number of photons) about 2.6, 1.4, 0.8 and 1.6% for the neutron capture, 4.438MeV, 7.653MeV and 9MeV levels respectively. Observed peak values are 2.16, 4.60, 7.97 and 9.27MeV visible energy for each process, but these correspond to be 2.22, 4.66, 8.034 and 9.42MeV visible energy.

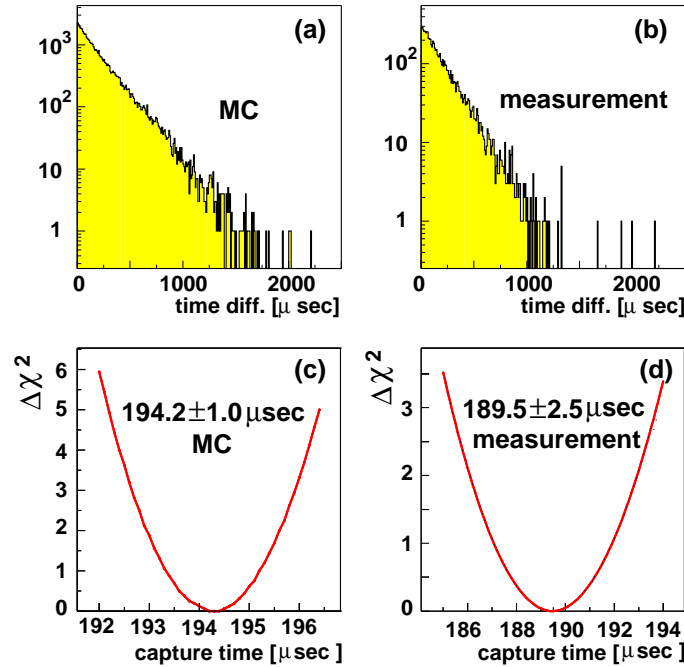


Figure 5.10: Time distribution of the neutron capture on proton and mean capture time in the MC and the Am-Be calibration. (a) Expected time distribution by the MC with moderator geometry. (b) Measured time difference from the prompt event (4 ~ 5.5 MeV for visible energy) to the delayed event (1.5 ~ 2.6 MeV for visible energy). (c) Evaluation of capture time for the MC data using maximum likelihood method: $\tau_{\text{capture}} = 194.2 \pm 1.0 \mu\text{sec}$. (d) Evaluation of capture time for the Am-Be calibration data using maximum likelihood method; $\tau_{\text{capture}} = 189.5 \pm 2.5 \mu\text{sec}$.

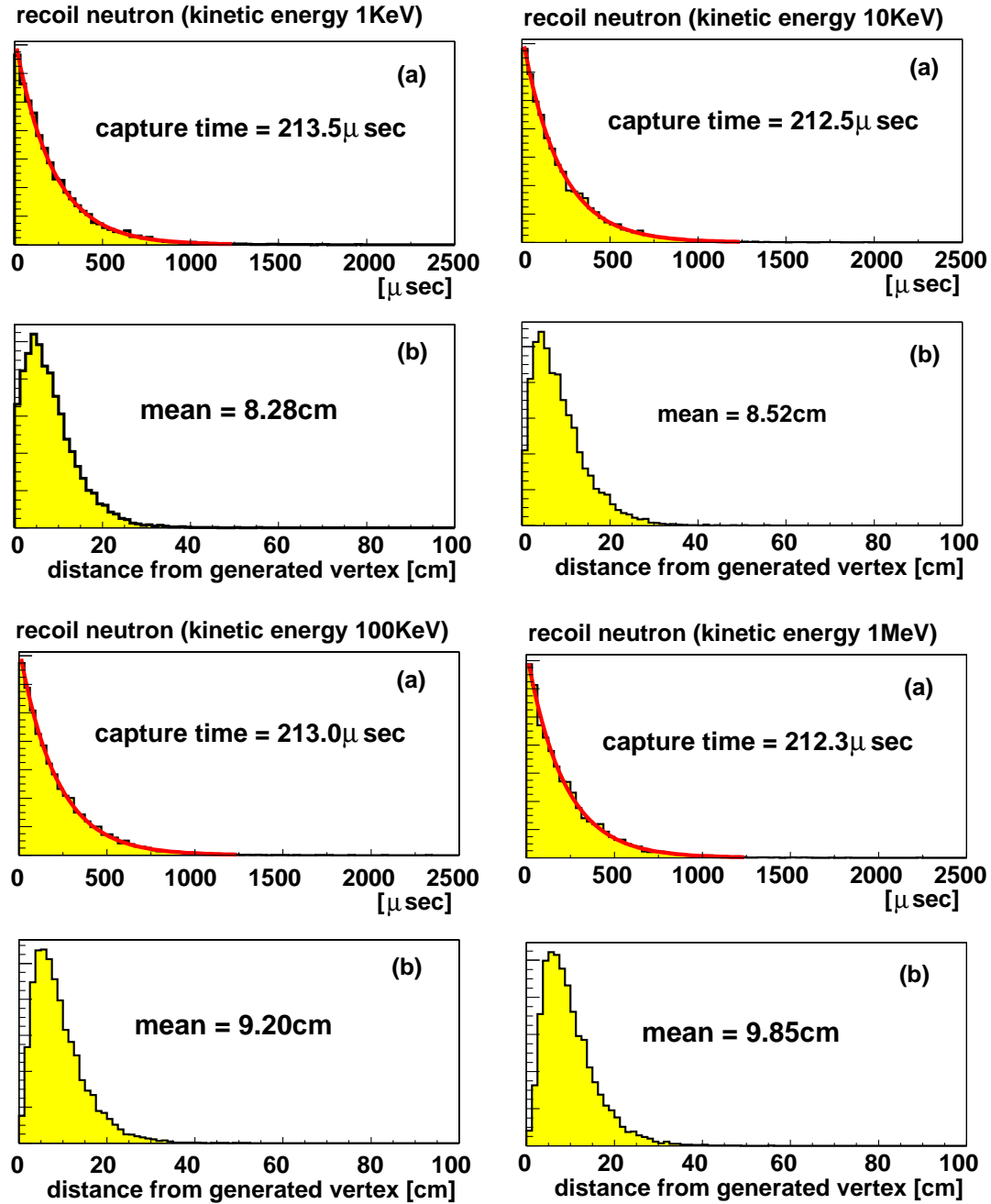


Figure 5.11: MC simulation of the recoil neutron. Four types of recoil kinetic energy are assumed: 1, 10, 100KeV and 1MeV. In each figure, the (a) shows time interval from the neutron is generated to be captured on proton, and the (b) shows the distance from the generated vertex to the captured vertex.

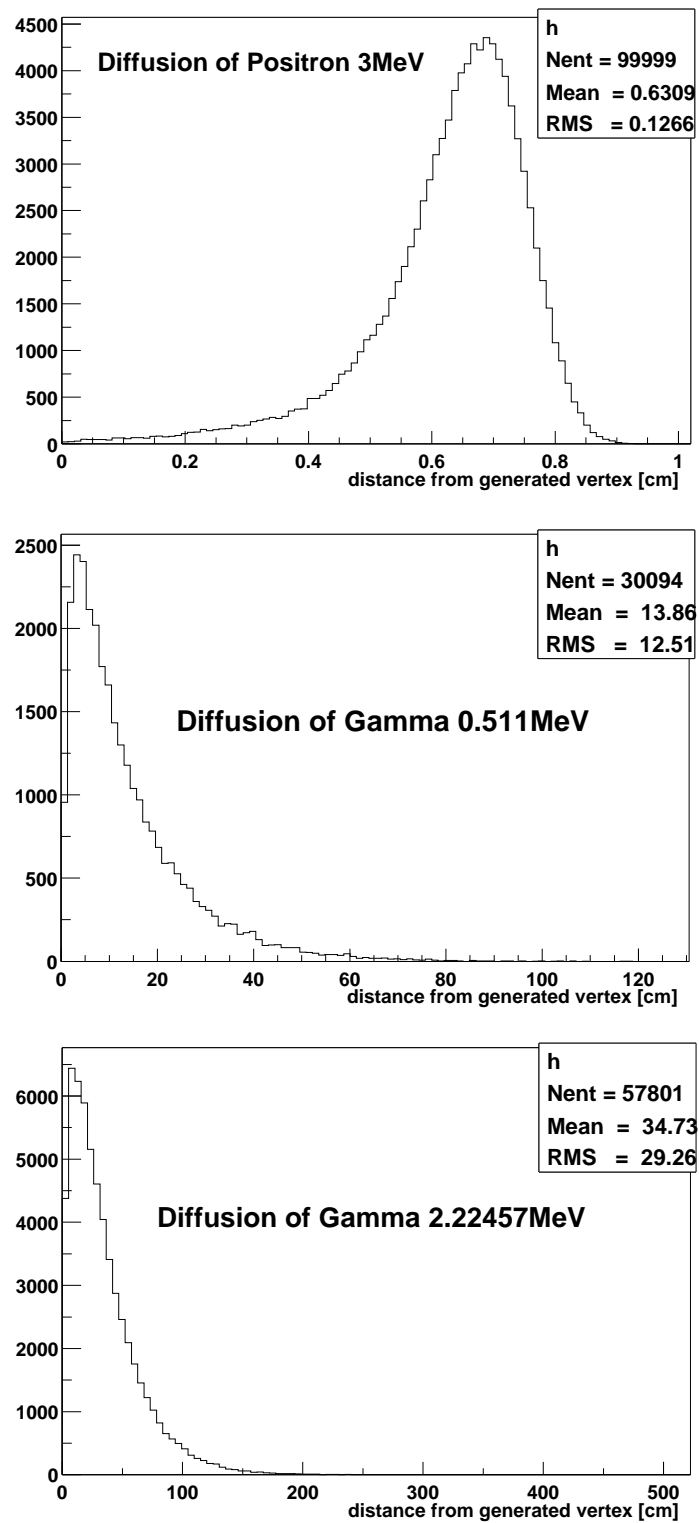


Figure 5.12: Diffusions of the positron 3MeV, 0.511 and 2.22457MeV of γ in the MC are shown.

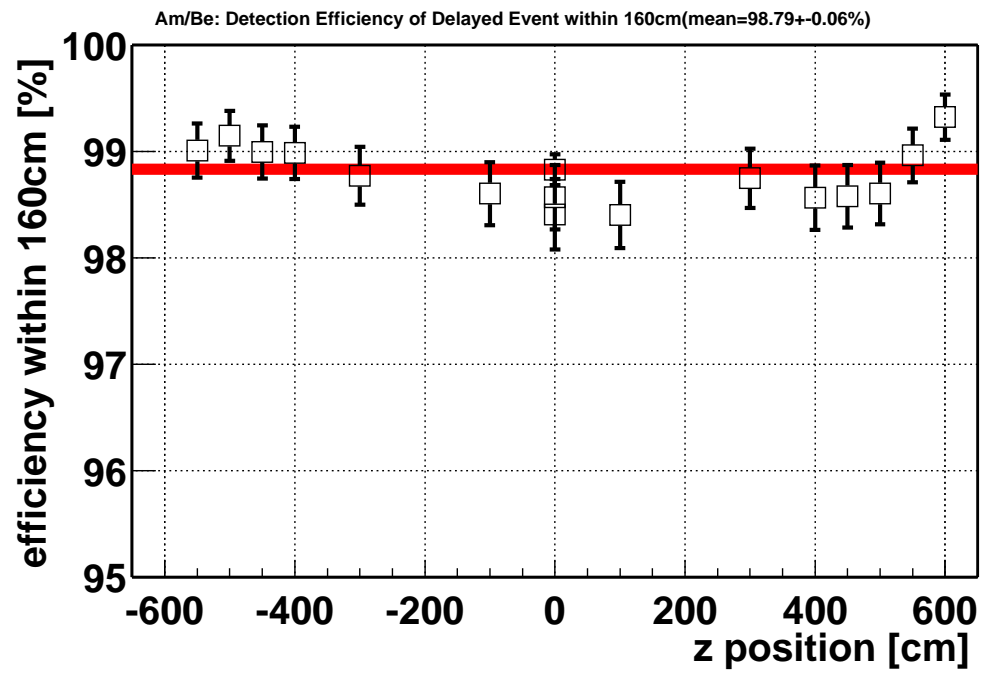


Figure 5.13: Detection efficiencies of the neutron capture event within 160cm at various z position are shown. Square markers indicate measurement results of the Am-Be calibration. The thick line indicates the prediction of the simulation (98.83%). The Am-Be calibration agrees with the prediction of the simulation within 0.5%,

5.3 Live Time Calculation

Exact calculation for the number of neutrino is essential for the neutrino disappearance experiment like a KamLAND, because the result of the experiment will be wrong if its calculation is wrong. The number of $\bar{\nu}_e$ events is calculated from the how long time the detector was sensitive for the $\bar{\nu}_e$ detection and the flux of $\bar{\nu}_e$. Livetime is defined as above “how long time the detector was sensitive for the $\bar{\nu}_e$ detection”. The livetime is calculated with

- **runtime** . . . time of the data taking for each run.
- **deadtime** . . . time of no data taking period or data taking is incorrect.
- **vetotime** . . . unused period at the analysis for the background rejection.

The runtime is defined as;

$$\text{runtime} = (\text{time of the last event in the run}) - (\text{time of the first event in the run})$$

Usually, the event rate of the history event is about 200 Hz and its time interval is about 5 msec. Thus, uncertainty of the run start time and the run stop time is about 5 msec, and it corresponds about $6 \times 10^{-5}\%$ of uncertainty for the 24 hours runtime. Total runtime from March 4 to October 6, 2002 (run164 - run1466) is 163.80 days (+ 9.27 days of bad run).

5.3.1 Deadtime

Deadtime finding

The deadtime is classified to 4 types

- **bad run**
The data quality is very worse. For example, the number of bad-channels is many or cluster because of the HV supply or electronics problem, the trigger rate or muon rate is strange These runs are not used conservatively. Currently, this is 9.27 days (5.4 %) of total run time from March 4 (run164) to October 6 (run1466), 2002.
- **bad period (half-badrun)**
This is a kind of the bad run, a part of run is worse condition like a badrun. This period is coming within a few hours before or after some trouble. This gives 0.5% deadtime to total run time.
- **interval between trigger disable and enable**
The disable flag is recorded when the trigger module is busy and disable to work, and the enable flag is recorded when the trigger status is recovered². It gives rise to about 0.67% deadtime to the total runtime except for the bad run.
- **large time interval more than 100 msec**
The data packet from the trigger is broken when the data flow network is busy. This illegal packet is difficult to interpret sometimes, and this is ignored at the event building process. At the result, the large time interval is made. The time intervals between each history event is shown in Figure 5.14. The time interval more than 100 msec is unusual and the large time interval is treated as the deadtime. Like this dead time is 0.079% of total good run time.

²Actually, disable flag was missing sometimes before run876. At that case, last event before enable flag was assumed which has disable flag.

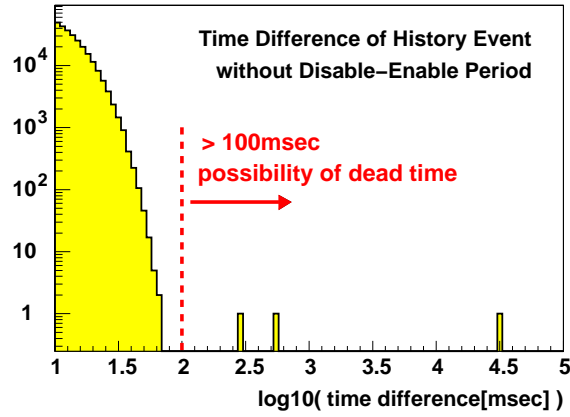


Figure 5.14: Time intervals between each history event is shown. Sometimes, there are large time intervals more than 100 msec. This is caused by illegal data packet from trigger module.

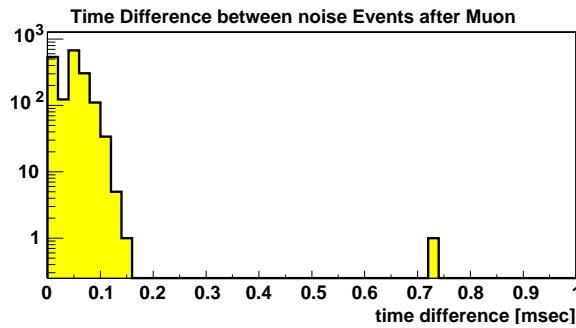


Figure 5.15: Time interval of noise event after last muon is shown. This noisy period goes on for about 150 μ sec because of the ringing in the front-end electronic.

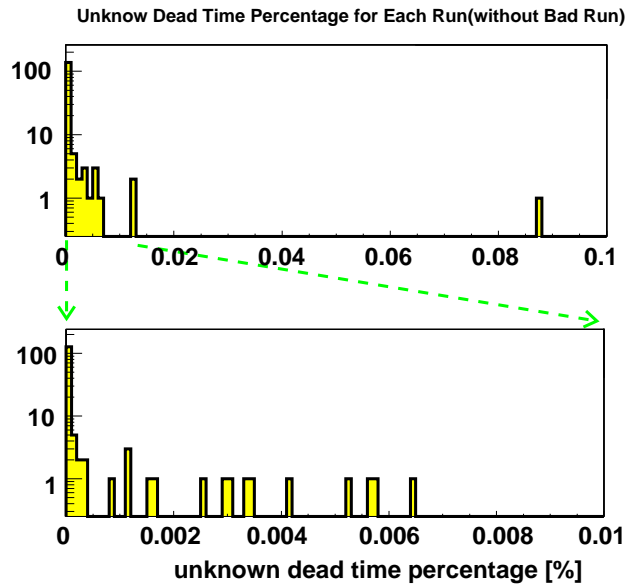


Figure 5.16: This figure shows the ratio of unknown deadtime in percentage. Usually, it is much less than 0.01% for almost all run, but it is more than 0.01% in sometimes. Anyway, percentage of unknown deadtime is less than 0.1% and average of it is 0.0069%. This value is addressed as systematic error of livetime calculation.

Noisy period

Usually, multiple noise events are coming after muon event. But sometimes, multiple noise events are coming without any muon before within $150 \mu\text{sec}$ ³. Figure 5.15 shows time difference between each noise event after muons. The noise events continue for $150 \mu\text{sec}$ following muons. Thus, there is a possibility of missing muon or unknown very short deadtime if there is a noisy period without any muon. It should be treated as, “There should be very energetic muon, and the whole detector should be veto for 2sec to reject the background of spallation products, conservatively.” Actually, there were several multi-neutron event candidates after noisy period like in a run834. The definition of the noisy period is,

- **noisy period**

There are plural noise events within 1 msec without any muon. The whole volume of the detector should be veto for 2 sec after this period.

Accidental tagging rate of it is $2.5 \times 10^{-8} \text{ Hz}$ because the accidental tagging rate of noise event is $5 \times 10^{-3} \text{ Hz}$ (see Section 3.9), i.e. $(5 \times 10^{-3} \text{ Hz}) \times (5 \times 10^{-3} \text{ Hz}) \times 1 \text{ msec} = 2.5 \times 10^{-8} \text{ Hz}$.

Uncertainty of deadtime finding

The trigger is sending a special flag periodically per sec, and it is called 1 PPS trigger. This is not coming during the Supernova trigger mode, but it is enabled during this period from run876. This 1 PPS trigger helps to check the uncertainty of the deadtime because $[\text{runtime} - \text{deadtime} - (\text{Supernova trigger period})]$ should be equal to $[(\text{number of 1PPS trigger}) \times 1 \text{ sec}]$. Unknown deadtime ratio is defined,

$$1 - \frac{(\text{number of 1PPS trigger}) \times 1 \text{ sec}}{\text{runtime} - \text{deadtime} - (\text{Supernova trigger period})}$$

and the percentage is 100 times of it. Figure 5.16 shows its percentage for each run. It is less than 0.1% and average of it is 0.0069%. Thus, uncertainty of the deadtime finding is addressed with this value 0.0069%.

5.3.2 Detector veto time

The veto for the detector is applied after every muon event and after every deadtime.

The muon is classified four grades and three different types of veto are applied for each muon as described in Section 4.3.4,

- Low Charge Muon ($Q \leq 40,000 \text{ p.e.}$)
Whole volume of the detector is veto for 2 msec
- Energetic Muon ($Q > 40,000 \text{ p.e.}$ & $\Delta Q \geq 10^6 \text{ p.e.}$)
Whole volume of the detector is veto for 2 sec (2,000 msec)
- Miss Reconstructed Muon ($Q > 40,000 \text{ p.e.}$ & $\text{badness} \geq 100$)
Whole volume of the detector is veto for 2 sec (2,000 msec)
- Well Reconstructed Muon (but not energetic one, $Q > 40,000 \text{ p.e.}$ & $\text{badness} < 100$ & $\Delta Q < 10^6 \text{ p.e.}$)

³The reason is the ringing on FEE

Whole volume of the detector is veto for 2 msec, and then cylindrical volume around muon track within 3 m ($\Delta L \leq 3\text{m}$) is veto for 2 sec. The cylindrical veto is only applied to the delayed event.

Where Q means the total charge sum of each muon event, ΔQ means the residual charge of each muon event (see Section 3.8.3). The $\Delta Q = 10^6 \text{p.e.}$ corresponds $\sim 3\text{GeV}$ extra energy deposition. The badness is the grade of reconstruction. The reason why these veto are adopted is described in section 4.3.3 and 4.3.4.

After the deadtime, whole volume of the detector should be veto for 2 sec because there is a possibility the energetic muon came into the detector just before the detector revive. At the beginning of each run, the 2 sec veto for the whole volume is adopted because of the same reason. Moreover, the 2 sec veto is also adopted after the noisy period as mentioned in the last section.

About 11% of runtime in the fiducial volume (5 m fiducial radius) is veto by the spallation cut, 1.6% and 0.4% of the runtime are veto after the deadtime and the noisy period respectively.

5.3.3 Livetime calculation

The livetime for each run is calculated using runtime and deadtime and veto information for each muon. Checking the time and volume overlap at each veto is essential for the livetime calculation. Uniform distributed events for the position and the time which generated by the simple MC simulation is used to avoid the over calculation or under calculation caused by the time and volume overlap. The ratio of livetime/runtime defined as,

$$\frac{\text{livetime}}{\text{runtime}} = \frac{(\text{number of events with applying all cut})}{(\text{number of events without applying all cut})} \quad (5.20)$$

Accuracy of calculation is depends on time intervals of generated events. 1.4×10^9 events were used for 163.8 days runtime data set, and its uncertainty is 0.001%. The efficiency of the detector living is strongly related with spallation cut except half-bad run (Figure 5.17).

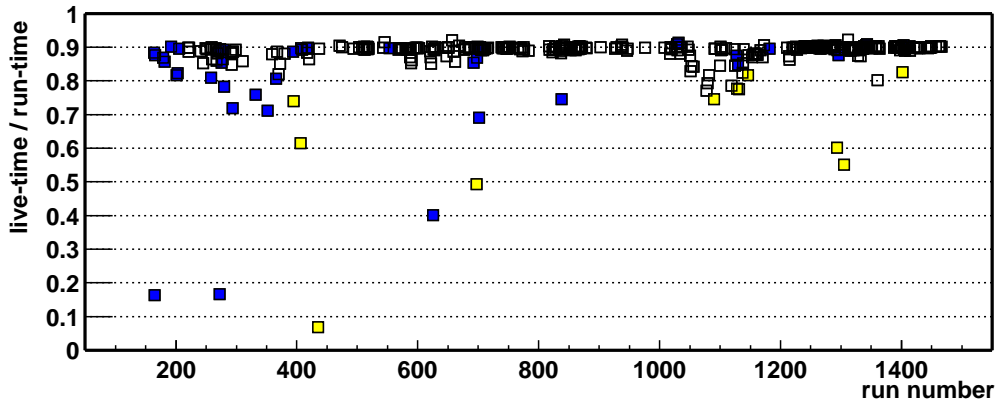


Figure 5.17: It is ratio of livetime/runtime for each run. Dark shaded (blue) markers mean badrun, half-bad run is shown in thin shaded (yellow) marker. Mean inefficiency of detector alive is about 11% and this is same as spallation cut efficiency for the livetime of detector.

Another calculation is applied to check previous method, while it can handle only time overlap of each veto and muon track correlated veto volume is calculated with numerical calculation. The calculation result of this numerical method is 1 % smaller than previous event

counting method. The over calculation, 11% of 11% is applied for veto time calculation, in this method. Anyway, the livetime calculation is cross checked.

The systematic uncertainty of the livetime calculation is addressed with a quadratic sum of uncertainty of the runtime $\sim 10^{-4}$ %, the deadtime finding 0.069% and the accuracy of calculation 0.001%,

$$\sqrt{(\sim 10^{-4})^2 + 0.069^2 + 0.001^2} \simeq 0.069\%.$$

The total livetime from March 4 to October 6, 2002 (run164 - run1466) is 145.09 days for 163.80 days runtime, and ratio of them is 88.6 % ⁴.

⁴This is a little bit smaller than spallation cut efficiency because of half-badrun.

Chapter 6

Anti-Neutrino Event Selection

The $\bar{\nu}_e$ candidates are selected by the delayed coincidence, which is very powerful for the accidental background rejection. About 4.4×10^8 events in 163.8 days data set are reduced to be about 25,000 events by noise/flasher cut, muon veto and the delayed coincidence. The accidental background is strongly rejected by the fiducial cut ($\sim 25,000 \rightarrow 173$ events). Finally, spallation cut and deadtime veto reject the correlated background, like ^8He and ^9Li . The number of remained $\bar{\nu}_e$ candidates is 86 events, and 54 events of them have ≥ 2.6 MeV prompt energy.

The ratio of $(N_{\text{detected}} - N_{BG})/N_{\text{expected}}$ is $0.611 \pm 0.085(\text{stat}) \pm 0.041(\text{syst})$, and the probability of no-disappearance is 0.05%. Therefore, the significance of the reactor $\bar{\nu}_e$ disappearance is 99.95%. This is the strong evidence for the reactor $\bar{\nu}_e$ disappearance. The stability of $\bar{\nu}_e$ detection rate is observed by the correlation between the detected event rate and the expected event rate. The detected event rate is always lower than the expected event rate. The consideration about the disappearance from the viewpoint of the neutrino oscillation is described in the next chapter.

Table 6.1: Summary of the significance for reactor $\bar{\nu}_e$ disappearance

	LAT (≥ 0.9 MeV)	HAT (≥ 2.6 MeV)
number of detected	86	54
number of expected w/o efficiency, sys.error	158.82	110.79
number of expected w/ efficiency, sys. error	124.40 ± 7.45	86.78 ± 5.59
expected BG (0TW Geo $\bar{\nu}_e$ + 0TW Geo reactor)	2.91 ± 1.12	0.95 ± 0.99
ratio=(detected-BG)/expected	—	$0.611 \pm 0.085(\text{stat}) \pm 0.041(\text{syst})$
significance(Prob. no oscillation)	—	0.05%

6.1 Selection Criteria

Based on the study of the background, deadtime and efficiency study, $\bar{\nu}_e$ selection criteria are decided as follows,

1. Delayed Coincidence

- (a) Time correlation cut ($0.5 \mu\text{sec} \leq \Delta T \leq 660 \mu\text{sec}$)
At least, 95% of neutron is captured within 660 μsec because the thermal neutron capture time is $\tau = 212.5 \pm 8.1 \mu\text{sec}$ (Section 5.2.2). On the other hand, the detection efficiency of very short time interval less than about 300nsec from previous event is too low abnormally (Section 4.2). Conservatively, within 0.5 μsec (500 nsec) should be ignored.
- (b) Vertex (space) correlation cut ($\Delta R \leq 1.6m$)
83.61% efficiency is given (Section 5.2.3).
- (c) Delayed energy window cut ($1.8 \text{ MeV} \leq E_{\text{delayed}} \leq 2.6 \text{ MeV}$)
98.85% efficiency is given (Section 3.7).

2. Fiducial Cut

- (a) Fiducial radius cut ($R \leq 5 \text{ m}$)
- (b) Cylindrical cut within 1.2 m along central vertical axis (z-axis) only for the delayed events. This cut eliminates the radiation from thermometers which are deployed along z-axis.

Decided from the accidental coincidence study (Section 4.5). Moreover, vertex reconstruction uncertainty is smaller as fiducial radius is smaller.

3. Spallation Cut (Section 4.3.4)

- (a) Veto whole volume for 2 msec following all muon
- (b) Veto whole volume for 2 sec following energetic or miss reconstructed muon
- (c) Cylindrical cut ($\Delta L \leq 3 \text{ m}$) along muon track for 2 sec following non-energetic muon, this cut is only applied to delayed event.

4. Deadtime Veto (veto whole volume for 2 sec as energetic muon)

There is a possibility that missing muon creates the spallation products (Section 5.3).

The detection efficiency is 78.3% under this selection criteria (see Table 5.1).

6.2 Event Reduction

The $\bar{\nu}_e$ candidates are selected along to following reduction,

- 1. Bad-run Reduction (reduction factor 0.95)
runtime 173.07 days \rightarrow 163.80 days (4.41×10^8 events)
- 2. Noise and Flasher Cut (reduction factor 0.72)
 $4.41 \times 10^8 \rightarrow 3.19 \times 10^8$ events

3. Muon Separation (reduction factor 0.98)
 $3.19 \times 10^8 \rightarrow 3.14 \times 10^8$ events
4. Muon Veto (reduction factor 0.78)
 $3.14 \times 10^8 \rightarrow 2.44 \times 10^8$ events
5. Delayed Coincidence Selection (reduction factor 1.0×10^{-4})
 $2.44 \times 10^8 \rightarrow 25,395$ events
6. Fiducial Cut (reduction factor 6.8×10^{-3})
 $25,395 \rightarrow 173$ events
7. Spallation Cut and Deadtime Veto (reduction factor 0.50)
 $173 \rightarrow 86$ events
 (86 events above 0.9 MeV threshold, 54 events above 2.6 MeV threshold)

Correlation of the total charge sum with reduction 1 ~ 4, noise, flasher cut, muon separation and muon veto, is shown in Figure 6.1. All of low charge events are noise event, and clear neutron capture peak is founded in muon veto spectrum.

Decreasing of ^{208}Tl rate is accompany with the fiducial radius and it is strongly correlated with the accidental rate (Figure 6.2) as mentioned in Section 4.5. This ^{208}Tl rate increase the accidental background because its energy is synchronized with the delayed energy window

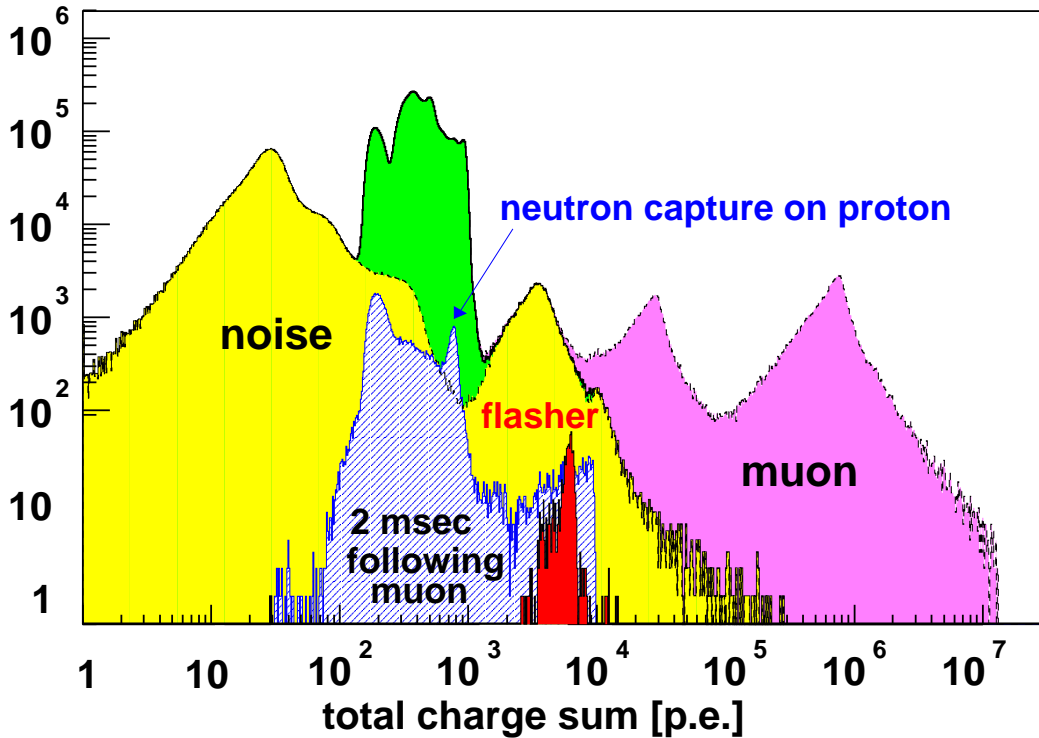


Figure 6.1: Correlation of the event reduction with total charge sum. Thin shaded area is the noise event, deep shaded area is the flasher event. Events, which are within 2 msec after muon, are shown as the hatched area. Dashed line which is not shaded corresponds to muon event. And, solid line which is not shaded means reduced event set.

(Many of 2.616 γ -ray of ^{208}Tl are attenuated and visible energy of attenuated γ comes into the delayed energy window). Therefore, the prompt energy spectrum of the delayed coincidence event inherits the single spectrum shape when it is not applied the fiducial cut. On the other hand, several MeV radiation from thermometers are rejected with the cylindrical cut along the central z-axis.

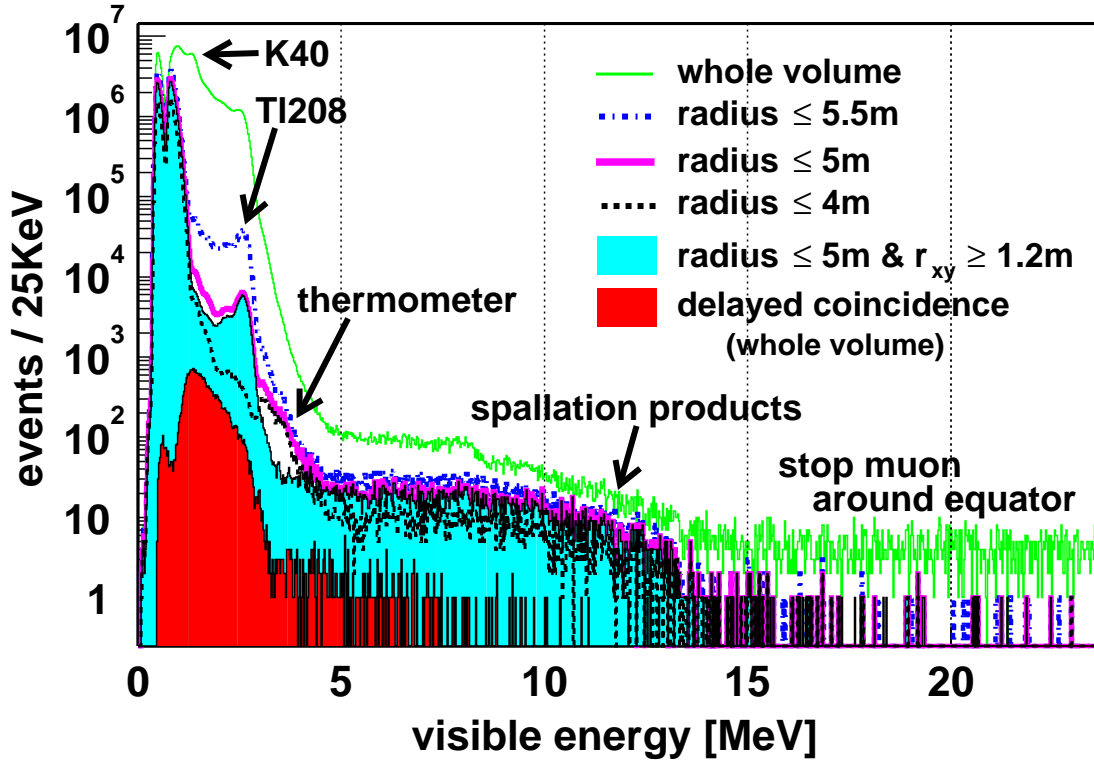


Figure 6.2: Correlation of the energy spectrum and fiducial radius, after noise & flasher cut, muon separation and muon veto. Definition of each spectrum is described in the figure. “ $r_{xy} \geq 1.2\text{m}$ ” means the central z-axis cut, which is the reduction of the radiation from thermometer, bottom flange. Some of stopping or clipping muons is not regarded as muon event because there is no PMT along the equator of the detector. These miss tagged muons are shown with the word “stop muon around equator”. Dark (red) shaded area means prompt events from delayed coincidence selection, $0.5 \leq \Delta T \leq 660 \mu\text{sec}$ and $\Delta L \leq 1.6 \text{ m}$, within whole volume.

The delayed coincidence selection gives the best reduction factor $1/10,000$, and the reduction factor of the fiducial cut (6.8×10^{-3}) indicates the attenuation of ^{208}Tl gamma ray (Figure 6.3). After the spallation cut and the deadtime veto, numbers of remaining $\bar{\nu}_e$ candidates below 20 MeV are 86 events. Because of the ambiguity associated with Geo $\bar{\nu}_e$ below 2.49 MeV [39], $\bar{\nu}_e$ candidates are classified to two types data sets based on different energy thresholds: the low analysis threshold (LAT) having a prompt energy threshold of 0.9 MeV and the high analysis threshold (HAT) having a prompt energy threshold of 2.6 MeV. Numbers of $\bar{\nu}_e$ candidates are 86 events and 54 events for LAT and HAT respectively.

Vertex distribution of the $\bar{\nu}_e$ candidates also helps us to understand the validity of the fiducial cut (Figure 6.4). Clear correlation of prompt and delayed events are shown in Figure 6.5,

6.6 and 6.7. The space-time correlation of the prompt and delayed events are in good agreement with expectations, and observed mean neutron capture time is $188 \pm 23 \mu\text{sec}$.

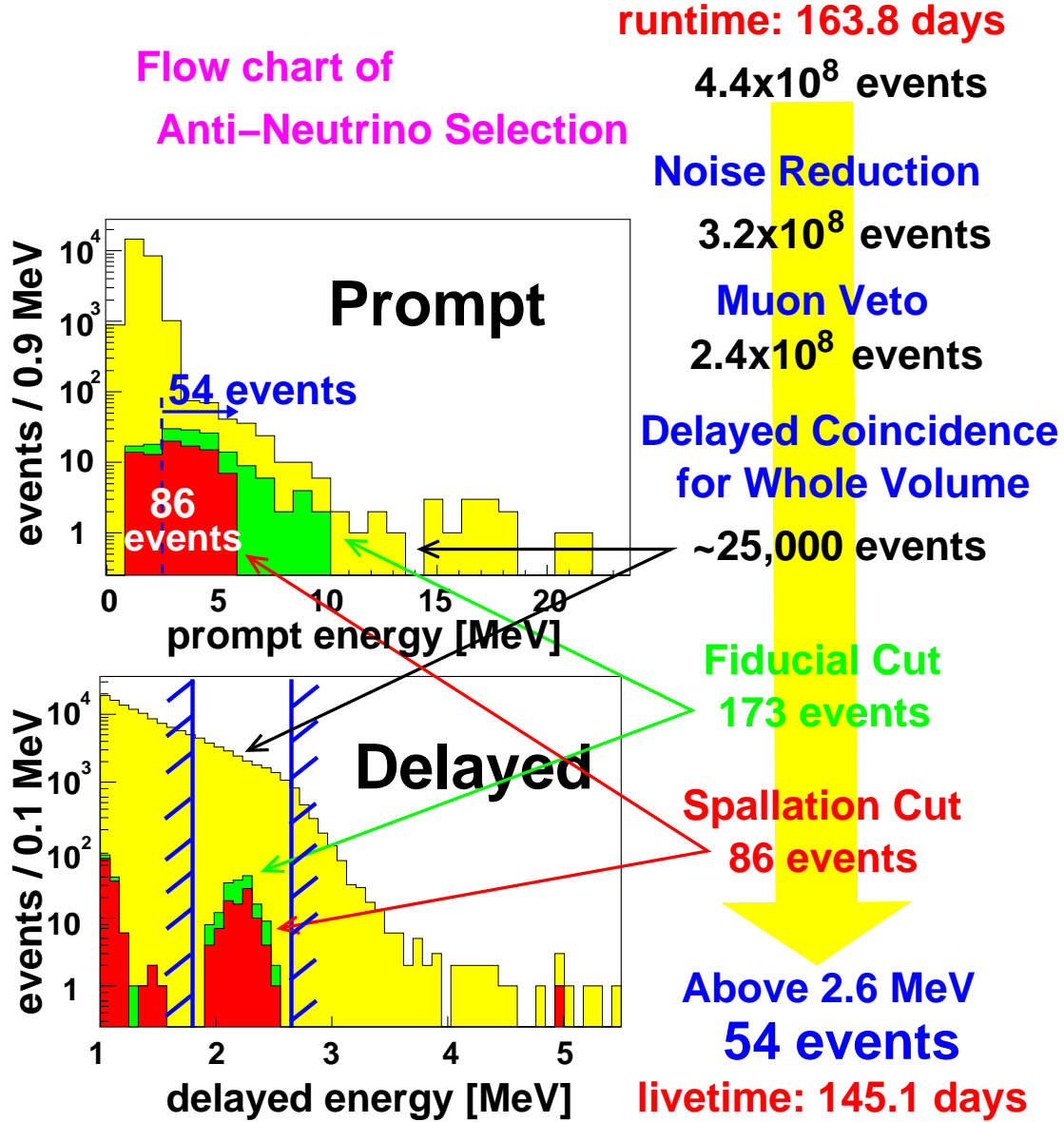


Figure 6.3: Flow chart of $\bar{\nu}_e$ selection. About 4.4×10^8 events in 163.8 days runtime data set are reduced to about 25,000 events after delayed coincidence selection. Accidental coincidence background events are rejected strongly by the fiducial cut which decided from accidental background study (Section 4.5). Remained events are reduced to be half by the spallation cut which based on spallation background (correlated background) study (Section 4.3). Livetime which is effective time for $\bar{\nu}_e$ detection is reduced to 145.1 days by the muon veto, spallation cut, and deadtime veto.

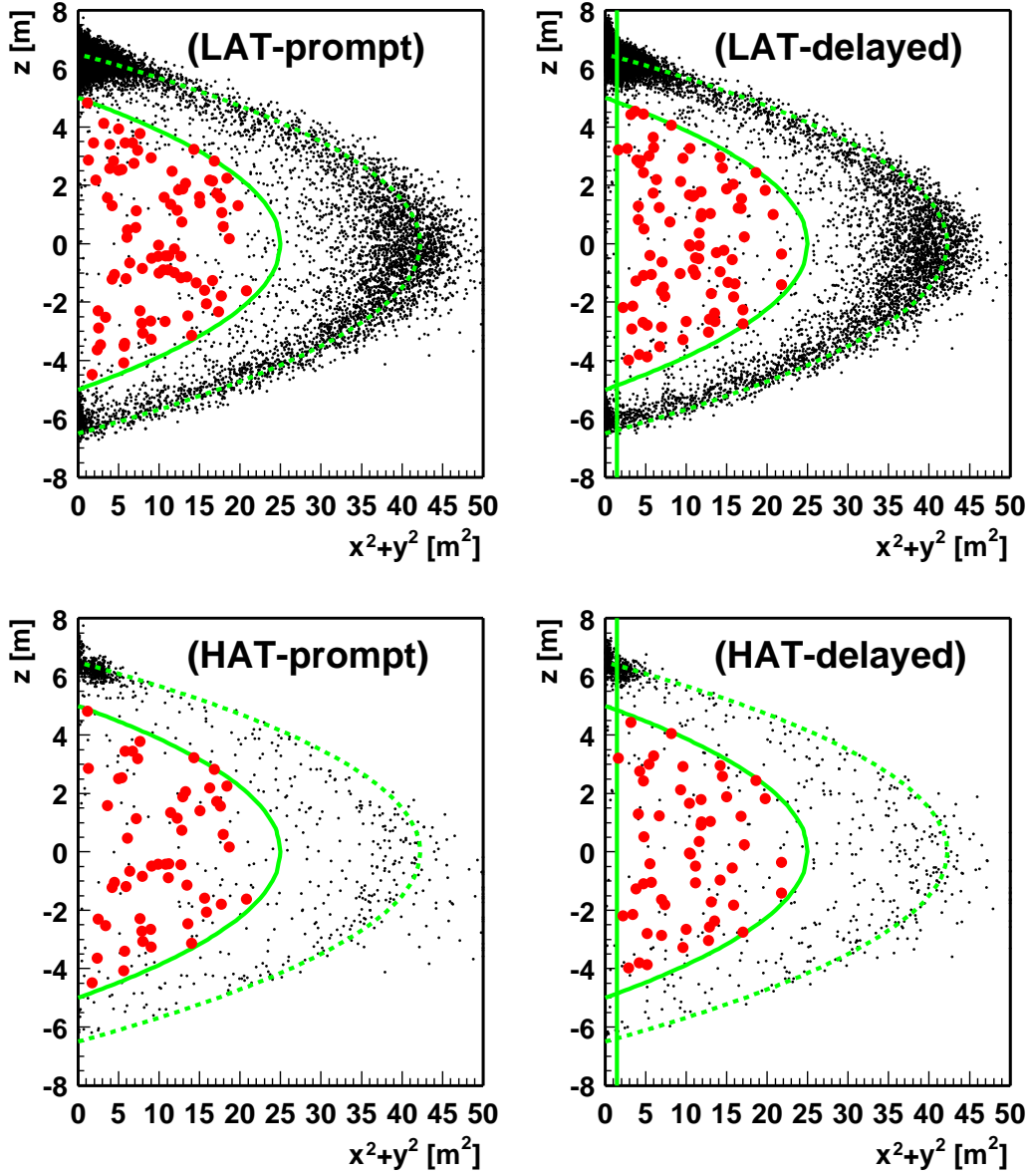


Figure 6.4: Distribution of events after delayed-coincidence selection, $\Delta R \leq 1.6m$ and $\Delta T \leq 660\mu\text{sec}$. “LAT-prompt, delayed” mean prompt and delayed events above 0.9 MeV analysis threshold, and “HAT-” mean higher analysis threshold case. A veto for 2 msec after muon has been already applied. Large Markers mean after other cuts, fiducial, central vertical axis cut and spallation cut. The dashed line means balloon radius and the solid line means boundary of the fiducial. Only delayed events are applied for central vertical axis cut.

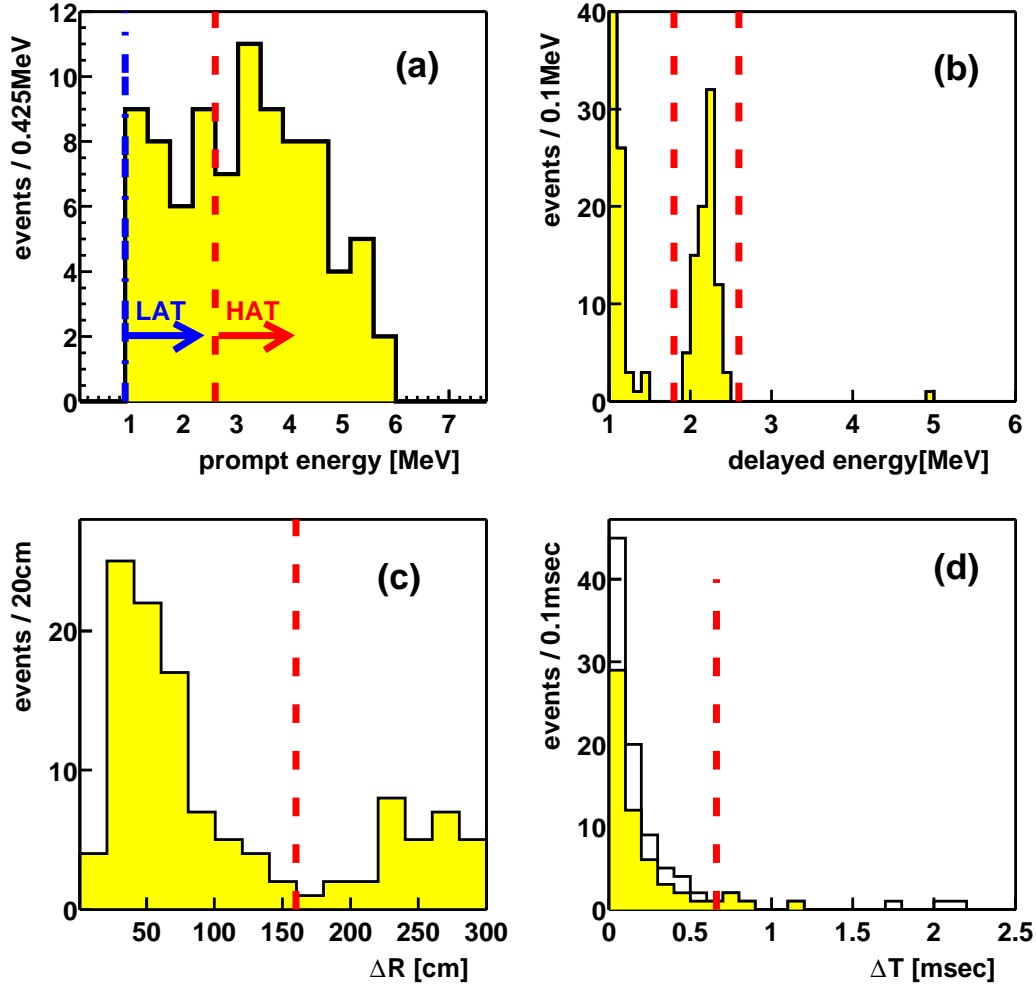


Figure 6.5: Profiles of $\bar{\nu}_e$ candidates are shown.

- (a) Prompt energy spectrum: Dashed line means higher analysis threshold and dash-dot-dash one means lower analysis threshold.
- (b) Delayed energy spectrum: Sandwiched region between two dashed lines is delayed energy window.
- (c) Space correlation, vertex difference, between prompt event and delayed one: Dashed line shows a boundary of cut 1.6 m.
- (d) Time difference from prompt event to delayed event. shaded histogram means HAT data set, non shaded histogram means LAT. Dashed line shows boundaries of $\Delta T \leq 660 \mu\text{sec}$.

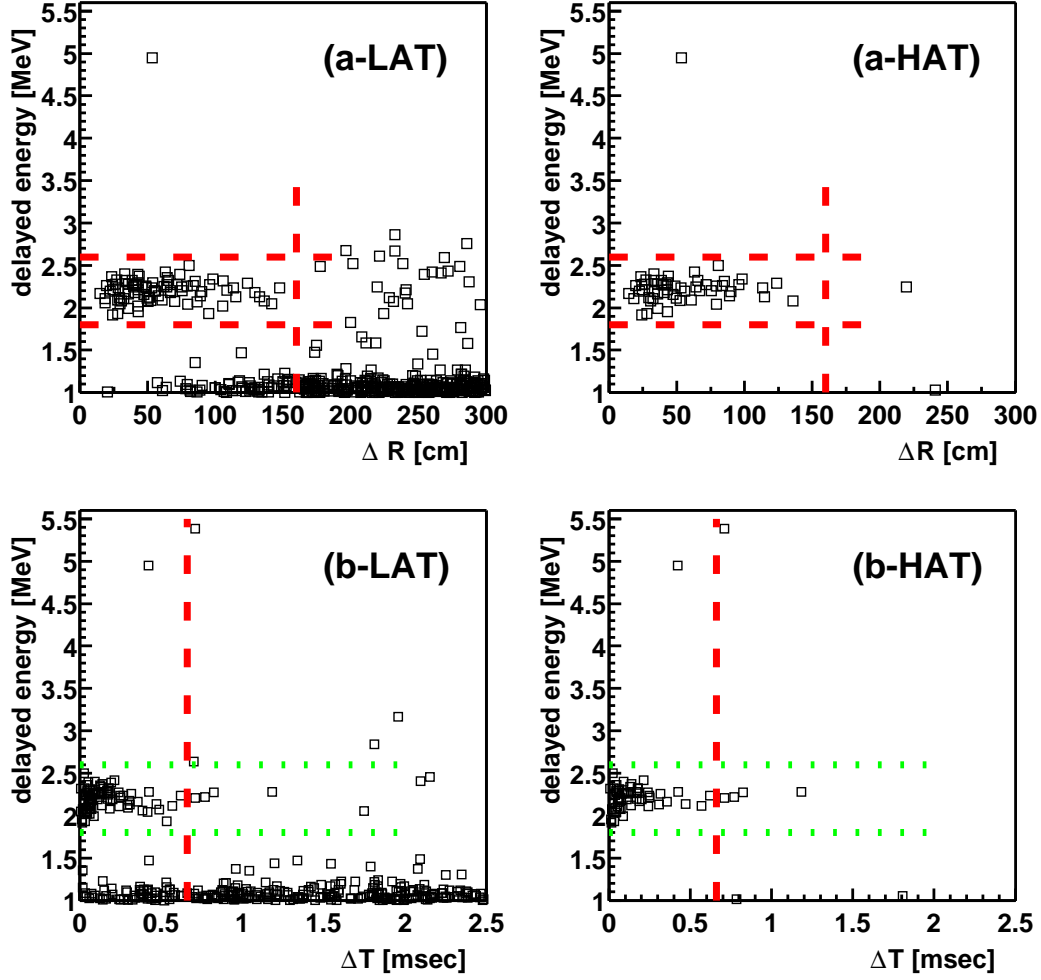


Figure 6.6: Correlation between delayed energy and vertex (a-LAT/HAT), time (b-LAT/HAT) difference from prompt event to delayed event, ΔR and ΔT . LAT and HAT mean lower (0.9MeV) and higher (2.6MeV) analysis thresholds respectively. In (a-LAT/HAT), the region surrounded with dashed lines is $\bar{\nu}_e$ signal region. And, (b-LAT/HAT), regions surrounded with dotted lines, dashed line is also $\bar{\nu}_e$ signal region. HAT data are very clean event set.

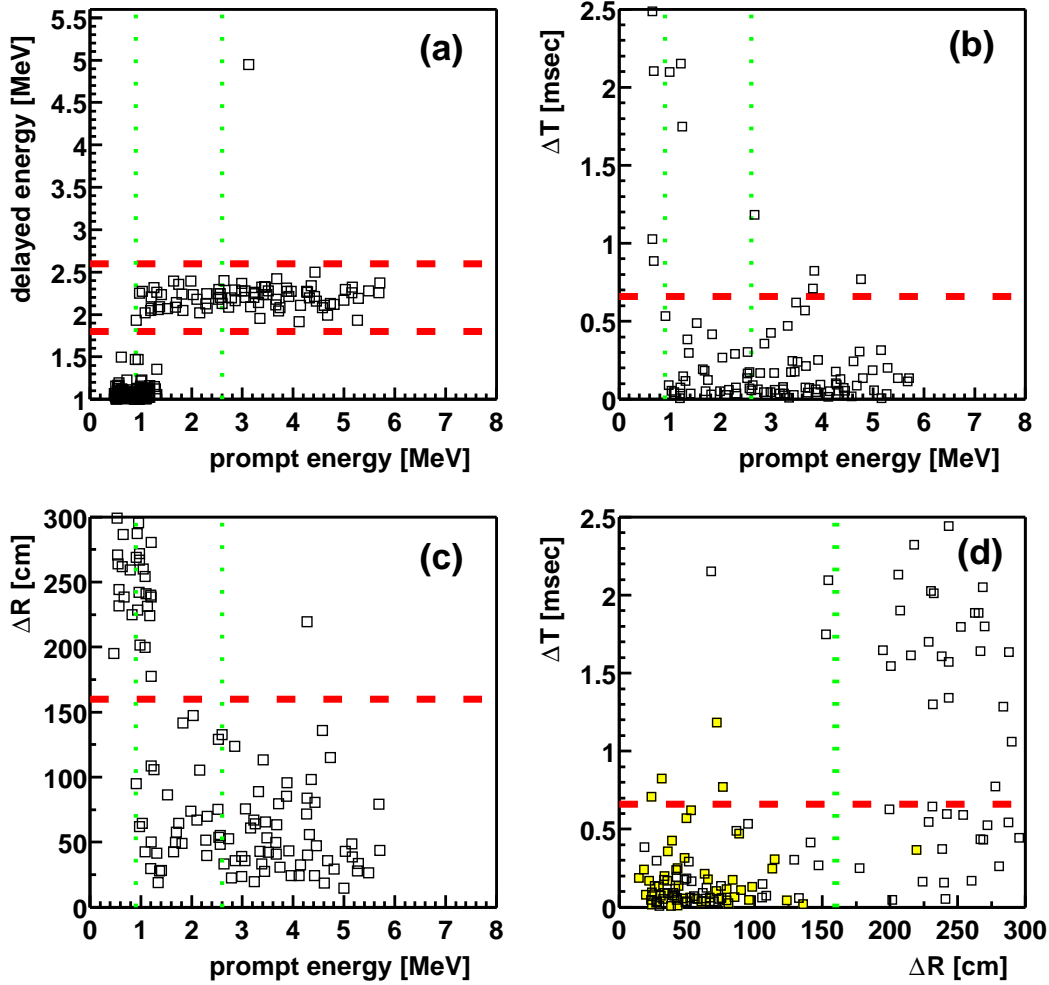


Figure 6.7: Correlation of prompt energy with (a) delayed event energy, (b) difference of each time, (c) difference of reconstructed vertices, and (d) correlation of differences time and vertex. Dotted line shows LAT or HAT analysis threshold in (a), (b) and (c), or the boundary of space correlation in (d). Sandwiched region with two dashed lines in (a) is the delayed energy window region for $\bar{\nu}_e$ detection. Dashed line in (b) and (d) indicate boundary of the time difference between prompt and delayed events, $\Delta T \leq 660 \mu\text{sec}$. Shaded marker in (d) means HAT and another means LAT data.

6.3 Significance of Reactor Anti-Neutrino Disappearance

The significance of the disappearance, actually the probability of no disappearance is calculated with following function,

$$Prob.(no\ disappearance) = \frac{1}{\sqrt{2\pi\sigma^2}} \int \exp \left[-\frac{(N_{expected} + N_{bg} - x)^2}{2\sigma^2} \right] \times \sum_{n=0}^{\lambda} \frac{\lambda^x}{x!} e^{-\lambda} dx \quad (6.1)$$

where λ is number of detected events and $\sigma = \sqrt{\sigma_{syst}^2 + \sigma_{BG}^2}$. Expected numbers of reactor $\bar{\nu}_e$ are 124.40 ± 7.22 and 86.78 ± 5.48 events for LAT and HAT respectively (Chapter 5). And expected backgrounds are 2.91 ± 1.12 and 0.95 ± 0.99 events for LAT and HAT in case the Geo- $\bar{\nu}_e$ contribution is ignored (Chapter 4.1). The significance is given only for HAT data due to the ambiguity associated with Geo $\bar{\nu}_e$ below 2.49MeV [39]. The probability of the no disappearance is 0.05% and the ratio of $(N_{detected} - N_{BG})/N_{expected}$ is $0.611 \pm 0.085(stat) \pm 0.041(syst)$. Thus, the deficit of events is inconsistent with the expected rate for standard $\bar{\nu}_e$ propagation at least 99.95% confidence level. This is the strong evidence for the reactor $\bar{\nu}_e$ disappearance. On the other hand, a scaled no-oscillation energy spectrum shape is consistent at 53% C.L. as determined by Monte Carlo.

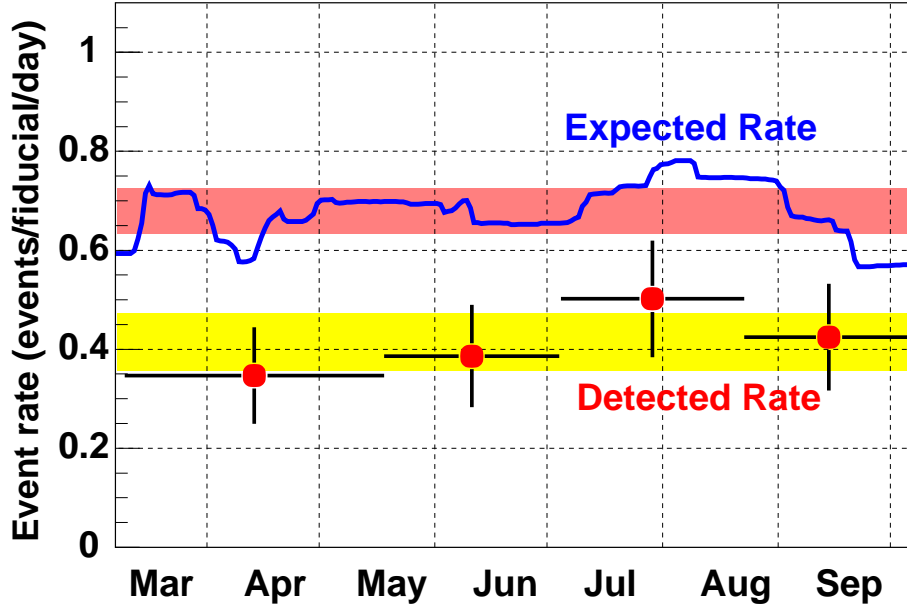


Figure 6.8: Detected and expected event rate of $\bar{\nu}_e$. The detected event rate is very stable in time and has good correlation with the expected event rate. The detected event rate is always lower than the expected event rate. The time correlation between detected and expected $\bar{\nu}_e$ rate is checked by Kolmogorov-Smirnov (KS) test. A KS probability of 89% is obtained for 2.6 MeV analysis threshold (55% for 0.9 MeV analysis threshold).

Stability of $\bar{\nu}_e$ detection rate is checked by the correlation between detected event rate and the expected event rate from nuclear reactors. The detected event rate is very stable in time and has good correlation with the expected event rate is observed as shown in Figure 6.8. This figure also indicates the detected event rate is always lower than the expected event rate.

The correlation with expected $\bar{\nu}_e$ rate is checked by using Kolgomorov-Smirnov (KS) test. KS probabilities are 55% and 89% for LAT and HAT respectively. The ambiguity of Geo $\bar{\nu}_e$ contribution and a few events of accidental background make it worse for LAT.

The KamLAND experiment has seen, for the first time, the disappearance of reactor $\bar{\nu}_e$. Figure 6.9 shows the ratio between measurement and expected flux for KamLAND as well as previous reactor experiments as a function of the average distance from the source. **All SMA, LOW and VAC but the LMA solar neutrino solution are excluded assuming the CPT invariance. It is therefore no exaggeration to say that the last subject of the solar neutrino anomaly is solved.** This is well explained in next chapter.

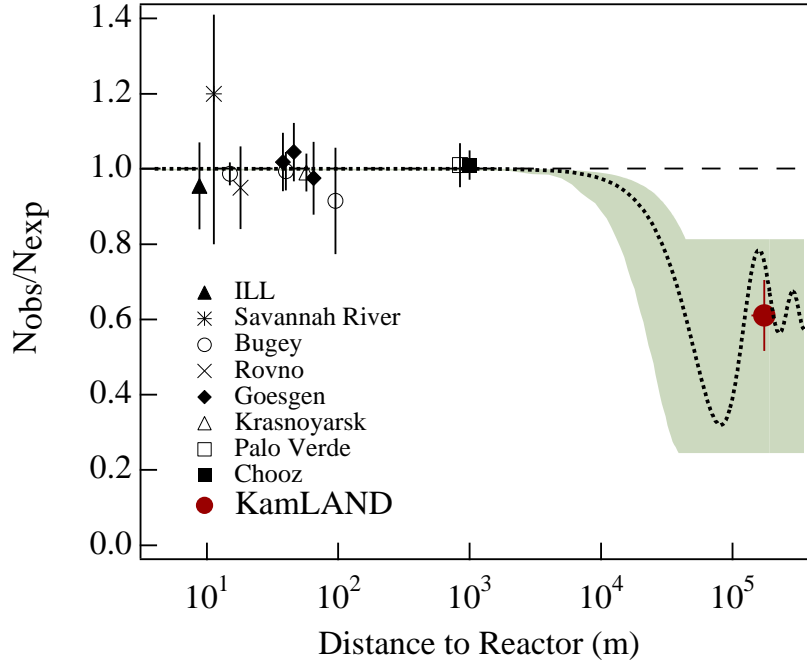


Figure 6.9: History of reactor $\bar{\nu}_e$ disappearance searches, the ratio of measured and expected $\bar{\nu}_e$ flux from reactor experiments [31]. The solid circle is the KamLAND result plotted at the flux-weighted average distance of ~ 180 km. The shaded region indicates the range of flux predictions corresponding to 95% C.L. LMA region from a global analysis of the solar neutrino data [51]. The dotted curve, $\sin^2 2\theta = 0.833$ and $\Delta m^2 = 5.5 \times 10^{-5} \text{ eV}^2$, is representative of the best-fit LMA prediction before KamLAND results and the dashed curve is expected for no oscillations.

Chapter 7

Oscillation Analysis

The evidence for the reactor $\bar{\nu}_e$ disappearance has already been described in the previous chapter. It could be caused by neutrino oscillations. In the context of two-flavor neutrino oscillation with CPT invariance, hypothesis test (“rate” analysis) between the detected event rate and the expected rate for each oscillation parameter set excludes all but LMA solar neutrino oscillation solutions (Section 7.1).

The neutrino oscillation gives rise to not only the disappearance of (anti-)neutrino but also the energy spectrum distortion. These characteristics lead to check the existence of the oscillation due to the energy distortion, as well as to find out the solution of the oscillation parameter set. At the second section, a measurement of two neutrino flavor oscillation parameters is performed using the maximum likelihood method for the energy spectrum shape distortion and observed $\bar{\nu}_e$ rate (“rate + shape” analysis). In this analysis, some free and variable parameters are used in χ^2 to evaluate the oscillation parameter set, and are chosen to minimize $\chi^2 + const.$ (actually, $-2\ln L$ [52]) for each oscillation parameter set.

$$\chi^2 + const. = \chi_{rate}^2 - 2\ln L_{NoBG} - 2\ln L_{shape} + \chi_{shape-deformation}^2$$

Numbers of Geo $\bar{\nu}_e$ ’s are defined as free parameters, n_u and n_{th} . And the other background events are defined as variable parameter whose variable range is limited by $-2\ln L_{NoBG}$ based on the estimated values in Chapter 4. On the other hand, there are some energy dependent uncertainties. These are handled with the shape deformation or energy scale redefinition. Of course, these ranges limited by each uncertainty, $\chi_{shape-deformation}^2$ corresponds to its limitation term.

Currently, Δm^2 is limited $6 \sim 8 \times 10^{-5} \text{ eV}^2$ at 90% C.L. with no limitation for mixing angle, but higher statistics may be essential for higher confidence. For mixing angle, higher angle is favored but its allowed range is not narrow: $\theta = 27^\circ \sim 63^\circ$ at 90% C.L. with no limitation for Δm^2

Matter effects and 3 generation analysis are also discussed in this chapter. The matter effects cause the tiny difference for the oscillation analysis. The sensitivity for θ_{13} is also discussed at the last section, but it is not sensitive.

7.1 Hypothesis test using $\bar{\nu}_e$ Rate above 2.6MeV

In the context of two-flavor neutrino oscillation with CPT invariance, hypothesis test between the detected event rate and the expected rate for each oscillation parameter set excludes all but LMA solar neutrino oscillation solutions. The definition of χ^2 is as follows,

$$\chi^2 = \frac{(R_{detected} - R_{theoretical})^2}{\sigma_{stat.}^2 + \sigma_{sys.}^2} \quad (7.1)$$

$$= \left(\frac{N_{detected} - N_{BG}}{N_{expected}} - \frac{n_{reactor}}{N_{expected}} \right)^2 / (\sigma_{stat.}^2 + \sigma_{sys.}^2) \quad (7.2)$$

$N_{expected}$: expected number of reactor $\bar{\nu}_e$ events for no oscillation case

N_{BG} : expected number of background events

$n_{reactor}$: expected number of reactor $\bar{\nu}_e$ events for each Δm^2 and θ

$\sigma_{sys.}, \sigma_{stat.}$: sigma of the ratio $R_{detected}$

The contour plots of Figure 7.1 and 7.2 helps us to understand that the SMA, LOW and VAC solar neutrino solutions are completely excluded more than 99.9 % C.L. and the LMA solution is only remain. Moreover, a lower part of LMA solution is excluded. Projections of χ^2 to the Δm^2 and the $\sin^2 2\theta$ axis are shown in Figure 7.3, these indicate instinctive information for the exclusion of SMA, LOW and VAC solutions.

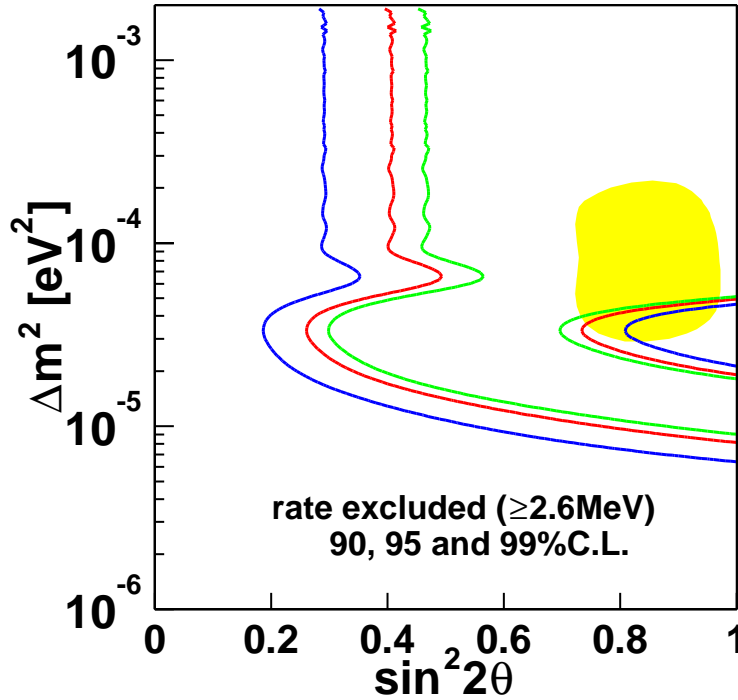


Figure 7.1: Excluded region of neutrino oscillation parameters by using the “Rate” analysis above 2.6MeV energy threshold. Excluded region is outside of solid line, and 90, 95 and 99% C.L. lines are shown. Shaded area indicates LMA region from the global analysis using results of solar neutrino experiments [51]. All solar neutrino solutions but a higher part of the LMA are excluded.

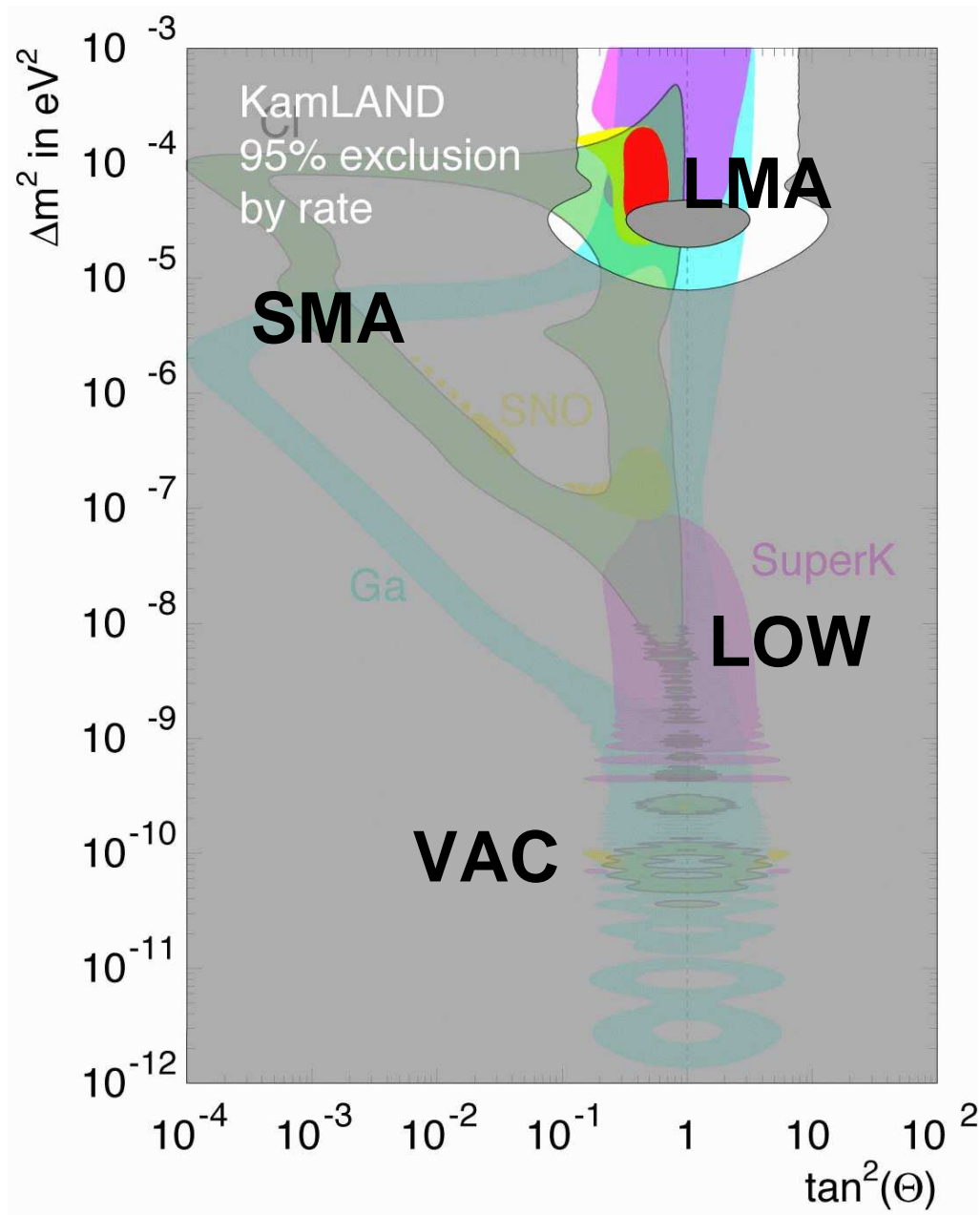


Figure 7.2: KamLAND excludes SMA, LOW, VAC and a part of LMA solutions [4]. It is convinced that the LMA is only solution to explain solar neutrino anomaly.

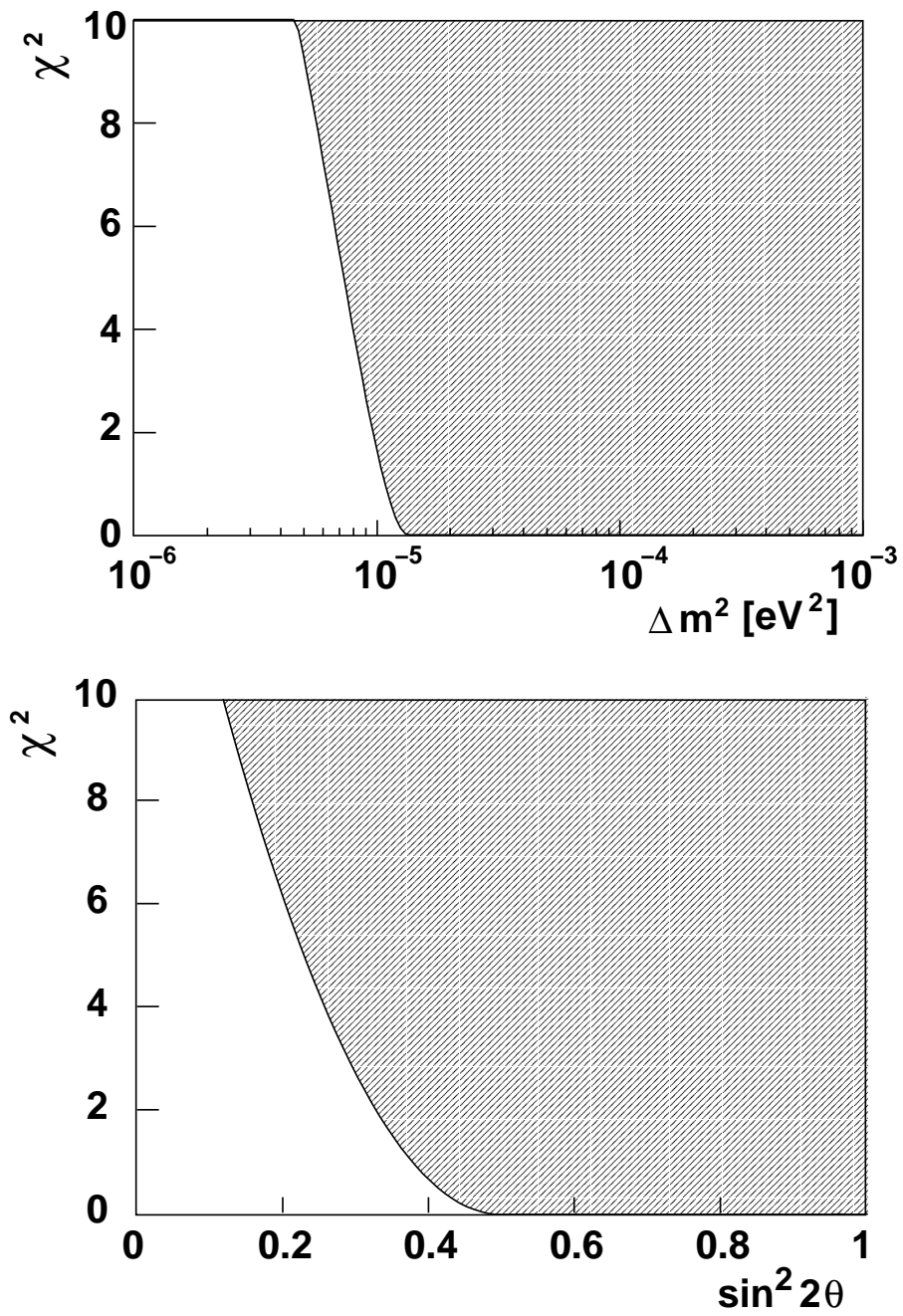


Figure 7.3: Projection of χ^2 to Δm^2 and $\sin^2 2\theta$ axis in rate analysis above 2.6MeV energy threshold. Low Δm^2 ($< 8 \times 10^{-6} \text{ eV}^2$ at 95% C.L.) and low mixing angle ($\sin^2 2\theta < 0.27$ at 95% C.L.) are excluded.

7.2 Rate + Shape Analysis

The neutrino oscillation gives rise to not only disappearance of (anti-)neutrino but also energy spectrum distortion, its survival probability is a function of some parameters, i.e, mixing angle(θ) and Δm^2 , energy and flight length of (anti-)neutrino. These characteristics of neutrino leads to check the existence of the oscillation due to the energy distortion, as well as to find out the solution of the oscillation parameter set. Besides, it is expected that Δm^2 will be determined precisely under the specific condition, that is the good energy resolution and almost the same neutrino flight length as in our KamLAND experiment. Because Δm^2 is described as $\Delta m^2 \sim E_{\bar{\nu}_e}/L$. Here, parameters estimation using maximum likelihood method [52] is shown in the following, by using the energy spectrum shape distortion of $\bar{\nu}_e$ and the observed $\bar{\nu}_e$ rate.

In this analysis, some free and variable parameters are used in χ^2 to evaluate oscillation parameter set, and are chosen to minimize χ^2 for each oscillation parameter set. The χ^2 consists of “rate evaluation part” and “shape distortion part” as follows,

$$\begin{aligned}\chi^2(\theta, \Delta m^2) &= (\chi_{rate}^2 + \chi_{NofBG}^2) \Leftarrow \text{rate evaluation part} \\ &\quad + (\chi_{shape}^2 + \chi_{shape-deformation}^2) \Leftarrow \text{shape distortion part} \quad (7.3) \\ &= \chi_{rate}^2 - 2\ln L_{NofBG} \\ &\quad - 2\ln L_{shape} + \chi_{shape-deformation}^2 + \text{const.} \quad (7.4)\end{aligned}$$

The explanation for these two terms are described in Section 7.2.1 for “rate evaluation part” and in Section 7.2.2 and Section 7.2.3 for “shape distortion part”.

7.2.1 The χ^2 and the Likelihood for Anti-Neutrino and Background Event Rate

Geo $\bar{\nu}_e$, accidental coincidence, spallation products(neutron emitters, ^8He and ^9Li) and fast neutron are main background events for reactor $\bar{\nu}_e$ detection, but only spallation and fast neutron backgrounds are considered for the HAT data set others are negligible for HAT.

However, nobody knows correct numbers for some of those background events, especially the ones for Geo $\bar{\nu}_e$ contribution, and its U/Th-ratio. And the expected number of spallation events which has large statistical error: 0.94 ± 0.85 events above 2.6 MeV prompt energy (1.1 ± 1.0 events above 0.9 MeV prompt energy). So, those numbers of background events are treated as different kinds of parameter set for each background case in this analysis, which is explained below.

- **Geo $\bar{\nu}_e$ (n_u and n_{th})**

Both of U and Th chain are treated as free parameters. No correlation between n_u and n_{th} because of model independence.

- **Accidental coincidence ($n_{acci.}$)**

This is a variable parameter. The variable range is limited by adding the extra χ^2 (actually $\chi^2 + \text{const.}$) which is obtained from $-2\ln L_{accidental}(n_{acci.})$ whose p.d.f. is Poisson distribution for $n_{acci.}$. The mean value of this function is given by the expected number of accidental coincidence, 1.81 events for LAT.

- **Spallation products, ^8He and ^9Li , (n_{he} and n_{li})**

Those are also variable parameters. They are limited by adding $-2\ln L_{spallation}(n_{he} + n_{li})$ whose p.d.f. is a convoluted function of Poisson gaussian distribution. Here The mean value of Poisson distribution is given by the expected mean number of spallation events

and sigma of the gaussian in the convoluted function is given by the statistical error of its expected value.

- **Fast neutron**

The very conservative upper limit is given for this background. This limit is, actually, small (<0.5 events) that it may be treated as “0 event”. Instead, this value is used as one of the systematic errors.

- **Correlated events at U, Th chain**

The expected number is negligible (Chapter 4).

- **Atmospheric $\bar{\nu}_e$**

The expected number is 1.02×10^{-4} . This is also negligible.

Now, χ^2 (actually $\chi^2 + \text{const.}$) for the limitation of parameter ranges is defined as,

$$\chi_{NoBG}^2 = -2\ln L_{NoBG} + \text{const.} \quad (7.5)$$

$$= -2\ln L_{accidental}(n_{acci.}) \\ -2\ln L_{spallation}(n_{he} + n_{li}) + \text{const.} \quad (7.6)$$

and χ^2 for anti-neutrino disappearance, χ_{rate}^2 is defined as follows including variable parameters described above and the expected value($n_{reactor}$) from reactors for each oscillation parameter set,

$$\chi_{rate}^2 = \frac{(N_{detected} - n_{reactor} - n_{acci.} - n_u - n_{th} - n_{he} - n_{li})^2}{\sigma_{stat.}^2 + \sigma_{sys.}^2} \quad (7.7)$$

Here, $\sigma_{stat.} = \sqrt{n_{reactor}}$ and $\sigma_{sys.} = n_{reactor} \times \delta_{sys.}$. Because, statistical uncertainties of background events, $n_{acci.}$, n_{he} and n_{li} , have already included in χ_{NoBG}^2 and the systematic error is assigned for reactor $\bar{\nu}_e$ detection.

7.2.2 Likelihood for Energy Spectrum Shape Distortion

The p.d.f. of likelihood, f_{shape} , is introduced to evaluate the energy spectrum shape distortion and this consists of the expected prompt energy spectrum of reactor $\bar{\nu}_e$ events($f_{reactor}(E)$) for each oscillation parameter set, U and Th chain($f_u(E)$, $f_{th}(E)$) of Geo $\bar{\nu}_e$, accidental coincidence ($f_{accidental}(E)$), ^8He ($f_{he}(E)$) and ^9Li ($f_{li}(E)$), which is thus given by,

$$f_{shape} = f_{shape}(E; n_{reactor}, n_u, n_{th}, n_{acci.}, n_{he}, n_{li}) \quad (7.8)$$

$$= \sum_k n_k f_k(E) / \sum_k n_k \quad (k = reactor, accidental, u, th, he, li) \quad (7.9)$$

$$\Leftrightarrow \chi_{shape}^2 \propto -2\ln L_{shape} \quad (7.10)$$

$$= -2 \sum_i \ln [f_{shape}(E_i; n_{reactor}, n_u, n_{th}, n_{acci.}, n_{he}, n_{li})] \quad (7.11)$$

Where, p.d.f. should be re-normalized when parameters are redefined every time.

7.2.3 Consideration of the Spectrum Uncertainty

Expected values, spectra and data, all of them have energy dependent uncertainties of, i.e. $\bar{\nu}_e$ spectrum[44], the vertex bias, the energy resolution and the energy scale. This can be also interpreted that it is possible to redefine expected energy spectrum or energy scale of data, whose variation ranges, however, should be limited with degrees of their uncertainties. Of course, it is need to be considered some effects from them. So, in this analysis, those variation ranges are limited by adding the extra $\chi^2(\chi_{shape_deformation}^2)$ for each variation, which depends on its own variation($A \times \sigma_{sys.}(E)$). The $\sigma_{sys.}(E)$ is the energy dependent systematic error. Hence,

$$\chi_{shape_deformation}^2 = (A \times \sigma_{sys.}(E) / \sigma_{sys.}(E))^2 = A^2 \quad (7.12)$$

Each $\chi_{shape_deformation}^2$ is defined as the square of the ratio of its variation to its systematic error. Therefore, the total $\chi_{shape_deformation}^2$ with all uncertainties which gives the spectrum uncertainties is defined as,

$$\chi_{shape_deformation}^2 = \sum_k A_k^2 \quad (k \text{ means following items}) \quad (7.13)$$

Now, various components which may distort the energy spectrum are introduced below,

- **Uncertainty of $\bar{\nu}_e$ spectrum[44]**
It is described in Section 5.1 and [44] for this. Figure 5.4 shows uncertainty of this. The energy spectrum is deformed with adding $\chi_{shape_deformation}^2$ for this uncertainty, and find a χ^2 minimum for each parameter set.
- **Spectrum uncertainty due to decay of long-life nuclei [47]**
Contribution from long life nuclei is $0.68 \pm 0.34\%$ of all the expected anti-neutrino events. This uncertainty has already been applied to χ_{rate}^2 as a systematic error of the event rate. On the other hand, the spectrum shape uncertainty below 2.8MeV is less than 0.34% below 2.8MeV for prompt energy. There is no sensitivity in the $\theta - \Delta m^2$ plain because this energy region is almost the same as the one in the case of Geo $\bar{\nu}_e$, which is treated as free parameters, and because the uncertainty is, needless to say, very small.
- **Uncertainty of vertex bias**
Uncertainty of the reconstructed vertex has energy dependence with the energy dependent vertex correction. And the behavior of this correction is shown in Figure 7.4. This yields the large uncertainty for the energy spectrum shape and the number of events. The magnitude due to this correction is treated as the systematic error of the vertex bias conservatively. Therefore, the expected spectrum for each oscillation parameter set can be varied in order to minimize χ^2 for it, however, the variable range is limited by the extra χ^2 , as in (7.12).
- **Uncertainty of energy scale**
The energy scale correction is required to correct the non-linearity of the visible energy, and this has the energy dependence and structural uncertainty because of two parameters considered. They are the contribution of the Čerenkov light and the magnitude of the quenching. Both of them were estimated with various calibration results, i.e., $^{68}\text{Ge}(2\gamma, 2 \times 0.511\text{MeV})$, $^{65}\text{Zn}(\gamma, 1.116\text{MeV})$, $^{60}\text{Co}(2\gamma, 1.173+1.333\text{MeV})$, neutron captured gamma ($\gamma, 2.22457\text{MeV}$ for proton and 4.9468MeV for ^{12}C) and Am-Be(γ ,

7.654MeV). Figure 3.37 shows the best fit parameters with their uncertainties. These parameters are chosen to minimize χ^2 which includes the re-defined energy scale and $\chi^2_{shape_deformation}$ for each oscillation parameter set.

- **Uncertainty of 1 p.e. threshold and dark current**

The shape distortion caused by them is the same as a the case of higher Čerenkov contribution, which is described in Section 3.7.2. This uncertainty can be handled with same technique described in the previous item.

- **Uncertainty of energy resolution**

This uncertainty causes the uncertainty of energy spectrum, which is shown in Figure 7.5 for the no-oscillation spectrum case. In this figure, 20% worse energy resolution is applied more than 4m radius sphere within 5m fiducial sphere(see the transparency of last collaboration meeting). This is assigned as a conservative systematic error for it. The spectrum difference is less than 0.15% at whole energy range without low(<2MeV) and high(> 6.8MeV) energy region. The spectrum can be varied slightly larger at this energy region because the low energy region is close to the threshold of $\bar{\nu}_e p \rightarrow n e^+$ reaction and the number of $\bar{\nu}_e$ events above 8MeV is almost zero, which means there are no significant dependences on oscillation parameter set. In addition, there are free parameters exist at low energy region, and the number of events above 6.8MeV range is much smaller($\sim 1.5\%$) than the one in the whole energy region. Therefore, the variation of spectrum is negligible, in fact, effective spectrum difference is less than 0.15%.

- **Spectrum distortion of Geo $\bar{\nu}_e$**

Geo $\bar{\nu}_e$ spectra are distorted by some affections. However, they are negligible for the oscillation analysis of reactor $\bar{\nu}_e$. It is summarized as follows,

- U/Th ratio

There is no limitation for U/Th ratio. And spectrum shape of Geo $\bar{\nu}_e$ changes if this ratio changes. However, there is no affection for oscillation analysis because numbers of Geo $\bar{\nu}_e$ from ^{238}U and ^{232}Th are treated as free parameters, n_u and n_{th} .

- Neutrino oscillation and the distribution of neutrino sources

The neutrino oscillation causes the distortion in Geo $\bar{\nu}_e$ energy spectrum as reactor $\bar{\nu}_e$. This distortion depends on the oscillation parameter set and distance from $\bar{\nu}_e$ sources to the detector. The magnitude of the distortion for each parameter set is shown in Figure 7.7, 7.8 and 7.9 based on 3 type models for the distribution of neutrino source (Figure 7.6). Matter(MSW) effect is also considered in this calculation. Its distortion is less than 9% without excluded region by the rate analysis, 99% C.L. $\Delta m^2 \leq 6 \times 10^{-6} \text{eV}^2$. χ^2 difference, actually difference of $-2\ln L$, is calculable if Geo $\bar{\nu}_e$ spectrum has 10% distortion as mentioned above, and it is shown in Figure 7.10. Their variations are at most with degree of 0.02~0.06, the distortion of Geo $\bar{\nu}_e$ has no sensitivity for the oscillation analysis. Moreover, Figure 7.11 shows it with much more drastic distortions, but these are just test.

Notable things are the energy range of Geo $\bar{\nu}_e$ is very narrow(0.9~2.6MeV) and it is as if two regions(0.9~1.6MeV and 1.6~2.6MeV) because of independent two free parameters n_u, n_{th} . This is one of reasons that the distortion Geo $\bar{\nu}_e$ spectrum has no sensitivity for oscillation analysis.

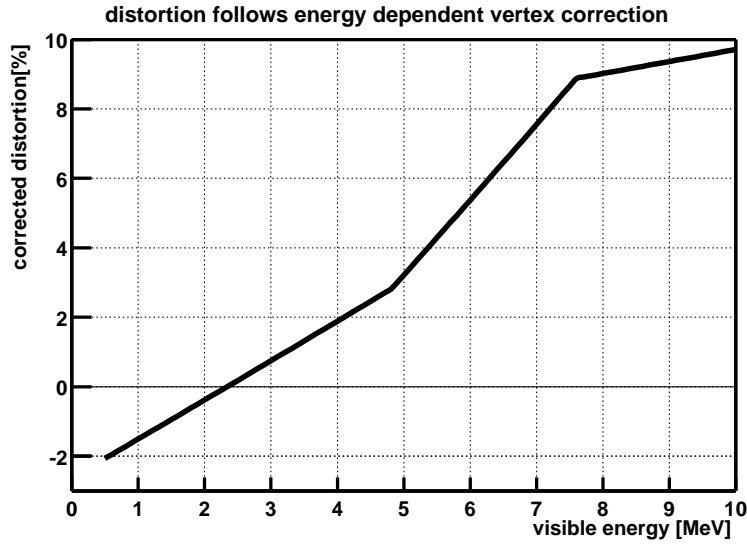


Figure 7.4: Energy spectrum distortion follows energy dependent vertex correction. The uncertainty of this correction need to be considered, and its amplitude of the correction should be the systematic error of vertex bias, conservatively.

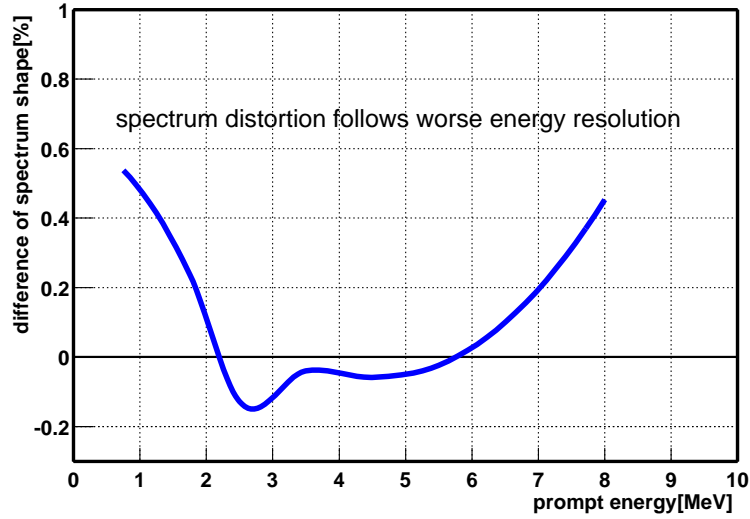


Figure 7.5: Energy spectrum difference at no oscillation case when energy resolution is 20% worse above 4m radius within 5m radius fiducial volume. It is almost less than 0.1% difference at 2~6.5MeV energy region and less than 0.5% at analysis energy range. Spectrum shape difference follows energy resolution uncertainty can be negligible because those differences is very small and there are free parameters($\text{Geo}\bar{\nu}_e$) at low energy($<2.8\text{MeV}$) region moreover number of events above 6.8MeV range is much small($\sim 1.5\%$ of all range).

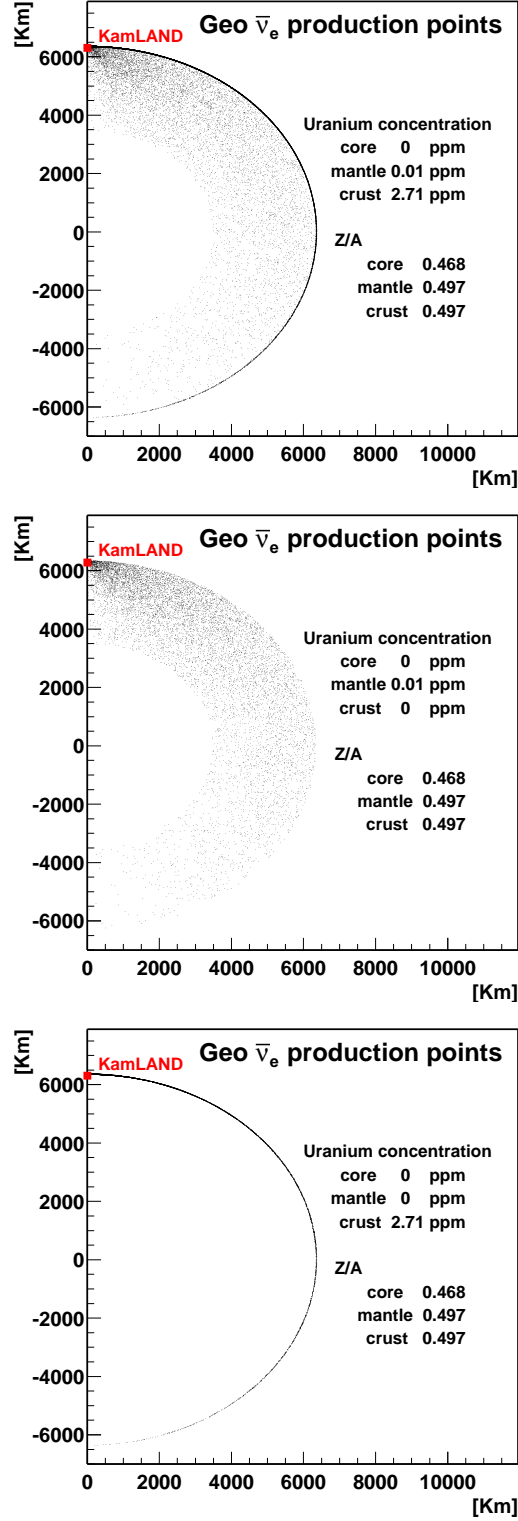


Figure 7.6: These figures means that the geo $\bar{\nu}_e$ generated points plotted on Z-R plane for its oscillation calculation with matter effect based on three type models, top figure shows Geo $\bar{\nu}_e$ production information based on “standard distribution model”, middle one shows it based on “mantle rich distribution model” and bottom one shows it based on “crust rich distribution model”. Points are very densed where close to KamLAND, and this means that the biggest $\bar{\nu}_e$ contribution is those generated in shorter distance from KamLAND.

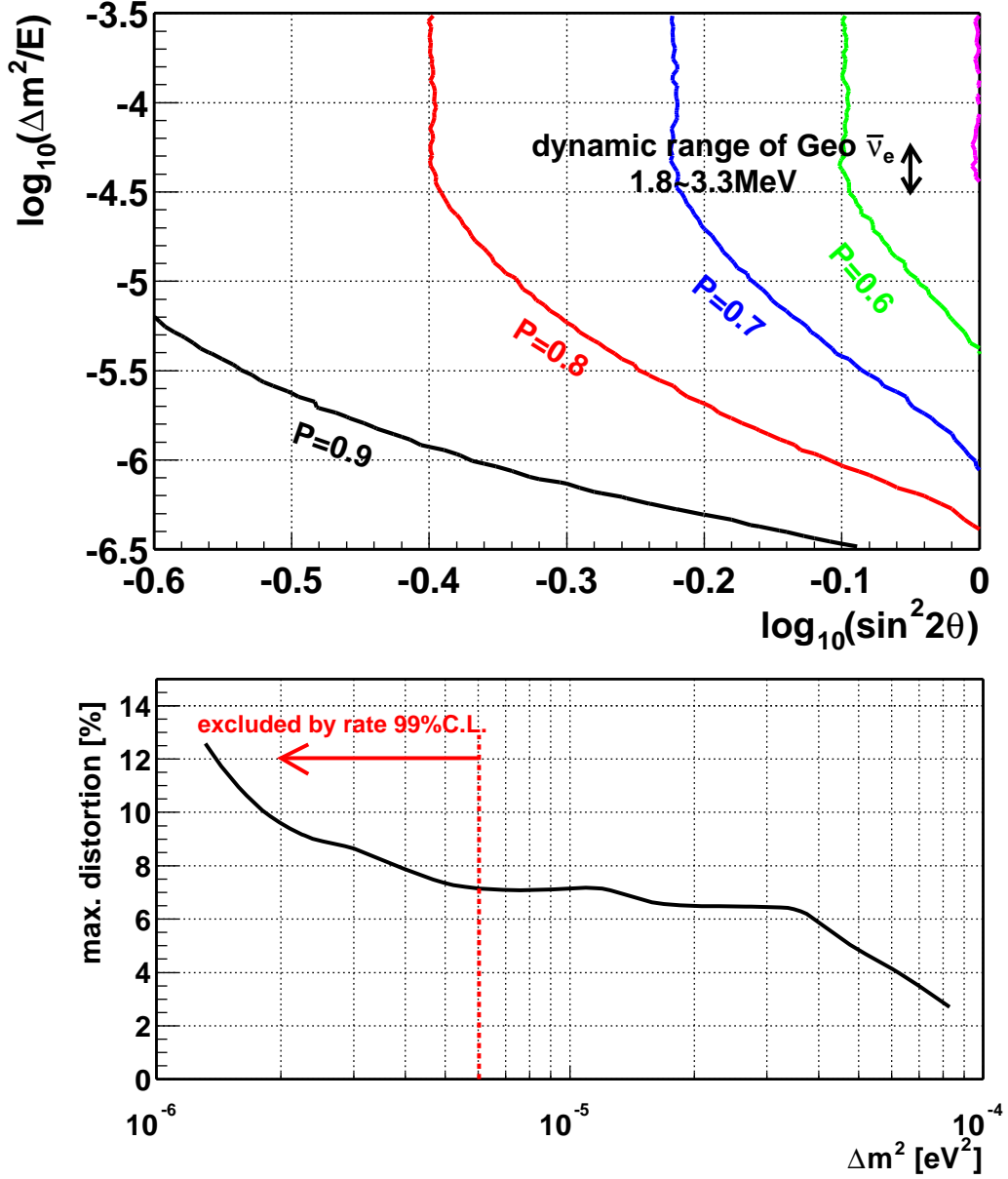


Figure 7.7: Upper figure is the contour plot with respect to the survival probability(P) of $\text{geo } \bar{\nu}_e$ including its oscillation with matter effect. The distribution of neutrino sources are assumed “standard distribution model”(Figure-7.6). The vertical arrow means dynamic range of $\text{Geo } \bar{\nu}_e$ which can be detected in the KamLAND. Magnitude of spectrum distortion can be described as the ratio of a survival probability of the edges of the dynamic range to the other edge of it for each oscillation parameter set. The direction of the distortion is always same direction, higher energy is higher and lower energy lower. Lower figure shows the maximum magnitude of distortion for each Δm^2 . Maximum distortion is less than 8% because lower Δm^2 than $6 \times 10^{-6} \text{ eV}^2$ is excluded at 99% C.L. by the rate analysis.

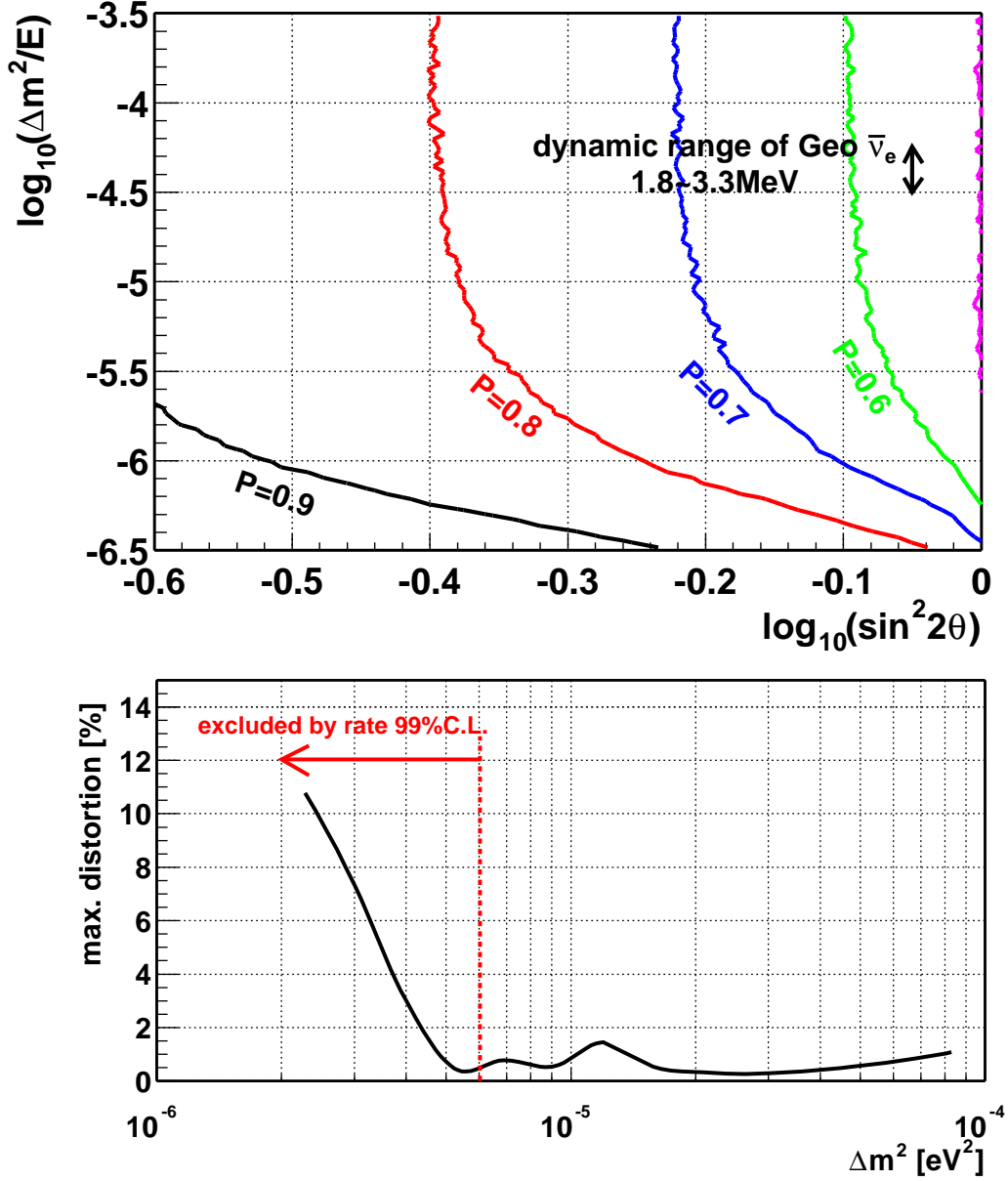


Figure 7.8: Upper figure is the contour plot with respect to the survival probability(P) of geo $\bar{\nu}_e$ including its oscillation with matter effect. The distribution of neutrino sources are assumed “mantle rich distribution model”(Figure-7.6). The vertical arrow means dynamic range of Geo $\bar{\nu}_e$ which can be detected in the KamLAND. Magnitude of spectrum distortion is defined with the ratio of survival probabilities for both edge of arrow for each oscillation parameter set. The direction of the distortion is always same direction, higher energy is higher and lower energy lower. Lower figure shows the maximum magnitude of distortion for each Δm^2 . Maximum distortion is less than 2% because lower Δm^2 than $6 \times 10^{-6} \text{ eV}^2$ is excluded at 99% C.L. by the rate analysis.

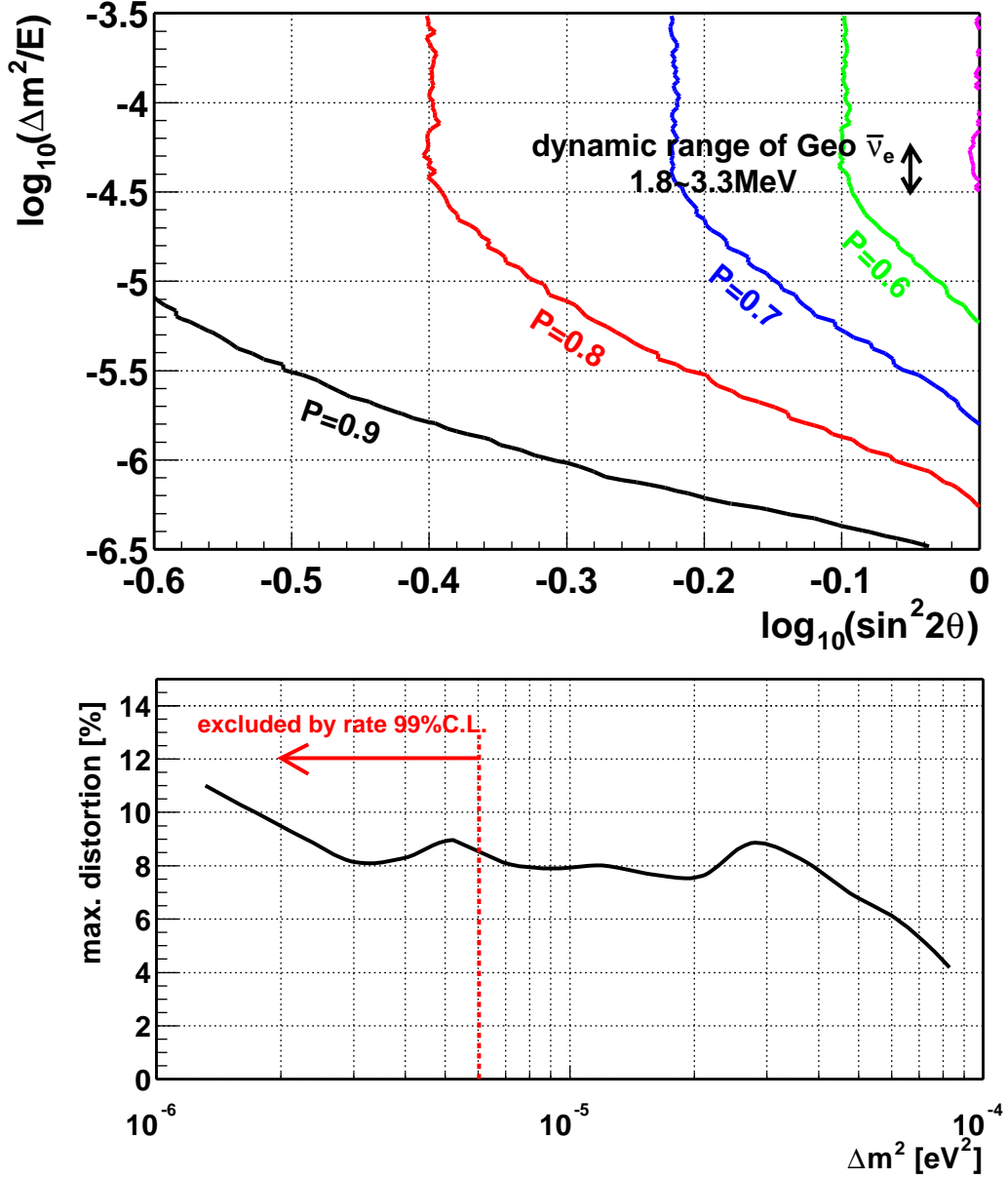


Figure 7.9: Upper figure is the contour plot with respect to the survival probability(P) of geo $\bar{\nu}_e$ including its oscillation with matter effect. The distribution of neutrino sources are assumed “crust rich distribution model”(Figure-7.6). The vertical arrow means dynamic range of Geo $\bar{\nu}_e$ which can be detected in the KamLAND. Magnitude of spectrum distortion is defined with the ratio of survival probabilities for both edge of arrow for each oscillation parameter set. The direction of the distortion is always same direction, higher energy is higher and lower energy lower. Lower figure shows the maximum magnitude of distortion for each Δm^2 . Maximum distortion is less than 9% because lower Δm^2 than $6 \times 10^{-6} \text{eV}^2$ is excluded at 99%C.L. by the rate analysis.

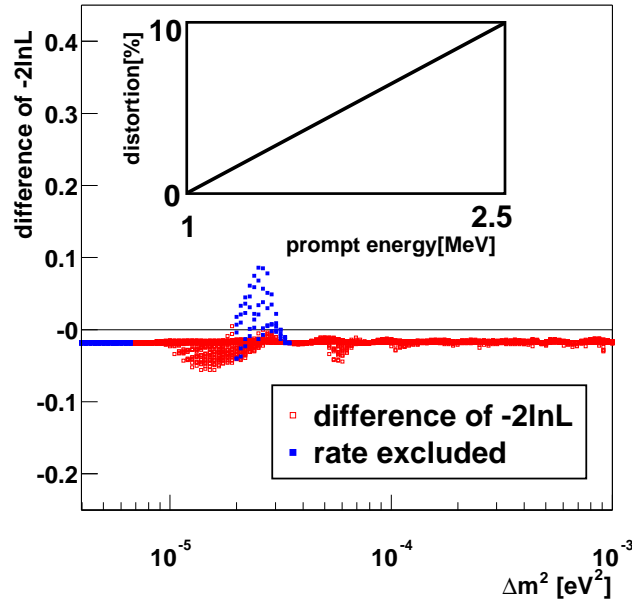


Figure 7.10: This figure is the projection of the difference of absolute value in $-2\ln L(\leftrightarrow \chi^2 + \text{const.})$ onto the Δm^2 axis, by taking the maximum distortion of geo $\bar{\nu}_e$ into consideration with the estimation of the simulation (Figure-7.7, 7.8 and 7.9). The filled square markers depict the values of region excluded by rate analysis. Their variations are at most with degree of 0.02~0.06, the distortion of Geo $\bar{\nu}_e$ has no sensitivity for the oscillation analysis.

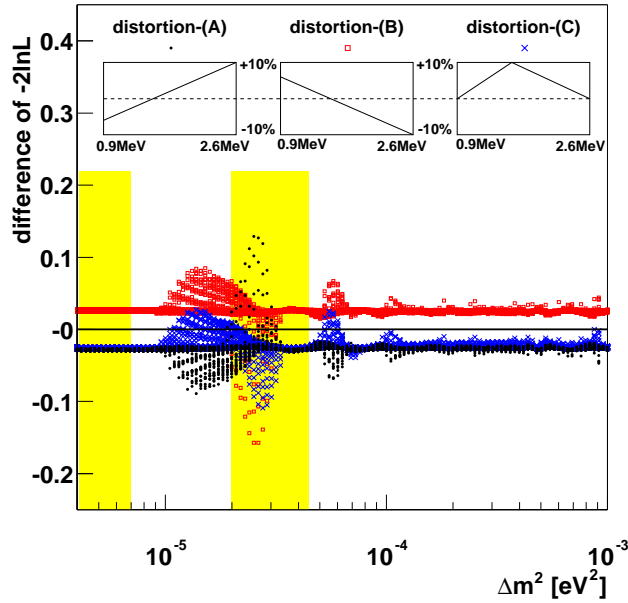


Figure 7.11: This figure shows the relation between the Δm^2 and the variation of $-2\ln L(\leftrightarrow \chi^2 + \text{const.})$ assuming 3 types of distortion. The magnitude of these distortion is almost twice larger than that in the actual case, and most of this result from just type (A). And the shade region is where is already excluded by the rate analysis above 2.6 MeV. Their variations are still less than 0.02~0.1 without shaded region, and also have no sensitivity for oscillation analysis.

7.2.4 Analysis results at 2.6 MeV threshold case

Result from only energy spectrum information

The sensitivity of spectrum shape is evaluated by the analysis with only the energy spectrum information without event rate information. This “shape only” analysis is performed without χ^2_{rate} in Eq.(7.4). The best fit parameters in the physical region yields;

$$\sin^2 2\theta = 1.0, \quad \Delta m^2 = 6.9 \times 10^{-5} \text{ eV}^2$$

$$(n_{aci}, n_{he}, n_{li}) = (0, 1, 0),$$

while the global minimum occurs slightly outside of the physical region at $\sin^2 2\theta = 1.01$ with the same Δm^2 . The allowed region is shown in Figure 7.12. Around $\Delta m^2 \sim 7 \times 10^{-5} \text{ eV}^2$ region is favored while there is no sensitivity for lower mixing angle.

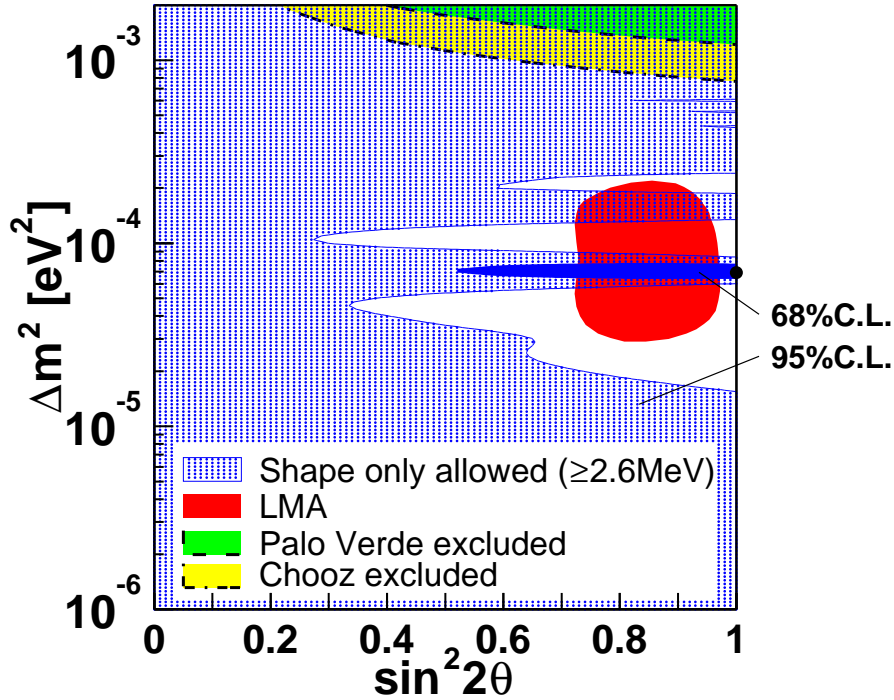


Figure 7.12: Allowed region from shape only analysis above 2.6 MeV data set. The best fit parameters are: $\sin^2 2\theta = 1.0$, $\Delta m^2 = 6.9 \times 10^{-5} \text{ eV}^2$.

Result from rate + shape information

The best fit parameters in from “rate + shape” analysis is same as “shape only” result, i.e.

$$\sin^2 2\theta = 1.0, \quad \Delta m^2 = 6.9 \times 10^{-5} \text{ eV}^2$$

$$(n_{aci}, n_{he}, n_{li}) = (0, 1, 0).$$

The prompt energy spectra of detected data and best fit parameters is shown in Figure 7.13. The allowed region in $\Delta m^2 - \sin^2 2\theta$ plane is shown in Figure 7.14. The lower mixing angle is rejected by the rate information. Overlap region with LMA solution is $5.8 \sim 8.3 \times 10^{-5}$ and $1.3 \sim 1.8 \times 10^{-4} \text{ eV}^2$ at 95% C.L. for Δm^2 . $\Delta\chi^2$ projection to Δm^2 axis and $\sin^2 2\theta$ axis give more detail information as shown in Figure 7.15. $\Delta m^2 \sim 7 \times 10^{-5} \text{ eV}^2$ is favored but its confidence level is not strong currently: $6 \sim 8 \times 10^{-5} \text{ eV}^2$ at 90% C.L. ($\Delta\chi^2 = 2.71$) with no limitation for the mixing angle. Higher degree is favored for the mixing angle, but its allowed range is not narrow $\theta = 27^\circ \sim 63^\circ$ at 90% C.L.

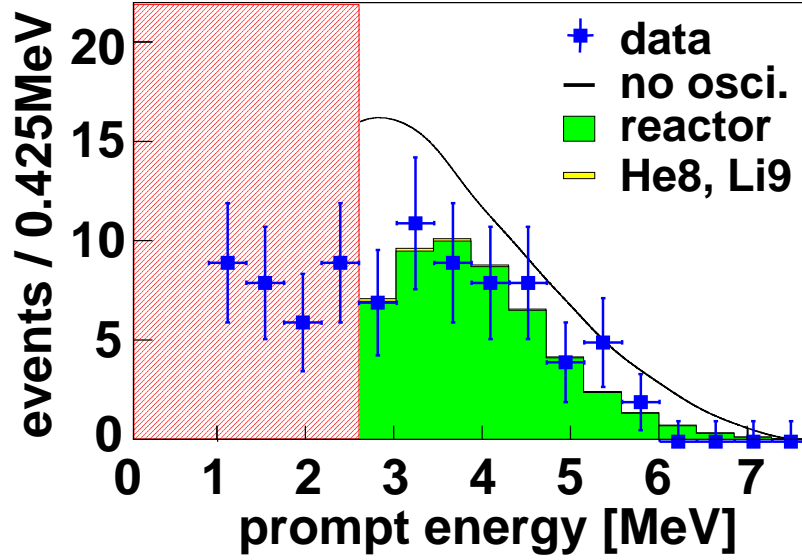


Figure 7.13: Prompt energy spectra of data (marker) and best fit parameters (histogram) of “rate+shape” analysis above 2.6 MeV data set. The best fit parameters are $\sin^2 2\theta = 1.0$, $\Delta m^2 = 6.9 \times 10^{-5} \text{ eV}^2$. The solid line means the prompt energy spectrum in no oscillation case.

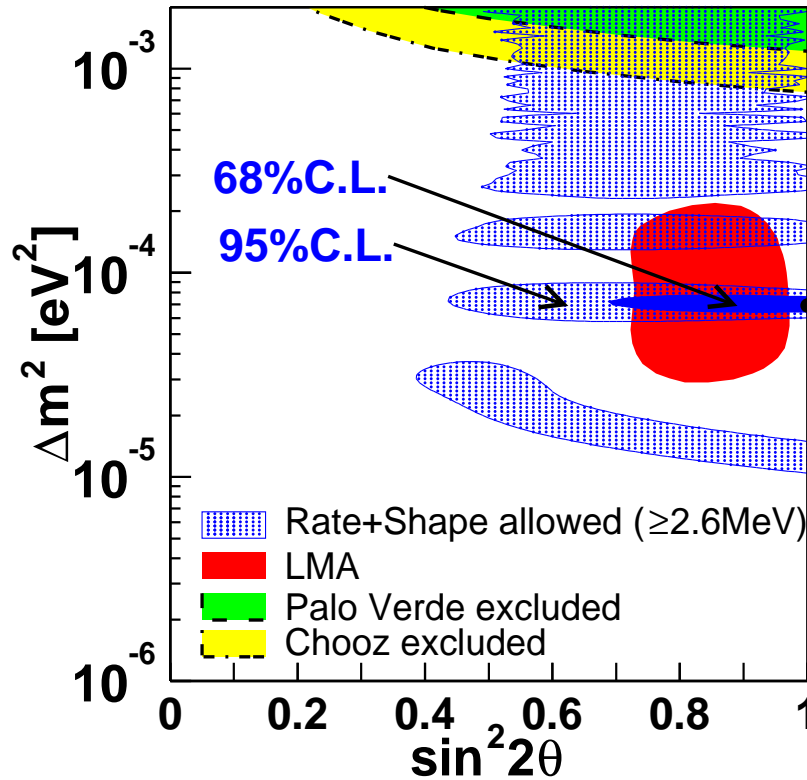


Figure 7.14: Allowed region of “rate+shape” analysis above 2.6 MeV data set. The best fit parameters are: $\sin^2 2\theta = 1.0$, $\Delta m^2 = 6.9 \times 10^{-5} \text{ eV}^2$. The lower mixing angle is rejected by the rate information. Overlap region with LMA[51] is $5.8 \sim 8.3 \times 10^{-5}$ and $1.3 \sim 1.8 \times 10^{-4} \text{ eV}^2$ at 95% C.L. for Δm^2 .

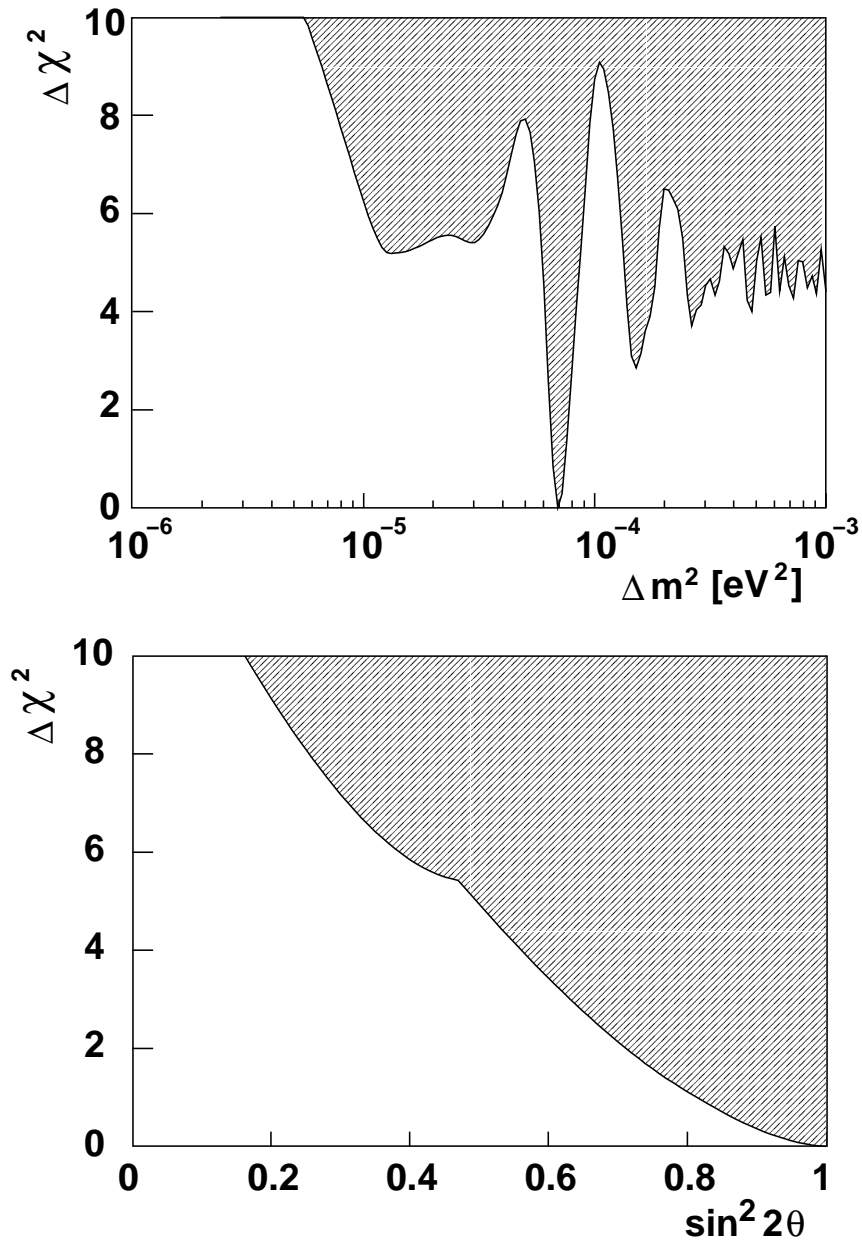


Figure 7.15: $\Delta\chi^2$ projection to Δm^2 axis and $\sin^2 2\theta$ axis above 2.6 MeV data set. $\Delta m^2 = 6 \sim 8 \times 10^{-5} \text{ eV}^2$ is favored but the confidence level is 90% C.L. ($\Delta\chi^2 = 2.71$), currently. Higher degree of the mixing angle is favored but the allowed range is not narrow $\theta = 27^\circ \sim 63^\circ$ at 90% C.L.

7.2.5 Analysis results at 0.9 MeV threshold case

Result from only energy spectrum information

The best fit parameters of “shape only” analysis above 0.9 MeV analysis threshold are;

$$\sin^2 2\theta = 0.99, \quad \Delta m^2 = 6.9 \times 10^{-5} \text{ eV}^2$$

$$(n_{aci.}, n_{he}, n_{li}, n_u, n_{th}) = (2, 1, 0, 3, 5).$$

The allowed region is shown in Figure 7.16. It is almost same contour as higher threshold case, but its sensitivity is worse than that because of extra free parameters for Geo $\bar{\nu}_e$'s.

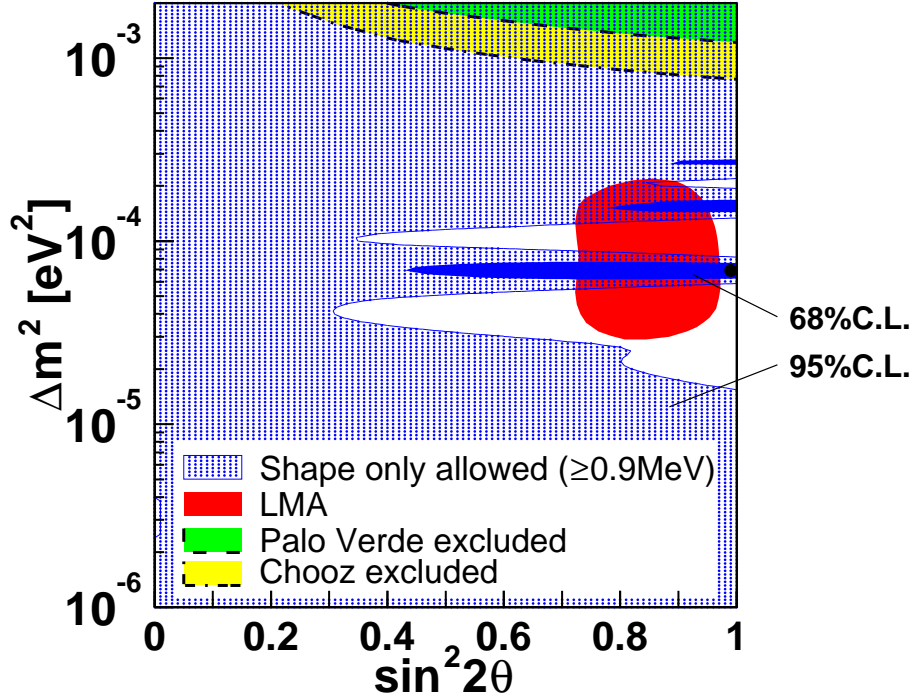


Figure 7.16: Allowed region from shape only analysis above 0.9 MeV data set. The best fit parameters are $\sin^2 2\theta = 0.99$ and $\Delta m^2 = 6.9 \times 10^{-5} \text{ eV}^2$.

Result from rate + shape information

The best fit parameters of “rate + shape” analysis is a little different from “shape only” result. These values are;

$$\sin^2 2\theta = 0.91, \quad \Delta m^2 = 6.9 \times 10^{-5} \text{ eV}^2$$

$$(n_{aci.}, n_{he}, n_{li}, n_u, n_{th}) = (2, 1, 0, 4, 5).$$

The prompt energy spectra of detected data and best fit parameters is shown in Figure 7.17. Contributions of accidental background and Geo $\bar{\nu}_e$ are observed in lower energy range (0.9 ~ 2.6 MeV). The allowed region in Δm^2 - $\sin^2 2\theta$ plane is shown in Figure 7.18, and $\Delta\chi^2$ projections to Δm^2 axis and $\sin^2 2\theta$ axis are shown in Figure 7.19. These are also almost same as higher threshold analysis case, but sensitivities are little worse because of extra free parameters for Geo $\bar{\nu}_e$'s. At the best fit, the intensity of Geo $\bar{\nu}_e$'s corresponds to ~ 40 TW radiogenic heat generation according to model Ia in [39]. However, for the same model, Geo $\bar{\nu}_e$'s production powers from 0 to 110 TW are still allowed at 95% C.L. with the same oscillation parameters. In Figure 7.20, all results from “rate” analysis and two types of “rate + shape” analysis are drawn in a same plane. The good agreement is observed in two types of threshold analysis.

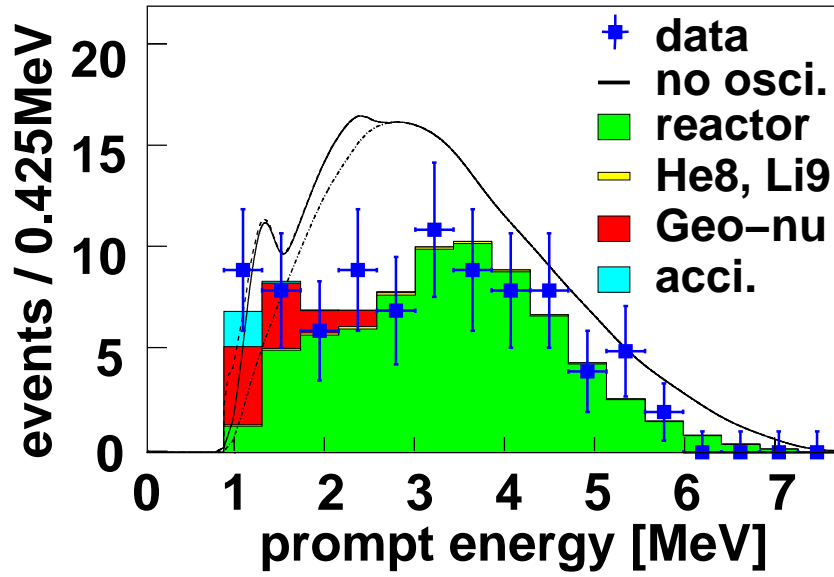


Figure 7.17: Prompt energy spectra of data (marker) and best fit parameters (histogram) of “rate+shape” analysis above 0.9 MeV data set. The best fit parameters are $\sin^2 2\theta = 0.91$ and $\Delta m^2 = 6.9 \times 10^{-5} \text{ eV}^2$. The solid line means the prompt energy spectrum in no oscillation case. Contributions of accidental background and Geo $\bar{\nu}_e$ ’s are observed in lower energy range (0.9 ~ 2.6 MeV). The numbers of Geo $\bar{\nu}_e$ ’s events for the best fit are four for ^{238}U and five for ^{232}Th , which corresponds to ~ 40 TW radiogenic heat generation according to model Ia in [39]. However, for the same model, Geo $\bar{\nu}_e$ ’s production powers from 0 to 110 TW are still allowed at 95% C.L. with the same oscillation parameters.

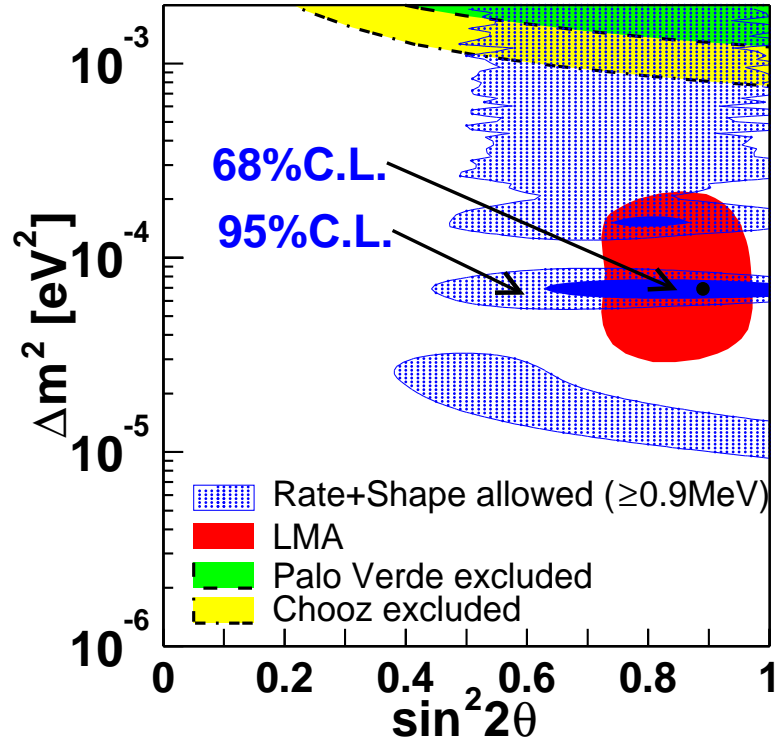


Figure 7.18: Allowed region of “rate+shape” analysis above 0.9 MeV data set. The best fit parameters are $\sin^2 2\theta = 0.91$ and $\Delta m^2 = 6.9 \times 10^{-5} \text{ eV}^2$. The allowed region is almost same as higher threshold case, but its sensitivity is little worse than that because of free parameters for Geo $\bar{\nu}_e$.

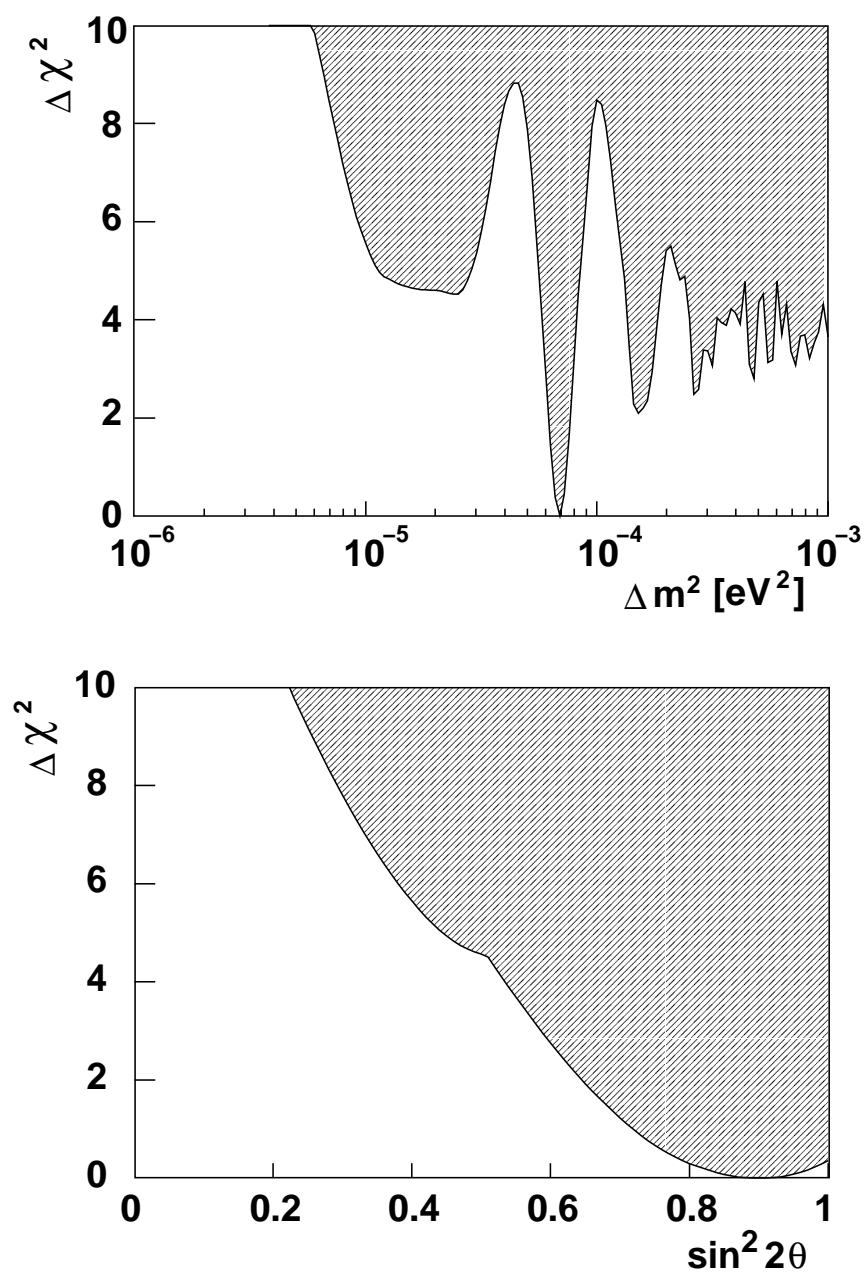


Figure 7.19: $\Delta\chi^2$ projection to Δm^2 axis and $\sin^2 2\theta$ axis above 0.9 MeV data set. These are almost same as higher threshold case.

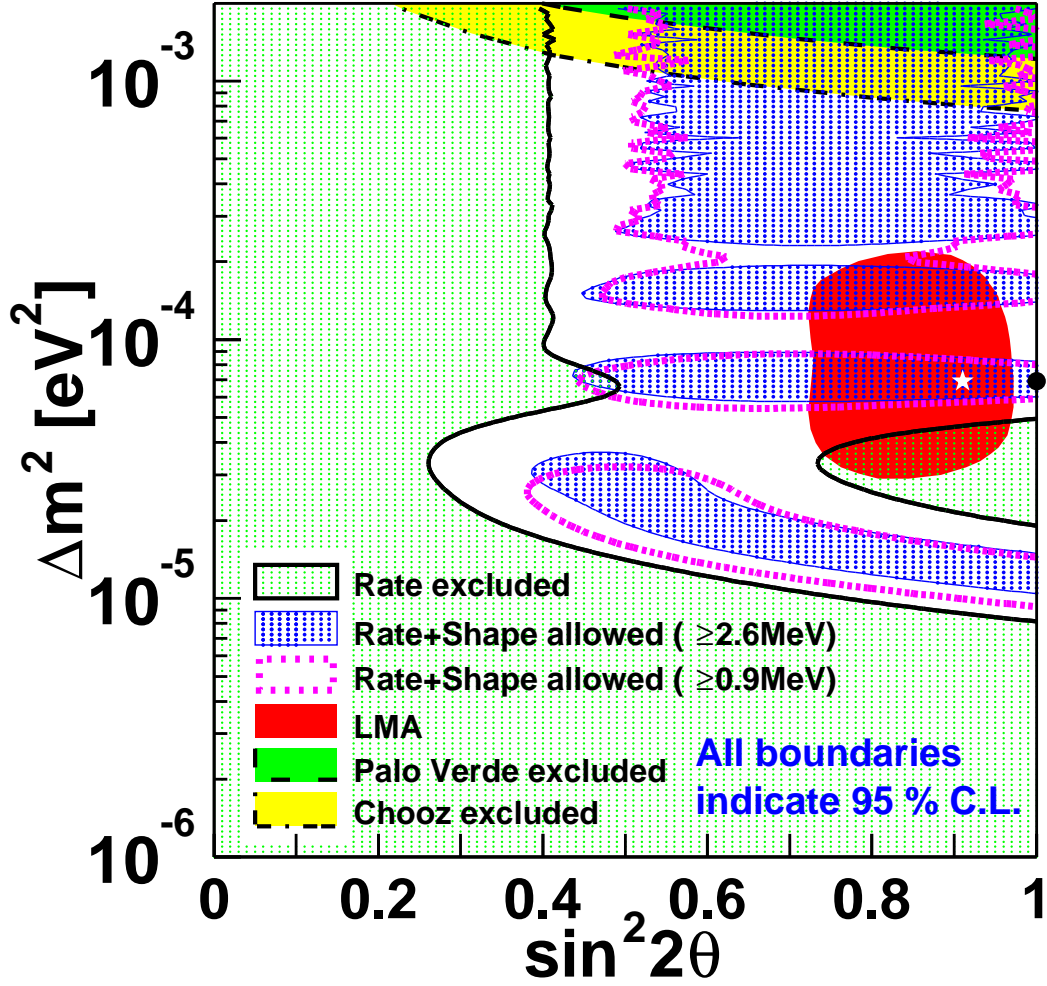


Figure 7.20: Excluded region of neutrino oscillation parameters for the “Rate” analysis at 95% C.L. and 95% C.L. allowed region for the “Rate + Shape” analysis above 2.6MeV energy threshold (“HAT”) and above 0.9MeV one (“LAT”) from KamLAND. Time correlation between prompt and delayed events are within $660\mu\text{sec}$. These allowed regions are consistent with each other. The thick dot indicates the best fit parameters for HAT analysis in the physical region: $\sin^2 2\theta = 1.0$ and $\Delta m^2 = 6.9 \times 10^{-5} \text{eV}^2$, and the star marker indicates the best fit parameters for LAT analysis: $\sin^2 2\theta = 0.91$ and $\Delta m^2 = 6.9 \times 10^{-5} \text{eV}^2$. At the top are the 95% C.L. excluded region from CHOOZ[11] and Palo Verde[23] experiments, respectively. The 95% C.L. allowed region of the ‘Large Mixing Angle’(LMA) solution of solar neutrino experiments[51] is also shown.

7.3 Matter effects in reactor anti-neutrino analysis

Currently, the matter effects is ignored for reactor $\bar{\nu}_e$ analysis because the path length in the Earth is small (~ 200 km). However, the matter effects cause the difference for the oscillation analysis as shown in Figure 7.21, and it has been already described in [53]. The constant density of the crust is assumed ($\rho = 2.7 \text{ g/cm}^3$) for the estimation of the matter effects. In fact, the density varies around 10 % in various area in Japan. But 10 % difference of the crust density gives 0.5 % of difference for the reactor $\bar{\nu}_e$ event rate. The maximum affection is +4.3 % at $\sin^2 2\theta=0.86$, $\Delta m^2=3.5 \times 10^{-5} \text{ eV}^2$.

Figure 7.22 and 7.23 show the difference between vacuum oscillation case and matter oscillation case for “rate” and “rate + shape” analysis. Differences are observed, while these are tiny.

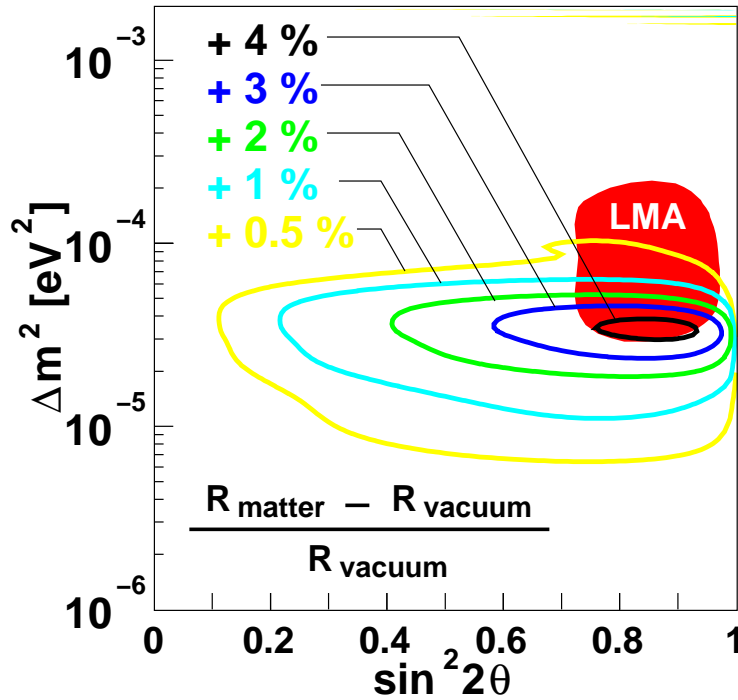


Figure 7.21: Affection of the matter effect in KamLAND reactor $\bar{\nu}_e$ analysis. R_{matter} (R_{vacuum}) means reactor anti-neutrino event rate considered with (without) matter effect. The maximum affection is +4.3 % at $\sin^2 2\theta=0.86$, $\Delta m^2=3.5 \times 10^{-5} \text{ eV}^2$. 2.7 g/cm^3 is assumed as the density of the crust. The density varies around 10 % in various area in Japan. 10 % difference of the crust density gives 0.5 % of difference for the reactor $\bar{\nu}_e$ event rate.

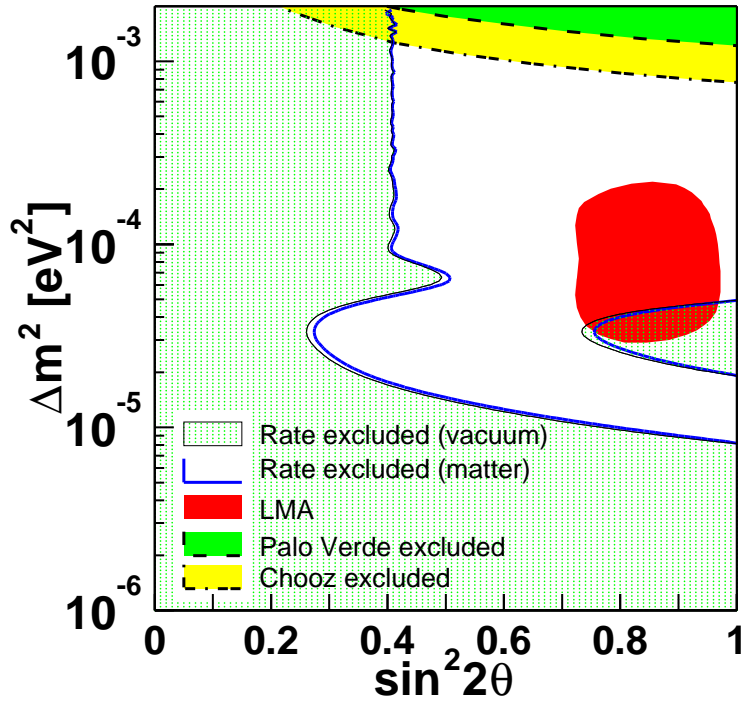


Figure 7.22: Affection of the matter effect for the “rate” analysis. The sensitivity for $\sin^2 2\theta$ is a little changed. Both of boundaries indicate 95% C.L.

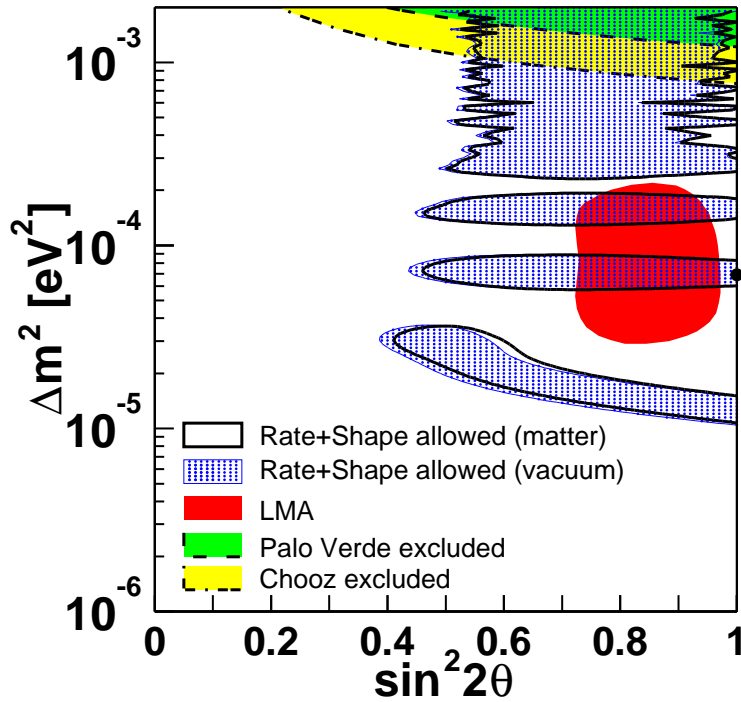


Figure 7.23: Affection of the matter effect for the “rate + shape” analysis above 2.6 MeV analysis threshold. Both of best fit parameters are same for each other, and both of boundaries indicate 95% C.L. It is almost no affection for the sensitivity of Δm^2 currently, but a tiny difference is observed for the mixing angle.

7.4 Sensitivity for the 3 generation oscillation analysis

The oscillation analysis for 3 generation is essential to measure θ_{12} . According to Eq.(1.16), the survival probability of $\bar{\nu}_e$ is,

$$P(\bar{\nu}_e \rightarrow \bar{\nu}_e) = \sin^4 \theta_{13} + \cos^4 \theta_{13} \left[1 - \sin^2 2\theta_V \sin^2 \left(\frac{1.27 \Delta m_{23}^2 [\text{eV}^2] l [\text{m}]}{E [\text{MeV}]} \right) \right], \quad (7.14)$$

where relations, $\Delta m_{13} \sim \Delta m_{23}$ and $\sin^2 \left(\frac{1.27 \Delta m_{23}^2 [\text{eV}^2] l [\text{m}]}{E [\text{MeV}]} \right) \sim \frac{1}{2}$ ($l \sim 180 \text{ km}$ and $E \sim 4 \text{ MeV}$), are assumed.

The sensitivity for θ_{13} is shown in Figure 7.24. In this figure, $\Delta m_{12}^2 = 6.9 \times 10^{-5} \text{ eV}^2$ is assumed. KamLAND has no sensitivity for θ_{13} by contrast with CHOOZ exclusion [11].

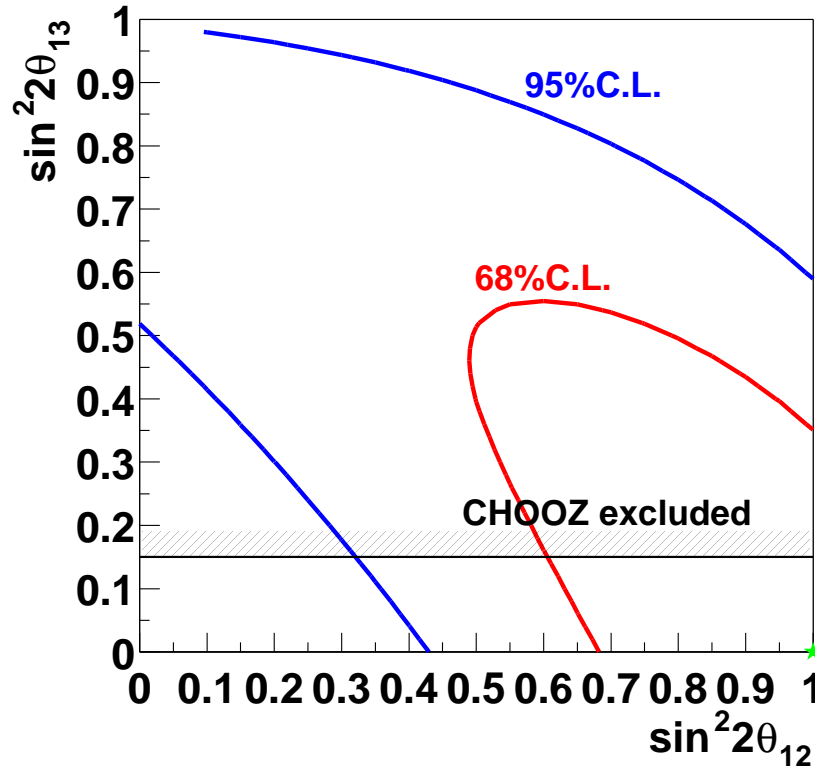


Figure 7.24: Sensitivity for θ_{13} by supposing $\Delta m_{12}^2 = 6.9 \times 10^{-5} \text{ eV}^2$. Allowed region from maximum likelihood analysis is drawn. The best fit parameters are $\sin^2 \theta_{12} = 1.0$ and $\sin^2 \theta_{13} = 0.0$. KamLAND has no sensitivity for θ_{13} by contrast with CHOOZ exclusion [11].

The lower angle is allowed for θ_{12} because of the limitation for θ_{13} . Figure 7.25 shows allowed region for Δm_{12}^2 and $\sin^2 2\theta_{12}$.

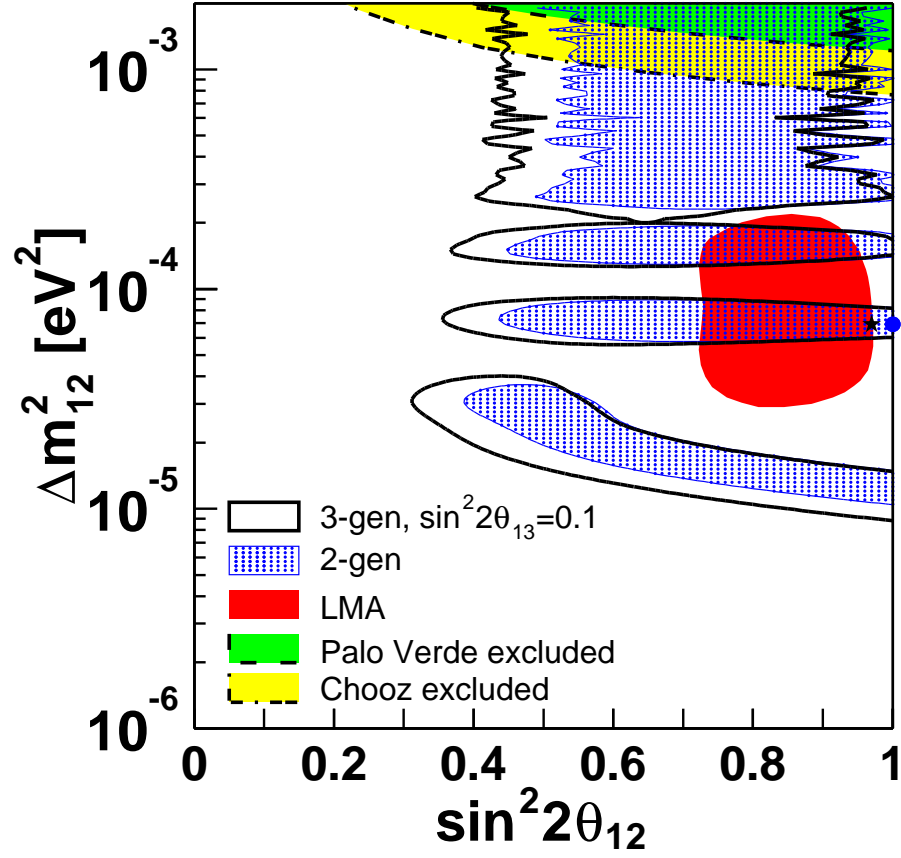


Figure 7.25: Sensitivity for Δm^2_{12} and $\sin^2 2\theta_{12}$ at $\sin^2 2\theta_{13} = 0.1$ case. 2 generation analysis case is drawn in the same plane for the comparison, while it cannot be drawn in the same plane actually. The lower angle is allowed for θ_{12} because of the limitation for θ_{13} .

Chapter 8

Summary

The solar neutrino anomaly, deficit of solar neutrinos, had not been solved more than 30 years. Recently, neutrino oscillation of ν_μ and flavor transition of solar neutrinos are evident. Yet, oscillation parameters of ν_e to explain the deficit of solar neutrinos had not been determined strictly. The LMA region is the most convincing parameter region from the global analysis using all solar neutrino experiments. But there was no experiment to determine it by itself. The determination of oscillation parameters is the last subject for the solar neutrino anomaly.

The KamLAND, which is a $\bar{\nu}_e$ detector containing a 1,000 tons of large volume liquid scintillator, started data taking from January 22, 2002. The data set for reactor $\bar{\nu}_e$ analysis is during a period from March 4 through October 6, 2002, the total runtime for the analysis is 163.80 days. A systematic error for reactor $\bar{\nu}_e$ detection at this period is 6.43%.

The $\bar{\nu}_e$ is detected via correlated two events, i.e. prompt event of positron ($E_{\bar{\nu}_e} - 0.78\text{MeV} > 1.022\text{ MeV}$) and delayed event of neutron capture gamma ($\sim 2.22\text{ MeV}$). The positron and the neutron are generated from inverse β -decay ($\bar{\nu}_e + p \rightarrow n + e^+$). The delayed coincidence selects these correlated events, and its selection criteria are;

- Time correlation cut ($0.5\ \mu\text{sec} \leq \Delta T \leq 660\ \mu\text{sec}$)
- Vertex correlation cut ($\Delta R \leq 1.6\text{m}$)
- Delayed energy window cut ($1.8\text{ MeV} \leq E_{\text{delayed}} \leq 2.6\text{ MeV}$).

The accidental background is strongly suppressed by them, and the reduction factor is about 1/10,000.

The fiducial cut, muon veto, spallation cut and deadtime veto are applied for the background rejection.

The fiducial cut criteria are decided by the study of the accidental coincidence background,

- Fiducial radius cut ($R \leq 5\text{ m}$)
- Cylindrical cut within 1.2 m along central vertical axis (z-axis) only for the delayed events. This cut eliminates the radiation from thermometers which are deployed along z-axis.

Its reduction factor is about 1/140.

The spallation cut, muon veto and deadtime veto criteria are decided based on the study of spallation products and deadtime,

- Veto whole volume for 2 msec following muon
- Veto whole volume for 2 sec following energetic muon or miss track reconstructed one.
- Veto cylindrical region ($r \leq 3\text{ m}$) along muon track for 2 sec following non-energetic muon, this cut is only applied to the delayed event.

After the delayed coincidence selection, the fiducial and spallation cuts, remained number of $\bar{\nu}_e$ candidates is 86 events.

Due to the ambiguity associated with Geo $\bar{\nu}_e$ below 2.49 MeV for the prompt energy, the analysis of reactor $\bar{\nu}_e$ is performed above 2.6 MeV prompt energy usually. The analysis with lower energy region (≤ 0.9 MeV) is used for the consistency check of analysis. The contributions of Geo $\bar{\nu}_e$'s are handled as free parameters in the oscillation analysis. The number of detected reactor $\bar{\nu}_e$ candidate above 2.6 MeV prompt energy is 54 events.

The delayed coincidence selection and fiducial cut reject un-correlated accidental background to 0.009 events ($\sim 0.02\%$ of $\bar{\nu}_e$ candidates). Spallation cut, muon veto and deadtime veto reject the correlated background derived from spallation, and remained spallation background is 0.94 ± 0.85 events ($\sim 1.7\%$ of $\bar{\nu}_e$ candidates). Fast neutron background is < 0.5 events ($< 1\%$ of $\bar{\nu}_e$ candidates), which is estimated based on the measurement using the delayed coincidence and outer detector hit information. Total number of background is 0.95 ± 0.99 events above 2.6 MeV prompt energy ($\sim 2\%$ of $\bar{\nu}_e$ candidates).

The information of each reactor is provided from each reactor frequently. Especially, it is provided every hour when reactor operation is changed. The reactor $\bar{\nu}_e$ flux is calculated from the reactor thermal power and fuel composition of each reactor within 2.29% accuracy. The efficiency of $\bar{\nu}_e$ detection is 78.3%, and it is calibrated with radioactive sources, ^{68}Ge , ^{65}Zn , ^{60}Co and Am-Be. The spallation cut and muon and deadtime veto reduce the analysis livetime to be 145.09 days, it is 88.6% of the runtime. The number of expected reactor $\bar{\nu}_e$ events in no oscillation case is 86.78 ± 5.59 events above 2.6 MeV prompt energy.

The ratio of $(N_{\text{detected}} - N_{\text{BG}})/N_{\text{expected}}$ is $0.611 \pm 0.085(\text{stat}) \pm 0.041(\text{syst})$. The observed $\bar{\nu}_e$ rate is clearly fewer than the expectation. The significance of the disappearance for reactor $\bar{\nu}_e$ is 99.95%. In the context of two-flavor neutrino oscillation with CPT invariance, hypothesis test between the detected event rate and the expected rate for each oscillation parameter set excludes all but LMA solar neutrino oscillation solutions. It is no exaggeration to say that the last subject of the solar neutrino anomaly is solved.

The neutrino oscillations also cause the energy spectrum distortion. This distortion is related with oscillation parameters, especially for Δm^2 . Therefore, more precise parameter estimation is performed using the prompt energy spectrum distortion as well as the event rate. Currently, $\Delta m^2 = 6 \sim 8 \times 10^{-5} \text{ eV}^2$ is favored at 90% C.L., but higher statistics may be essential for higher confidence. For mixing angle, higher degree is favored but its allowed range is not narrow: $\theta = 27^\circ \sim 63^\circ$ at 90% C.L. The analysis with lower threshold is consistent.

In conclusion, all solar neutrino solutions but LMA are excluded with observing the reactor $\bar{\nu}_e$ disappearance in KamLAND. The measured oscillation parameter region is consistent with LMA. The result of this thesis indicates that Δm^2 is higher than $5 \times 10^{-5} \text{ eV}^2$ if the global analysis of solar neutrino experiments is true. This may be a good news for future experiments to measure CP violation in the lepton sector.

Appendix A

KamLAND collaboration

K. Eguchi,¹ S. Enomoto,¹ K. Furuno,¹ J. Goldman,¹ H. Hanada,¹ H. Ikeda,¹ K. Ikeda,¹ K. Inoue,¹ K. Ishihara,¹ W. Itoh,¹ T. Iwamoto,¹ T. Kawaguchi,¹ T. Kawashima,¹ H. Kinoshita,¹ Y. Kishimoto,¹ M. Koga,¹ Y. Koseki,¹ T. Maeda,¹ T. Mitsui,¹ M. Motoki,¹ K. Nakajima,¹ M. Nakajima,¹ T. Nakajima,¹ H. Ogawa,¹ K. Owada,¹ T. Sakabe,¹ I. Shimizu,¹ J. Shirai,¹ F. Suekane,¹ A. Suzuki,¹ K. Tada,¹ O. Tajima,¹ T. Takayama,¹ K. Tamae,¹ H. Watanabe,¹ J. Busenitz,² Z. Djurcic,² K. McKinny,² D.-M. Mei,² A. Piepke,² E. Yakushev,² B.E. Berger,³ Y.D. Chan,³ M.P. Decowski,³ D.A. Dwyer,³ S.J. Freedman,³ Y. Fu,³ B.K. Fujikawa,³ K.M. Heeger,³ K.T. Lesko,³ K.-B. Luk,³ H. Murayama,³ D.R. Nygren,³ C.E. Okada,³ A.W. Poon,³ H.M. Steiner,³ L.A. Winslow,³ G.A. Horton-Smith,⁴ R.D. McKeown,⁴ J. Ritter,⁴ B. Tipton,⁴ P. Vogel,⁴ C.E. Lane,⁵ T. Miletic,⁵ P. Gorham,⁶ G. Guillian,⁶ J. Learned,⁶ J. Maricic,⁶ S. Matsuno,⁶ S. Pakvasa,⁶ S. Dazeley,⁷ S. Hatakeyama,⁷ M. Murakami,⁷ R.C. Svoboda,⁷ B.D. Dieterle,⁸ M. DiMauro,⁸ J. Detwiler,⁹ G. Gratta,⁹ K. Ishii,⁹ N. Tolich,⁹ Y. Uchida,⁹ M. Batygov,¹⁰ W. Bugg,¹⁰ H. Cohn,¹⁰ Y. Efremenko,¹⁰ Y. Kamyshev,¹⁰ A. Kozlov,¹⁰ Y. Nakamura,¹⁰ C.R. Gould,¹¹ H.J. Karwowski,¹¹ D.H. Markoff,¹¹ J.A. Messimore,¹¹ K. Nakamura,¹¹ R.M. Rohm,¹¹ W. Tornow,¹¹ A.R. Young,¹¹ and Y.-F. Wang¹²

¹ Research Center for Neutrino Science, Tohoku University, Sendai 980-8578, Japan

² Department of Physics and Astronomy, University of Alabama, Alabama 35487, USA

³ Physics Department, University of California at Berkeley and Lawrence Berkeley National Laboratory, Berkeley, California 94720, USA

⁴ W. K. Kellogg Radiation Laboratory, California Institute of Technology, Pasadena, California 91125, USA

⁵ Physics Department, Drexel University, Philadelphia, Pennsylvania 19104, USA

⁶ Department of Physics and Astronomy, University of Hawaii at Manoa, Honolulu, Hawaii 96822, USA

⁷ Department of Physics and Astronomy, Louisiana State University, Louisiana 70803, USA

⁸ Physics Department, University of New Mexico, Albuquerque New Mexico 87131, USA

⁹ Physics Department, Stanford University, California 94305, USA

¹⁰ Physics Department, University of Tennessee, Tennessee 37996, USA

¹¹ Triangle Universities Nuclear Laboratory, Durham, NC 27708, USA and

Physics Departments at Duke University, North Carolina State University, and the University of North Carolina at Chapel Hill

¹² Institute of High Energy Physics, Beijing 100039, People's Republic of China

Appendix B

Trigger Types

The different triggers can be enabled or disabled in almost any combination at run begin. The trigger types are;

- ID global trigger
This is based on the total ID Nsum being above the ID global trigger threshold (200hits). It issues a global acquisition trigger to the ID FEE cards.
- ID prompt & delay trigger
The prompt trigger is based on the total ID Nsum being above the prompt threshold (200hits). It issues a global acquisition trigger to the ID FEE cards and opens a 1 msec window for the delayed trigger. The delayed trigger is based on the total ID Nsum being above the delayed threshold (120hits) during this window. It issues a global acquisition trigger to the ID FEE cards.
- ID prescale trigger
This is based on the total ID Nsum being above the ID global trigger threshold (200hits), but it only issues a global acquisition trigger to the ID FEE cards for a fraction of each second.
- ID history trigger
This is based on the total ID Nsum being above the ID history trigger threshold (120hits) and is issued every 25nsec while above threshold up to a maximum of 200nsec. It does not issue any external triggers.
- 5 inch trigger
This is based on the total 5 inch Nsum being above the 5 inch trigger threshold. It issues a global acquisition trigger to the ID FEE cards (note the 5 inch tubes FEE card is in crate 1).
- OD top, upper side, lower side, and bottom global trigger
This is based on the total Nsum from the OD tubes in that section being above that section's threshold (6, 5, 6, 7 hits). It issues a global acquisition trigger to the OD FEE cards.
- OD top, upper side, lower side, and bottom history trigger
This is based on the total nsum from the OD tubes in that section being above that section's threshold (6, 5, 6, 7 hits) and is issued every 25nsec while above threshold up to a maximum of 200nsec. It does not issue an external trigger.

- ID or OD calibration forced trigger
This is based on a trigger input from any calibration device (timing calibration with laser etc). It issues a forced acquisition trigger to the ID or OD FEE cards. The PMT signal must arrive around 40nsec after the trigger command.
- ID or OD calibration global trigger
This is based on a trigger input from any calibration device (timing calibration with laser etc). It issues a global acquisition trigger to the ID or OD FEE cards. The timing for this command should be correct if the system was set-up correctly for the ID or OD calibration forced trigger.
- ID or OD calibration delayed trigger
This is based on a trigger input from any calibration device (timing calibration with laser etc) delayed by 375nsec. It does not issue an external trigger. This is used to calculate the occupancy of the calibration device.
- Acquire trigger
This sends one of forced acquisition A or B, acquire clock A or B, test-pulser A or B, acquire pedestal A or B, test-pulser followed by forced acquisition A or B, or test-pulser no acquisition, to all FEE cards. The number of triggers and period can be adjusted, and they can be issued in the middle of a run.
- OD to ID trigger
This sends a global trigger command to all ID crates for every 10 OD global triggers.
- ID to OD trigger
This sends a global trigger command to the OD crate for every ID global trigger.
- 1pps trigger
This is based on the GPS 1 pps signal. It does not issue an external trigger.
- GPS trigger
This is issued at the start of run and every 32 seconds thereafter. It issues an interrupt to the GPS VME module to capture the time. This trigger can not be disabled.
- Supernova trigger
This based on there being 48 events with total ID Nsum above 772 in 0.84 seconds (\sim run875) or 8 events greater than 772 in 0.8 second. This is veto for 1msec after 1250hits event from run936 (1300hits event from run876 \sim run935, no veto before run876). This sends an interrupt to the DAQ, notifying the shift person so data acquisition is not stopped. It also puts the trigger into a predefined data acquisition state for
 - 4 minutes $\cdots \sim$ run875
 - 2 minutes \cdots run876 \sim run935
 - 1 minutes \cdots run936 \sim

1pps and 5inch trigger was disable in this periods before run876. Currently that state is global triggers with a threshold of 200 and history trigger with a threshold of 100.
- Macro singles trigger
This is based on the total ID Nsum being above the global threshold, this is prescaled

to every n th event and issues a short stop to the FME (optional FEE, Front end Macro Electronics) 40us later.

- Macro coincidence trigger
This is based on the same as the delayed trigger and issues a long stop to the FME 200us later.
- Macro random trigger
This is issued every 32 seconds and issues a short stop to the FME.
- Macro muon trigger
This is based on the total ID Nsum being above the Macro muon threshold for a specified amount of time and issues a short stop to the FME 40us after the condition is met.

Table B.1: Trigger types as recorded by the trigger

trigger-type (HEX)	Function (* Can not occur at the same time # Can not occur at the same time)
000:000:001	ID global trigger
000:000:002	ID history trigger
000:000:004	5 inch trigger
000:000:008	1pps trigger
000:000:010	acquire trigger: forced acquisition A *
000:000:020	acquire trigger: forced acquisition B *
000:000:030	acquire trigger: clock acquisition A *
000:000:040	acquire trigger: clock acquisition B *
000:000:050	acquire trigger: test pulser acquisition A *
000:000:060	acquire trigger: test pulser acquisition B *
000:000:070	acquire trigger: pedestal acquisition A *
000:000:080	acquire trigger: pedestal acquisition B *
000:000:090	acquire trigger: test pulser followed by forced acquisition A *
000:000:0a0	acquire trigger: test pulser followed by forced acquisition B *
000:000:0b0	acquire trigger: test pulser no acquisition *
000:000:100	prescale trigger
000:000:200	GPS trigger
000:000:400	delayed calibration trigger
000:000:800	supernova trigger
000:001:000	ID calibration forced trigger: source 1 #
000:002:000	ID calibration forced trigger: source 2 #
000:003:000	ID calibration forced trigger: source 3 #
000:004:000	ID calibration forced trigger: source 4 #
000:005:000	ID calibration forced trigger: source 5 #
000:006:000	OD calibration forced trigger: source 1 #
000:007:000	OD calibration forced trigger: source 2 #
000:009:000	ID calibration global trigger: source 1 #
000:00a:000	ID calibration global trigger: source 2 #
000:00b:000	ID calibration global trigger: source 3 #
000:00c:000	ID calibration global trigger: source 4 #
000:00d:000	ID calibration global trigger: source 5 #
000:00e:000	OD calibration global trigger: source 1 #
000:00f:000	OD calibration global trigger: source 2 #
000:100:000	OD global trigger top section
000:200:000	OD global trigger upper side section
000:400:000	OD global trigger lower side section
000:800:000	OD global trigger bottom section
001:000:000	Delayed trigger
002:000:000	Prompt trigger
004:000:000	OD to ID trigger
008:000:000	ID to OD trigger
010:000:000	OD history trigger top section
020:000:000	OD history trigger upper side section
040:000:000	OD history trigger lower side section
080:000:000	OD history trigger bottom section
400:000:000	Trigger disabled
800:000:000	Trigger enabled

Appendix C

Decay of ^{238}U , ^{232}Th and ^{40}K

C.1 ^{238}U series

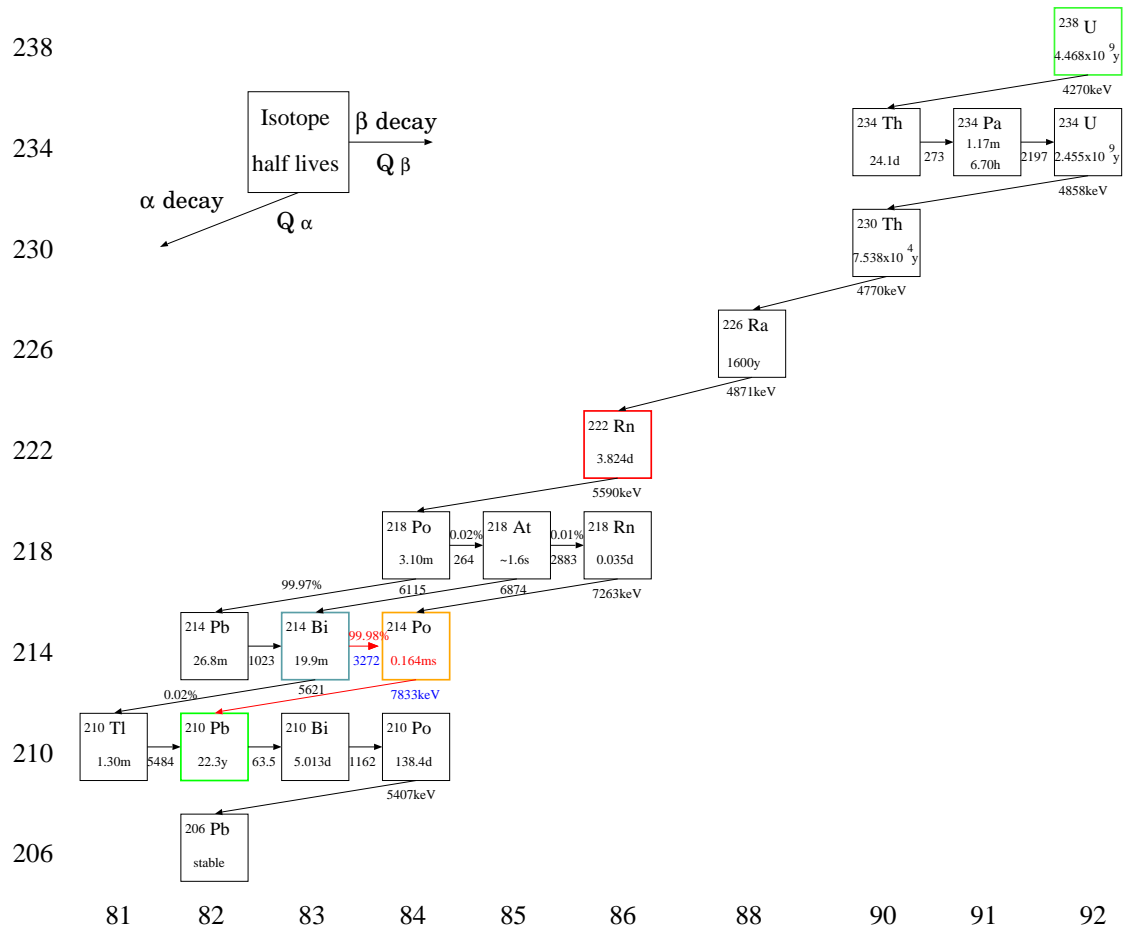
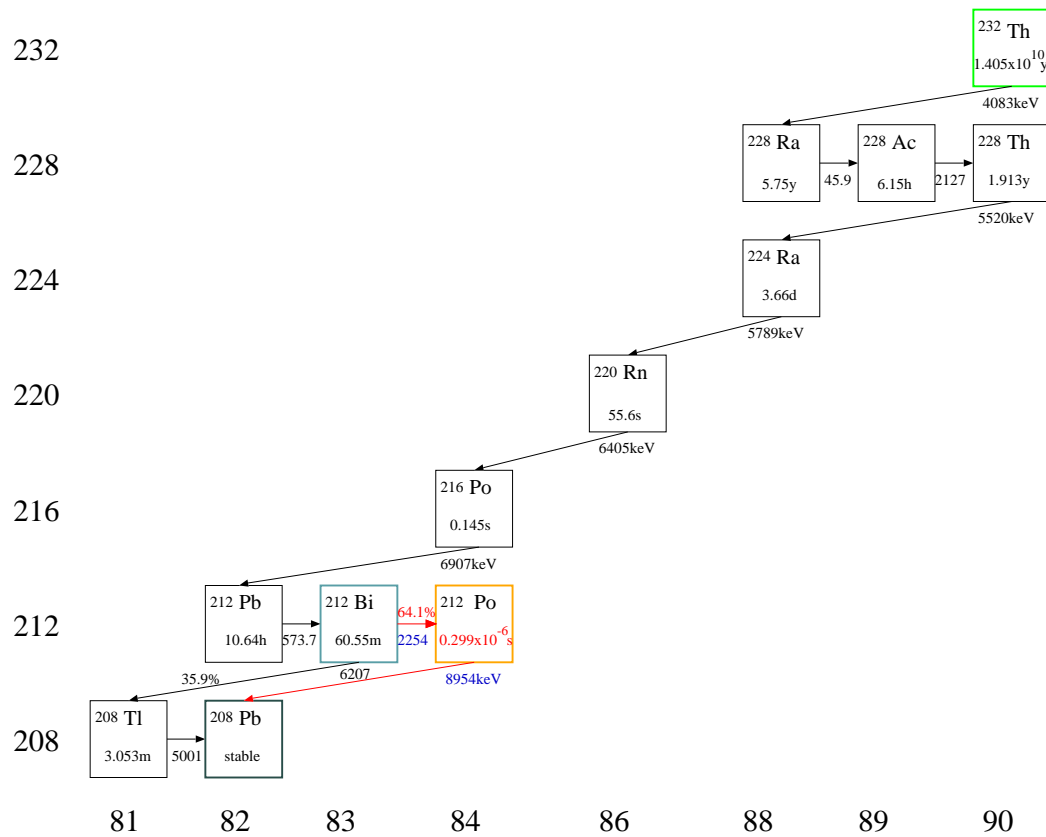
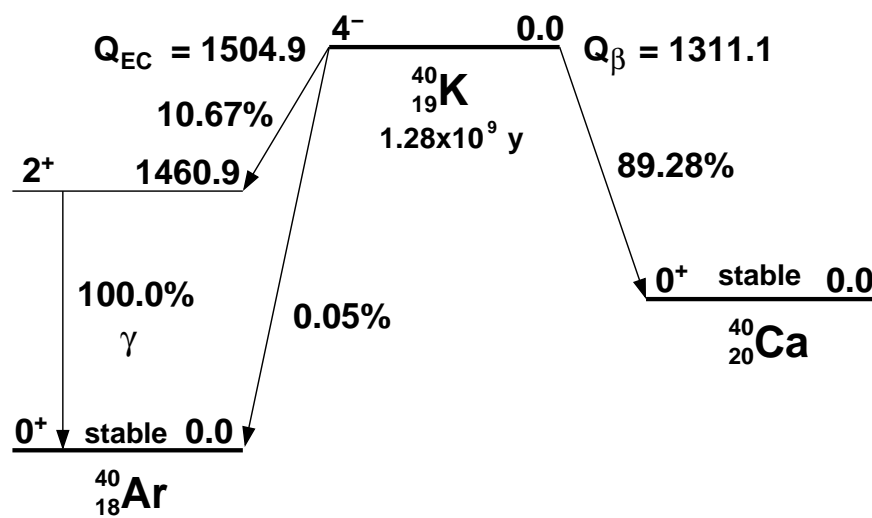


Figure C.1: Decay chain of ^{238}U series

C.2 ^{232}Th seriesFigure C.2: Decay chain of ^{232}Th seriesC.3 Level diagram for ^{40}K Figure C.3: Level diagram for ^{40}K

Isotope	Energy (keV)	BR (%)	Isotope	Energy (keV)	BR (%)	Isotope	Energy (keV)	BR (%)
^{238}U ($4.468 \times 10^9\text{y}$)	E_α		^{226}Ra (1600y)	E_α		^{214}Bi	E_γ	
	4220	20.9		4685	5.55		609	43.7
	4270	79.0		4871	94.45		665	1.45
	E_γ			E_γ			768	4.61
	50	20.9		186	5.55		934	2.94
^{234}Th (24.10d)	E_β		^{222}Rn (3.824d)	E_α			1120	14.9
	86	2.9		5590	99.92		1155	1.65
	106	7.6	^{218}Po (3.10m)	E_α			1281	1.46
	107	19.2		6115	99.979		1377	3.77
	199	70.3	^{214}Pb (26.8m)	E_β			1402	1.55
	E_γ			184	2.35		1408	2.85
	30	5.66		489	1.04		1416	1.00
	63	4.89		671	46		1509	2.17
	92	19.1		727	40.5		1661	1.06
	93	2.79		1023	9.3		1730	2.90
	113	2.19		E_γ			1847	2.06
				242	1.07		2119	1.17
				295	39.5		2204	4.86
				352	46.5			
			^{214}Bi (19.9m)	E_β		^{214}Po (164 μs)	E_α	
^{234}Pa (1.17m) (6.70h)	E_β			790	1.45	^{210}Tl (1.30m)	E_β	
	386	1.55		824	2.74		1379	2
	415	8		1068	5.54		1604	7
	435	2.8		1153	4.14		1238	5.92
	460	1.14		1255	2.9		1859	24
	474	45.4		1261	1.66		2024	10
	503	7.0		1277	1.38		2414	10
	644	19.4		1382	1.59		4205	30
	1002	1.1		1425	8.26		4386	20
	1069	2.9		1508	16.9	^{210}Pb (22.3y)	E_β	
^{234}U ($2.455 \times 10^9\text{y}$)	E_α			1542	17.5		17	84
	4805	28.42		1729	3.05		64	16
	4858	71.38		1894	7.18		E_γ	
	E_γ			3272	19.9		47	84
	53	28.42				^{210}Bi (5.013d)	E_β	
^{230}Th ($7.538 \times 10^4\text{y}$)	E_α						1163	100
	4702	23.4				^{210}Po (138.4d)	E_α	
	4770	76.3					5407	100
	E_γ							
	68	23.4						

Table C.1: Decay chain of ^{238}U

Isotope	Energy (keV)	BR (%)	Isotope	Energy (keV)	BR (%)	Isotope	Energy (keV)	BR (%)
^{232}Th ($1.405 \times 10^{10}\text{y}$)	E_α		^{228}Ac	E_γ		^{212}Pb (10.64h)	E_β	
	4018	22.1		58	74.1		158	5.17
	4083	77.9		99	3.71		335	82.5
	E_γ			129	11.2		574	12.3
^{228}Ra (5.75y)	64	22.1		209	4.05		E_γ	
	E_β			270	4.43	^{212}Bi (60.55m)	239	82.6
	39	100		279	1.37		300	4.88
	E_γ			322	1.64		E_α	
^{228}Ac (6.15h)	7	100		338	11.7		6167	25.13
	E_β			409	1.29		6207	9.75
	403	1.57		463	2.96		E_β	
	439	2.6		504	1.64		633	1.87
	444	1.18		509	1.37		741	1.43
	481	4.18		563	2.52		1527	4.36
	489	1.15		755	1.07		2254	55.46
	596	8.1		795	4.40		E_γ	
	959	3.54		836	1.49		40	25.6
	974	5.6		911	24.1		328	4.02
	1004	5.82		965	4.79		727	6.45
	1104	3.0		969	4.79		785	1.13
	1158	31.0		1631	1.97		1621	1.50
	1731	11.6	^{228}Th (1.9131y)	E_α		^{212}Po (299ns)	E_α	
	1940	1.9		5436	28.2		8954	100
	2069	10		5520	71.1	^{208}Tl (3.053m)	E_β	
				E_γ			1040	3.09
^{224}Ra (3.66d)			^{224}Ra (3.66d)	84	28.2		1292	24.5
				E_α			1526	21.8
				5548	5.06		1803	48.7
				5789	94.94		E_γ	
			^{220}Rn (55.6s)	E_γ			277	2.66
				241	5.06		511	8.89
				E_α			583	30.0
				6405	99.89		861	5.28
			^{216}Po (0.145s)	E_α			2616	35.3
				6907	99.9981			

Table C.2: Decay chain of ^{232}Th

Appendix D

Nuclear Level Diagrams of Calibration sources

D.1 ^{68}Ge

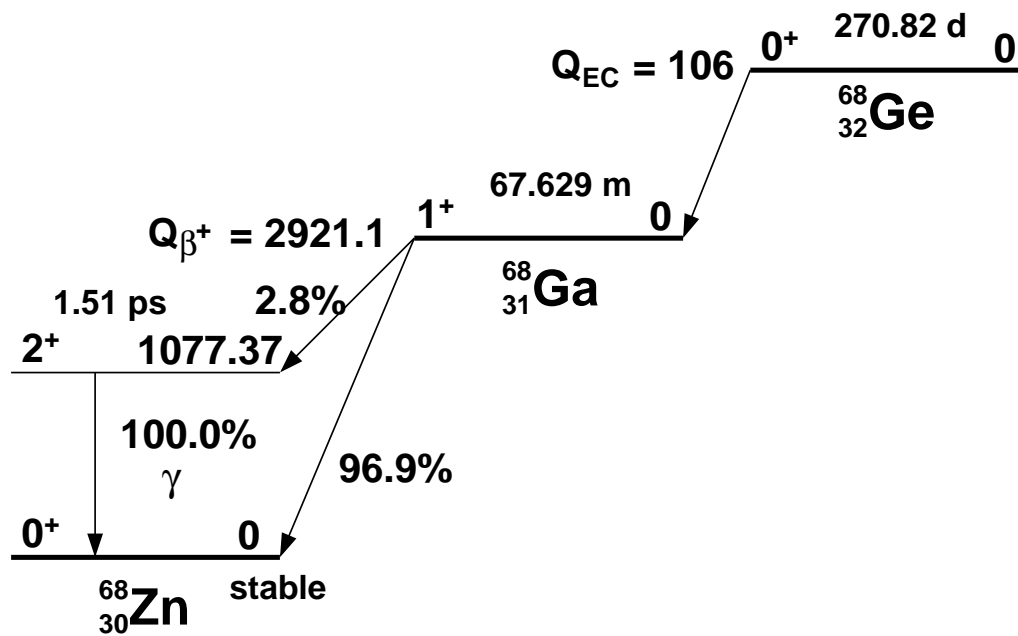
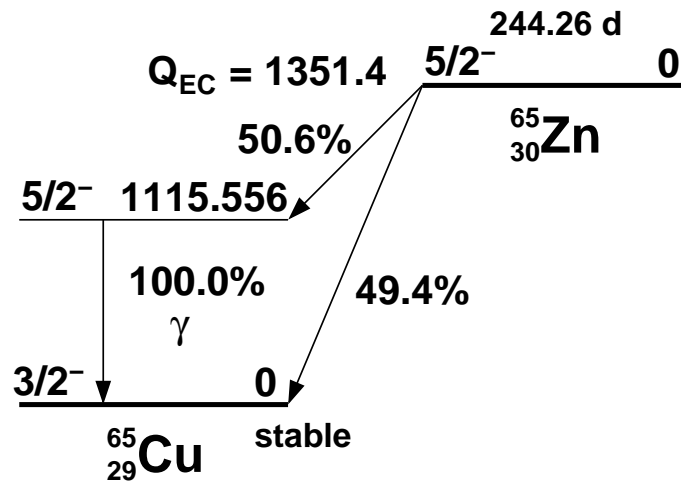
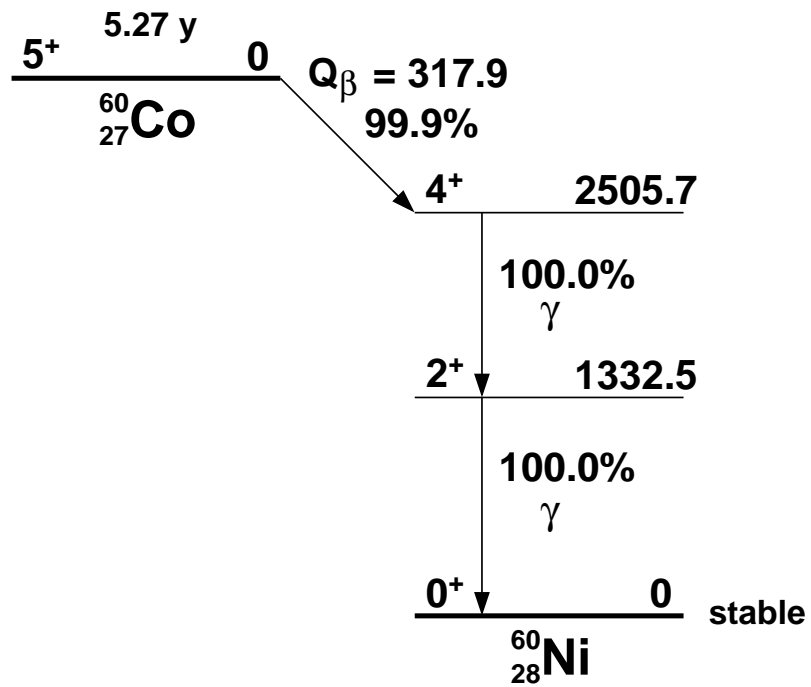


Figure D.1: Level diagram for ^{68}Ge

D.2 ^{65}Zn Figure D.2: Level diagram for ^{65}Zn D.3 ^{60}Co Figure D.3: Level diagram for ^{60}Co

Bibliography

- [1] J. N. Bahcall. <http://neutrinooscillation.org/>.
- [2] Y.Fukuda et al. *Physical Review Letters*, 81:1562–1567, 1998.
- [3] Q.R. Ahmad et al. *Physical Review Letters*, 89:011301, 2002.
- [4] These figures are made by H. Murayama. 2002.
- [5] Y. Itow et al. *hep-ex/0106019*, 2001.
- [6] P. Vogel. *Physical Review*, D29:1918–1922, 1984.
- [7] F. Reines and C.L. Cowan Jr. *Physical Review*, 113:273, 1959.
- [8] D. Harmer R. Davis and K. Hoffman. *Physical Review Letters*, 20:1205, 1968.
- [9] Z. Maki, M. Nakagawa, and S. Sakata. *Prog. Theor. Phys.*, 28:870, 1962.
- [10] M. Kobayashi and T. Masukawa. *Prog. Theor. Phys.*, 13:652, 1973.
- [11] M. Apolonio et al. *Physics Letters*, B466:415, 1999.
- [12] Y. Nagashima. *Progress of High Energy Physics (in Japanese)*. Asakura, 1999.
- [13] T. Yanagida. *Proceedings of the Workshop on Unified Theory and Baryon Number in the Universe*. KEK, Tsukuba, Japan, 1979.
- [14] M. Fukugita and A. Suzuki, editors. *Physics and Astrophysics of Neutrinos*. Springer Verlag.
- [15] Y.Totsuka Y.Suzuki, editor. *Neutrino Physics and Astrophysics*, 293-298. North Holland, 1999.
- [16] J.N. Bahcall, M.H. Pinsonneault, and S. Basu. *Astrophysics*, 555:990, 2001.
- [17] J. N. Bahcall. *Neutrino Astrophysics*. Cambridge University Press, 1989.
- [18] J.N. Bahcall, S. Basu, and M.H. Pinsonneault. *Physics Letter*, B433:1–8, 1998.
- [19] K.S. Hirata et al. *Physical Review*, D44:2241, 1991.
- [20] J.N. Abdurashitov et al. *Physical Review*, C60:055801, 1999.
- [21] P. Anselmann et al. *Physics Letter*, B327:377, 1994.
- [22] K.S. Hirata et al. *Physics Letter*, B205:416, 1988.

- [23] F. Boehm et al. *Physical Review*, D64:112001, 2001.
- [24] K. Ishihara. *Ph.D. thesis*, Tokyo univ., 1999.
- [25] Y.Fukuda et al. *Physical Review Letters*, 85:3999, 2000.
- [26] M. Shiozawa. presented at the xxth int. conf. on neutrino physics and astrophysics, munich. 2002.
- [27] M.H. Ahn et al. *Physical Review Letters*, accepted now, 2002.
- [28] Q.R. Ahmad et al. *Physical Review Letters*, 87:071301, 2001.
- [29] S. Fukuda et al. *Physical Review Letters*, 86:5651, 2001.
- [30] S. Fukuda et al. *Physical Review Letters*, 86:5656, 2001.
- [31] Particle Data Group. *Physical Review*, D66:010001–406, 2002.
- [32] H. Kume et al. *Nuclear Instrument and Method*, 205:443, 1986.
- [33] O. Tajima. master thesis, 2000.
- [34] P. Vogel and J.F. Beacom. *Physical Review*, D60:053003, 1999.
- [35] P. Zacek et al. *Physical Review*, D34:2621, 1986.
- [36] A. Kurylov et al. *hep-ph/0211306*, 2002.
- [37] T. Mitsui. *internal note of KamLAND*.
- [38] W.R.Leo. *Techniques for Nuclear and Particle Physics Experiments*. Springer Verlag.
- [39] R.S.Raghavan et al. *Physical Review Letters*, 80:635, 1998.
- [40] T. Hagner et al. *Astroparticle Physics*, 14:33, 2000.
- [41] T.K. Gaisser et al. *Physical Review*, D38:85–95, 1988.
- [42] K.Schreckenbach et al. *Physics Letters*, B160:325–330, 1985.
- [43] A.A. HAHN et al. *Physics Letters*, B218:365–368, 1989.
- [44] P.Vogel et al. *Physical Review*, C24:1543–1553, 1981.
- [45] B. Achkar et al. *Physics Letters*, B374:243, 1996.
- [46] L.H. Miller. *Ph.D. thesis*, Stanford univ., 2000.
- [47] V.I.Kopeikin et al. *Physics of Atomic Nuclei*, 64-5:849–854, 2001.
- [48] <http://wwwinfo.cern.ch/asd/geant4/geant4.html>.
- [49] F. Ajzenberg-Selove et al. *Physical Review*, 120:500, 1960.
- [50] D.E. Alburger et al. *Physical Review*, 119:1970, 1960.
- [51] G. L. Fogli et al. *Physical Review*, D66:053010, 2002.
- [52] Glen Cowan. *Statistical Data Analysis*. Clarendon press Oxford, 1998.
- [53] J.N. Bahcall, M.C. Gonzalez-Garcia, and C. Pena-Garay. [*hep-ph/0212147*], 2002.